OSCILLATORY FLOW IN CURVED TUBES

THOMAS MULLIN

DOCTOR OF PHILOSOPHY

UNIVERSITY OF EDINBURGH

OCTOBER 1978

ABSTRACT

A theoretical and experimental study of laminar fully-developed flow in a curved tube under the influence of a sinusoidal pressure gradient is presented. Several unexpected flow features were found and explanations are given for these.

The governing equations are linearised by expansions in terms of an amplitude parameter $G = \frac{2K'^2a^3}{R\nu^2\omega^2}$ where a is the radius of the tube, R the radius of curvature, ν the kinematic viscosity and K and ω are the amplitude and frequency of the pressure gradient respectively. Numerical solutions are found using the finite Hankel transform technique and these are valid for arbitary values of the frequency parameter $\alpha = a\sqrt{\omega/\nu}$. Closed form solutions are then found in the limits $\alpha \to 0$ and $\alpha \to \infty$ and agreement with the work of previous studies is found.

A photon-correlation system is described which has successfully been employed to measure oscillatory air flow in glass tubes down to 3.6 m.m. in diameter. A sampled version of the signal from a laser Doppler optical arrangement has been used to construct velocity profiles at different phase positions in both fully-developed and developing curved tube flows. Peak Reynolds numbers were $\sim$ 100 and the α range concerned was $\sim$ 0.5 - 5.

General agreement between theory and experiment is found to be good and it is shown that the frequency parameter has the greatest influence on flow distribution.

PREFACE

The work presented in this thesis was carried out over the period Oct. 1975 - Oct. 1978, and is submitted for the PH.D degree according to the University regulations.

I would like to thank Prof. W. Cochran for his support in obtaining the grant which enabled me to carry out this research and for the use of the facilities in the Physics Dept. My supervisors, Dr. Clive A. Greated, Director of the Fluid Dynamics group, and Dr. Ian Grant are thanked for suggesting the project and for their continuing encouragement throughout.

I am indebted to Dr. Frank Smith of Imperial College, London for his helpful discussions on the theory presented and for reading and criticising the original draft of this section. Mr. Douglas Molyneux constructed most of the experimental apparatus and I am grateful for his dedication and skill in producing a reliable system.

Dr. M.A.S. Ross gave me a clear insight into the fluid dynamics involved in this problem and she is thanked for her inspiration and sympathetic ear.

My wife, Sylvia not only supported me throughout this research but also volunteered to type this thesis. This work is therefore dedicated to her and to our children, Zoe and Graham.

Finally, the support of S.R.C. is acknowledged for providing me with a grant for this period.

T. Mullin

CONTENTS

C H A P T E R 1

REVIEW OF PREVIOUS RESEARCH INTO OSCILLATORY AND CURVED TUBE FLOWS

INTRODUCTION

This chapter will present a review of the work which has played a significant role in the understanding of both oscillatory and curved tube flows. Both theorectical and experimental work will be discussed in each sub-section, leading finally to a survey of work done on oscillatory flow in curved tubes, the topic of this study.

1.1 OSCILLATORY FLOW IN A STRAIGHT PIPE

Oscillatory flow in a straight pipe is well understood and there have been several theoretical and experimental studies which are in agreement. Sexl (1930) solved the Navier-Stokes equations for a long straight pipe with periodic pressure gradient and no radial flow. The solutions he obtained explained the "annular effect" found in the experiments of Richardson and Tyler (1929) in which at certain frequencies higher axial velocity components were found off the axis of the tube.

The flow is controlled by the frequency parameter

$\alpha = \frac{a\sqrt{\omega}}{\sqrt{\nu}}$ Womersley (1957), where a is the radius of the tube, ω is the radial frequency of the applied pressure gradient, and ν is the kinematic viscosity. For low values of this parameter the flow is quasi-steady and each profile is Poiseuille in form. As α increases, the fluid in the centre of the pipe begins to behave inviscidly lagging behind the applied pressure gradient, giving rise to complex velocity profiles, (see Uchida (1956) for details). At values of $\alpha > 10$, the fluid can be considered as an inviscid central core with thin boundary layers along the walls as the oscillation time of the flow is now much shorter than the time for vorticity to diffuse from the wall.

Experimental studies range from the hot wire work of Richardson and Tyler to more recent studies of Denison and Stevenson (1970) who used laser anemometry in a water/glycerine mixture, and obtained good agreement with theory. Thus oscillatory flow in a straight pipe, which is one of the flow situations where an exact solution to the Navier-Stokes equations is found, has been understood for some time.

1.2 STEADY FLOW IN A CURVED TUBE

From a theoretical standpoint, fully developed steady flow in a curved tube has been extensively studied by both analytical and numerical techniques.

The classic work of Dean (1927, 1928) was the first approach to the problem and although several other workers using similar methods have studied the problem, it was not until the work of McConalogue and Srivastava (1968) that any real progress was made analytically. Recently, Collins and Dennis (1975) solved the Navier-Stokes equations for this case using a finite-difference scheme, providing solutions covering a great deal of the practical range of interest.

The generally accepted physical explanation of the events occurring as fluid flows in a curved pipe are as follows. When a fluid flows in a curved pipe it experiences a centrifugal force due to the curvature. A pressure gradient is set up across the pipe to balance this centrifugal force, the pressure being greatest at the outside of the curve, lower at the top and bottom of the tube and least at the inner side of the curve. This has the effect of producing a secondary flow in the plane of the tube at right angles to the axial flow, which has the familiar D - type formation predicted by Dean. The secondary flow, acting outwards in the centre of the tube, modifies the axial velocity such that the higher velocity components move towards the outside of the curve.

The Navier-Stokes equations for this problem are very complex, however Dean showed that by assuming the curvature of the pipe to be small, then the equations can be greatly simplified. The centrifugal terms are

retained in the approximate equations and it is these approximate equations which are used for many of the studies of curved tube flow.

Dean then employed a perturbation scheme about straight pipe flow in terms of $K = \frac{2 W_o^2 a^3}{R \nu^2}$ where W_o is a typical velocity, a is the radius of the tube, R the radius of curvature and ν the kinematic viscosity, and obtained solutions for the secondary flow equation and the axial velocity to order K. He continued his expansion of the axial velocity equation up to order K^3 considering only the terms affecting the volume flow rate.

The main effect of the secondary flow is to reduce the volume flow rate compared with a straight pipe with the same applied pressure gradient. Using this friction factor loss comparison, Dean showed that his expansion was valid for $K \leq 576$. White (1929) showed experimentally that flows of the same Reynolds number but different K values had friction coefficients which lay on a single curve. Thus K is a dynamical similarity coefficient and the small curvature assumption made by Dean is justified.

Dean and Hurst(1959) used a simplified two-dimensional scheme to investigate primarily the axial flow equation. They made the crude assumption that the main effects of the secondary flow are concentrated in the centre of the

tube and in this region it can be replaced by a uniform stream. This simplifies the axial velocity equation to a form of Bessel's equation and produced results for the loss in flow rate which agree with the experiments of White.

McConalogue and Srivastava extended the original work of Dean solving the small curvature equations by reducing them to ordinary differential equations, using Fourier analysis. The range of validity of this work was for their parameter $D \leq 605.72$ where $D = 96$ corresponds to the upper limit of Deans work. They found good agreement with earlier experimental work.

The experiments of White indicate that the laminar flow range of practical interest may be up to $D \backsim 5000$. In order to investigate the higher Dean number flows, the small curvature equations have been treated by numerical methods Greenspan (1973), Collins and Dennis (1975) and boundary layer techniques, Barua (1963). The work of Collins and Dennis is in good agreement with experiment, with McConalogue and Srivastava and also agrees with the theory of Barua for values of $D \geq 2000$. Greenspan, on the other hand, has used a coarse grid in his finite difference approximation and the scheme breaks down for $D \backsim 5000$. Collins and Dennis showed the importance of using a fine mesh and as a result do not agree with the results of Greenspan over most of the Dean number range.

The experimental work on fully developed curved tube flow is mainly that of White (1929) and Adler (1934). White investigated the friction coefficient for various

curved pipes coiled in a helix and showed that all coefficients lay on a unique curve for varying Dean number. The coefficients departed from this curve at points where it was assumed turbulence had set in. This assumption was later confirmed experimentally by G. I. Taylor (1929), who injected dye into curved glass tubes and observed the transition to turbulence.

Adler confirmed the work of White and thus the small curvature approximation of Dean was shown to be a good one for, at least, curvatures up to $\delta^{1}/15$. He also made detailed axial velocity measurements which were of very good quality and were made using a pitot tube.

Thus fully developed steady flow has been thoroughly investigated from both a theoretical and experimental point of view, although there is room for more experimental work using modern non-intrusive measuring techniques such as the laser-Doppler-velocimeter.

1.3 ENTRY FLOW INTO A CURVED TUBE

The problem of entry flow of a steady, incompressible viscous fluid into a curved tube has received little attention, much of it being only in the last eight years. There appears to be no generally accepted theory as yet, although some detailed experimental work has been done.

Smith (1976) considered the case of a fully developed straight pipe flow entering a uniformly curved section. The conditions imposed on the flow were those

of large but finite Reynolds number and very small curvature. The flow was considered as consisting of two regions in the curved section, a central core and a boundary layer region along the walls.

The wall shear maximum was found to occur initially at the inside of the curve and in fact even upstream of the bend, the shear distribution was found to be governed by the downstream conditions. The secondary flow, induced by centrifugal effects, eventually overtakes the assumed two region state and streamlines become closed, moving the peak in the axial shear to the outside of the curve. The cross-over is predicted to be 1.51 radii downstream of the start of the curve and found to be independent of Reynolds number. The peak in the axial velocity in the core, drifts straight across the bend to the outside of the curve under the action of the secondary flow and the fully developed state is finally reached.

Another study of developing flow was made by Yao and Berger (1975) who considered the case of a uniform entry profile. The Reynolds number was again assumed large so that the boundary layer method of Barua could be used and his fully developed solution was assumed as the final state. It was found that the central core remained uniform until the thickening inner boundary layer displaced the axial velocity peak towards the outside of the curve and the fully developed state reached.

Perhaps the most important conclusion of the work was that the entrance length, at least for high Reynolds numbers, is shorter for a curved pipe than it is for a corresponding straight pipe. The entrance length was found to be inversely proportional to the square root of the Dean number.

Finally Singh (1974) considered the cases of (1) constant dynamic pressure at the entrance and (II) uniform entry. However, curvature does not play an important part in the solution and is only valid for 2.5 tube radii downstream of the start of the bend. The main conclusions reached are that the shear maximum is initially towards the inside of the curve, the cross-over occurring at 1.9 radii for the entry condition (1) and 0.95 radii for condition (II)

Thus the theoretical work is still in its infancy, probably the extensions suggested by Smith to his theory to encompass other profile shapes would be a good method to adopt.

The experimental work of Agrawal, Talbot and Gong (1978) provides an extensive coverage of uniform entry flow into a curved tube. Using laser anemometry they measured axial and secondary velocities at 7 stations around two curved tubes of curvature ratios $^1/_7$ and $^1/_{20}$.

In order to explain their results they considered the developing flow to consist of an inviscid core surrounded by a ring-vortex boundary layer. The ring

vortex, travelling with the axial velocity, moves different angular distances around the curve in unit time giving the boundary layer a second component of vorticity. This has the effect of establishing a secondary flow which thickens the boundary layer at the inner wall and keeps the boundary layer thin at the outer wall.

The core is assumed to initially develop towards its inviscid fully developed state of axial velocity peak towards the inside of the curve. This, it is assumed, would require inward secondary motion within the core. Unfortunately, none of the measurements were made in this early stage of development, although the peak in the axial velocity is found to persist towards the inside at the first two measuring stations. This is explained as the "fully developed" state of the inviscid core prior to modification by the secondary flow.

The secondary flow measurements indicate progression towards the fully developed state with flow inwards around the boundary and outwards along the plane of the bend. However, secondary flow reversals are found to occur as the fully developed state is approached and this is interpreted as three-dimensional separation at the inside edge of the curve. Another interesting feature of the measurements made is the occurrence of a double peak in the axial velocity at higher Dean numbers. This was also observed by Olsen (1971) who made measurements in

a similar situation using a pulsed hot-wire technique.

Olsen studied both flat and parabolic entrance profiles at various Dean numbers in tubes of curvature $^1/_{4.66}$ and $^1/_{16}$. The results of the flat entrance profile are in qualitative agreement with Agrawal et al in that the peak of the axial velocity goes initially towards the inside of the curve and also the appearance of the double peaked profile at higher Dean numbers. Olsen explains the double peaked profile in terms of an "overshoot" in the secondary flow causing some of the higher axial velocity at the outside of the curve to be moved to the inside of the curve. The results of both investigators would appear to support this, in that the occurrence of the double peak is accompanied by an increase in secondary flow.

The flat entry profile is distorted with a peak towards the inside of the curve even at 0^o round the bend. This influence of the upstream conditions is not found in the parabolic case and the distortion is explained as the potential flow limit. However, the results would appear to indicate that this is a function of both the curvature and the Dean number and perhaps finite curvature is not the only cause of this distortion.

The parabolic inlet profile, on the other hand, has its peak velocity distorted directly towards the outside of the curve when the secondary flow takes effect. This is in agreement with the assumption of Smith but more

detailed measurement would have to be made close to the wall to verify the predictions about the shear stresses in the inlet of the bend.

The work of Olsen has been largely ignored by the later studies discussed above, but it contains many detailed measurements which are of a high quality. Along with the work of Agrawal et al this could serve to guide future theoretical studies which ought to involve the distortion of the central core. There is also a need for more detailed experimental work to be done on the establishment of secondary flow which is not clear as yet.

1.4 FULLY DEVELOPED OSCILLATORY FLOW IN A CURVED TUBE

The first theoretical study of this problem was carried out by Lyne (1970), who considered the high frequency regime. Here, as discussed earlier, the flow can be considered as consisting of a central inviscid core surrounded by a very thin boundary layer. Thus the techniques of boundary layer theory were applied to the small curvature equations.

Initially, an expansion was used in terms of the frequency parameter β $(= \sqrt{\frac{2}{\alpha}})$ which is small. Solutions were found to the boundary layer equations up to order β and it was found that the secondary flow consisted of a steady part plus a component oscillating at twice the frequency of the applied pressure gradient.

In order to progress with the equations for the secondary flow in the central core, a further expansion had to be used in terms of R_s , the Reynolds number of the steady secondary flow. The secondary flow in the interior was found to be steady and flowing in the opposite direction to that for steady flow in a curved tube. A further limit $R_s \to \infty$ was taken and the secondary flow was found to have the same form as the small R_s case.

The secondary flow in the boundary layer proceeds as in the steady flow case from outer wall to inner around the wall of the tube but now returns along the edge of the core. A secondary boundary layer is formed as in the case of Stuart (1963) and the central core is dragged round causing flow in the central plane to be in the opposite sense to that for steady flow.

Lyne carried out a rather crude experiment to verify his conclusions. This consisted of bending a plastic pipe in a circle and oscillating the water contained in it in a sinusoidal fashion using a piston pump. By injecting dye into the pipe he could observe that the steady component of the secondary flow was reversed when $\beta = 0.05$.

As $\beta \to \infty$ the quasi-steady flow region is approached with the normal outward secondary flow. The cross-over point between these regimes can be found from the analysis of Lyne to be $\beta \sim 0.11$ ($\alpha = 12.86$).

The next analysis of the problem was carried out by Zalosh and Nelson (1973) who attempted to cover the whole frequency range. They linearised the small curvature equation by expanding in terms of the curvature and thus essentially they were perturbing the straight pipe solution. The work relied heavily on the thesis of Zalosh (1970) which contained a major error in the derivation of the third momentum equation.

The linearised equations are solved using finite Hankel integral transforms and there is an error in the application of this in the first order secondary flow equation. The effect of this is to give too low a value to the transition α value where reverse secondary flow occurs. A further expansion is used in the quasi-steady limit which states that the Dean type solution is obtained for the first order axial velocity perturbation, but this is incorrect.

Finally, the boundary layer approach is tried for the region $\alpha > 10$ and this predicts a transition α value of 10.7 which is greater than the Hankel transform value but less than that of Lyne. This is to be expected since the approximation of Lyne is of a higher order. Thus most of the work of Zalosh and Nelson is incorrect although the method used is good and in fact will be used later in this thesis.

The bulk of the theoretical work to date is thus due to Lyne who considered mainly the secondary flow field and found the axial flow field to be undisturbed

by the curvature.

Bertelsen (1975) carried out experiments on oscillating oil in a plexi-glass U-tube. He used a stroboscopic lamp with aluminium dust particles in the flow to estimate secondary flow parameters. All experiments were carried out in a tube of curvature 0.1 at R_s values O(1) in the frequency parameter range $\alpha = 12 - 31$.

Agreement between the experiments and the theory of Lyne was found to be good except that a distortion of the central core was found for $\alpha < 21$. This took the form of a thicker boundary layer at the outside of the curve, which Bertelsen showed was due to the finite curvature of the tube used in the experiment. He did this by expanding the full Navier-Stokes equations in terms of the curvature. Using the solution of Lyne he obtained a solution for the axial velocity up to order (a/R) for both the axial and the secondary velocities.

The results obtained for the secondary flow now gave good agreement with the theory, but the axial velocity results indicate that the peak in velocity is displaced towards the inside of the curve at all phase positions. This point is not discussed by Bertelsen but it would appear to be similar to the findings of the studies on entrance flow. Bertelsen also observed the transition from the two vortex to the four vortex system predicted by Lyne. He found that this occurred in his system at an alpha value > 12.3 giving some confirmation of the

value obtained by Lyne.

Other experimental work has been carried out by Munson (1975) who also used a flow visualisation technique to estimate secondary flow parameters over the alpha range 0.7→32. In these experiments he timed the motion of a streak of neutrally buoyant dye moving across the plane of the bend under the action of the steady secondary flow component. The results indicate a steady decline in the steady secondary flow as alpha increases eventually reversing at $\alpha = 13.4$, which is in close agreement with the theory of Lyne. The R_s value is only quoted for one frequency and it is not clear if the R_s value was kept constant over the full frequency range. Further, the small alpha case would seem to indicate that the steady component becomes constant as $\alpha \rightarrow 0$, which is in agreement with the quasi-steady work of Zalosh.

A further experiment was performed by Munson (1976) in which he considered the case of an oscillating torus with the enclosed fluid initially stationary. Using a similar technique to previously, he found that the secondary flow was reversed at all frequencies of oscillation. Expanding the small curvature equations in terms of α^2 he found that this reverse flow was also predicted from theory. The explanation given of this phenomenon is that the "centrifugal force gradient of the primary flow" is in the opposite sense to that for

slowly oscillating fluid in a stationary torus.

A more general approach to the problem was attempted by Smith (1975), who considered the case of an oscillating pressure gradient superimposed on a mean. This introduces a third parameter into the small curvature equations, viz. the steady flow Dean number. The interplay between the oscillatory part and the steady part was found to be complicated. In the oscillatory limit however, agreement was found with Lyne in the high frequency limit and with Dean in the quasi-steady limit.

Thus the study of oscillatory flow in a curved tube has been restricted to high and low frequency limits from a theoretical standpoint. The transition region between these two regions is complex, as is the transition region in straight pipe flow. Experimentally, there is a need for a more detailed study of the problem to be made at all alpha values.

CHAPTER 2

THEORETICAL STUDY OF OSCILLATORY FLOW IN A CURVED TUBE

INTRODUCTION

This chapter contains solutions to the Navier-Stokes equations for laminar flow under the influence of a sinusoidal pressure gradient in a circular pipe bent in an arc of a circle of small curvature. The equations are derived from the corresponding steady flow equations and are found to be controlled by an amplitude parameter G, and a frequency parameter α. Initially, a perturbation scheme is employed in terms of G and the resulting linearised equations solved, using finite Hankel transforms.

However, it is found that as the frequency parameter α increases, the integrals involved in the transformation process require large amounts of computer time before convergence can be assured. This is because they involve the products of Kelvin's functions, which become large as α increases, and Bessel functions, and thus the integrals are highly oscillatory. It will be shown that the equations used here reduce to the second order equations of Lyne (1970) as $\alpha \to \infty$ and that in this limit the boundary layer method is a good approximation at least for the secondary flow.

In order to gain a physical insight into the effect of each term in the expansion, each linearised equation

Figure (2.1.1) Co-ordinate System

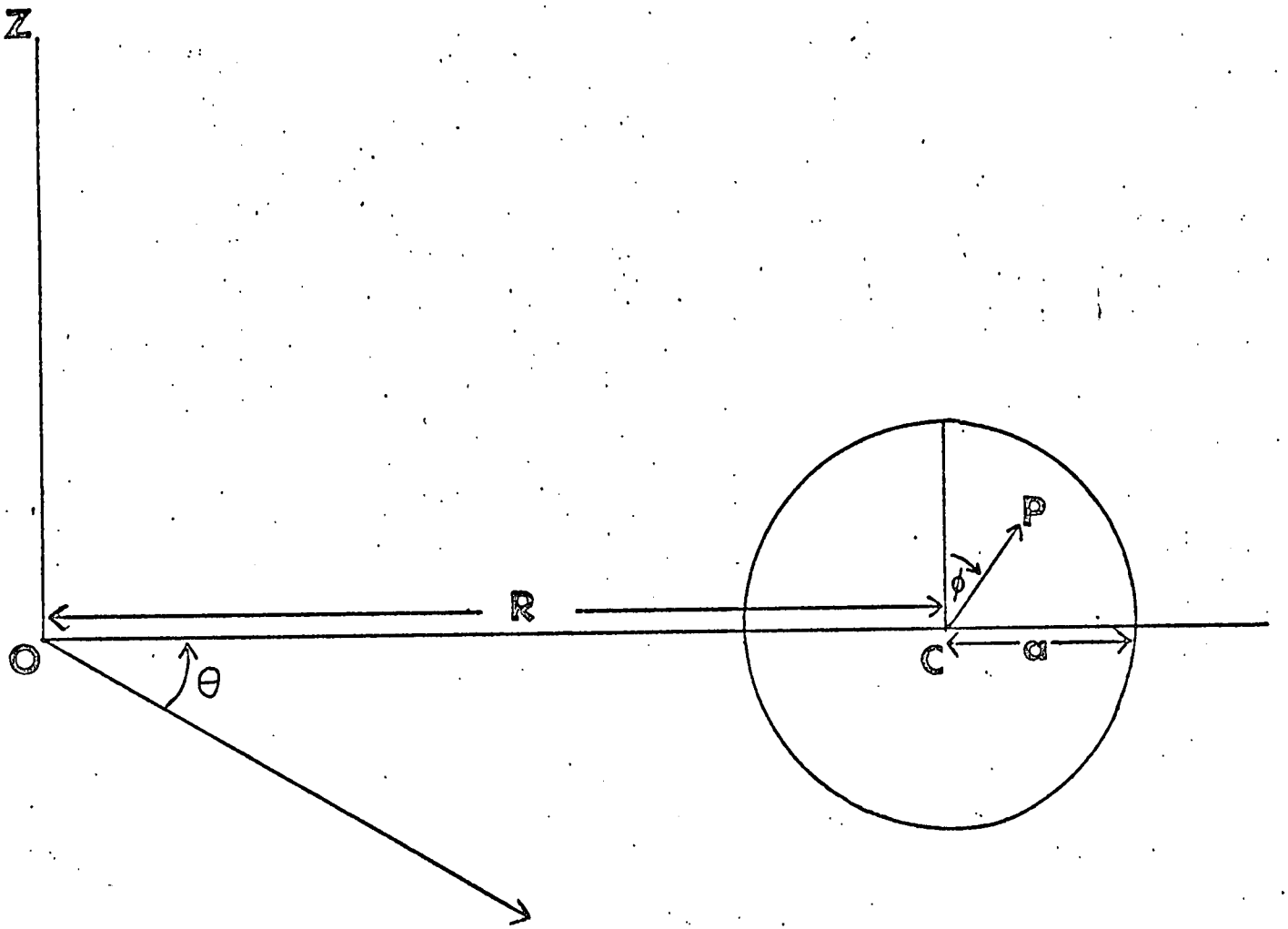

is further expanded in terms of α^2 in the limit $\alpha \to 0$. The results of this expansion are given in sections 2.6 - 2.8.

The Hankel transform solution is therefore most useful in the intermediate α range between the quasi-steady and boundary layer regions where viscosity acts over varying amounts of the tube depending upon the phase and frequency parameter. This gives rise to complicated velocity profiles which cannot be approximated in any obvious simple manner.

2.1 THE EQUATIONS OF MOTION

This study will use the full Navier-Stokes equations for the flow situation as the starting point. The system of co-ordinates to be used are shown in Fig.(2.1.1.)

A circular pipe of radius a is coiled in a toroid around an axis OZ such that a section of the pipe is specified by an axial plane through the pipe which makes an angle θ' to the fixed axial plane. The radius of the circle in which the pipe is coiled is given by R and this will be used to specify the non-dimensional radius of curvature (a/R) used later in the analysis.

Any point P within a plane of the pipe will be specified by the orthogonal co-ordinates (r', ϕ, θ') and the components of velocity corresponding to these co-ordinates will be given by U', V', and W' respectively.

Thus U' will be in the direction CP, V' perpendicular to U' and in the plane of the cross-section and W' perpendicular to this plane.

The steady flow case was first studied by Dean (1928) and it is his approach that will be followed here. A fully developed oscillatory flow situation will be assumed to exist in the plane of interest and thus U', V' and W' will be assumed independent of θ'. Of course P, the pressure along the pipe, will not be independent of θ' but a simple form will be assumed for P later in the analysis.

The unsteady Navier-Stokes equations follow directly from those of Dean as:-

$$\frac{\partial U'}{\partial t} + U' \frac{\partial U'}{\partial r'} + \frac{V'}{r'}\frac{\partial U'}{\partial \phi} - \frac{V'^2}{r'} + \frac{W'^2 \sin\phi}{R + r' \sin\phi} =$$

$$- \frac{\partial}{\partial r'}\left(\frac{P}{\rho}\right) - \nu\left(\frac{1}{r'}\frac{\partial}{\partial \phi} + \frac{\cos\phi}{R + r'\sin\phi}\right)$$

$$\left(\frac{\partial V'}{\partial r'} + \frac{V'}{r'} - \frac{1}{r'}\frac{\partial U'}{\partial \phi}\right) \quad \text{---------} \quad (2.1.1)$$

$$\frac{\partial V'}{\partial t} + \frac{V'}{r'}\frac{\partial V'}{\partial \phi} + U'\frac{\partial V'}{\partial r'} + \frac{U'V'}{r'} - \frac{W'^2 \cos\phi}{R + r'\sin\phi} =$$

$$-\frac{1}{r'}\frac{\partial}{\partial \phi}\left(\frac{P}{\rho}\right) + \nu\left(\frac{\partial}{\partial r'} + \frac{\sin\phi}{R + r'\sin\phi}\right)\left(\frac{\partial V'}{\partial r'} + \frac{V'}{r'} - \frac{1}{r'}\frac{\partial U'}{\partial \phi}\right) \quad \text{----------} \quad (2.1.2)$$

$$\frac{\partial W'}{\partial t} + U' \frac{\partial W'}{\partial r'} + \frac{V'}{r'} \frac{\partial W'}{\partial \phi} + \frac{U'W' \sin \phi}{R+r' \sin \phi} + \frac{V'W' \cos \phi}{R+r' \sin \phi} =$$

$$- \frac{1}{R+r' \sin \phi} \frac{\partial}{\partial \theta}\left(\frac{P}{\rho}\right) + \nu\left[\left(\frac{\partial}{\partial r'} + \frac{1}{r'}\right)\left(\frac{\partial W'}{\partial r'}\right.\right.$$

$$\left.\left. + \frac{W' \sin \phi}{R+r' \sin \phi}\right) + \frac{1}{r'} \frac{\partial}{\partial \phi}\left(\frac{1}{r'} \frac{\partial W'}{\partial \phi} + \frac{W' \cos \phi}{R+r' \sin \phi}\right)\right] - - - (2.1.3)$$

For an incompressible fluid in this situation, the equation of continuity is given by:-

$$\frac{\partial U'}{\partial r'} + \frac{U'}{r'} + \frac{U' \sin \phi}{R+r' \sin \phi} + \frac{1}{r'} \frac{\partial V'}{\partial \phi} + \frac{V' \cos \phi}{R+r' \sin \phi} = 0 - -(2.1.4)$$

In order to make some progress with these equations the simplifying assumption that the curvature is very small i.e. $(a/R) \prec\prec 1$ will be made. Whilst greatly simplifying the equations, the main effects of curvature are retained in terms such as $\frac{V'^2}{r'}$, although the effects of finite curvature may play an important role as shown by Bertelsen (1975). The following equations now result :-

$$\frac{\partial U'}{\partial t} + U' \frac{\partial U'}{\partial r'} + \frac{V'}{r'} \frac{\partial U'}{\partial \phi} - \frac{V'^2}{r'} - \frac{W'^2 \sin \phi}{R} = - \frac{\partial}{\partial r'}\left(\frac{P}{\rho}\right)$$

$$- \frac{\nu}{r'} \frac{\partial}{\partial \phi}\left(\frac{\partial V'}{\partial r'} + \frac{V'}{r'} - \frac{1}{r'} \frac{\partial U'}{\partial \phi}\right) - - - (2.1.5)$$

$$\frac{\partial V'}{\partial t} + U' \frac{\partial V'}{\partial r'} + \frac{V'}{r'} \frac{\partial V'}{\partial \phi} + \frac{U'V'}{r'} - \frac{W'^2 \cos \phi}{R} = -\frac{1}{r'} \frac{\partial}{\partial \phi}\left(\frac{P}{\rho}\right)$$

$$+\nu \frac{\partial}{\partial r'}\left(\frac{\partial V'}{\partial r'} + \frac{V'}{r'} - \frac{1}{r'} \frac{\partial U'}{\partial \phi}\right) - - - - \quad (2.1.6)$$

$$\frac{\partial W'}{\partial t} + U' \frac{\partial W'}{\partial r'} + \frac{V'}{r'} \frac{\partial W'}{\partial \phi} = -\frac{1}{R} \frac{\partial}{\partial \theta}\left(\frac{P}{\rho}\right) + \nu\left(\frac{\partial^2 W'}{\partial r'^2} + \frac{1}{r'} \frac{\partial W'}{\partial r'}\right.$$

$$\left. + \frac{1}{r'^2} \frac{\partial^2 W'}{\partial \phi^2}\right) \quad - - - - - \quad (2.1.7)$$

$$\frac{\partial U'}{\partial r'} + \frac{U'}{r'} + \frac{1}{r'} \frac{\partial V'}{\partial \phi} = 0 \quad - - - \quad (2.1.8)$$

From equation (2.1.8) the stream function $f(r, \phi)$ can be introduced such that:-

$$U' = -\frac{1}{r'} \frac{\partial f}{\partial \phi}, \qquad V' = \frac{\partial f}{\partial r'} \quad - - - \quad (2.1.9)$$

The pressure terms in equations (2.1.5) and (2.1.6) can be eliminated by differentiating (2.1.5) w.r.t. ϕ, (2.1.6) w.r.t. r' plus multiplication by -r' and adding the resulting equations. This process plus substitution for U' and V' using (2.1.9) leads to the vorticity equation:-

$$-r' \frac{\partial}{\partial t}\left(\nabla^2 f\right) + \left(\frac{\partial f}{\partial \phi} \frac{\partial}{\partial r'} - \frac{\partial f}{\partial r'} \frac{\partial}{\partial \phi}\right)\nabla^2 f + \frac{2W'}{r'}$$

$$\left(r' \cos \phi \frac{\partial W'}{\partial r'} - \sin \phi \frac{\partial W'}{\partial \phi}\right) = -\nu r' \nabla^4 f - - \quad (2.1.10)$$

The third momentum equation becomes:-

$$\frac{\partial W'}{\partial t} + \frac{1}{r'}\left(\frac{\partial f}{\partial r'}\frac{\partial W'}{\partial \phi} - \frac{\partial f}{\partial \phi}\frac{\partial W'}{\partial r'}\right) = -\frac{1}{R}\frac{\partial}{\partial \theta'}\left(\frac{P}{e}\right) + \nu\nabla^2 W' \quad - - - - \quad (2.1.11)$$

where:- $\nabla^2 = \frac{\partial^2}{\partial r'^2} + \frac{1}{r'}\frac{\partial}{\partial r'} + \frac{1}{r'^2}\frac{\partial^2}{\partial \phi^2}$,

the ordinary Laplacian operator in polar co-ordinates.

A sinusoidal pressure gradient which has no mean part is imposed on the flow such that:-

$$-\frac{1}{R}\frac{\partial}{\partial \theta'}\left(\frac{P}{e}\right) = K' \cos \omega t \quad - - - - \quad (2.1.12)$$

where K' is the amplitude of the applied pressure gradient and ω is the angular frequency.

Using the following non-dimensionalisation procedure on the two equations a more convenient form is obtained.

$$r = \frac{r'}{a}, \qquad \tau = \omega t, \qquad \psi = \frac{f}{\nu}, \qquad w = \frac{W'\omega}{K'}$$

Equation (2.1.10) becomes:-

$$\frac{a^2\omega}{\nu}\frac{\partial}{\partial \tau}\left(\nabla^2\psi\right) - \frac{1}{r}\left(\frac{\partial \psi}{\partial \phi}\frac{\partial}{\partial r} - \frac{\partial \psi}{\partial r}\frac{\partial}{\partial \phi}\right)\nabla^2\psi$$

$$-\frac{2K'^2 a^3}{R\nu^2\omega^2}\frac{w}{r}\left(r\cos\phi\frac{\partial w}{\partial r} - \sin\phi\frac{\partial w}{\partial \phi}\right) = \nabla^4\psi$$

$$- - - \quad (2.1.13)$$

and equation (2.1.11) becomes:-

$$\frac{a^2\omega}{\nu}\frac{\partial w}{\partial \tau} + \frac{1}{r}\left(\frac{\partial \psi}{\partial r}\frac{\partial w}{\partial \phi} - \frac{\partial \psi}{\partial \phi}\frac{\partial w}{\partial r}\right) = \frac{a^2\omega}{\nu}\cos\tau + \nabla^2 w \quad - \quad - \quad (2.1.14)$$

This gives rise to two parameters which will be called the control parameters of the equations. The first of these is $\alpha = a\sqrt{\frac{\omega}{\nu}}$ as defined by Womersley (1955), which may be interpreted in the following way. Schlichting (1932) argued that the oscillatory boundary layer will have thickness of order $(\nu/\omega)^{\frac{1}{2}}$ due to the diffusion of vorticity with period $2\pi/\omega$ and thus α is the ratio of this to the characteristic length, in this case the radius of the tube.

For low frequencies, the flow is thus dominated by viscous effects while for large frequencies oscillatory effects become important, leaving viscosity to act only along the walls of the pipe. Therefore, there is a low frequency quasi-steady regime, a high frequency boundary-layer flow regime and a transition stage between the two.

The second control parameter is $G = \frac{2K'^2 a^3}{R\nu^2\omega^2}$.

If the pressure gradient amplitude is re-written as $W_o\omega$, where W_o is the mean velocity along the centre line of the pipe, then G is seen to reduce to the same expansion parameter as used by Dean. However, W_o is itself a function of α for a fixed value of K' but is almost independent of α in the quasi-steady limit. The relationship becomes more complicated as α increases,

as shown by Uchida,(1956). G may also be written as $2\alpha^2 R_s$ where $R_s \equiv \frac{K'^2 a}{R\nu\omega^3}$ as defined by Smith (1976) and Lyne (1970). R_s is in fact the Reynold's number of the steady component of the secondary flow. The equations are now expanded in terms of G and since the expansion is valid for all α values this implies that the expansion is only valid for R_s, O(1). Thus equating equal powers of G the following approximate equations result.

The expansions:-

$$w = w_0 + Gw_1 + G^2 w_2 + - - - -$$

$$\psi = G\psi_1 + G^2\psi_2 + - - - - - -$$

Give:-

$$\alpha^2 \frac{\partial w_0}{\partial \tau} - \left(\frac{\partial^2 w_0}{\partial r^2} + \frac{1}{r}\frac{\partial w_0}{\partial r}\right) = \alpha^2 \cos\tau - - - \quad (2.1.17)$$

$$\alpha^2 \frac{\partial(\nabla^2\psi_1)}{\partial\tau} - \nabla^4\psi_1 = w_0 \cos\phi \frac{\partial w_0}{\partial r} - - - \quad (2.1.18)$$

$$\alpha^2 \frac{\partial w_1}{\partial\tau} - \nabla^2 w_1 = \frac{1}{r}\frac{\partial\psi_1}{\partial\phi}\frac{\partial w_0}{\partial r} - - - - \quad (2.1.19)$$

$$\alpha^2 \frac{\partial}{\partial\tau}\left(\nabla^2\psi_2\right) - \nabla^4\psi_2 = \frac{w_0}{r}\left(r\cos\phi\frac{\partial w_1}{\partial r} - \sin\phi\frac{\partial w_1}{\partial\phi}\right)$$

$$+ w_1 \cos\phi \frac{\partial w_0}{\partial r} + \frac{1}{r}\left(\frac{\partial\psi_1}{\partial\phi}\frac{\partial}{\partial r} - \frac{\partial\psi_1}{\partial r}\frac{\partial}{\partial\phi}\right)\nabla^2\psi_1$$

$$- - - - \quad (2.1.20)$$

The zeroth order equation corresponds to the straight pipe equation for which there is a well known exact solution. The other equations do not have a closed form solution and will be evaluated using the Hankel integral transform method of Sneddon (1946). Unfortunately, this method presented many practical problems since it required the numerical evaluation of highly oscillatory integrals.

However, at small values of the frequency parameter a further expansion in α^2 on the approximate equation will be used to obtain closed form solutions which are valid up to $\alpha \sim 1.0$. At values of $\alpha > 10$ it will be shown that the boundary layer technique of Lyne is probably a good method and reasonable agreement between the Hankel transform solutions and those of the boundary layer method is found. Therefore the Hankel transform method will be shown to be a most useful method of dealing with the equations in the transition region between quasi-steady and boundary layer type flows.

2.2 STRAIGHT PIPE SOLUTION

The equation for w_o is given by:-

$$\alpha^2 \frac{\partial w_o}{\partial \tau} - \left(\frac{\partial^2 w_o}{\partial r^2} + \frac{1}{r} \frac{\partial w_o}{\partial r} \right) = \alpha^2 \cos \tau \quad ---(2.2.1)$$

A solution of this equation is sought of the form:-

$$w_o (r, \Upsilon) = \text{Re} (g(r) e^{i\Upsilon})$$

where Re means real part of.

Substitution of this expression into (2.2.1) leads to:-

$$\frac{d^2 g(r)}{dr^2} + \frac{1}{r} \frac{dg(r)}{dr} - i\alpha^2 g(r) = -\alpha^2 \quad - - - (2.2.2)$$

This equation has a solution, as given by Uchida (1956)

$$g(r) = - i \left\{ 1 - \frac{J_o (i^{3/2} \alpha r)}{J_o (i^{3/2} \alpha)} \right\} \quad - - - \quad (2.2.3)$$

with the boundary condition w_o and thus g(r) must remain finite in the centre of the tube and zero at the walls.

The more useful form of the solution can be found using the relationship:-

$$J_o (i^{3/2} x) = \text{ber } x + i \text{ bei } x$$

where ber and bei are Kelvin's functions. Writing the solution in real part only the following is obtained:-

$$w_o = B \cos \Upsilon + (1-A) \sin \Upsilon - \quad - \quad - \quad (2.2.4)$$

where:-

$$B = \frac{\text{bei}\alpha \ \text{ber}\alpha r - \text{ber}\alpha \ \text{bei}\alpha r}{\text{bei}^2\alpha + \text{ber}^2\alpha}$$

$$A = \frac{\text{bei}\,\alpha\,\text{bei}\,\alpha r + \text{ber}\,\alpha\,\text{ber}\,\alpha r}{\text{bei}^2\alpha + \text{ber}^2\alpha}$$

2.3 FIRST ORDER SECONDARY FLOW EQUATION

From equation (2.1.18)

$$\alpha^2 \frac{\partial}{\partial \tau}(\nabla^2 \psi_1) - \nabla^4 \psi_1 = w_o \frac{\partial w_o}{\partial r} \cos \phi \quad - - - (2.3.1)$$

Using the results of the previous section the R.H.S. may now be evaluated as:-

$$\text{R.H.S.} = \cos \phi \left\{ (B \cos \tau + (1-A) \sin \tau) \left(\frac{dB}{dr} \cos \tau - \frac{dA}{dr} \sin \tau \right) \right\} - - - \quad (2.3.2)$$

where:-

$$\frac{dB}{dr} = \alpha \left(\frac{\text{bei}\,\alpha\,\text{ber}'\alpha r - \text{ber}\,\alpha\,\text{bei}'\alpha r}{\text{bei}^2\alpha + \text{ber}^2\alpha} \right)$$

$$\frac{dA}{dr} = \alpha \left(\frac{\text{bei}\,\alpha\,\text{bei}'\alpha r + \text{ber}\,\alpha\,\text{ber}'\alpha r}{\text{bei}^2\alpha + \text{ber}^2\alpha} \right)$$

This leads to:-

$$\text{R.H.S.} = \frac{\cos \phi}{2} \left\{ \left[B \frac{dB}{dr} - (1-A) \frac{dA}{dr} \right] + \left[B \frac{dB}{dr} + (1-A) \frac{dA}{dr} \right] \cos 2\tau + \left[(1-A) \frac{dB}{dr} - B \frac{dA}{dr} \right] \sin 2\tau \right\}$$

$$- - - - (2.3.3)$$

The boundary conditions which must be obeyed by any solution to (2.3.1) are the usual no-slip conditions i.e. $\frac{\partial \psi_1}{\partial r}$ and $\frac{\partial \psi_1}{\partial \phi}$ are both zero at the edge of the pipe and also remain finite in the centre.

From equation (2.3.3.) it would seem to be appropriate to seek a solution of equation (2.3.1) of the form:-

$$\psi_1 = \psi_{10}\ (r, \phi) + \psi_{12}\ (r, \phi)\ e^{i2\tau}$$

This can be interpreted as a steady secondary flow component plus a component at twice the frequency of the applied pressure gradient. This is a well known phenomenon in other oscillatory flow problems (see e.g. J. T. Stuart (1963))

Substitution of this formulation of the secondary flow into (2.3.1) leads to the following equations:-

$$\nabla^4 \psi_{10} = \left\{ (1-A) \frac{dA}{dr} - B \frac{dB}{dr} \right\} \frac{\cos \phi}{2} \quad - - \quad (2.3.4)$$

$$2 i \alpha^2 \nabla^2 \psi_{12} - \nabla^4 \psi_{12} = \left\{ B \frac{dB}{dr} + (1-A) \frac{dA}{dr} + i \left[B \frac{dA}{dr} - (1-A) \frac{dB}{dr} \right] \right\} \frac{\cos \phi}{2} \quad - - - \quad (2.3.5)$$

The only variation with ϕ on the R.H.S. of these equations which appears is the factor cos ϕ and so now separable solutions are assumed of the form:-

$$\psi_{10} = C_o (r) \frac{\cos \phi}{2}$$

and:-

$$\psi_{12} = C_2(r)\frac{\cos\phi}{2}$$

and the following equations for $C_o(r)$ and $C_2(r)$ result:-

$$\left(\frac{d^2}{dr^2} + \frac{1}{r}\frac{d}{dr} - \frac{1}{r^2}\right)^2 C_o = (1-A)\frac{dA}{dr} - B\frac{dB}{dr} \quad - - \quad (2.3.6)$$

$$2i\alpha^2\left(\frac{d^2}{dr^2} + \frac{1}{r}\frac{d}{dr} - \frac{1}{r^2}\right)C_2 - \left(\frac{d^2}{dr^2} + \frac{1}{r}\frac{d}{dr} - \frac{1}{r^2}\right)^2 C_2 = B\frac{dB}{dr} + (1-A)\frac{dA}{dr} + i\left[B\frac{dA}{dr} - (1-A)\frac{dB}{dr}\right] \quad - - - - \quad (2.3.7)$$

The new boundary conditions for these equations can be obtained from the original boundary conditions and these are:-

$$C_o = \frac{dC_o}{dr} = 0 \quad \text{at } r = 1$$

and:-

$$C_2 = \frac{dC_2}{dr} = 0 \quad \text{at } r = 1$$

The form of the L.H.S. of the above equations would suggest that the Hankel integral transform may be appropriate to aid a solution. The form of the finite Hankel transform is given by Sneddon (1946) as:-

$$\bar{F}(\xi_j) = \int_0^1 F(r)\, J_\mu(\xi_j r)\, r\, dr$$

with the inversion formula:-

$$F(r) = 2 \sum_{j=1}^{\infty} \frac{\bar{F}(\xi_j)\, J_\mu(\xi_j r)}{\left[J'_\mu(\xi_j)\right]^2}$$

where μ is the order of the Bessel function and ξ_j is the jth eigen value of the equation:-

$$J_\mu(\xi_j) = 0$$

Tranter (1951) has shown that the finite Hankel transform of the Laplacian in polar co-ordinates is given by:-

$$\overline{\left(\frac{d^2}{dr^2} + \frac{1}{r}\frac{d}{dr} - \frac{\mu^2}{r^2}\right) F} = -\xi_j\, F(1) J'_\mu(\xi_j) - \bar{F}(\xi_j)\, \xi_j^2$$

and it is readily found that the Hankel transform of the bi-harmonic operator is:-

$$\overline{\left(\frac{d^2}{dr^2} + \frac{1}{r}\frac{d}{dr} - \frac{\mu^2}{r^2}\right)^2 F} = -\xi_j \left(\frac{d^2F}{dr^2} + \frac{1}{r}\frac{dF}{dr} - \frac{\mu F}{r^2}\right)_{r=1} J'_\mu(\xi_j) + \xi_j^4 \bar{F}(\xi_j)$$

Applying the second of these formulas to equation (2.3.6) and using the relevant boundary conditions gives:-

$$\left\{_{j}^{4}\ \bar{C}_o\ (\{_j) = I_1 - I_2 + \{_j \left.\frac{d^2C_o}{dr^2}\right|_{r=1} J_1'\ (\{_j)$$

- - - - (2.3.8)

where:-

$$I_1 = \int_o^1 (1-A)\ \frac{dA}{dr}\ J_1\ (\{_j\ r)\ rdr$$

and:-

$$I_2 = \int_o^1 B\ \frac{dB}{dr}\ J_1\ (\{_j\ r)\ rdr$$

The second derivative appearing on the R.H.S. of eq.(2.3.8) cannot be evaluated directly since it is not specified in the boundary conditions. However, it may be determined using the boundary condition on the first derivative in the following way:-

From the inversion formula:-

$$\frac{dC_o}{dr} = 2 \sum_{j=1}^{\infty} \frac{\bar{C}_o\ (\{_j)}{\left[J_1\ (\{_j)\right]^2}\ \frac{dJ_1}{dr}\ (r\{_j) = 0 \text{ at } r = 1$$

Therefore:-

$$\left.\frac{dC_o}{dr}\right|_{r=1} = 2\sum_{j=1}^{\infty} \frac{\bar{C}_o}{J_o(\xi_j)}\xi_j = 0$$

Substituting for $\bar{C}_o$ from (2.3.8.) leads to:-

$$\left.\frac{d^2C_o}{dr^2}\right|_{r=1} = -\frac{\sum_{j=1}^{\infty}\left[\left\{I_1(\xi_j)-I_2(\xi_j)\right\}/\left\{\xi_j^3 J_o(\xi_j)\right\}\right]}{\sum_{j=1}^{\infty}\left(\frac{1}{\xi_j^2}\right)} \quad - - - \quad (2.3.9)$$

In practice, the summations can only be taken over a finite number of terms and by using up to 20 terms in the summation series, convergence was assured for values of α in the range 0 - 10. (See Appendix B for details.) The integrals were evaluated using the Gaussian quadrature formula of Stroud (1966), as were all the integrals in this study.

The transformed equation (2.3.7.) is given by:-

$$-2i\alpha^2\xi_j^2\bar{C}_2(\xi_j)+\xi_j\left.\frac{d^2C_2}{dr^2}\right|_{r=1} J_1'(\xi_j)-\xi_j^4\bar{C}_2(\xi_j)$$

$$= I_2 + I_1 + i(I_3 - I_4) - - - - \quad (2.3.10)$$

where $I_3 = \int_0^1 B \frac{dA}{dr} J_1(\xi_j r)\, r\, dr$

$I_4 = \int_0^1 (1-A) \frac{dB}{dr} J_1(\xi_j r)\, r\, dr$

Therefore:-

$$\bar{C}_2(\xi_j) = \frac{I_1+I_2+ i(I_3-I_4) - \xi_j \left.\frac{d^2C_2}{dr^2}\right|_{r=1} J_o(\xi_j)}{-\xi_j^2 (2i\alpha^2 + \xi_j^2)} \quad \text{---(2.3.11)}$$

If now the R.H.S. is rationalised into its real and imaginary parts and a form assumed for C_2 such that:-

$$C_2 = C_{2R} + i\, C_{2I}$$

where C_{2R} is the real part and C_{2I} is the imaginary part of C_2 then the following expressions result:-

$$\bar{C}_{2R}(\xi_j) = \frac{\left[(I_1+I_2)\xi_j^2 + 2\alpha^2(I_3-I_4) - \xi_j^3 \left.\frac{d^2C_{2R}}{dr^2}\right|_{r=1} J_o(\xi_j) - \xi_j 2\alpha^2 \left.\frac{d^2C_{2I}}{dr^2}\right|_{r=1} J_o(\xi_j)\right]}{-\xi_j^2 (4\alpha^4 + \xi_j^4)}$$

(2.3.12)

$$\bar{C}_{2I}(\xi_j) = \left[\xi_j^2 (I_3 - I_4) - 2\alpha^2 (I_1 + I_2) + 2\alpha^2 \xi_j \left.\frac{d^2 C_{2R}}{dr^2}\right|_{r=1} J_o(\xi_j) - \xi_j^3 \frac{d^2 C_{2I}}{dr^2}\right] \Big/ \left[-\xi_j^2 (4\alpha^4 + \xi_j^4)\right]$$

- - - - - - - (2.3.13)

Again the second derivatives on the R.H.S. of the equations may be determined in the same way as for C_o.

$$\left.\frac{d^2 C_{2R}}{dr^2}\right|_{r=1} = \frac{2\alpha^2 S_3 S_4 - S_1 S_2}{S_2^2 + 4\alpha^4 S_3^2}$$

- - - (2.3.14)

and

$$\left.\frac{d^2 C_{2I}}{dr^2}\right|_{r=1} = \left[2\alpha^2 S_3 \frac{d^2 C_{2R}}{dr^2} - S_4\right] / S_2$$

- - - (2.3.15)

where:-

$$S_1 = \sum_{j=1}^{\infty} \frac{(I_1 + I_2)\xi_j^2 + 2\alpha^2 (I_3 - I_4)}{-\xi_j (4\alpha^4 + \xi_j^4) J_o(\xi_j)}$$

$$S_2 = \sum_{j=1}^{\infty} \frac{\xi_j^2}{4\alpha^4 + \xi_j^4}$$

$$S_3 = \sum_{j=1}^{\infty} \frac{1}{4\alpha^4 + \xi_j^4}$$

and:-

$$S_4 = \sum_{j=1}^{\infty} \frac{\xi_j^2 (I_3 - I_4) - 2\alpha^2 (I_1 + I_2)}{-\xi_j (4\alpha^4 + \xi_j^4) J_0(\xi_j)}$$

Thus the stream function ψ_1 can be obtained by combining the solutions of equations (2.3.4) and (2.3.5) Therefore:-

$$\psi_1 = \frac{\cos \phi}{2} \left[C_0 + C_{2R} \cos 2\tau - C_{2I} \sin 2\tau \right]$$

- - - - - - (2.3.16)

where C_0, C_{2R} and C_{2I} are given by their respective inversion formulae.

2.4 FIRST ORDER AXIAL VELOCITY PERTURBATION

From equation (2.1.19):-

$$\alpha^2 \frac{\partial w}{\partial \tau}_1 - \nabla^2 w_1 = \frac{1}{r} \frac{\partial \psi}{\partial \phi} \frac{\partial w_0}{\partial r} \quad - - - \quad (2.4.1)$$

with boundary conditions $w_1 = 0$ at $r = 1$. The R.H.S. of this equation is obtained from equations (2.3.16) and (2.2.4). Thus:-

$$\text{R.H.S.} = - \frac{\sin \phi}{4r} \left\{ \left(2C_o \frac{dB}{dr} + C_{2R} \frac{dB}{dr} + C_{2I} \frac{dA}{dr} \right) \cos \tau \right.$$
$$- \left(2C_o \frac{dA}{dr} - C_{2R} \frac{dA}{dr} + C_{2I} \frac{dB}{dr} \right) \sin \tau + \left(C_{2R} \frac{dB}{dr} \right.$$
$$\left. \left. - C_{2I} \frac{dA}{dr} \right) \cos 3\tau - \left(C_{2R} \frac{dA}{dr} + C_{2I} \frac{dB}{dr} \right) \sin 3\tau \right\}$$

$$- - - - \quad (2.4.2)$$

Thus a solution of (2.4.1) is suggested of the form:-

$$w_1 = \text{Const.} \times \text{Re.} \left\{ D_1(r)\, e^{i\tau} + D_3(r)\, e^{i3\tau} \right\} \sin \phi$$

which would imply a perturbation at the applied frequency plus a third harmonic. This leads to the following equations:-

$$\frac{d^2 D_1}{dr^2} + \frac{1}{r} \frac{dD_1}{dr} - \frac{D_1}{r^2} - \alpha^2 i D_1 = \frac{1}{r} \left[(2 C_o + C_{2R}) \frac{dB}{dr} \right.$$

$$+ C_{2I} \frac{dA}{dr}\Big] + \frac{i}{r}\Big[(2C_o - C_{2R}) \frac{dA}{dr} + C_{2I} \frac{dB}{dr}\Big]$$

$$- - - - - (2.4.3)$$

$$\frac{d^2D_3}{dr^2} + \frac{1}{r} \frac{dD_3}{dr} - \frac{D_3}{r^2} - 3\alpha^2 iD_3 = \frac{1}{r}\Big[C_{2R} \frac{dB}{dr} - C_{2I} \frac{dA}{dr}\Big]$$

$$+ \frac{i}{r} \Big[C_{2R} \frac{dA}{dr} + C_{2I} \frac{dB}{dr}\Big] \quad - - - - (2.4.4)$$

Now using Hankel integral transforms in a manner similar to that described in the previous section together with the appropriate boundary conditions the equations become:-

$$\bar{D}_1 (\xi_j) = - \frac{I_5 - i I_6}{(\xi_j^2 + i\alpha^2)} \quad - - - - (2.4.5)$$

$$\bar{D}_3 (\xi_j) = - \frac{I_7 - i I_8}{(\xi_j^2 + 3 i\alpha^2)} \quad - - - - (2.4.6)$$

where:-

$$I_5 (\xi_j) = \int_o^1 \Big[(2C_o + C_{2R}) \frac{dB}{dr} + C_{2I} \frac{dA}{dr}\Big] J_1(\xi_j r)\, dr$$

$$I_6 (\xi_j) = \int_o^1 \Big[(2C_o - C_{2R}) \frac{dA}{dr} + C_{2I} \frac{dB}{dr}\Big] J_1(\xi_j r)\, dr$$

$$I_7(\xi_j) = \int_0^1 \left[C_{2R} \frac{dB}{dr} - C_{2I} \frac{dA}{dr} \right] J_1(\xi_j r)\, dr$$

$$I_8(\xi_j) = \int_0^1 \left[C_{2R} \frac{dA}{dr} + C_{2I} \frac{dB}{dr} \right] J_1(\xi_j r)\, dr$$

Using a similar technique to that used in the previous section and writing the transformed solutions in real and imaginary form then:-

$$\bar{D}_{1R}(\xi_j) = \frac{-I_5 \xi_j^2 - I_6 \alpha^2}{\xi_j^4 + \alpha^4} \quad - - - (2.4.7)$$

$$\bar{D}_{1I}(\xi_j) = \frac{I_5 \alpha^2 - I_6 \xi_j^2}{\xi_j^4 + \alpha^4} \quad - - - (2.4.8)$$

$$\bar{D}_{3R}(\xi_j) = \frac{-I_7 \xi_j^2 - 3\alpha^2 I_8}{\xi_j^4 + 9\alpha^4} \quad - - - (2.4.9)$$

$$\bar{D}_{3I}(\xi_j) = \frac{3\alpha^2 I_7 - \xi_j^2 I_8}{\xi_j^4 + 9\alpha^4} \quad - - - (2.4.10)$$

Using the inversion formula:-

$$D(r) = 2 \sum_{j=1}^{\infty} \frac{\bar{D}(\xi_j) J_1(r\xi_j)}{\left[J_0(\xi_j) \right]^2}$$

then the functions D_{1R} , D_{1I} , D_{3R} and D_{3I} may be computed and thus a solution for w found. When this solution is combined with the straight pipe solution the following form of the axial velocity results:-

$$w = B\cos\tau + (1-A)\sin\tau + G\frac{\sin\phi}{4}\left[D_{1R}\cos\tau - D_{1I}\sin\tau + D_{3R}\cos 3\tau - D_{3I}\sin 3\tau \right] \quad - - - - \quad (2.4.11)$$

2.5 SECOND ORDER SECONDARY FLOW EQUATION

The secondary flow results presented so far, do not take into account the influence of the redistributed velocity field arising from the curvature. In order to include this the next higher order perturbation must be calculated. Thus from equation (2.1.20)

$$\alpha^2\frac{\partial}{\partial\tau}(\nabla^2\psi_2) - \nabla^4\psi_2 = \frac{w_o}{r}\left(r\cos\phi\frac{\partial w_1}{\partial r} - \sin\phi\frac{\partial w_1}{\partial\phi}\right) + w_1\cos\phi\frac{\partial w_o}{\partial r} + \frac{1}{r}\left(\frac{\partial\psi_1}{\partial\phi}\frac{\partial}{\partial r} - \frac{\partial\psi_1}{\partial r}\frac{\partial}{\partial\phi}\right)\nabla^2\psi_1 \quad - - - \quad (2.5.1)$$

The R.H.S. of this equation may be evaluated using the results of the preceding sections. However, as can be seen, the algebra is very long and involved and therefore only the results will be presented here. The details of the calculations may be found in Appendix A. The result is:-

$$\Psi_2 = \frac{\sin 2\phi}{8}\left[H_{20} + H_{22R}\cos 2\tau - H_{22I}\sin 2\tau + H_{24R}\cos 4\tau - H_{24I}\sin 4\tau\right] - - - \quad (2.5.2)$$

The functions H_{20} etc. are obtained in the usual manner from the appropriate Hankel inversion formulae, the only difference being the use of a second order Hankel transform due to the presence of sin 2 ϕ. The boundary conditions used are the same as for Ψ_1 since they are homogeneous.

The solution shows that there is a further contribution to the steady component of the secondary flow, together with a second and now a fourth order harmonic component. The full solution for secondary flow is given by:-

$$\Psi = \frac{G\cos\phi}{2}\left[C_o + C_{2R}\cos 2\tau - C_{2I}\sin 2\tau\right] + \frac{G^2\sin 2\phi}{8}\left[H_{20} + H_{22R}\cos 2\tau - H_{22I}\sin 2\tau + H_{24R}\cos 4\tau - H_{24I}\sin 4\tau\right] - - - \quad (2.5.3)$$

The stream line patterns were created on a Calcomp graph plotter by generating an array of points over the tube, using the above equation for Ψ. A fixed value for the stream function was then chosen and fitted to these points using linear interpolation along the radii. The subsequent data points in r and $\emptyset$ were split into two parts and plotted using a cubic spline interpolation routine.

SMALL α APPROXIMATION

2.6 STRAIGHT PIPE EQUATION

Using equation (2.2.1) and employing an expansion scheme in terms of α^2 since now α is considered small, the following equations arise for a fourth order approximation:-

$$(\alpha^2)^1 \left| \frac{\partial^2 w_{oo}}{\partial r^2} + \frac{1}{r}\frac{\partial w_{oo}}{\partial r} = -\cos\tau \right. \quad ---- (2.6.1)$$

$$(\alpha^2)^2 \left| -\frac{\partial w_{oo}}{\partial \tau} + \frac{\partial^2 w_{o1}}{\partial r^2} + \frac{1}{r}\frac{\partial w_{o1}}{\partial r} = 0 \right. \quad ----(2.6.2)$$

$$(\alpha^2)^3 \left| -\frac{\partial w_{o1}}{\partial \tau} + \frac{\partial^2 w_{o2}}{\partial r^2} + \frac{1}{r}\frac{\partial w_{o2}}{\partial r} = 0 \right. ----(2.6.3)$$

$$(\alpha^2)^4 \left| -\frac{\partial w_{02}}{\partial \tau} + \frac{\partial w_{03}}{\partial r^2} + \frac{1}{r}\frac{\partial w_{03}}{\partial r} = 0 \right. \quad - \quad - \quad - \quad (2.6.4)$$

The solution of (2.6.1) can be obtained using the steady solution of Dean (1928) as a guide, only now including a time-dependency in the form $\cos \tau$. Thus the solution is:-

$$w_{oo} = \left[\tfrac{1}{4} \left(1-r^2 \right) \right] \cos \tau \quad - \quad - \quad - \quad - \quad (2.6.5)$$

This represents the truly quasi-steady approximation given by e.g. Schlicting (1955) and shows that for very small α the flow distribution is Poiseulle and in phase with the applied pressure gradient.

Substitution of (2.6.3) into (2.6.2) gives:-

$$\frac{\partial^2 w_{01}}{\partial r^2} + \frac{1}{r}\frac{\partial w_{01}}{\partial r} = -\left[\tfrac{1}{4} \left(1-r^2\right) \right] \sin \tau \quad - \quad - \quad (2.6.6)$$

The solution of this equation is found by the method of undetermined co-efficients using the homogeneous boundary conditions, $w_{oi} = 0$ when $r = 1$ $(i = 1, 2, \ldots\ldots)$. It is given by:-

$$w_{01} = \left[\frac{1}{64} \left(3-4r^2 + r^4 \right) \right] \sin \tau \quad - \quad - \quad - \quad (2.6.7)$$

This represents the first order effects of inertia in the equations, and shows that in the central area of the tube, the flow moves out of phase with the applied pressure gradient as α increases.

Substitution of this solution into (2.6.3) gives:-

$$\frac{\partial^2 w_{o2}}{\partial r^2} + \frac{1}{r}\frac{\partial w_{o2}}{\partial r} = \left[\frac{1}{64}(3-4r^2+r^4)\right]\cos\tau \quad \text{---(2.6.8)}$$

Again using the method of undetermined co-efficients and the appropriate boundary conditions, the solution is found.

$$w_{o2} = -\frac{\cos\tau}{64}\left[\frac{19}{36} - \frac{3}{4}r^2 + \frac{1}{4}r^4 - \frac{r^6}{36}\right] \quad \text{---(2.6.9)}$$

This solution represents a component of velocity 180^o out of phase with the applied pressure gradient which becomes an important term when $\alpha \backsim 2$.

Finally the solution to (2.6.4) is found using (2.6.9) and is given by:-

$$w_{o3} = -\frac{\sin\tau}{256}\left[\frac{53}{144} - \frac{19}{36}r^2 + \frac{3}{16}r^4 - \frac{r^6}{36} + \frac{r^8}{576}\right]$$

$$- - - - \quad (2.6.10)$$

(2.6.10) is a component 180^o out of phase with the inertia component (2.6.7) and again becomes important when $\alpha \backsim 2$.

Thus the full solution for w_o is given by:-

Figure (2.6.1) Graph showing breakdown of small α approximation. A comparison was made between the velocity along the centre line given by equation (2.6.11) and the exact solution (2.2.4). The graph shows the % difference between the two as a function of α.

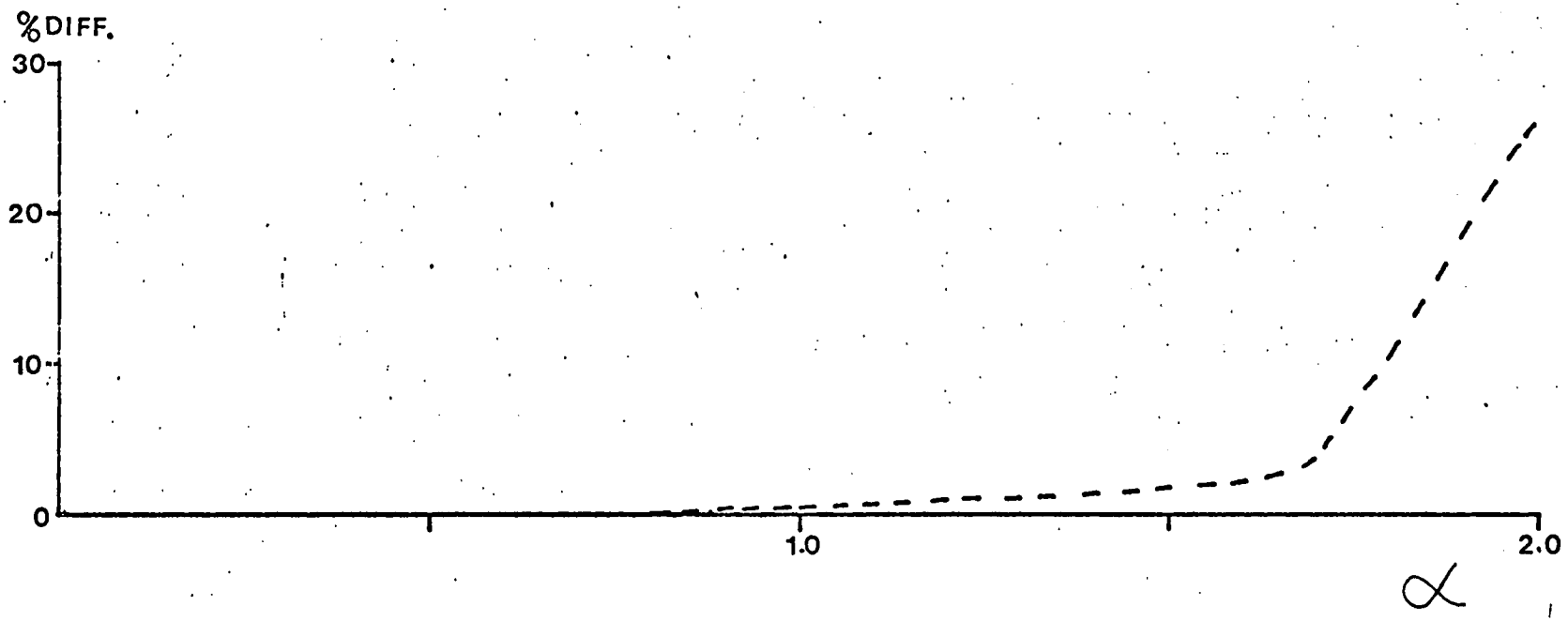

$$W_o = \alpha^2 W_{oo} + \alpha^4 W_{o1} + \alpha^6 W_{o2} + \alpha^8 W_{o3} + O\{\alpha^{10}\}$$

$$= \frac{\alpha^2}{4}(1-r^2)\cos\tau + \frac{\alpha^4}{64}(3-4r^2+r^4)\sin\tau$$

$$+ \frac{\alpha^6}{64}\cos\tau\left[-\frac{19}{36} + \frac{3}{4}r^2 - \frac{1}{4}r^4 + \frac{r^6}{36}\right]$$

$$+ \frac{\alpha^8}{256}\sin\tau\left[-\frac{53}{144} + \frac{19}{36}r^2 - \frac{3}{16}r^4 + \frac{r^6}{36} - \frac{r^8}{576}\right] \quad (2.6.11)$$

Fig. (2.6.1) shows a graph of the comparison between the exact straight pipe solution and the approximate solution given above for various alpha values. It is seen that the closed form solution given above breaks down rapidly for alpha > 1.5 and this will be taken as the limit of this approximation.

2.7 THE FIRST ORDER SECONDARY FLOW EQUATION

Using equation (2.3.1) and employing the following expansion scheme:-

$$\psi_1 = \alpha^4 \psi_{10} + \alpha^6 \psi_{11} + \alpha^8 \psi_{12} + \alpha^{10} \psi_{13} + O\{\alpha^{12}\}$$

$$- - - - \quad (2.7.1)$$

an approximate solution is found for the case when alpha is small.

Substitution of (2.6.11) gives for the R.H.S. of (2.3.1):-

$$\text{R.H.S.} = \cos\phi \Big\{ -\frac{\alpha^4}{8} r(1-r^2)\cos^2\tau + \frac{\alpha^6}{256}\sin 2\tau \, (10r^3-3r^5-7r) + \frac{\alpha^8}{4096}\Big[\Big(\frac{76}{9} r - 10r^3 + \frac{4}{3} r^5 + \frac{2}{9} r^7\Big) + \cos 2\tau \Big(\frac{292}{9} r - 54 r^3 + \frac{76}{3} r^5 - \frac{34}{9} r^7\Big)\Big] + \frac{\alpha^{10}\sin\tau\cos\tau}{4096}\Big[\Big(\frac{53}{16} r - \frac{76}{9} r^3 + \frac{3}{2} r^5 - \frac{4}{9} r^7 + \frac{r^9}{72}\Big) - \Big(\frac{19}{36} - \frac{3}{4} r^6 + \frac{1}{4} r^4 - \frac{r^6}{36}\Big)(r^2-2r) + \Big(\frac{3}{2} r - r^3 + \frac{r^5}{6}\Big)(3-4r^2+r^4) + (4-4r^2)\Big(\frac{19}{18} r - \frac{3}{4} r^3 + \frac{r^5}{6} - \frac{r^7}{72}\Big)\Big] \Big\} \quad - - - \quad (2.7.2)$$

Thus the following approximate equations arise:-

$$\nabla^4\psi_{10} = \cos\phi \, \frac{r}{8}(1-r^2)\cos^2\tau \quad - - - \quad (2.7.3)$$

$$\frac{\partial}{\partial\tau}(\nabla^2\psi_{10}) - \nabla^4\psi_{11} = \frac{\cos\phi}{256}(10r^3 - 7r - 3r^5)\sin 2\tau \quad - - - - (2.7.4)$$

$$\frac{\partial}{\partial \tau}(\nabla^2 \psi_{11}) - \nabla^4 \psi_{12} = \frac{\cos \phi}{4096}\left\{\left(\frac{76}{9}r - 10r^3 + \frac{4}{3}r^5 + \frac{2}{9}r^7\right)\right.$$

$$+ \cos 2\tau \left(\frac{292}{9}r - 54r^3 + \frac{76}{3}r^5\right.$$

$$\left.\left. - \frac{34}{9}r^7\right)\right\} - - - (2.7.5)$$

$$\frac{\partial(\nabla^2 \psi_{12})}{\partial \tau} - \nabla^4 \psi_{13} = \frac{\cos \phi}{256 \times 16 \times 36}\left(432r - 809r^3\right.$$

$$\left. + 447r^5 - 105r^7 + \frac{19}{2}r^9\right)$$

$$\sin \tau \cos \tau \quad - - (2.7.6)$$

The solution of the first order equation can be found using the steady solution of Dean as a guide. This leads to:-

$$\psi_{10} = \left\{\frac{\cos \phi}{144} r (1-r^2)^2 \quad (1-r^2/4)\right\} \frac{\cos^2 \tau}{16} - -(2.7.7)$$

To the first order approximation, the secondary flow would appear to be of the form of a steady component plus an oscillatory part of frequency twice that of the applied pressure gradient. This seems a reasonable

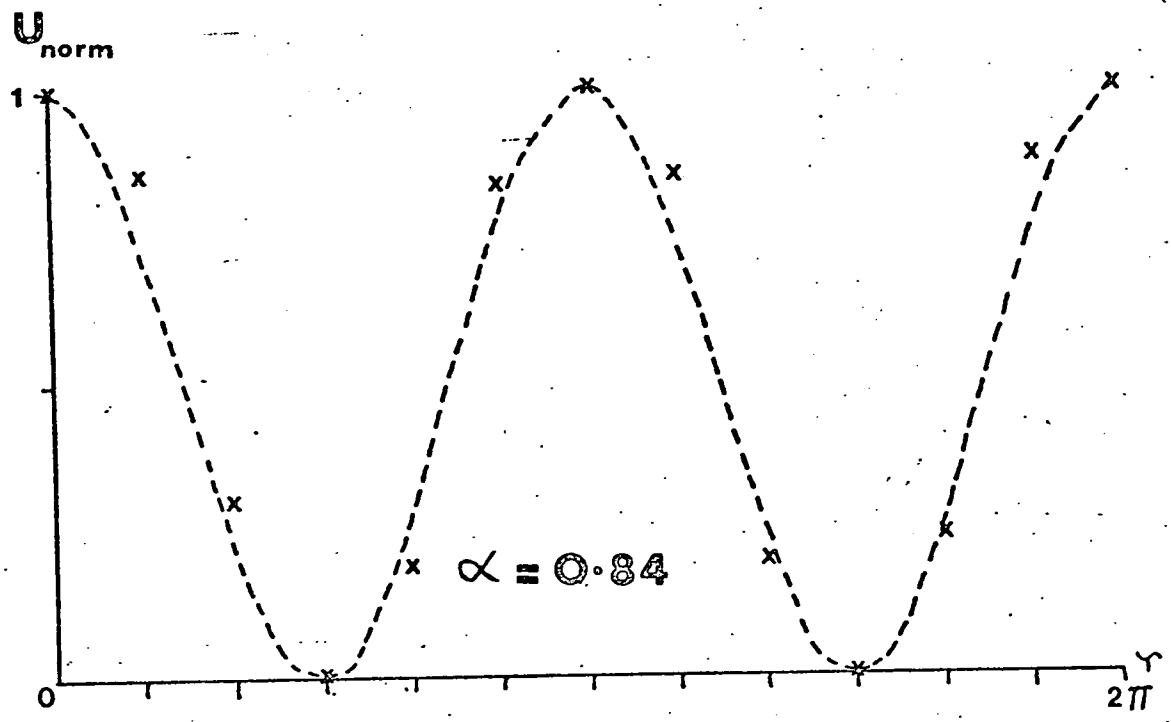

Figure (2.7.1)

Normalised secondary flow measured in the central plane of the tube.

x = measured points

– – – = Theoretical curve given by equation (2.7.7).

conclusion from an intuitive point of view since at very low alpha values one would expect the secondary flow to always flow outwards, no matter what axial direction the main flow is in. Also the magnitude of the secondary flow would be expected to follow the central velocity component, and thus remain in phase with the applied pressure gradient. This is indeed what is found experimentally and is shown in Fig. (2.7.1), where the secondary flow was measured in the central region of the tube.

Substitution of (2.7.7) into (2.7.4) and rearranging terms leads to :-

$$\nabla^4 \psi_{11} = \frac{\cos \phi \sin 2\tau}{2304} (81r - 126r^3 + 39r^5) \quad - (2.7.8)$$

The solution of this equation is found as follows. Initially, a solution is sought of the form:-

$$\psi_{11} = F(r) \cos \phi \sin 2\tau \quad - - - - \quad (2.7.9)$$

This leads to an equation for F(r) of the form:-

$$\left(\frac{d^2}{dr^2} + \frac{1}{r} \frac{d}{dr} - \frac{1}{r^2} \right)^2 F(r) = \frac{1}{2304} (81r - 126r^3 + 39r^5)$$

$$- - - \quad (2.7.10)$$

The equation is now solved as follows:-

$$F(r) = F_H(r) + F_P(r)$$

where $F_H(r)$ is the solution of the corresponding homogeneous equation and $F_P(r)$, the particular solution found by the method of variable co-efficients.

The solution of the homogeneous equation which remains finite at the axis is given by:-

$$F_H(r) = A\,r + B\,r^3 \quad - - - - \quad (2.7.11)$$

and the particular solution is :-

$$F_P(r) = \frac{540r^5 - 140r^7 + 13r^9}{32 \times 3840 \times 24} \quad - - - \quad (2.7.12)$$

The constants A and B may be determined by using the boundary conditions:-

$$F(r) = \frac{dF(r)}{dr} = 0 \quad \text{at } r = 1$$

Thus the total solution is given by:-

$$F(r) = \frac{299r - 712r^3 + 540r^5 - 140r^7 + 13r^9}{24 \times 3840 \times 32}$$

$$- - - - - - - - - \quad (2.7.13)$$

This component of secondary flow indicates outward secondary flow at some phase positions and reversal of the secondary flow between 90° and 180° in the pressure cycle, and also between 270° and 360°. However, the contribution to the secondary flow is small and is $\backsim 20\%$ of the first approximation. Thus the secondary flow will be directed outwards at all phase positions when $\alpha \backsim 1$, the limit of the first order expansion.

Now using this solution for Ψ_{11} to substitute into equation (2.7.5), the following equation for Ψ_{12} is obtained:-

$$-\nabla^4 \Psi_{12} = \cos\phi \left\{ \left(\frac{76r}{9} - 10r^3 + \frac{4}{3} r^5 + \frac{2}{9} r^7 \right) \frac{1}{4096} \right.$$

$$+ \frac{\cos 2\tau}{92160} \left(1086r - 2940 \frac{3}{4} r^3 + 1385r^5 \right.$$

$$\left. \left. - 150r^7 \right) \right\} \quad - - - - \quad (2.7.14)$$

The equation is solved in the same way as the previous one, this time looking for a solution of the form:-

$$\Psi_{12} = \Psi_{12s} + \Psi_{12u} \cos 2\tau$$

After a considerable amount of algebra, the following solution results:-

$$\Psi_{12} = \left[F_1(r) + F_2(r) \cos 2\tau \right] \cos\phi \quad - - - \quad (2.7.15)$$

where $F_1(r) = \left(\frac{-1199}{4800} r + \frac{68\frac{1}{2}}{120} r^3 - \frac{38}{96} r^5 + \frac{5}{64} r^7 - \frac{r^9}{320} - \frac{r^{11}}{4800}\right) \frac{1}{4096 \times 9}$

and $F_2(r) = \left(-2\frac{109}{128} r + 6\frac{127}{128} r^3 - 5\frac{21}{32} r^5 + 1\frac{97}{128} r^7 - \frac{33}{128} r^9 + \frac{r^{11}}{64}\right) \times \frac{1}{92160}$

The effect of the term Ψ_{12} is thus to produce inward streaming of both the steady and the oscillatory contribution. However, the total secondary flow remains outwards at all phase positions until $\alpha \backsim 2$, which is beyond the limit of this expansion.

Substitution of (2.7.15) into (2.7.6) and re-arranging terms leads to :-

$$\nabla^4 \psi_{13} = \left[611\ r - 1243^2/5r^3 + 717\ r^5 - 171r^7 + 15^1/2r^9\right] \frac{\sin 2\tau \cos \phi}{256 \times 32 \times 36} \quad - - - - \quad (2.7.16)$$

A solution is found in the same way as previous equations to be:-

$$\psi_{13} = F_3(r) \sin 2\tau \cos \phi \quad - - - \quad (2.7.17)$$

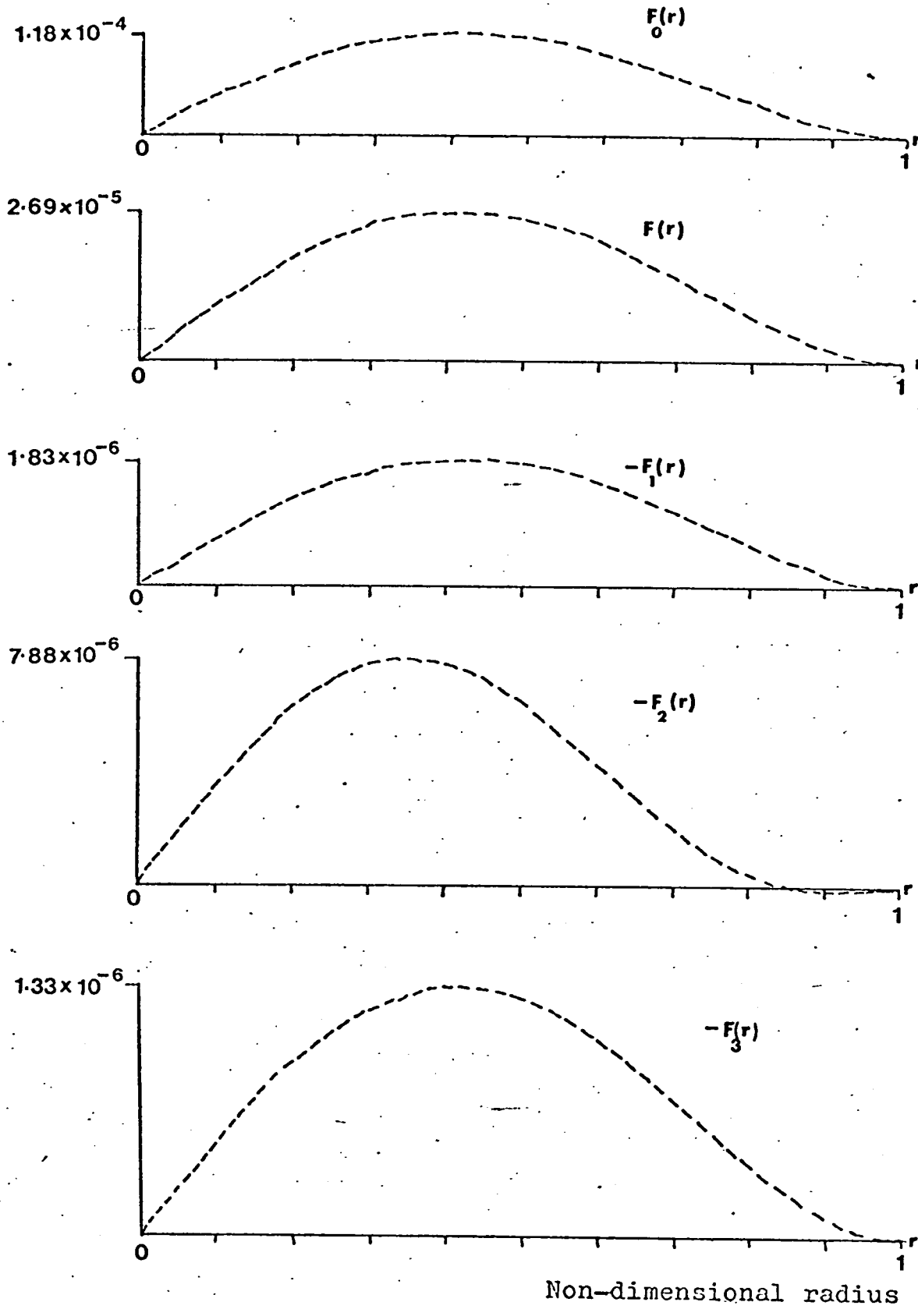

Figure (2.7.2) Functions $F_0(r)$ - $F_3(r)$ associated with small α secondary flow approximation plotted to show radial dependence.

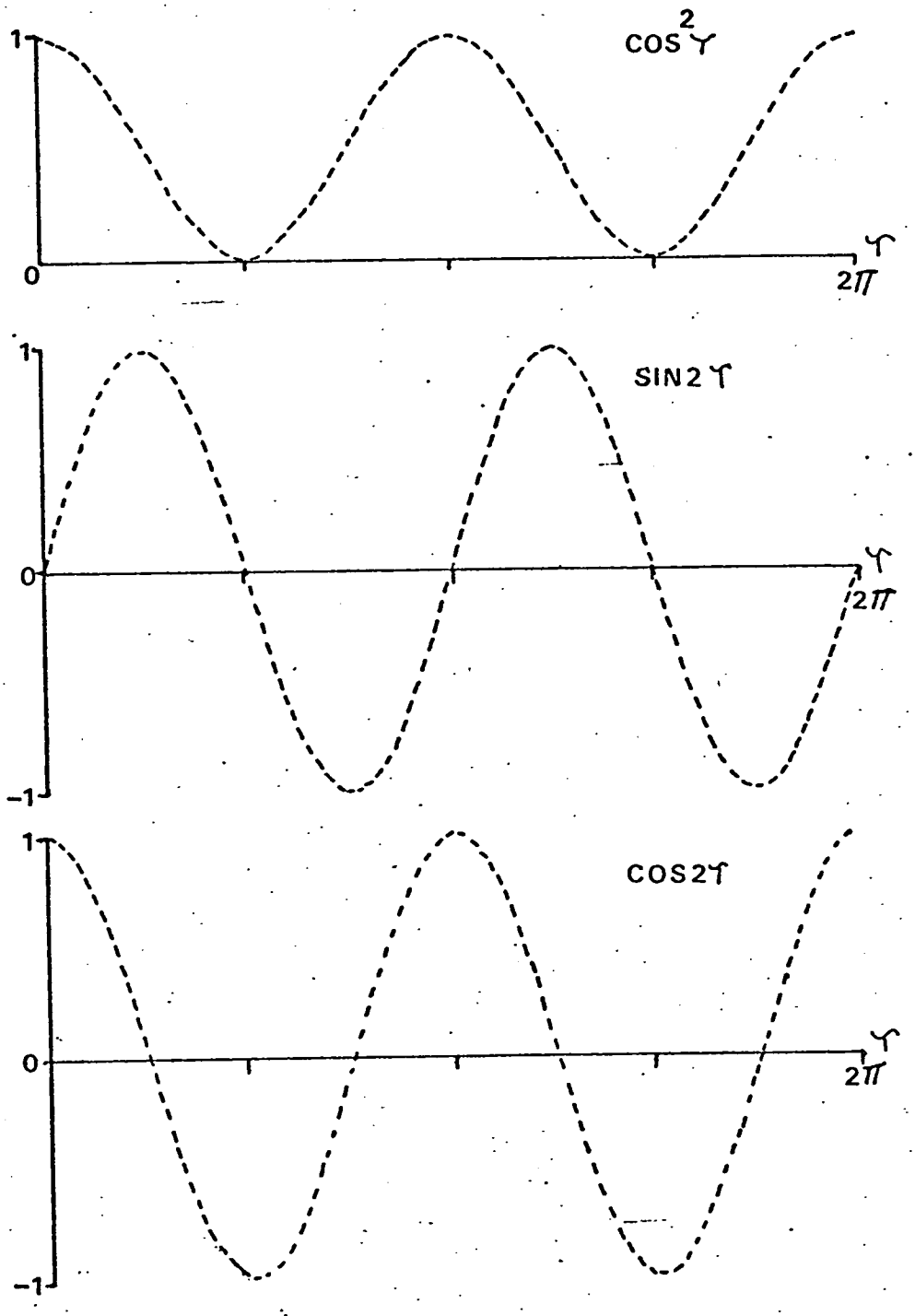

Figure (2.7.3) Time dependent functions associated with small α secondary flow approximation.

$$\text{where } F_3(r) = \left[-290\,\frac{13}{50}\,r + 726\,\frac{2}{5}\,r^3 - 611\,r^5 + 207\,\frac{7}{30}\,r^7 - 35\,\frac{17}{20}\,r^9 + 3\,\frac{21}{50}\,r^{11} - \frac{1}{7}\,r^{13} \right] \frac{1}{256 \times 192 \times 36 \times 32}$$

This term produces secondary flow which is 180° out of phase with ψ_{11} and thus acts as a correction term as alpha increases.

The final approximate solution for ψ_1 is thus given by :-

$$\psi_1 = \left\{ \alpha^4 F_0(r) \cos^2\tau + \alpha^6 F(r) \sin 2\tau + \alpha^8 \left[F_1(r) + F_2(r) \cos 2\tau \right] + \alpha^{10} F_3(r) \sin 2\tau + O\left\{ \alpha^{12} \right\} \right\} \cos\phi \quad - - - \quad (2.7.18)$$

$$\text{where } F_0(r) = \frac{r}{144 \times 16} (1-r^2)^2 (1-r^2/4)$$

The functions $F_0(r)$, $F(r)$, $F_1(r)$, $F_2(r)$ and $F_3(r)$ are shown in Fig. (2.7.2) and the appropriate time dependent functions are shown in Fig. (2.7.3). It should be noted that these are not plotted to scale but are given only to indicate the form of the function.

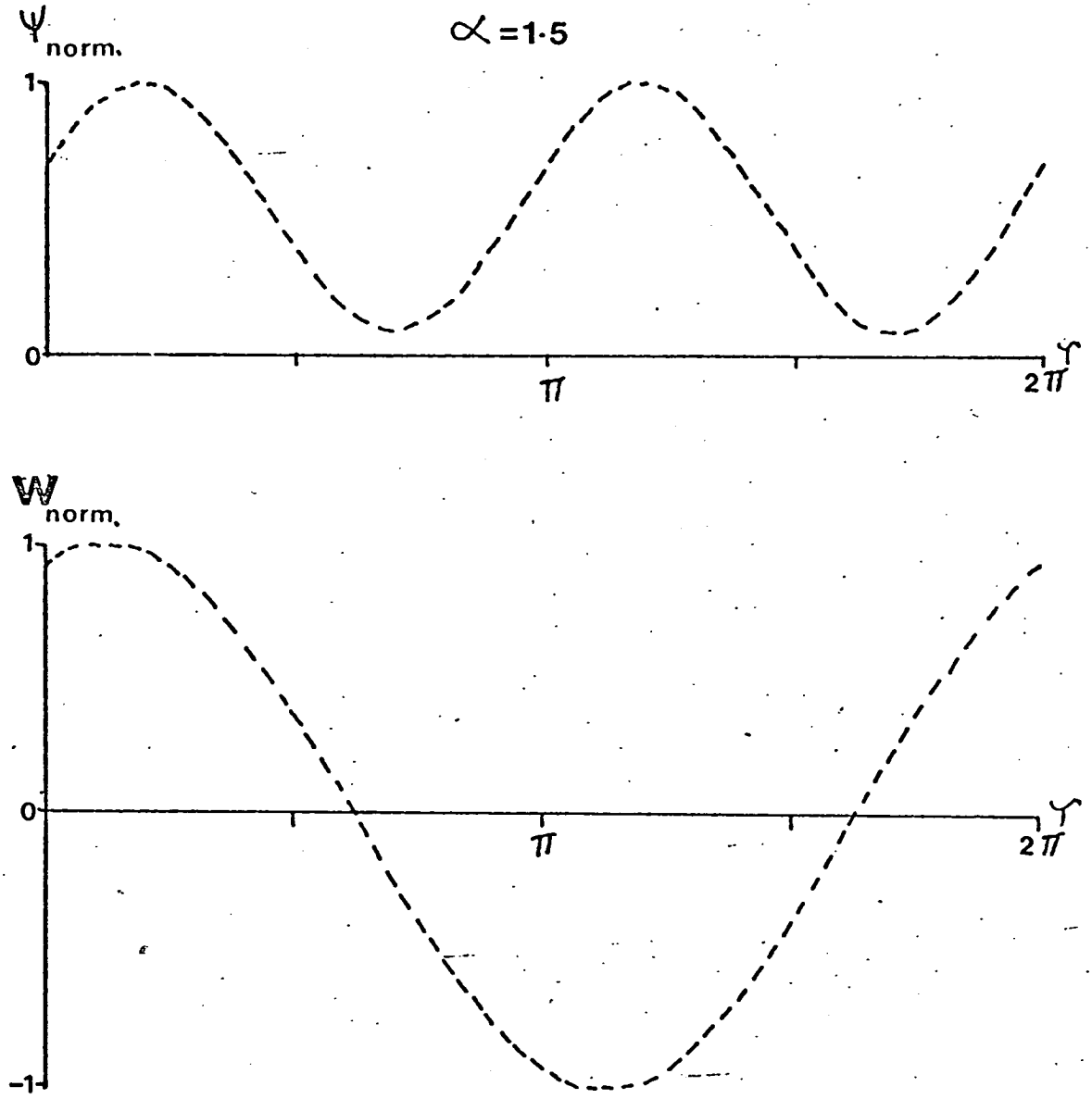

Figure (2.7.4) Plots of normalised secondary flow and axial velocity near the axis of the tube, showing the time dependency of the flow. Results obtained using equations (2.7.18) and (2.4.11).

All these functions except F_2 (r) have a peak at 0.4 - 0.45r indicating that this is the region of peak secondary flow. This is in good agreement with the Hankel transform solution for alpha values up to 1.5.

The function F_2 has a peak nearer to the axis of the tube and in fact, it reverses sign near the wall. This is in agreement with the flow pattern obtained at much higher alpha values where the core secondary flow is reversed while the boundary layer flow remains directed in the normal way.

Finally, Fig. (2.7.4) shows a plot of the non-dimensionalised function Ψ_1 for alpha value 1.5 as a function of time at position 0.05r, $\phi = 0^o$. It can be seen that the secondary flow is directed outwards at all phase positions and a comparison with the plot of central axial velocity drawn below it indicates that the secondary flow is in phase with this.

2.8 AXIAL FLOW PERTURBATION

The first order axial flow equation (2.4.1) can be solved in the same approximate manner as used in the preceding two sections. Using an expansion scheme in α^2 the following equations result:-

$$\nabla^2 w_{10} = -\frac{1}{2} \cos^3 \tau \, F_o(r) \sin \phi \quad - - - \quad (2.8.1)$$

$$\frac{\partial w_{10}}{\partial \tau} - \nabla^2 w_{11} = \left[\frac{1}{16} (2-r^2) F_o(r) + F(r) \right] \sin \tau$$

$$\cos^2 \tau \sin \phi \quad - \quad - \quad - \quad (2.8.2)$$

$$\frac{\partial w_{11}}{\partial \tau} - \nabla^2 w_{12} = \sin \phi \left[\frac{\cos \tau}{2} (F_1(r) + F_2(r) \cos 2\tau) \right.$$

$$+ \frac{F(r)}{16} (2-r^2) \sin^2 \tau \cos \tau -$$

$$\left. \frac{\cos^3 \tau F_o(r)}{64} \left(\frac{3}{2} - r^2 + \frac{r^4}{6}\right) \right] \quad (2.8.3)$$

$$\frac{\partial w_{12}}{\partial \tau} - \nabla^2 w_{13} = \sin \phi \left[\sin \tau \cos^2 \tau \left(- \frac{19}{36} + \frac{3}{4} r^2 \right.\right.$$

$$\left. - \frac{r^4}{6} + \frac{r^6}{72} \right) F_o(r)$$

$$- \frac{\cos \tau \sin 2\tau}{64} F(r) \left(r^2 - \frac{3}{2} - \frac{r^4}{6}\right)$$

$$- \frac{\sin \tau}{16} (r^2-2) (F_1(r) + F_2(r) \cos 2\tau)$$

$$\left. - \sin \tau \cos^2 \tau F_3(r) \right] \quad - \quad - \quad (2.8.4)$$

Again using the relevant equations of Dean as a guide, the solution of (2.8.1) is:-

$$w_{10} = \frac{\sin \phi}{32 \times 576} \left(\frac{19r}{40} - r^3 + \frac{3}{4} r^5 - \frac{r^7}{4} + \frac{r^9}{40} \right) \cos^3 \psi$$

- - - - (2.8.5)

Thus the first-order approximation in the quasi-steady regime indicates that the higher axial velocity components feature towards the outside of the curve at all phase positions. This is as one would expect intuitively since the situation should be realisable using different steady flow Dean numbers.

This solution is substituted into (2.8.2) and the following equation results:-

$$\nabla^2 w_{11} = (-687r + 1632r^3 - 1320r^5 + 420r^7 - 45r^9) \frac{\sin \psi \cos^2 \psi}{2949120} \sin \phi \quad - - - (2.8.6)$$

A solution of this equation is sought which is of the form:-

$$w_{11} = F_4 (r) \sin \psi \cos^2 \psi \sin \phi \quad - - (2.8.7)$$

The function $F_4 (r)$ is found by the method of undetermined co-efficients and using the no-slip boundary condition:-

$$w_{11} = 0 \text{ at } r = 1$$

and the condition that w_{11} must remain finite when r=0. Thus:-

$$F_4(r) = \frac{1}{2949120}\left(40\tfrac{1}{2}r - 85\tfrac{7}{8}r^3 + 68r^5 - 27\tfrac{1}{2}r^7 + 5\tfrac{1}{4}r^9 - \frac{3}{8}r^{11}\right) \quad (2.8.8)$$

This component will have the effect of reversing the direction of the shift in peak of the axial velocity between 90° and 110° and 270° and 290° in the pressure cycle. At these times the w_{10} term is small since it is multiplied by $\cos^3\tau$ and the effect of w_{11} term can become appreciable. This acts in the opposite direction and thus the first order effects of inertia can change the axial velocity distribution from the quasi-steady position.

Substitution of (2.8.7) into (2.8.3) leads to the following equation for w_{12}.

$$\nabla^2 w_{12} = -\sin\phi\left[\left\{F_4(r) + \frac{F_1(r)}{2} - \frac{F_2(r)}{2} + \frac{F(r)}{32}(2-r^2)\right\}\cos\tau - \cos^3\tau\left\{3F_4(r) - \frac{F(r)}{16}(2-r^2) + \frac{F_o(r)}{64}\left(\frac{3}{2} - r^2 + \frac{r^4}{6}\right)\right\}\right] \quad (2.8.9)$$

A solution for w_{12} is found which has the form:-

$$w_{12} = \left[F_5(r) \cos\Upsilon + F_6(r) \cos^3\Upsilon \right] \sin\phi \quad -(2.8.10)$$

where:-

$$F_5(r) = \left[213.79r - 459\,\frac{13}{90}\,r^3 + 368\,\frac{41}{42}\,r^5 - 153\,\frac{5}{9}\,r^7 + 33\tfrac{3}{4}\,r^9 - 3\,\frac{11}{12}\,r^{11} + \frac{53}{105}\,r^{13} \right] \times \frac{1}{24\times32\times32\times3840}$$

$$F_6(r) = \left[-177.126\,r + 377\tfrac{3}{4}\,r^3 - 305\,\frac{7}{8}\,r^5 + 136\,\frac{4}{9}\,r^7 - 35\tfrac{3}{4}\,r^9 + 4.82\,r^{11} - \frac{133}{504}\,r^{13} \right] \times \frac{1}{24\times16\times32\times3840}$$

The effect of the w_{12} term will be to reverse the axial velocity shift at phase positions where $\cos^3\Upsilon$ is comparable with $\cos\Upsilon$, e.g. 0° in the pressure cycle.

Substitution of (2.8.10) into (2.8.4) and re-arranging terms leads to:-

$$\nabla^2 w_{13} = -\sin\phi \left[\left\{ F_5(r) + \frac{(2-r^2)}{16} \left(F_1(r) - F_2(r)\right) \right\} \sin\Upsilon \right.$$

$$\left. + \cos^2\Upsilon \sin\Upsilon \cdot \left\{ F_2(r)\,\frac{(2-r^2)}{8} + F_3(r) + 3F_6(r) \right.\right.$$

$$- \frac{F_o(r)}{256} \left(\frac{19}{18} - \frac{3}{4} r^2 + \frac{r^4}{6} \frac{r^6}{72} \right) - \frac{F(r)}{32} \left(\frac{3}{2} - r^2 + \frac{r^4}{6} \right) \Bigg\} \Bigg]$$

- - - - (2.8.11)

A solution to this equation is found such that:-

$$w_{13} = \sin \phi \left[F_7(r) \sin\tau + F_8(r) \sin\tau \cos^2\tau \right] \quad (2.8.12)$$

where:-

$$F_7(r) = \Big[21.6029\, r - 56\frac{7}{40} r^3 + 54.778\, r^5 - 27.54\, r^7 + 8.558\, r^9 - 1.34\, r^{11} + 0.126\, r^{13} - 0.0069\, r^{15} \Big] \times \frac{1}{24 \times 32 \times 32 \times 3840}$$

$$F_8(r) = \Big[- 24.876\, r + 51.03\, r^3 - 41.93\, r^5 + 19.95\, r^7 - 4.98\, r^9 + 0.89\, r^{11} - 0.09\, r^{13} + 0.006\, r^{15} \Big] \times \frac{1}{8 \times 16 \times 32 \times 3840}$$

The main effect of w_{13} will thus be to produce a perturbation on the axial velocity at 90^o in the pressure cycle. When $\alpha \backsim 1$ there is an axial velocity component at 90^o and from the Hankel transform solution it can be seen that the axial velocity peak is displaced from the centre

Figure (2.8.1) Functions $F_4(r) - F_9(r)$ associated with small α axial velocity perturbation approximation, plotted to show radial dependence.

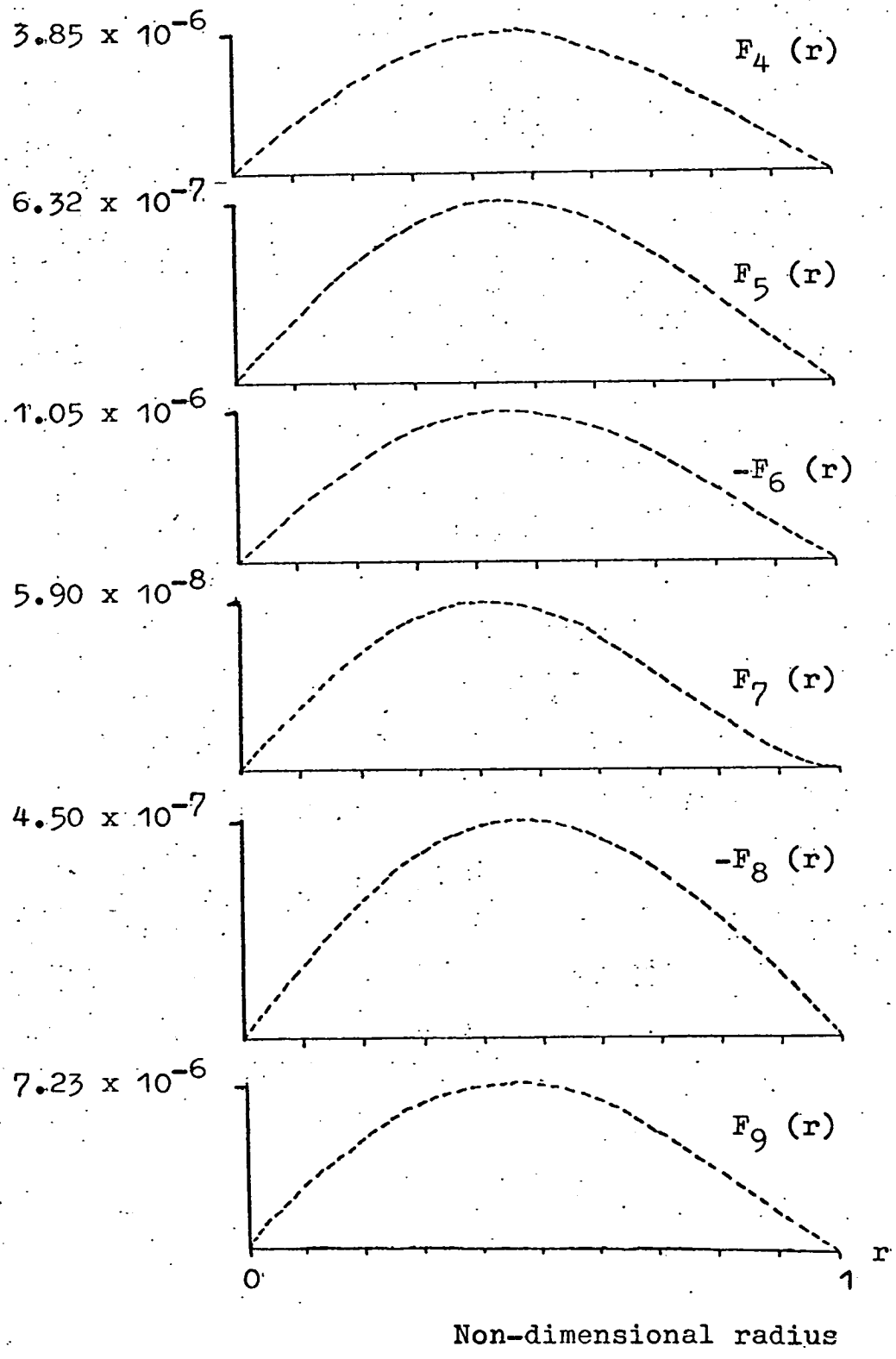

Figure (2.8.2) Time dependent functions associated with small α axial flow perturbation.

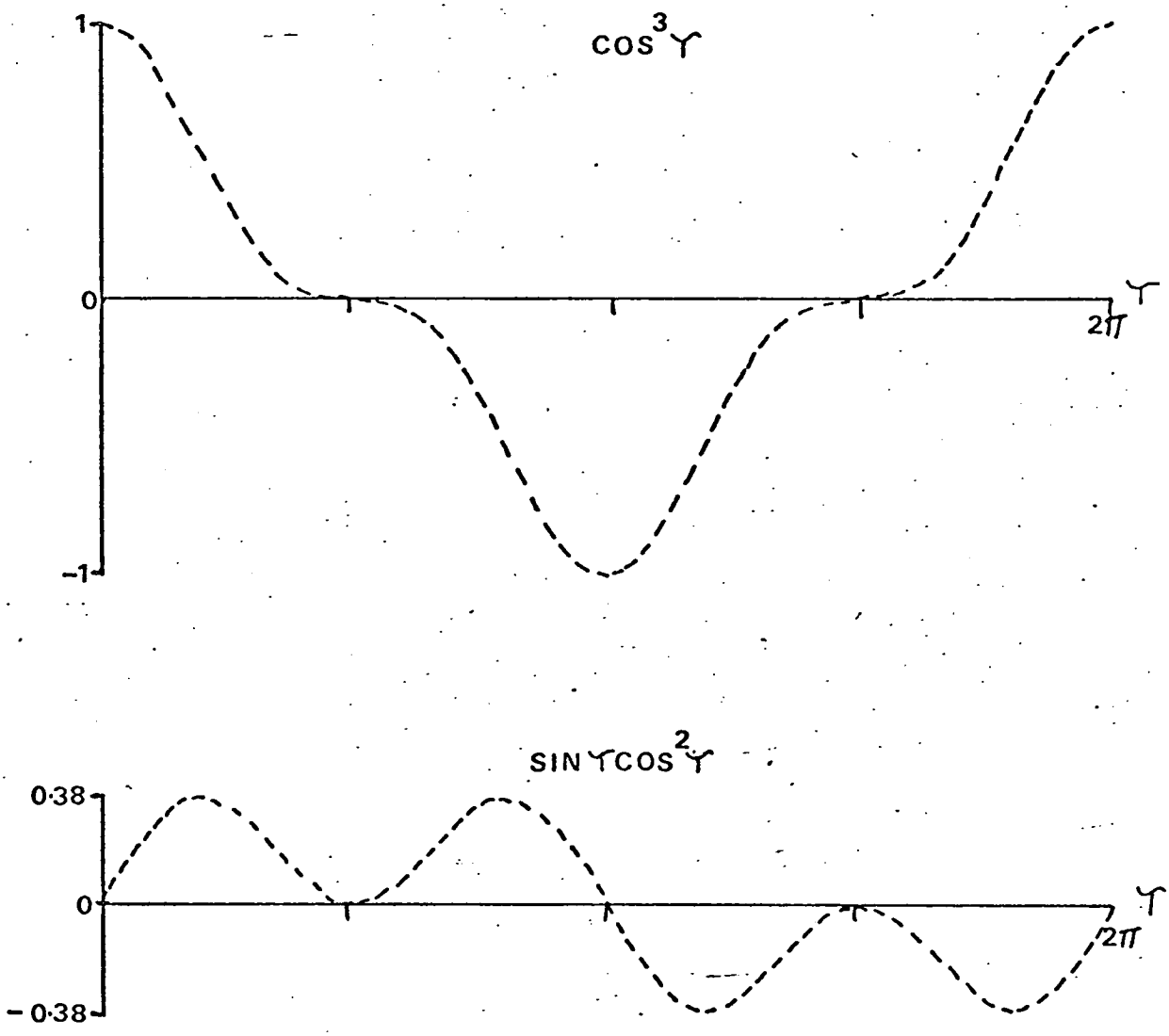

Figure (2.8.3) Normalised velocity time diagrams for straight pipe flow ———— and first order perturbation due to curvature - - - - - for radial positions 0.1r and 0.9r with α = 0.99.

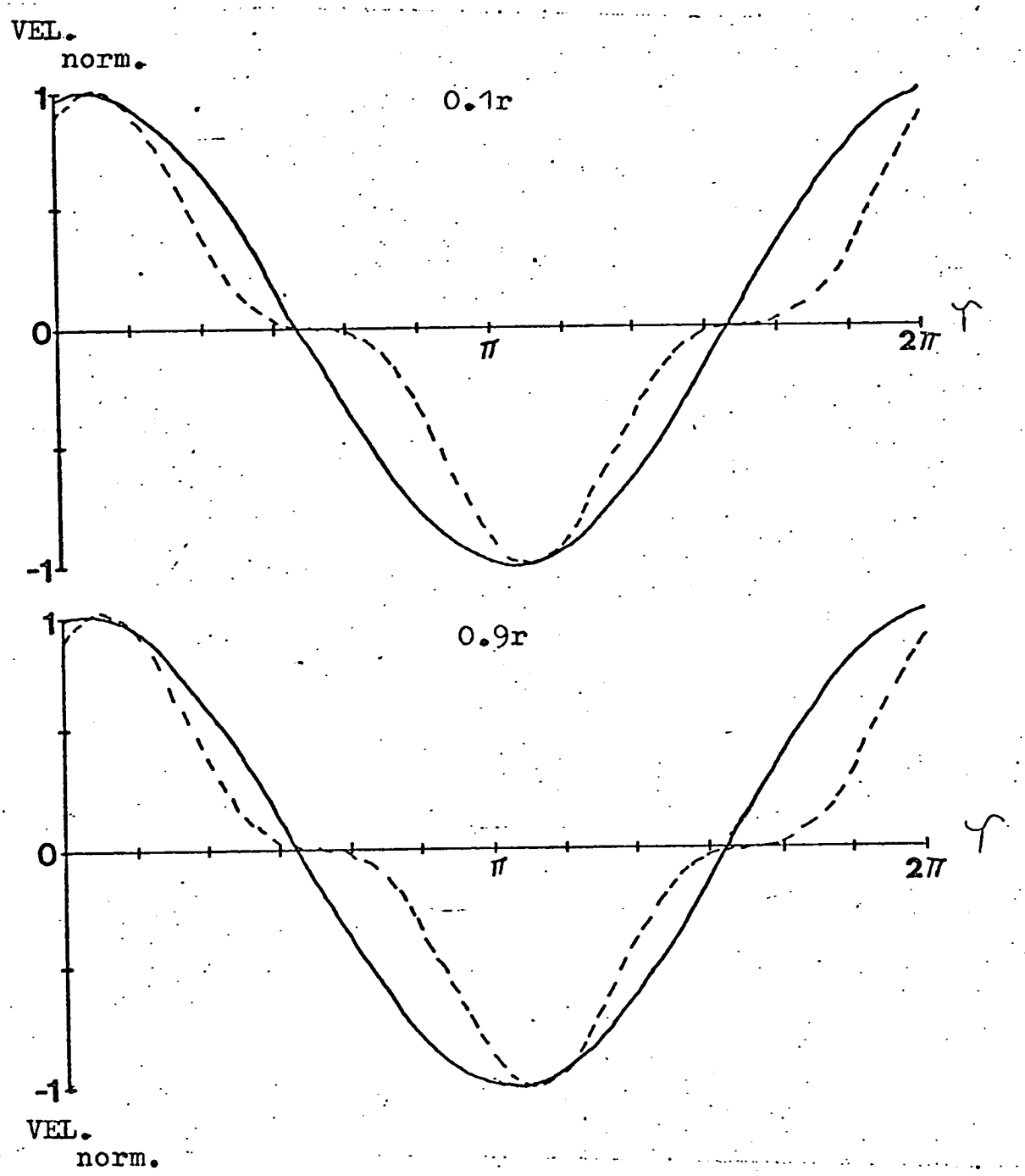

of the tube. Since the term w_{13} is the first in the series to indicate this, then $\alpha = 1$ will be taken as the upper limit of this expansion.

The full approximate expansion for w_1 is thus given by:-

$$w_1 = \alpha^6 \sin\phi \Big[F_9(r) \cos^3\tau + \alpha^2 F_4(r) \sin\tau\cos^2\tau + \alpha^4 (F_5(r)\cos\tau + F_6(r)\cos^3\tau) + \alpha^6 (F_7(r)\sin\tau + F_8(r)\sin\tau\cos^2\tau) + O\{\alpha^8\}\Big] \quad - - - - - - \quad (2.8.13)$$

The functions $F_4(r) - F_9(r)$ are shown in Fig.(2.8.1) and the time dependent functions are shown in Fig. (2.8.2). All functions except F_7, are similar in shape having peaks $\sim 0.45 - 0.5$ r from the axis of the tube. F_7 however, has a peak ~ 0.4 r and has a smaller gradient than the other functions towards the wall of the tube. This indicates that the effect of this inertia derived component is small towards the wall of the tube.

Finally, the function w_1 is plotted as a function of time at two radial positions, 0.9 r and 0.1 r, and is shown in Fig. (2.8.3). Also shown are velocity-time diagrams for the corresponding positions in a straight pipe.

At 0.9 r it can be seen that the perturbation is almost in phase with the straight pipe flow and thus

will act in the same direction at nearly all phase positions. However, at 0.1 r there is a larger phase lag between the perturbation and the straight pipe flow, causing the perturbation to act in the opposite direction at 105 -110° and 285 - 290° in the pressure cycle. The term which causes this, is the sin τ term in w_{13} which has little effect near the edge of the tube. Therefore, it would seem that reversal of the axial flow perturbation is initiated at the region in the cycle where the flow in the centre of the tube changes direction.

LARGE ALPHA APPROXIMATION

2.9 STRAIGHT PIPE EQUATION

The theory of oscillatory flow in a straight pipe in the limit $\alpha \rightarrow \infty$ is well understood, (Schlichting, 1955). The flow can be considered as consisting of two regions, an inviscid core plus thin boundary layers along the walls. Re-writing equation (2.2.1) one obtains:-

$$\frac{\partial w_o}{\partial \tau} - \frac{1}{\alpha^2} \nabla^2 w_o = \cos \tau \quad - - - - \quad (2.9.1)$$

Thus in the central core where viscosity is neglected the following approximate equation arises:-

$$\frac{\partial w_{oo}}{\partial \tau} = \cos \tau \qquad - - - - - \quad (2.9.2)$$

whence

$$w_{oo} = \sin \tau \qquad - - - - \quad (2.9.3)$$

In the boundary layer where viscosity is important only the highest order derivative in the Laplacian is retained. Thus:-

$$\frac{\partial^2 w_{o1}}{\partial \tau} - \frac{1}{\alpha^2} \frac{\partial^2 w_{o1}}{\partial r^2} = \cos \tau \quad - - - \quad (2.9.4)$$

The solution of this equation which satisfies the no-slip boundary conditions and matches with (2.9.3) is given by Lyne, (1970) as:-

$$w_{o1} = - \exp\left\{ - \frac{\alpha}{\sqrt{2}} (1-r) \right\} \sin \left\{ \tau - \frac{\alpha}{\sqrt{2}} (1-r) \right\}$$

$$- - - \quad (2.9.5)$$

Thus the full solution for w_o is given by:-

$$w_o = \sin \tau - e^{-X} \sin (\tau - X) \quad - - \quad (2.9.6)$$

where

$$X = \frac{\alpha}{\sqrt{2}} (1-r)$$

2.10 THE SECONDARY FLOW EQUATION

Using the results of the previous section the R.H.S. of equation (2.3.1) can be written as:-

$$\text{R.H.S.} = -\frac{\alpha}{\sqrt{2}}\Big\{ e^{-X}\sqrt{2}\cos(X-\pi/4) - e^{-2X} + e^{-2X}\sqrt{2}\cos(2\tau-2X+\pi/4) - e^{-X}\sqrt{2}\cos(2\tau-X+\pi/4)\Big\} \quad - - - \quad (2.10.1)$$

This indicates that the secondary flow consists of a steady part plus an oscillatory part. The unsteady secondary flow has frequency twice that of the applied pressure gradient and thus this form of solution is consistent with that found at the lower α values.

Thus (2.3.1) can be written as:-

$$\frac{\partial(\nabla^2\psi_1)}{\partial\tau} - \frac{\nabla^4\psi_1}{\alpha 2} = \frac{-1}{\alpha\sqrt{2}}\Big\{ e^{-X}\sqrt{2}\cos(x-\pi/4) - e^{-2x} + e^{-2x}\sqrt{2}\cos(2\tau - 2x+\pi/4) - e^{-x}\sqrt{2}\cos(2\tau - x+\pi/4)\Big\} \quad - - \quad (2.10.2)$$

In the central core where viscous effects are ignored:-

$$\frac{\partial(\nabla^2\psi_{10})}{\partial\tau} = 0 \quad - - - - - - \quad (2.10.3)$$

whilst in the boundary layer:-

$$\left(\frac{\partial}{\partial\tau} - \frac{\alpha^2}{2}\frac{\partial^2}{\partial\chi^2}\right)\frac{\partial^2\psi_{11}}{\partial\chi^2} = \frac{-2}{\alpha}\Big\{ e^{-\chi}\cos(\chi - \pi/4) - \frac{1}{\sqrt{2}} e^{-2\chi} + e^{-2\chi}\sqrt{2}\cos(2\tau - 2\chi + \pi/4) - e^{-\chi}\sqrt{2}\cos(2\tau - \chi + \pi/4)\Big\} \quad (2.10.4)$$

These two equations are similar to those used by Lyne in his boundary layer analysis. Therefore using his solutions as a guide the solution for equation (2.10.4) is given by:-

$$\psi_{11} = \frac{1}{\alpha^3}\Big\{ -\frac{\sqrt{2}}{4}\chi + \frac{5}{4\sqrt{e}} - \frac{\sqrt{2}}{8} e^{-2\lambda} - e^{-\chi}\cos(\chi - \pi/4) + \frac{5}{4\sqrt{2}} e^{-\sqrt{2}\chi}\cos(2\tau - \sqrt{2}\chi + \pi/4) - \frac{1}{8} e^{-2\chi}\cos(2\tau - 2\chi + \pi/4) - e^{-\chi}\cos(2\tau - \chi + \pi/4) + \left(\frac{9\sqrt{2}-10}{8\sqrt{2}}\right)\cos(2\tau + \pi/4)\cos\phi \quad - - - - \quad (2.10.5)$$

Equation (2.10.3) along with the matching conditions given by Lyne implies that:-

$$\Psi_{10} = y(r, \phi) \quad - - - - \quad (2.10.6)$$

Therefore in the limit $\alpha \to \infty$ the flow in the interior is steady.

Now using equation (2.1.20) the next approximation to the secondary flow in the interior may be obtained.

$$-\nabla^4 \Psi_{10} = \frac{1}{\alpha^2 r}\left(\frac{\partial \Psi_{40}}{\partial \phi}\frac{\partial}{\partial r} - \frac{\partial \Psi_{10}}{\partial r}\frac{\partial}{\partial \phi}\right)\nabla^2 \Psi_{10} \quad - - - - - \quad (2.10.7)$$

Using the following expansion scheme an approximate solution to (2.10.7) is found subject to the boundary and matching conditions given by Lyne.

$$\Psi_{10} = \Psi_{100} + \frac{1}{\alpha^2}\Psi_{101} + \frac{1}{\alpha^4}\Psi_{102} + \; - \; - \quad (2.10.8)$$

Thus using the solution of Lyne as a guide:-

$$\Psi_{10} = -\frac{r}{8}(1-r^2)\cos\phi - \frac{1}{\alpha^2}\left(\frac{r^2}{3072}\right)(1-r^2)^2\cos 2\phi$$

$$- \; - \; - \quad (2.10.9)$$

This result indicates that in the limit $\alpha \to \infty$ then the secondary flow in the interior region of the pipe is steady and flows in the opposite direction to that of the lower case. Clearly there must be a transition region between the small α "positive centrifuging" and the large α case. The exact α value at which this occurs is given by Lyne as 12.8 which has been confirmed experimentally by Bertelsen (1974) and Munson (1975). The value obtained by the Hankel transform technique is $\alpha \lesssim 11$, which is to be expected as the expansion scheme used by Lyne is of a higher order and is a better approximation. The boundary layer method will not be pursued here as much of this work has already been covered by Lyne and it is sufficient to see that the results agree in the limit $\alpha \to \infty$.

C H A P T E R 3

EXPERIMENTAL SYSTEM

INTRODUCTION

This chapter contains a description of the flow rig and pump developed for this series of experiments and also a discussion of the measurement technique used. The basic requirement of the pump, was that it should produce a purely oscillatory flow in the low to moderate frequency parameter range. The working fluid was chosen to be air since this would enable very low Re. No. flow to be achieved without many practical difficulties.

The flow system consisted of a pipe network and glass models which ranged in diameter from 3.6 - 6.2 m.m and thus this precluded the use of measuring probes which required to be placed in the flow. Laser-Doppler anemometry was used to measure the flow velocities since this is a non-intrusive technique which can have very good spatial resolution. Since the fluid used was air, and hence the amount of light scattered small, photon-correlation was chosen for signal-processing.

All the experiments were run at a room temperature of $25^{o}C$ giving a value for ν , the kinematic viscosity of air of 1.55×10^{-5} m^2 sec^{-1}. This value was calculated using Sutherland's law and the tabulated values given by Batchelor (1967).

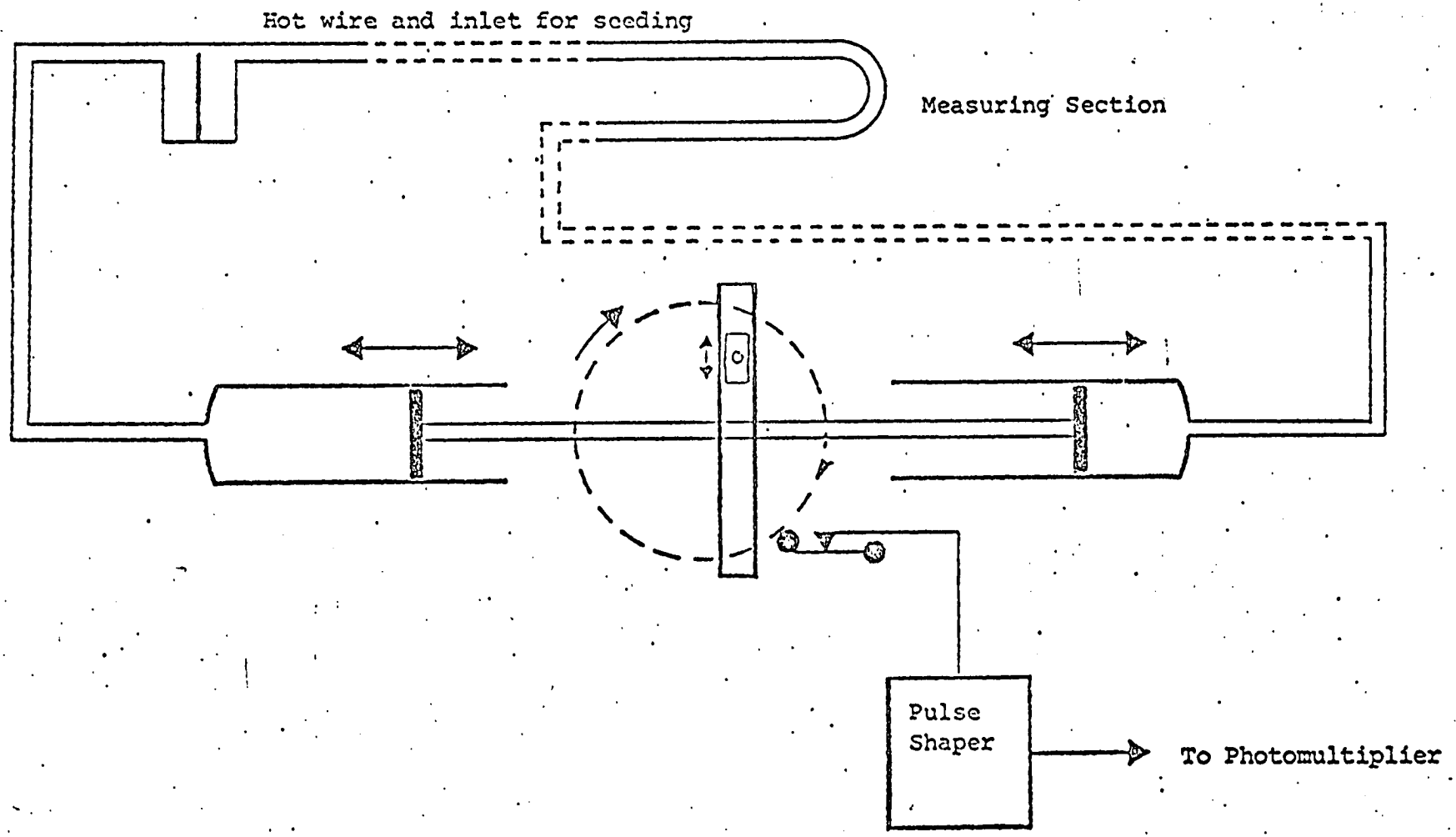

Figure (3.1.1)

Layout of flow rig

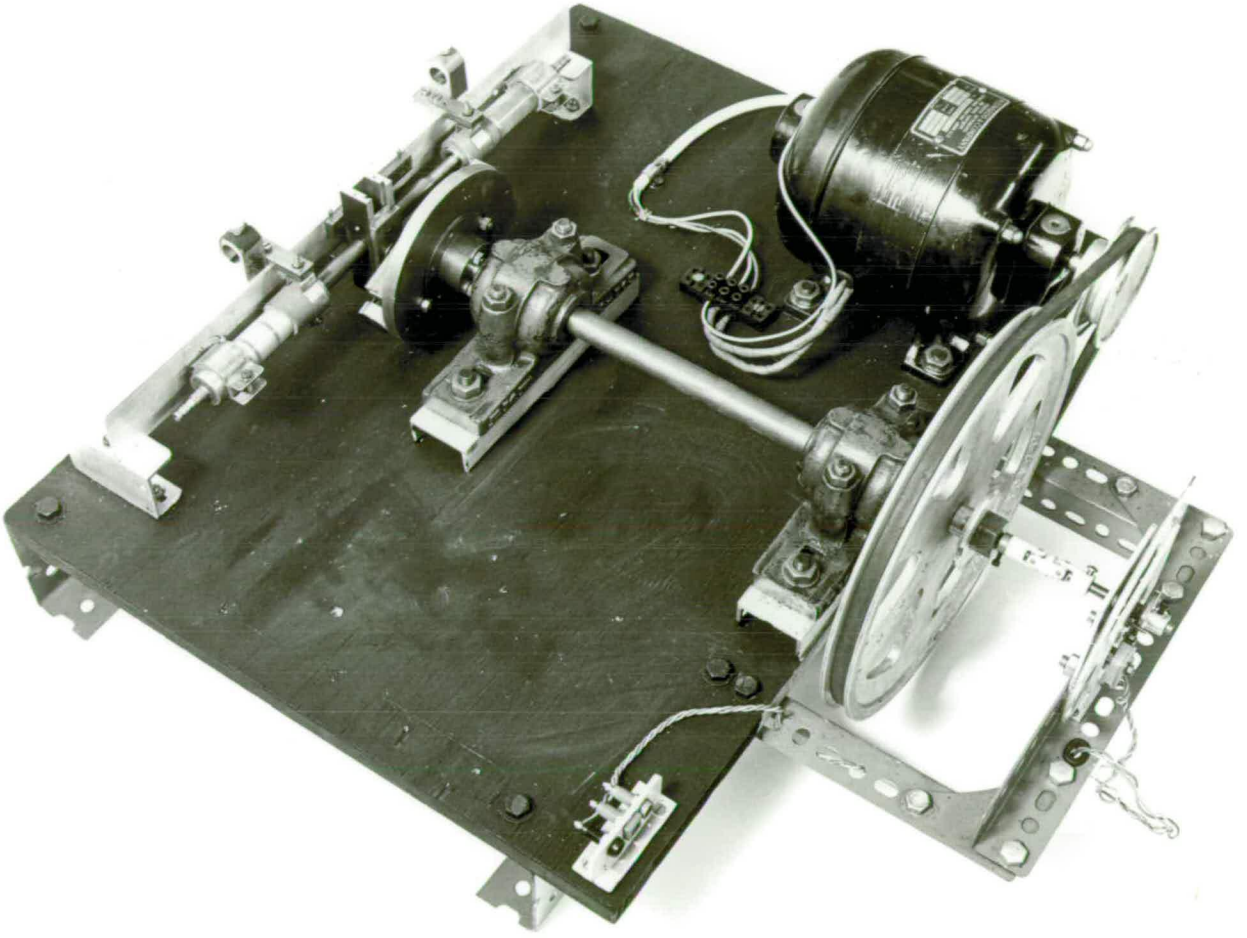

PLATE 1

FLOW INDUCER

3.1 FLOW RIG

The flow rig is shown schematically in Fig. (3.1.1) and also in Plate (1). The pump which is used to push the air back and forth through the model in a sinusoidal manner operates on the scotch-yoke principle and is a development of the type first suggested by Reynolds and Wyett (1974).

The pistons are rigidly inter-connected with a steel connecting-rod in the centre of which is a slider guide. The brass slider plate which moves up and down in the guide has a ball-race mounted in its centre. A spigot, mounted off-set on a rotating brass plate fits into the ball-race and since the locus of the spigot is a circle, the pistons move back and forth along the diameter of this circle, and thus purely sinusoidal motion is achieved. The novel linkage used in this particular system has incorporated into it a calibrated traverse which is used to vary the amount of offset of the spigot. Therefore the stroke length of the piston can be varied by a predetermined amount, thus changing the flow rate for a fixed frequency.

The rotating brass plate was driven round by a 220 V D.C. electric motor via a bearing mounted shaft and belt and pulley gearing system. The speed of the electric motor was varied using an electronic speed control based on the design of Gant (1967). The circuit

Figure (3.1.2) Circuit diagram of motor speed control

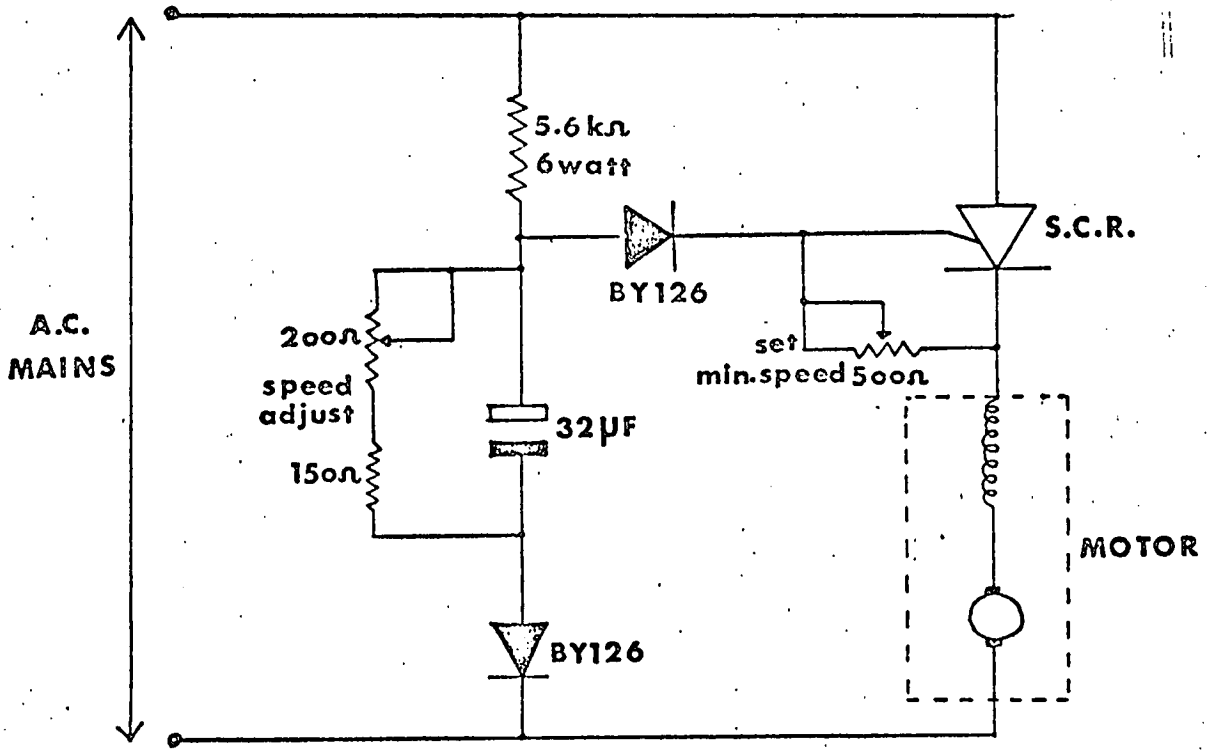

diagram is shown in Fig. (3.1.2) and uses the back e.m.f. generated in the motor coils in a feed-back loop to control the supply to the motor. This was a particularly successful design giving good torque characteristics at low speeds and a motor speed accuracy of $\sim$ 2% over a 17 hour operating period.

By varying the speed of the motor, the frequency of oscillation of the flow was changed. This also has the effect of changing the peak velocity and this could be compensated for by altering the piston displacement by the required amount. Also the gearing ratio of the driving mechanism could be altered to give a new range of parameters. This was a particularly useful feature when high frequency flows were required. Finally, the pistons and cylinders were made in two different matched pairs, one had an inside diameter of 2 cms. and the other was 1 cm. This enabled a reasonable stroke length to be maintained whilst keeping the flow rate down to the required level in the high frequency flow regime.

The entire pumping system was mounted on a heavy base-board which was rigid enough to prevent flexions in the various moving parts. The pump provided a versatile flow inducer which could operate satisfactorily in the range 0.33 - 15 Hz with a peak Re. N^{o}. capability of $\sim$ 200. Thus flow parameters of physiological interest could readily be reproduced.

Connection between the model and the pistons was

made using thick-walled plastic tubing. The length of the tube was chosen such that fully-developed flow could be achieved within the model. However, if the tubes were made too long this leads to undesirable losses. The peak Re. N^{o}. (based on mean velocity in the centre of the tube) was $\cap$ 100 in these studies, and thus entrance lengths were not a problem. Also, as shown by Gerrard and Hughes (1971), the entrance length decreases as the frequency parameter increases. The argument is given that viscosity acts over smaller portions of the flow at the higher frequencies and so the entrance length requirement is lessened.

The series of pipes provided a totally enclosed system which was advantageous due to the nature of the measuring technique employed. The laser-Doppler anemometer depends upon particles in the flow, scattering light from a measuring volume, placed at known points in the flow. The signal processing system used in this study does not require a continuous signal from the flow, and thus the amount of scattered light need only be small.

In conventional operating conditions, naturally occuring particles in an open-circuit flow, scatter sufficient light for velocity information to be gathered. The advantage of the closed-circuit system is that small quantities of pre-selected scatterers may be added to the flow and retained within the system for considerable periods of time. Each measurement made, required an experimental time of $\cap$ 4 minutes and thus the retention

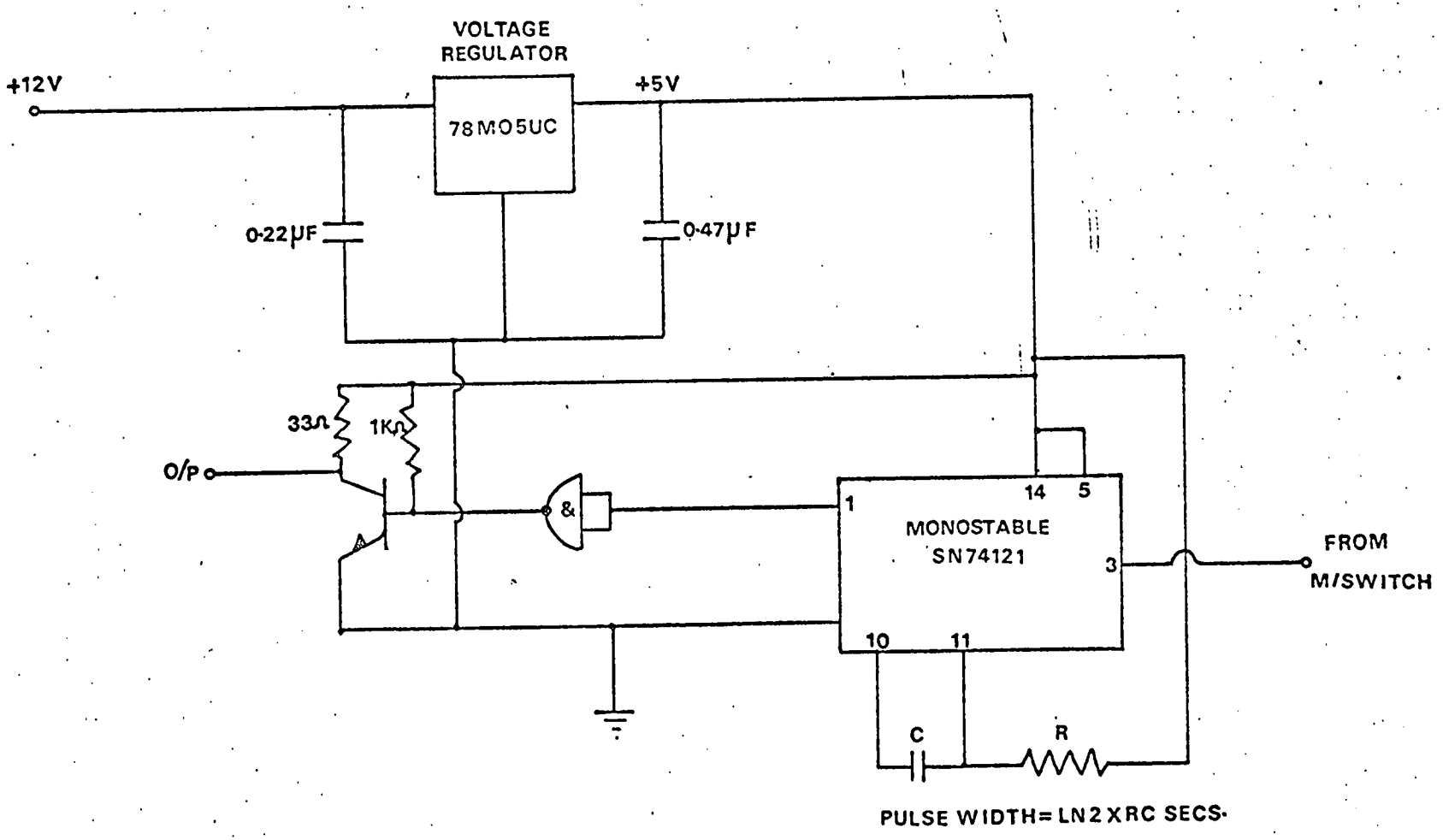

Figure (3.1.3) Circuit diagram for pulse shaper

of the light scattering or "seeding" particles was an important feature of the system. The seeds used were small quantities of cigarette smoke which have a mean particle size of 0.1 μm and are thus efficient scatterers of He - Ne laser light. The seeds are eventually lost by adhesion to the walls of the tubes, the deposits acting as a filter for the larger particles.

The flow in the system was continuously oscillating back and forth, but as information about the flow at a pre-selected point in the cycle was required, a means of sampling the signal had to be incorporated into the measuring system. The cycle is assumed to be repeated exactly, therefore if a particular phase point is selected and the information obtained at that point averaged over many cycles, then effectively "instantaneous"flow information is achieved.

The sampling system consisted of a disc with a notch cut into the edge, attached to the drive shaft of the pump. A bounce-free, Hall-effect microswitch was tripped using this device and employing the pulse-shaping circuit of Fig.(3.1.3) a pulse of pre-selected width was used to gate the output of the photo-multiplier. The sample width was made short enough to avoid averaging over too large a portion of a cycle, but long enough to make experimental time practical. A typical sample time was $\sim 0.5^{o}$ per cycle.

A hot wire was initially included in the flow system

Figure (3.1.4) Velocity time diagram for the centre of the tube when $\alpha = 0.83$. Crosses give the experimental points and solid curve gives theoretical result derived using the results of section (2.6).

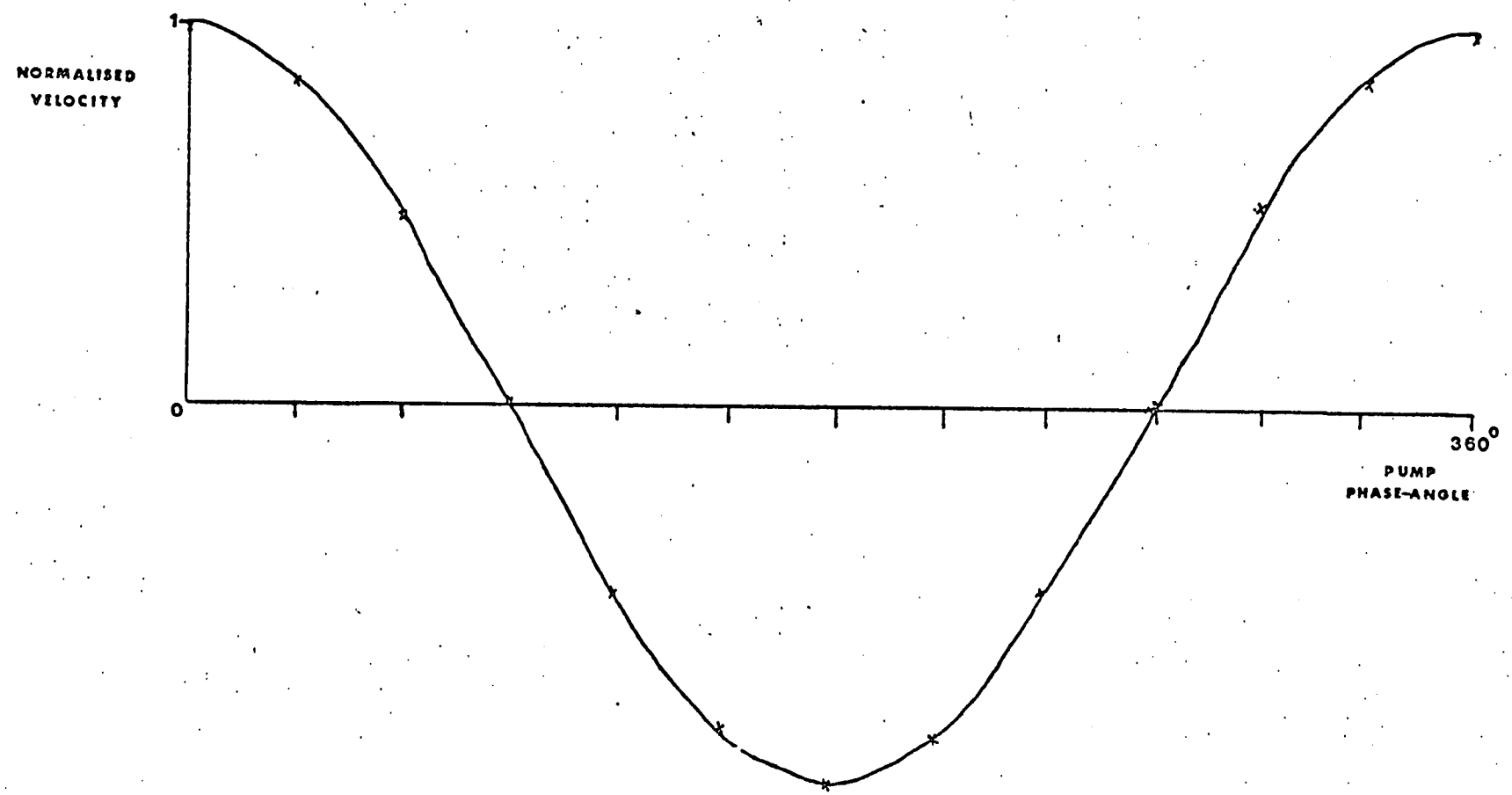

to give a visual display of the flow. The hot-wire could not detect the direction of the flow and gave a very distorted picture as the flow passed through zero. However, it was assumed that the peaks in the flow were faithfully reproduced and this was used as a check on the stability of the sampling system and on the frequency of the flow.

Before proceeding with the actual experiments, the flow in the centre of a straight pipe was measured at various phase points of equal interval to check if the flow was truly cosinusoidal and also to calibrate the sampling system. The result is shown in Fig. (3.1.4) and it is seen that agreement between experiment and theory is good. Once a few sample points had been checked, others were chosen by attaching a protractor to the sampling mechanism. Reliable flow information could then be obtained at pre-determined phase positions.

The flow rig plus measuring optics were mounted on a vibration isolating table manufactured by Ealing-Beck. The table was supported by a piston and tube arrangement which was pressurised using a nitrogen supply. Therefore, the experiment was isolated from both unwanted building vibrations and those caused by the pump itself. This was mounted on a separate unit, connection being provided via flexible tubing.

3.2 MODELS

The basic requirements of the models used were that they had to be of small diameter and have good optical properties. The small diameter tubes were necessary to provide realistic physiological flow parameter simulation in a simple manner. The optical quality of the models had to be such that there would be minimum distortion of the laser beams as they entered the model, and that most of the scattered light would be transmitted to the photo-multiplier.

For these reasons glass models were chosen and these were manufactured from precision bore pyrex tubing. The models were chemically cleaned before each series of experiments and this kept signal losses down to a minimum.

The first series of experiments were carried out using a straight 5 m.m. inside diameter precision bore perspex tube of length 15 cms., with the measurements being made in the middle of the length of tubing. This served as a useful starting point for the experiments in that well-proven theories exist for such flows and thus a reliable check with theory could be made.

The initial curved tube experiments were made using a 3.6 m.m. inside diameter tube of non-dimensional radius of curvature $^1/_{50}$. A 270° section of tube was used in these experiments, the measurements being made

at position 180^{o} round the curve, where it was assumed fully-developed conditions had been reached. This section of tube was made from a distillation rig and was manufactured by "cold-drawing" the tube. This ensured that the cross-section remains circular during the bending process.

The main set of experimental measurements were made using a model of curvature 1/7 which was chosen because of its physiological significance, i.e. its common occurrence in the lungs, Olsen (1971). The tube itself was manufactured in U-tube form from a section of precision bore 1.5 m.m. walled pyrex tube which had an inside diameter of 6.2 m.m.. The reason for choosing such a thick-walled tube was that this greatly reduced the distortion of the tube in the bending process. The skill of the glass-blower was tested in the manufacture of this model, and after almost forty rejects, a tube of circular cross-section with distortion $\sim 1.5\%$ was produced.

3.3 OPTICAL ARRANGEMENT

The laser-Doppler anemometer used in all the experiments to be described was operating in the differential-Doppler or "fringe" mode. In this configuration a single laser beam is split into two parts by a prism arrangement and the beams are then caused to

intersect in the region of interest in the flow by a lens system.

Each particle in the flow scatters light as it passes through the measuring volume and this light is Doppler shifted in frequency, depending on the velocity of the particle. Thus if a number of particles pass through various parts of the measuring volume with a range of velocities, then the resultant averaged Doppler frequency will be very complex, and retrieval of useful velocity information will be difficult if the distribution of velocities is not of a simple form.

However, if any velocity gradient across the fringe volume can be considered as linear, then it will be shown that the averaged Doppler frequency has the same value as that of light scattered by a single particle passing through the centre of the volume. Other velocity distributions have been considered by Kreid (1974) who showed that a complicated relationship exists even for relatively simple forms of velocity gradient. For this reason it is highly desirable to keep the measuring volume as small as possible relative to the size of the tube used. The most obvious method of achieving this, is to increase the angle between the beams since the length of the measuring volume is proportional to $^{1}/\sin\theta$ where 2θ is the angle between the beams. The simplest method of forming the volume is by use of a single lens to both focus the beams and cause them to intersect. The

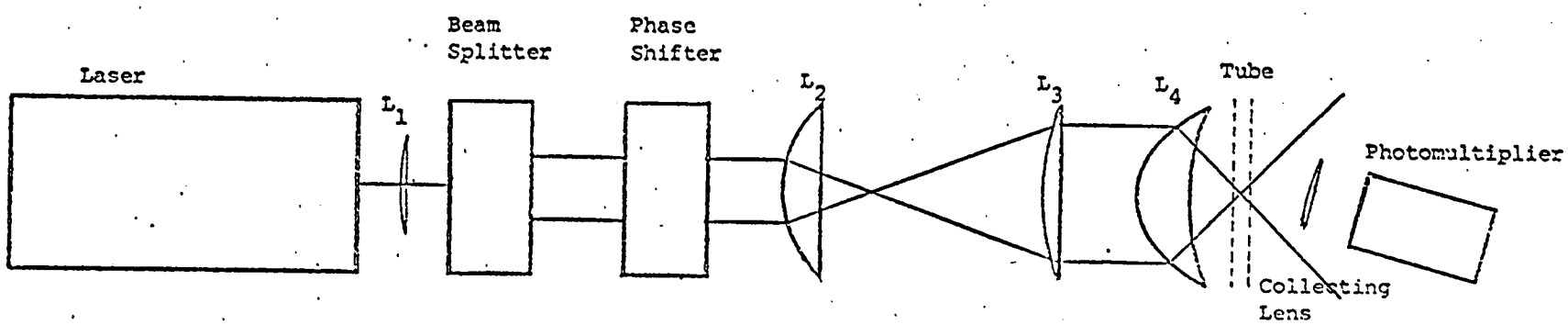

Figure (3.3.1)

Laser Doppler Optical System

large angle requirement means that the lens is necessarily used non-paraxially and as has been shown by Hanson (1973) this can lead to additional broadening of the Doppler signal.

The laser is operating in the TEM_{oo} mode and has a Gaussian intensity profile. Kogelnik (1965) investigated the effect of passing such a beam through a system of lenses and showed that unless the waist of the Gaussian beam was in the back-focal plane of the lens, it would not coincide with the front focal plane. The beam has the property that at the Gaussian waist, the wavefront is truly planar and the "fringes" formed at the intersection of two such planar beams would be linearly spaced.

However, in the system used here the beams intersect in the front focal plane of the lens, but the Gaussian waists are formed slightly in front of this position. The fringes formed are not uniformly spaced over the measuring volume which gives rise to a non-uniform signal. Therefore corrections for this source of unwanted broadening had to be made in the system used.

The actual system used as shown in Fig. (3.3.1) consisted of a 15 mW He-Ne laser, the beam of which is split using a Precision Devices beam splitter of fixed separation 2 cms. This is followed by a phase shifting device which alters the phase of the plane of polarisation of each beam in a linear manner using the Pockel's effect. The method of operation is described by Foord et.al.(1974).

The effect of the phase shifter is to give the Doppler beat frequency a bias of a pre-selected amount in a set direction. The resultant frequency measured gives the magnitude of the Doppler frequency and also its direction, depending upon whether it is greater or less than the bias frequency. This enables the direction of the flow to be determined which is useful, particularly near tube walls.

In order to increase the beam separation and thus increase the angle of intersection, lenses L2 and L3 were used in a telescope manner, which increased the separation to 4.4 cms. The telescope system also had the effect of increasing the radius of each beam which although considerably reducing the size of the measuring volume, also increased the unwanted broadening. The relatively fat beam is brought sharply to a focus and thus the distortion of the "fringes" is increased.

Lens L4 is an aspheric lens of focal length 3.8 cms. (f.No. 0.55) manufactured by the Oriel Corporation, U.S.A. and corrected for spherical aberration. This gave a final beam intersection cycle of 60.14°. Using the formulae of Kogelnik (1965) in conjunction with the analysis of Hanson (1973), the focal length and position of L1 was calculated. The effect of L1 is to minimise the amount of interference phase gradient broadening by adjusting the position of the Gaussian beam waists, such that they now almost coincide with the front focal plane of the lens. This also has the effect of increasing the length of the measuring volume, as the beam diameters are

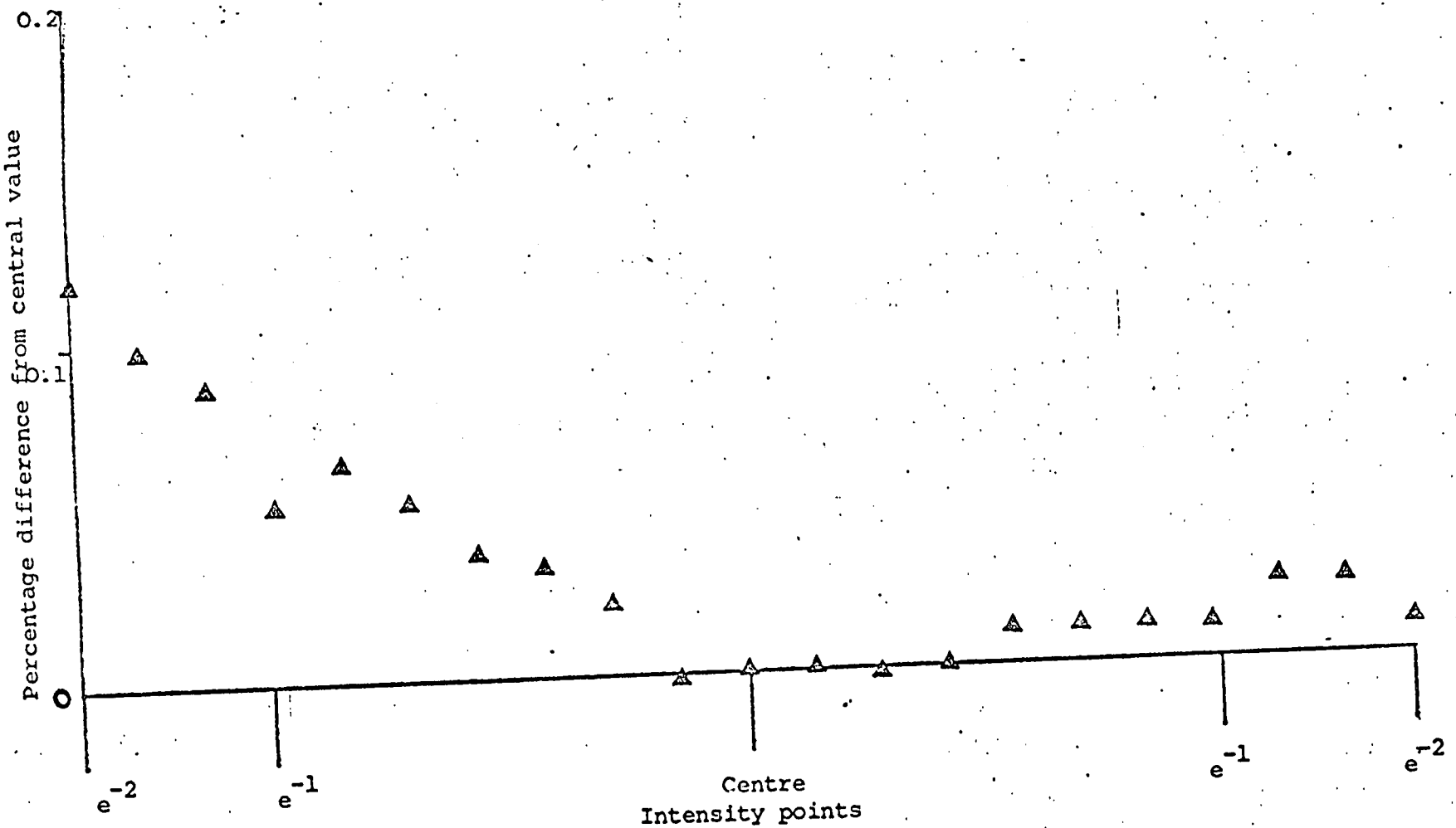

Figure(3.32)Variation of Doppler frequency across fringe volume

decreased after using the telescope system, but sufficient spatial resolution was maintained. The details of the calculations are given in Appendix C.

Therefore the final length of the measuring volume was 0.145 m.m. defined at the $1/e^2$ points of the intensity distribution, with 147 "fringes" contained within the volume. Thus even in the smallest diameter tube averaging only takes place over $\backsim$ 4% of the tube diameter. Also the fringe distortion broadening can be calculated to be $\backsim$ 0.3% and hence can be considered negligible.

An attempt was made to measure the actual broadening of the signal due to the above effects and any other imperfections in the lens system. This was done using a rotating perspex disc, mounted on a precision optical traverse, which was moved in steps of 0.01 m.m. through the measuring volume. The disc was driven at constant speed by a synchronous motor and the volume positioned so as to be as close to the centre of the disc as was possible, to minimise disc fluctuations. The results are shown graphically in Fig.(3.3.2) and indicate that there is a slight distortion towards one side of the volume but this is so small as can be considered negligible.

Another optical system has been used by Vlachos and Whitelaw (1974) using a mirror system and separate lenses for each beam. Using this method they obtained very small measuring volumes ($\backsim$0.08 m.m. defined at 1/e points), and had the advantage of being able to

control the position of the Gaussian beam waist precisely. However, their system has the distinct practical disadvantage of being very difficult to align. The method employed here is much simpler in design and can be aligned relatively easily whilst still giving good quality signals from small diameter tubes.

The scattered light was focussed by a collecting lens onto the face of the photo-multiplier tube. This particular system used the very good telephoto-lens arrangement designed by Malvern Instruments, which enabled precise focussing of the measuring volume onto the pinhole. One of the main problems encountered in laser-Doppler measurements in round tubes is the amount of flare generated at glass walls, but using a 200 micron pinhole this problem was minimised. Also, because of the mode of operation of the photon-correlator, the background noise became a pedestal level whilst the Doppler signal was still faithfully recorded.

The receiving optics were also used to locate the precise position of the measuring volume. By introducing a relatively large amount of smoke into the tube, the intersection of the beams was made clearly visible. Using a travelling microscope at right angles to the plane of the beams, and also making use of the receiving optics telescope, it was possible to determine when the edge of the fringe volume and the inner edge of the glass tube coincided. Thus by moving the glass tube and keeping

the optics in a fixed position for the experiments, it was possible to measure velocity profiles across the tubes. The position of the measuring point was known to within 0.01 m.m.

Thus using the system described above, measurements were made of velocity profiles in small diameter tubes on purely oscillatory flow. The fringe volume size was kept small, therefore the velocity gradient across the volume could be considered as linear and as shown in Appendix D, the actual Doppler frequency measured was equivalent to that generated by a series of particles passing through the centre of the fringe volume. The effect of the linear velocity gradient is merely to broaden the Doppler spectrum about this central value.

Using the result of Appendix D the velocity gradient was measured from several spectra and compared with the value expected for perfect Poiseulle profiles. The agreement between theory and experiment was found to be within 1% which gives further confirmation that the "fringes" formed within the measuring volume inside the tube are linearly spaced.

3.4 SIGNAL PROCESSING

The signal from the photo-multiplier was processed using the Malvern-Instruments photon-correlator, the precise details of the principle of operation are

described in Pike and Cummins (1977). The frequency of the auto-correlation function gives a direct measure of the Doppler difference frequency, and thus velocity information is obtained through the relationship:-

$$\omega_o = 4 \pi W' \sin \theta/\lambda \qquad - - - \quad (3.4.1)$$

W' = velocity

$\omega_o = 2\pi f_D$ where f_D is the Doppler-difference frequency

λ = wavelength of laser

Each correlation function when fully formed was sent through a data link to the Departmental P.D.P. 15 computer where it was stored on a magnetic disc. At the end of each experimental session, batches of correlation functions were transferred to an IBM 370 computer where they were analysed using a Fourier transform program.

A direct cosine Fourier transformation was used to obtain the spectra of the correlation functions using the relationship:-

$$\Phi (f_D) = R(o)\, T + 2\, T \sum_{s=1}^{m} R(sT) \cos (2\pi f_D sT);$$

$$f_D \leq \tfrac{1}{2} T \qquad - - - - - \quad (3.4.2)$$

where sT is the lag time for channel number s and m is the total number of correlation lags.

This method is particularly simple to apply and it

has been found Daudpota (1976), that it leads to accurate determination of the peak frequency. The variance may also be accurately determined provided that the correlogram has decayed to effectively a constant level within the range of channels available, (in this case 48 which was later extended to 72). The decay rate may be controlled using the optical phase shifter since this effectively imposes a variable mean velocity on the flow. Thus by choosing a suitable shift the variance of the spectrum can be found and therefore the velocity gradient may be accurately determined.

The cosine transformation has been used here in preference to the more usual F.F.T. methods since it returns the same number of Fourier co-efficients for data points. The F.F.T. would require extension of the correlation function to 2n points (where n is an integer) resulting in n/2 co-efficients. Also since the number of data points involved here is relatively small, the computing time saved using F.F.T. would be minimal. The zero lag value is not available on this correlator and is thus set in the program such that $R(o) \geq \max |R(sT)|$. The precise value chosen is unimportant since it only introduces a constant pedestal level into the spectrum. The value used in this study was $R(o) = 1.1 \max |R(sT)|$.

Using this transformation technique together with a peak detection and polynomial fitting routine, mean velocities were computed. Velocity profiles were

obtained and plotted on a Calcomp graph-plotter using a cubic spline package. A typical computation time for a mean velocity profile of 20 points was $\sim$45 seconds.

C H A P T E R 4

PRESENTATION AND DISCUSSION OF RESULTS

INTRODUCTION

This chapter contains a presentation and discussion of both the theorectical and experimental results obtained in this study. Comparisons will be made between the two sets of results and also with the earlier work of other researchers, in an attempt to find the range of validity of this work.

Firstly, results will be presented for fully developed oscillatory flow in a straight pipe. These measurements formed the initial stages of the experimental work and served as a useful system calibration procedure, since well-proven theoretical results are available.

The next section contains the results of the study of secondary flow in a curved pipe. The bulk of this work was theoretical in form due to the extreme practical difficulties involved in experimental measurements. However, two important sets of measurements were made and it is shown that the theoretical results are in reasonable agreement with these and also with earlier experimental studies.

The third part contains the results of measurements

made on developing oscillatory flow in a curved pipe. These were used to determine when fully developed conditions were achieved round the curve. Also, because of the wide variety of profile shapes available at the input to the curve at certain alpha values, different development procedures were observed. Comparison will be made between these results, earlier experimental studies involving steady flows and also some of the very limited theoretical work available.

Both theoretical and experimental results will be given in the next section on axial velocity distribution in fully developed oscillatory flow in a curved pipe. In the low frequency or quasi-steady flow region, general agreement is found between the results of this study and earlier steady flow work. As the frequency parameter increases, it is found that the flow has some unexpected features. However, agreement is found between the experimental and theoretical results.

Finally, an explanation is given for the flow patterns found in oscillatory flow in a curved tube in the transition region between the high and low frequency parameter regimes. Although precise details of the flow field are complicated it will be shown that the main features may be explained in terms of general trends in the flow.

4.1 STRAIGHT PIPE FLOW

The full solution to the Navier-Stokes equation for fully-developed oscillatory flow in a long straight pipe is given in section (2.2) by equation (2.2.4) in the form of Kelvin's functions. In order to gain further physical insight into the flow field for various alpha values, approximate solutions were found in the limits $\alpha \to 0$ and $\alpha \to \infty$ in sections (2.6) and (2.9) respectively.

The conclusion of (2.6) is that, to a first order approximation, when α is small, then the flow can be considered as quasi-steady, i.e. the velocity profile is Poiseuille at all phase positions of the pressure cycle and in phase with the applied pressure gradient. This flow regime is illustrated by the results given in Fig. (4.1.1) where velocity profiles were measured at 0°, 30° and 180° in the pressure cycle. The tube diameter was 5 m.m. and the frequency of oscillation 0.27 Hz, giving an alpha value of 0.83. The results are presented such that the dashed line in the theoretical curve and the crosses give the experimental points. It is seen that agreement between theory and experiment is good.

As α increases then as can be seen from section (2.6), the inertia terms become important and the low frequency approximation rapidly breaks down. The next set of experimental results, shown in Fig. (4.1.2), were

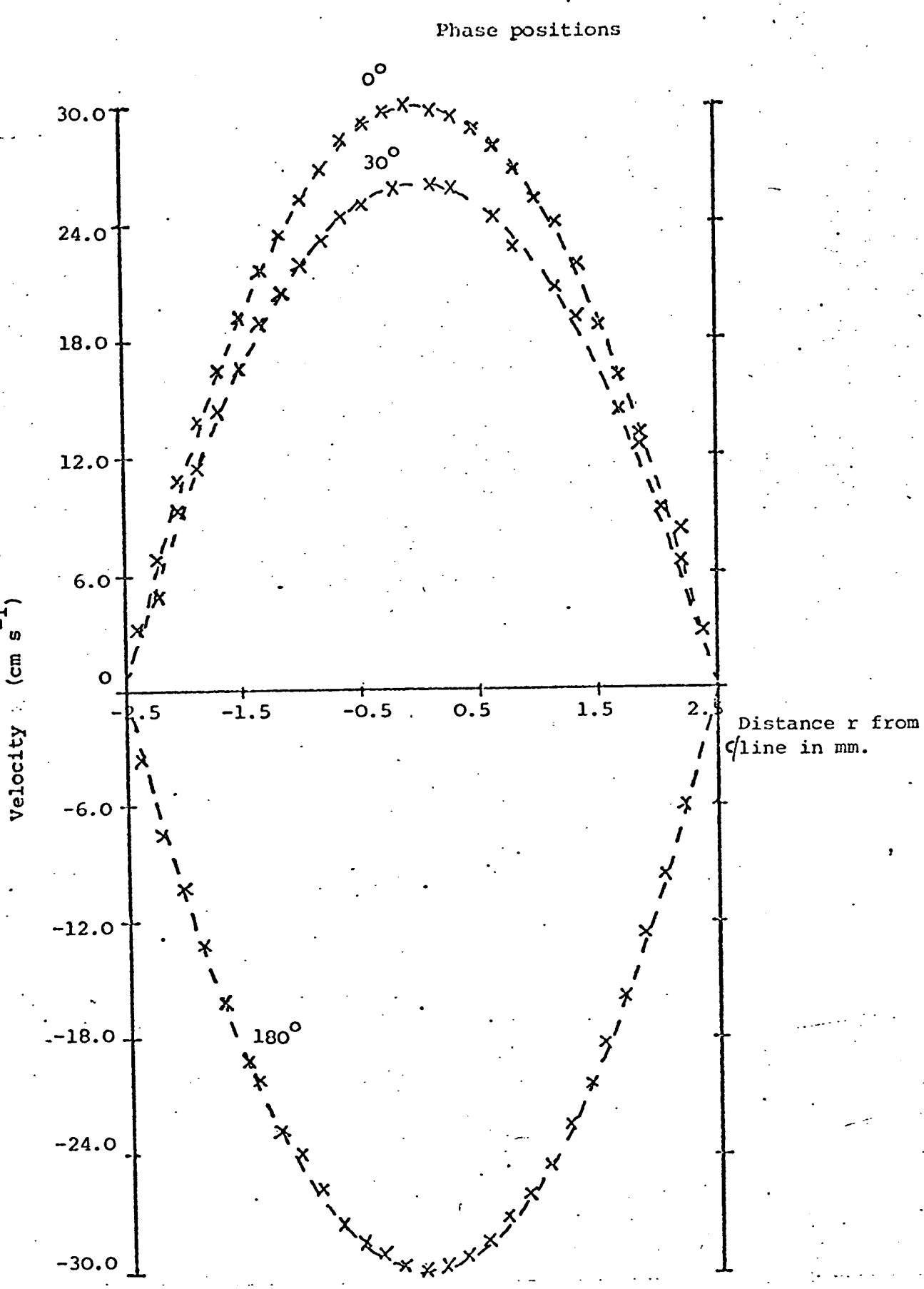

Figure (4.1.1)

Velocity profiles measured in 5 mm dia. tube

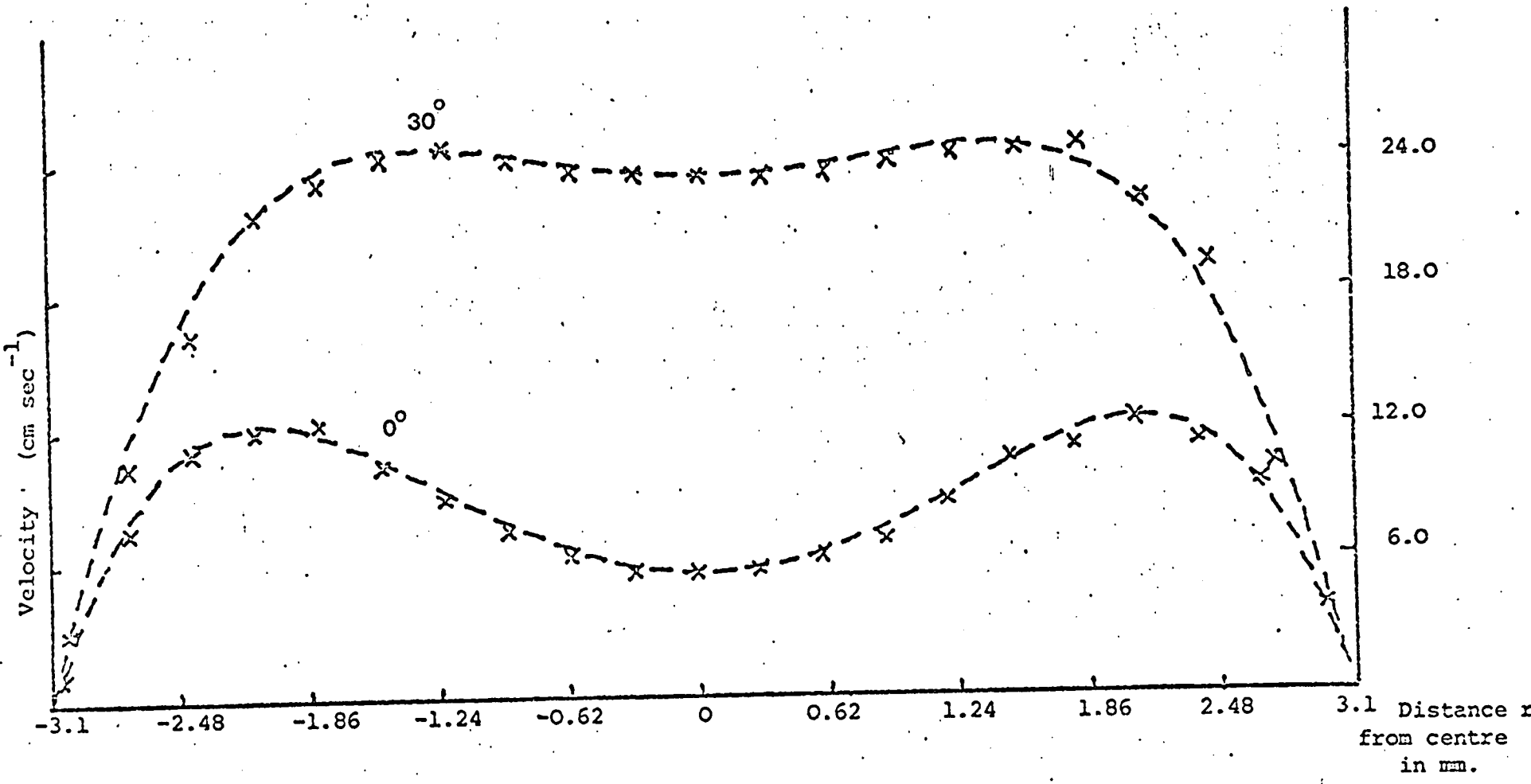

Figure (4.1.2)
Velocity profiles in 6.2 mm tube. x measured points - - - - predicted by equation (2.2.4)

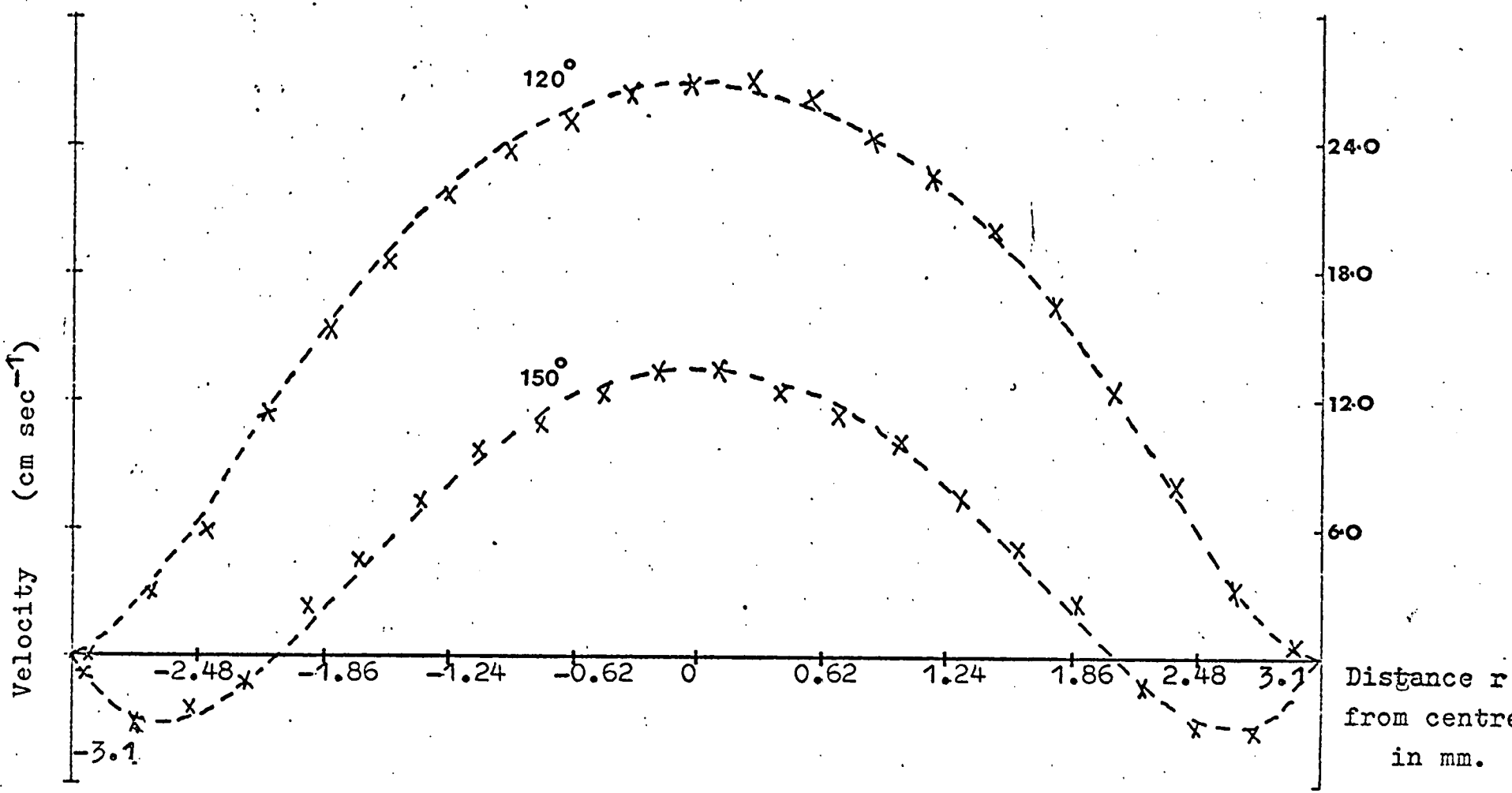

Figure (4.1.3)
Velocity profiles in 6.2 mm tube. x measured points - - - predicted by eqn.(2.2.4)

taken at an alpha value of 4.36 and therefore require the full solution for comparison. Now the frequency of oscillation was 4.88 and the diameter of the tube 6.2 mm. Comparison between theory and experiment is again found to be good for the two phase positions shown (0^{o} and 30^{o}).

Whereas in the quasi-steady case viscosity acts across the full width of the tube, now the time for vorticity generated at the walls to diffuse across the tube becomes comparable with the oscillation time of the flow. Thus the flow in the centre of the tube acts in an inviscid manner and lags the applied pressure gradient by $\backsim 90^{o}$. The remainder of the flow field is affected by vorticity to varying degrees, giving rise to the complicated flow profiles found.

Another way of picturing the development of the vorticity field throughout a cycle of the pressure gradient is that the slower moving fluid along the walls reacts first to the rapidly changing pressure gradient. The relatively faster moving fluid in the central region, which has a larger amount of momentum associated with it, takes a longer time to react, and thus there is a phase lag between the flow at the wall and that in the centre of the tube. This is illustrated in Fig. (4.1.3) where velocity profile measurements are shown for phase positions 120^{o} and 150^{o} in the cycle for α = 4.36. The flow at the wall is seen to react to the reverse pressure gradient before the central region. Again agreement between theory

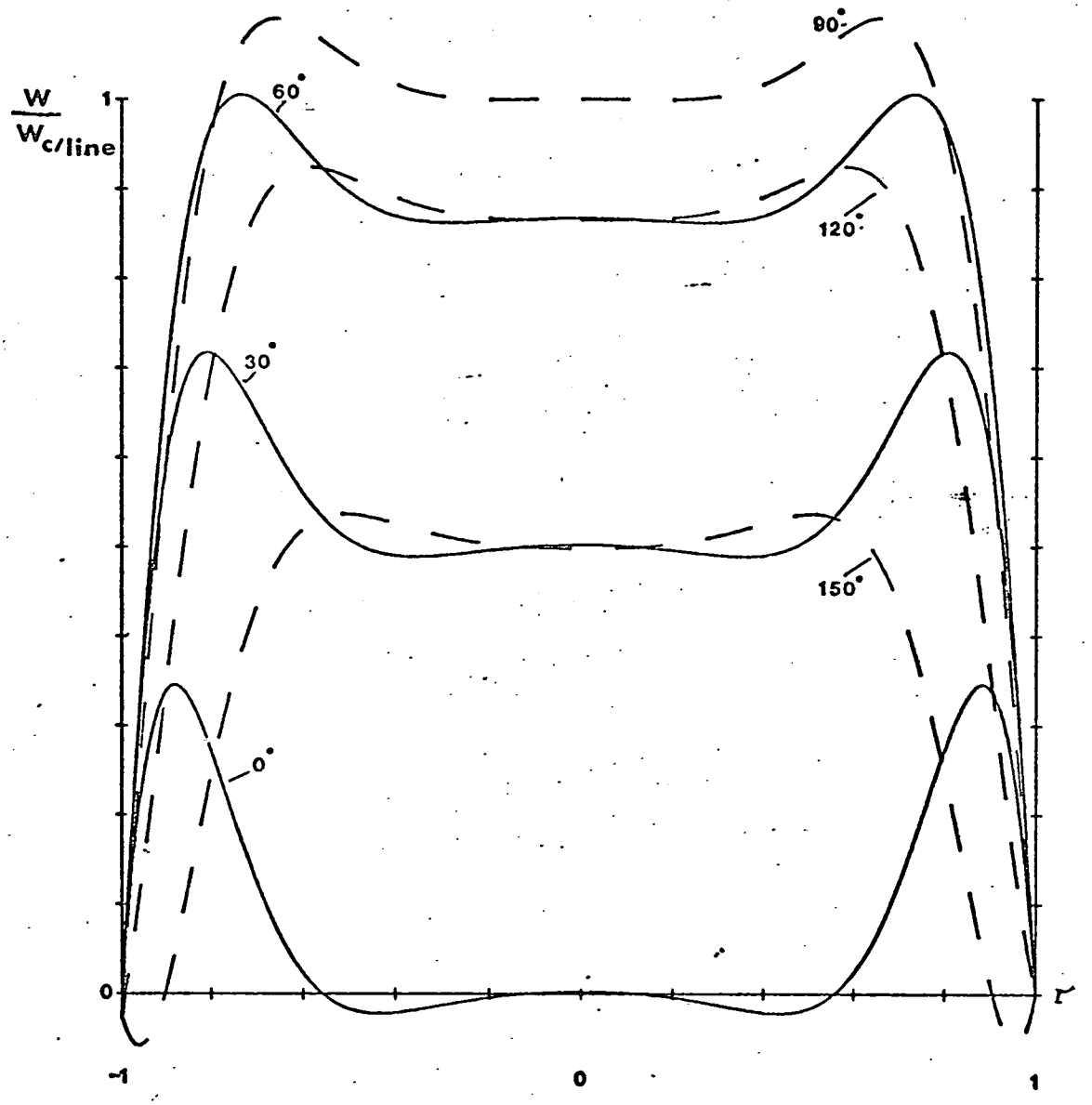

Figure (4.1.4)

Velocity profiles for a straight pipe with α = 10 derived using equation (2.9.5).

Figure (4.1.5) Phase lag between piston and pressure gradient plotted as a function of α.

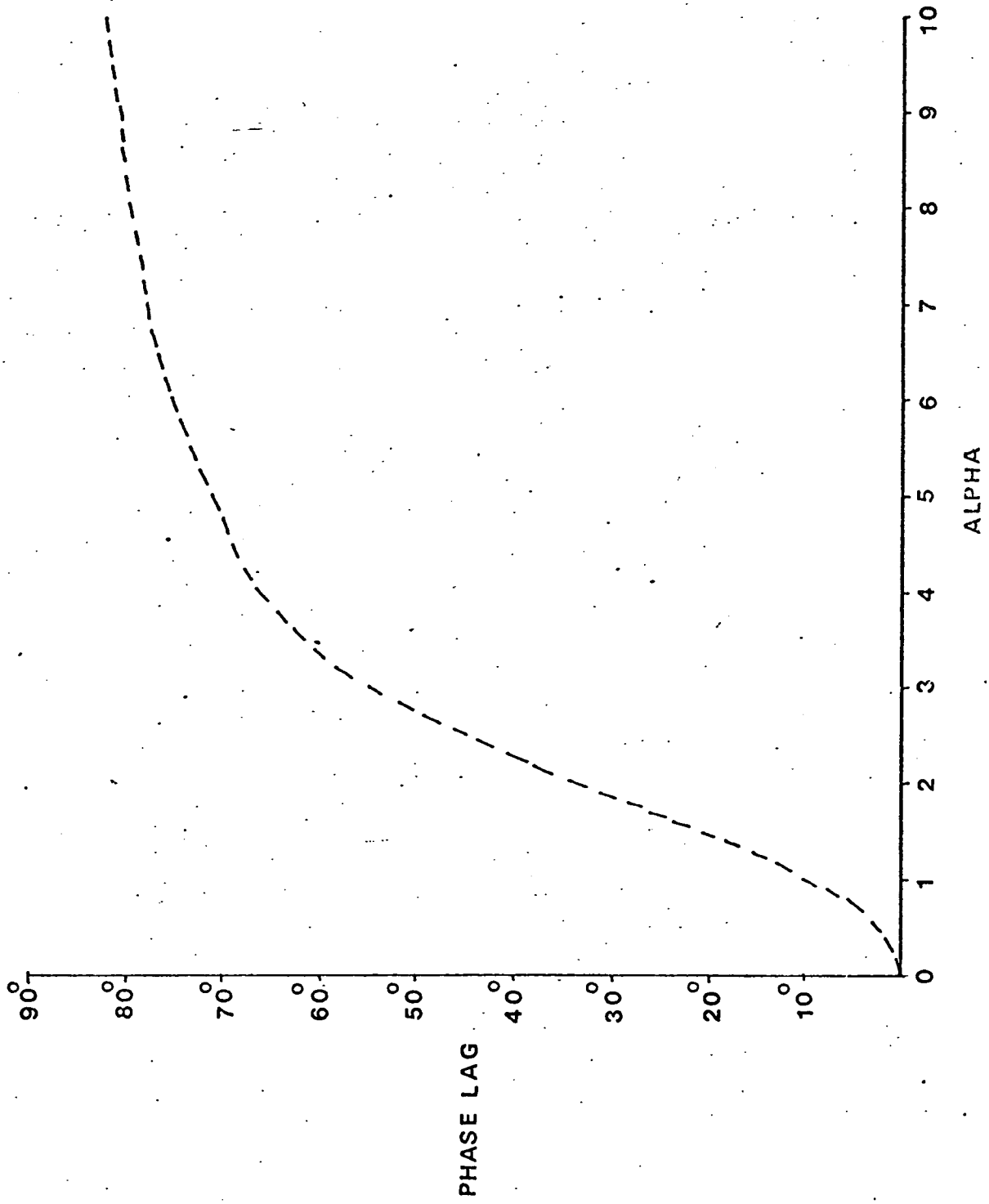

and experiment is found to be good.

Finally, the high alpha region is illustrated in Fig. (4.1.4). This flow regime is outside the capabilities of this experimental system but a few profiles are presented, derived from the approximate theoretical solutions of (2.9) to illustrate the form of the flow field. The profiles shown are those of 0° - 150° in the cycle at an alpha value of 10. Now it can be seen that the effects of viscosity are confined to thin boundary layer regions along the walls of the tube. The uniform central core, which is 90° out of phase with the applied pressure gradient, extends over $\sim 80\%$ of the tube.

All of the profiles measured in the straight pipe and the curved pipe will be related to each other by their phase positions in the pressure gradient. The piston velocity, which is the mean velocity, lags behind the pressure gradient for $\alpha > 1$. The exact relationship between the piston phase position and the pressure gradient phase is given in Fig. (4.1.5) derived from the results of Uchida (1956). Thus all measurements made may be related to the pressure gradient cycle and thus to the relevant theoretical results.

The sets of measurements reported, confirm that the pumping system is providing fully-developed oscillatory flow in the measuring regions and that the measuring system is faithfully reproducing the flow field.

4.2 SECONDARY FLOW IN A CURVED TUBE

A description of the origin of secondary flow in curved tubes will first be given using a method similar to that of Kàrmàn (1934). He derived the flow stability criterion of Lord Rayleigh (1916) for fluid flowing between rotating cylinders using a centripetal force, pressure gradient argument. Since the secondary flow patterns found theoretically and experimentally by Taylor (1923) for rotating cylinder flow are very similar to those found in curved tube flow, this seems to be a good starting point to understand the problem.

Consider the case of a tube of non-dimensional radius r bent in the shape of a toroid of radius R. Fluid of density ρ flows around the tube with velocity w, which is a function of r, under the action of a pressure gradient $-\frac{\partial p}{\partial \theta'}$ where θ' is the angular coordinate of the system. Since fluid elements are moving in circular paths, a centripetal force of magnitude $\frac{\rho w^2}{R+r}$ per unit volume is required for steady motion and this is provided by a pressure gradient $\left(-\frac{\partial p}{\partial r}\right)$.

Now consider a fluid element of velocity w_1 at radius $R + r_1$ and suppose the element is displaced to a radius $R + r_2$ which is greater than $R + r_1$. The angular momentum of the fluid element will remain constant and

thus its new velocity will be given by $\frac{(R + r_1)}{(R + r_2)} w_1$.

For this element to be in equilibrium at its new radius it would require a centripetal force $\rho \frac{(R + r_1)^2 w^2}{(R + r_2)^3}$.

However, the pressure gradient at radius $(R + r_2)$ provides an inward force of magnitude $\frac{\rho w_2^2}{R+r_2}$ where w_2 is the velocity at $R + r_2$. In general this force is not equal to the centripetal force required for the newly arrived element.

Therefore if $\frac{\rho w_2^2}{(R+r_2)} > \frac{\rho (R + r_1)^2 w_1^2}{(R + r_2)^3}$ then the fluid element will be forced back into its original position and a stable situation will exist. However if $\frac{\rho w_2^2}{(R+r_2)} < \frac{\rho (R + r_1)^2 w_1^2}{(R + r_2)^3}$ then the fluid element will tend to move further outwards and secondary streaming directed outwards in the centre of the tube will be produced.

In the case of a Poiseuille type of flow, one would expect outward secondary flow. The axial velocity peak would thus be moved by this towards the outside of the curve. The secondary flow returns around the walls of the tube giving the familiar D-type pattern first found theoretically by Dean (1928). This type of secondary

flow will therefore be found in the quasi-steady flow regime.

In the high frequency flow case the higher velocity components in the straight tube are positioned off-axis near the walls of the tube. Applying the same type of analysis as above, then the flow near the tube walls will be centrifugally unstable. Thus one may expect two counter-rotating vortices in the upper and lower halves of the tube which are confined to the wall regions.

At the central area of the tube the flow may become unstable to fluid element translation in the opposite direction i.e. inward secondary streaming. This can be considered as similar to the flow field investigated by G. I. Taylor where the two cylinders were rotated in opposite directions. A second vortex was found near the outer cylinder which rotated in the opposite sense to the stronger vortex at the inner cylinder. Thus in high alpha flow one would expect to find a four vortex system of secondary flow. The inner vortices will rotate in opposite directions to the outer vortices and will be weaker than the outer vortices. The effects of viscosity have been ignored in the above analysis, but as indicated by Stuart (1963), the main effect of viscosity is to stabilise the motion. Thus the transition region between low and high alpha may not be smooth as viscosity acts over varying amounts of the tube at different alpha values in this region.

Figure (4.2.1) Plot of steady part of secondary flow versus α for fixed value of G = 120. Values are given for the position 0.1 r in the central plane of the bend.

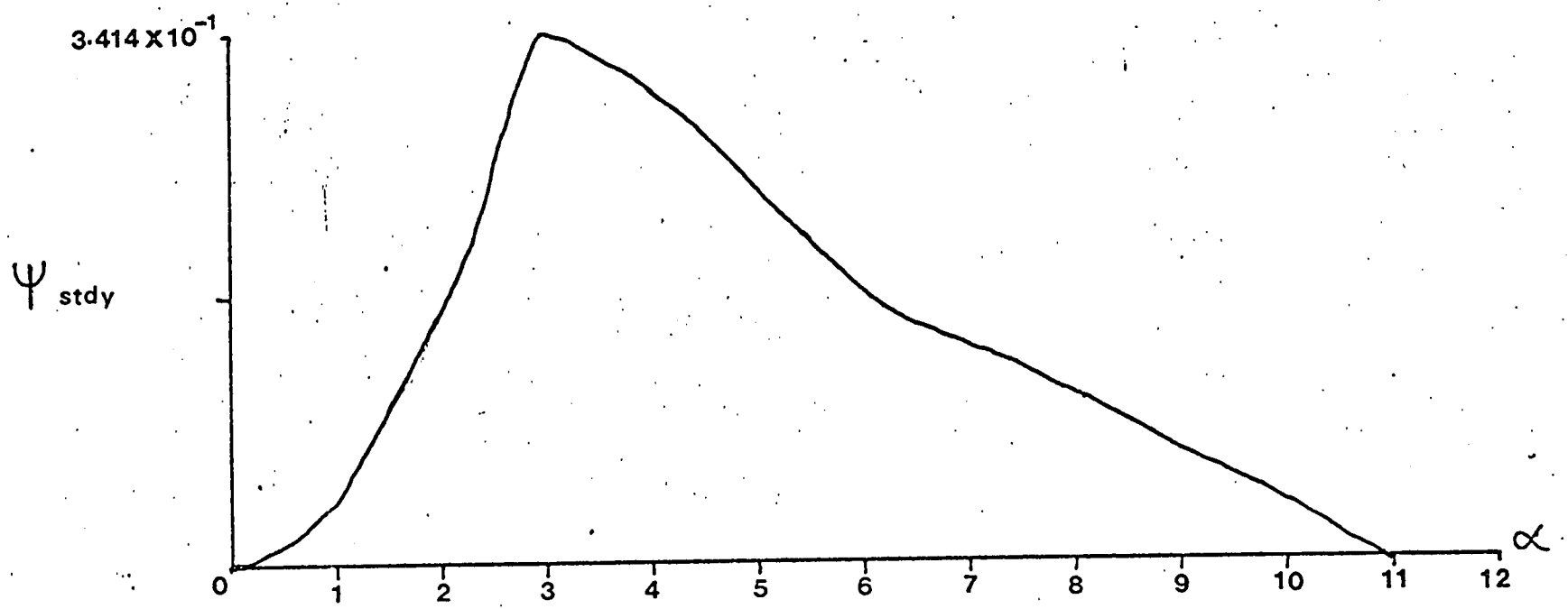

From the preceding argument, one would expect the secondary flow to be directed outwards at all phase positions in the quasi-steady regime. Thus if the pressure gradient varies as $\cos \Upsilon$ then the secondary flow will vary as $\cos^2 \Upsilon$ and a steady secondary flow will be produced as well as an oscillatory one. This has been confirmed experimentally, and the results are shown in Fig. (2.7.1) for the case when $\alpha = 0.84$.

Before considering the time dependent part of the secondary flow further, it is of interest to see how the steady secondary flow component varies with frequency parameter for a fixed value of G, the expansion parameter. This is shown in Fig (4.2.1) and it is clear that the steady component reaches a peak at $\alpha \lesssim 3$ before reducing to zero and reversing at $\alpha \lesssim 11$. These results may be compared with the experimental results of Munson (1975) and Bertelsen (1975).

The results of Munson are plotted as the non-dimensionalised secondary flow versus alpha. The non-dimensionalising parameter is R_s and thus as $\alpha \rightarrow 0$ the secondary flow approaches a constant level. This would be equivalent to dividing the above results by α^4 and thus the qualitative agreement would be good. The secondary flow approaches a constant level as $\alpha \rightarrow 0$ and approaches 0 as α increases, changing direction at $\alpha = 13.4$. Munson has already shown that his results are in agreement with the quasi-steady secondary flow

Figure (4.2.2) Steady component of secondary flow for various alpha values, with fixed G = 300.

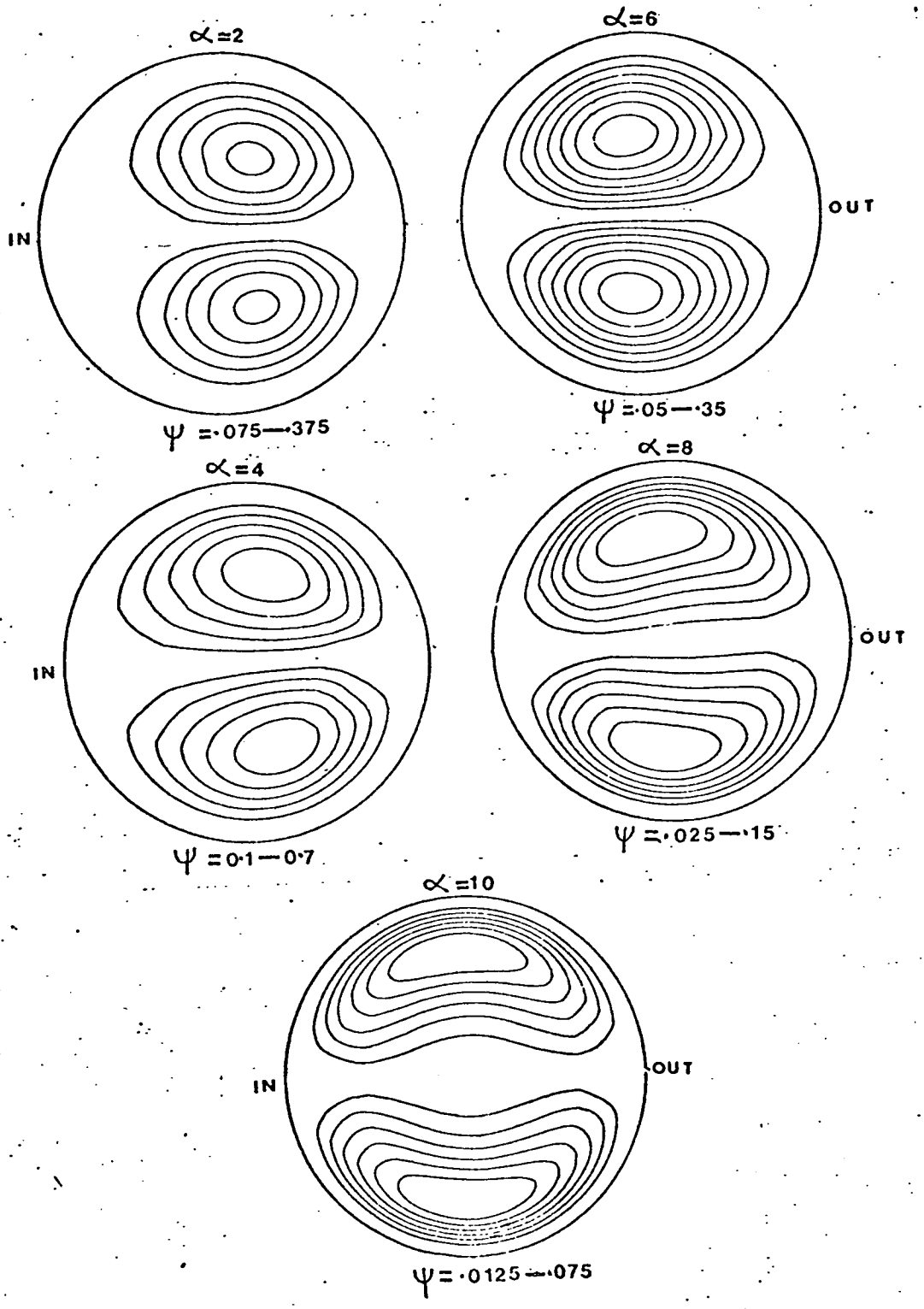

work of Zalosh and Nelson (1973), which in turn is in agreement with the results presented here. The cross-over value found experimentally is higher than the value predicted here, but it is in agreement with the boundary layer work of Lyne (1970). This is to be expected as his approximation is of higher order than the one presented here in the high frequency limit.

The work of Bertelsen is approximately in agreement with the previous results, finding the reversal of the secondary flow to occur between $\alpha = 12.3$ and 14.4, explaining that the actual alpha value where transition occurred was difficult to observe. This is conceivable since the secondary flow is very small over this region making measurements difficult unless R_s is large. Therefore the results of Munson may be suspect in this region, although the R_s values used are not quoted and may have been large.

The steady flow patterns produced for alpha values 2, 4, 6, 8 and 10 are shown in Fig. (4.2.2) for a fixed value of G, the amplitude parameter. It can be seen that for $\alpha = 2$ and 4 the centres of the vortices are displaced towards the outside of the bend to produce streamline patterns similar to those of McConalogue and Srivastava (1968). As alpha increases to 6 the centres move towards the inside of the bend and remain there until $\alpha = 10$. This thickening of the vortex core on the inside of the curve was found by Bertelsen in his experiment. He found that when $\alpha \leq 20$ this phenomenon occurred, and he

Figure (4.2.3) Secondary flow streamlines for the case $\alpha = 1$, G = 9216.

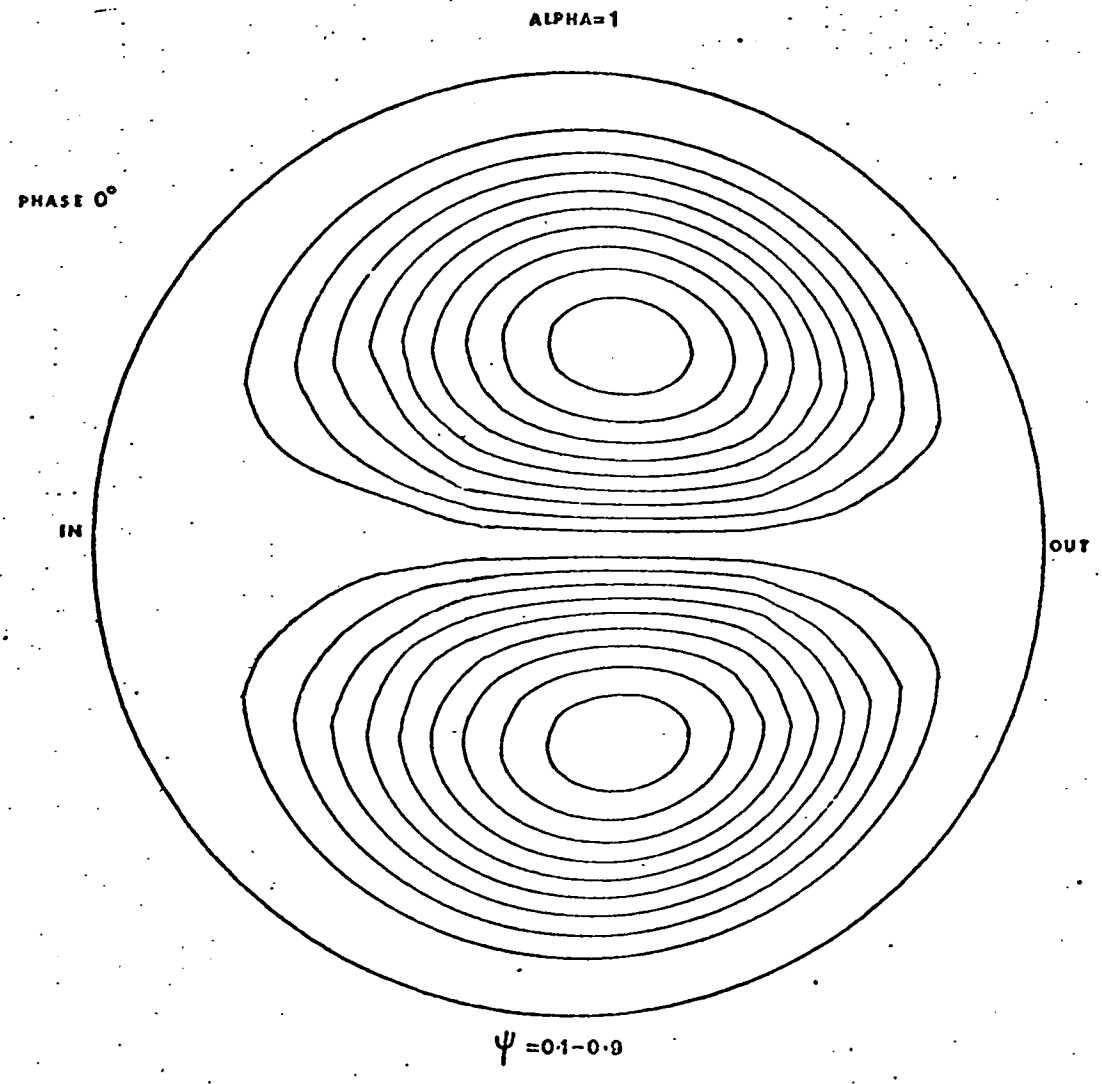

explained it in terms of the finite curvature of the tube used in his experiment. Further, he extended the work of Lyne by expanding the boundary layer equations in terms of the curvature and gained reasonable agreement between theory and experiment. Lyne in fact ignores the effect of curvature on the axial velocity distribution and this is probably why the effect does not appear in his results. From the results presented here, it may be concluded that the steady vortex core is thicker towards the inside of the curve for all curved tubes when $\alpha \geq 6$.

Another important feature of these flow patterns is the development of a stagnation zone in the centre of the tube. The central inviscid core of the flow grows as alpha increases and the centrifugal instability is confined towards the walls of the tube. It would appear from the results that development of the counter-rotating vortex in the centre of the tube occurs over a large α range. Therefore it is questionable if the boundary layer theory and approximations can be applied below the transition α value of 12.8 given by Lyne.

The full secondary flow streamlines are shown in Fig. (4.2.3) for $\alpha = 1$ phase position 0^{o} and G = 9216. The flow pattern is very similar to that produced by the steady flow work of McConalogue and Srivastava (1968) for the same G value. As shown in Appendix E, where the range of validity of this work is discussed, comparison is good at G = 9216 but falls off as G increases. Other plots

Figure (4.2.4) Secondary flow streamline patterns obtained when $\alpha = 3$ and $G = 300$

(a) Phase position 0° $\psi = 0.01 - 0.09$

(b) Phase position 60° $\psi = 0.2 - 1.0$

(c) Phase position 90° $\psi = 0.2 - 1.2$

(d) Phase position 150° $\psi = 0.04 - 0.24$

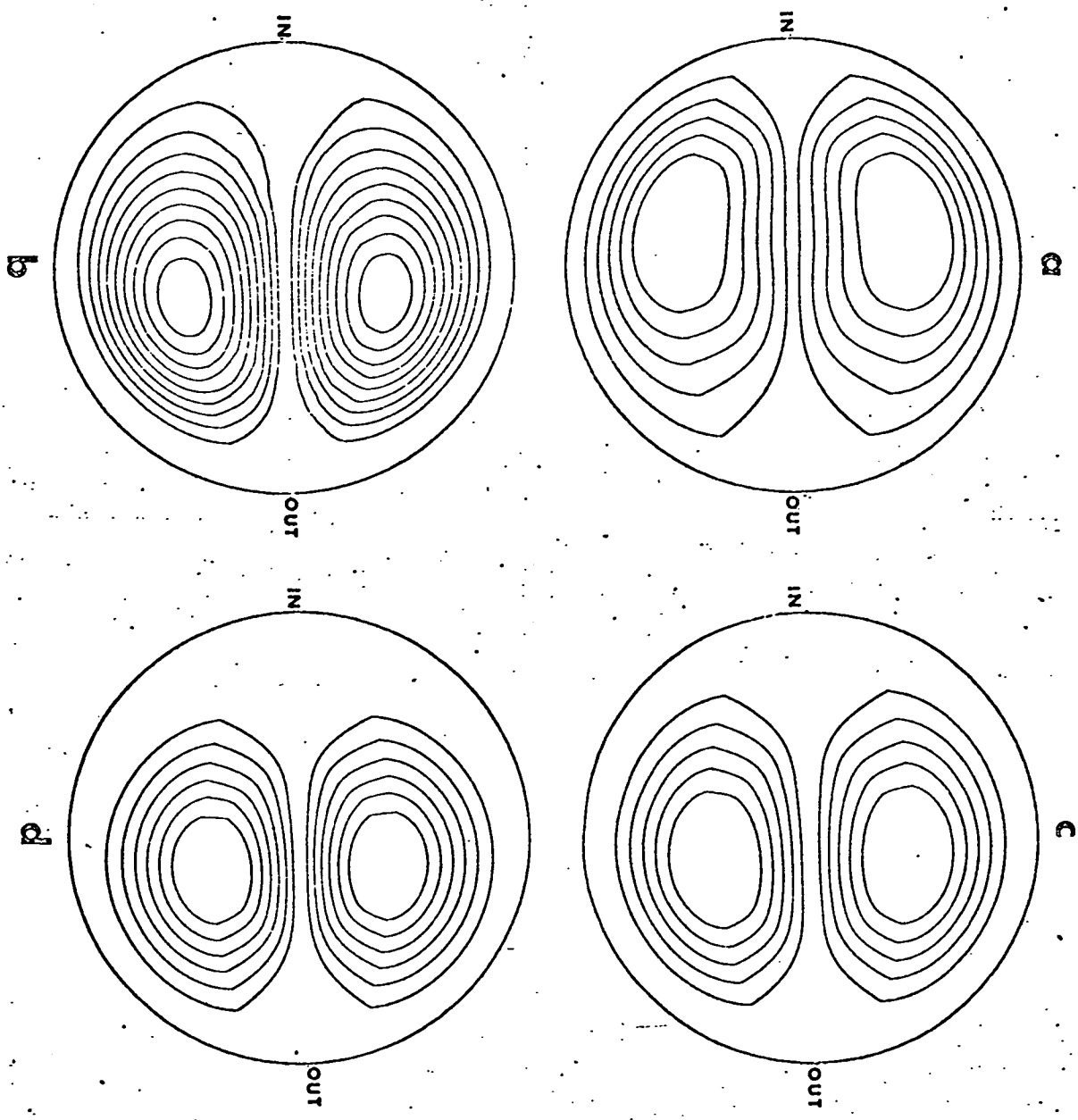

Figure (4.2.5) Secondary flow streamlines for the case α = 5, phase positions 0^0-150^0 with G = 300.

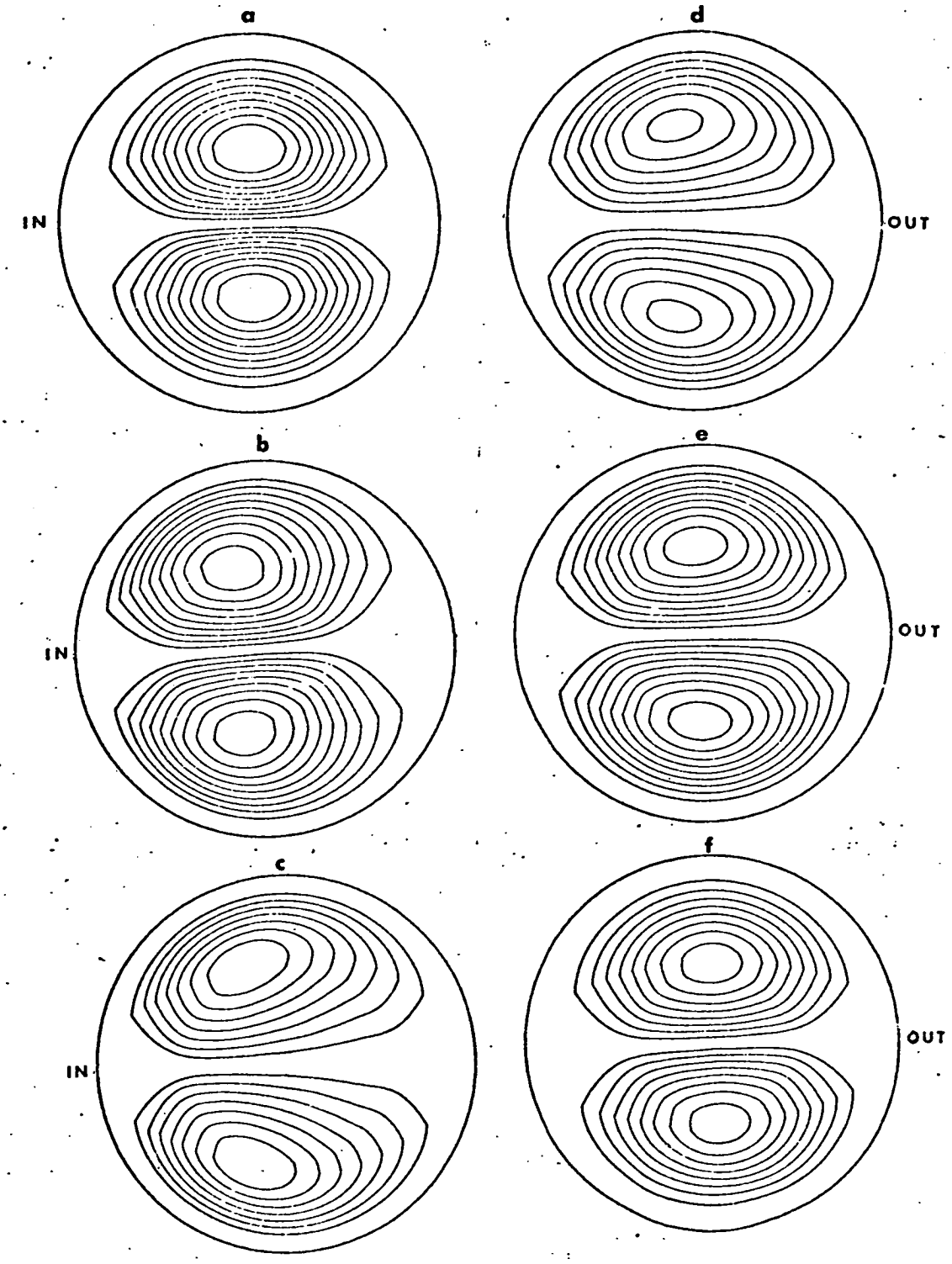

(a) Phase 0^0 ψ = 0.05 – 0.45

(b) Phase 30^0 ψ = 0.025-0.225

(c) Phase 60^0 ψ = 0.05 – 0.35

(d) Phase 90^0 ψ = 0.1 – 0.6

(e) Phase 120^0 ψ = 0.1-0.9

(f) Phase 150^0 ψ = 0.1 – 0.8

obtained at different phase positions indicate similar shapes as would be expected in the quasi-steady limit.

The effect of increasing α to 3 is now indicated in the secondary flow plots shown in Fig. (4.2.4). At 0° phase position, the centre of the vortices are displaced towards the inside of the curve and there is some indication of the beginnings of a stagnation region in the centre of the tube. Later in the cycle at phase position 60° the centres of the vortices move towards the outside of the curve and the secondary flow is now uniform in the centre of the tube. This pattern strongly resembles those of the quasi-steady patterns found earlier. Further on in the cycle up to 150° phase position, the centre of the vortices remain displaced towards the outside of the curve with uniform streaming in the centre of the tube.

The result of increasing α further to $\alpha = 5$ is shown in Fig. (4.2.5). Now the centre of the vortices remain displaced towards the inside of the bend until phase position 120°. The secondary flow in the centre of the tube is uniform and small in magnitude at the 30° phase position. The stagnation region expected in the centre of the tube is now indicated at the 60° and 90° phase positions. Further on in the cycle at 120° and 150° phase positions, the outward streaming becomes uniform in the centre of the tube with increased strength, compared with the 30° phase position. Thus this situation is

Figure (4.2.6) Normalised secondary flow and velocity plots for the tube centre when $\alpha = 4.36$. Experimental secondary flow measurements made at $D_{No} = 42.84$.

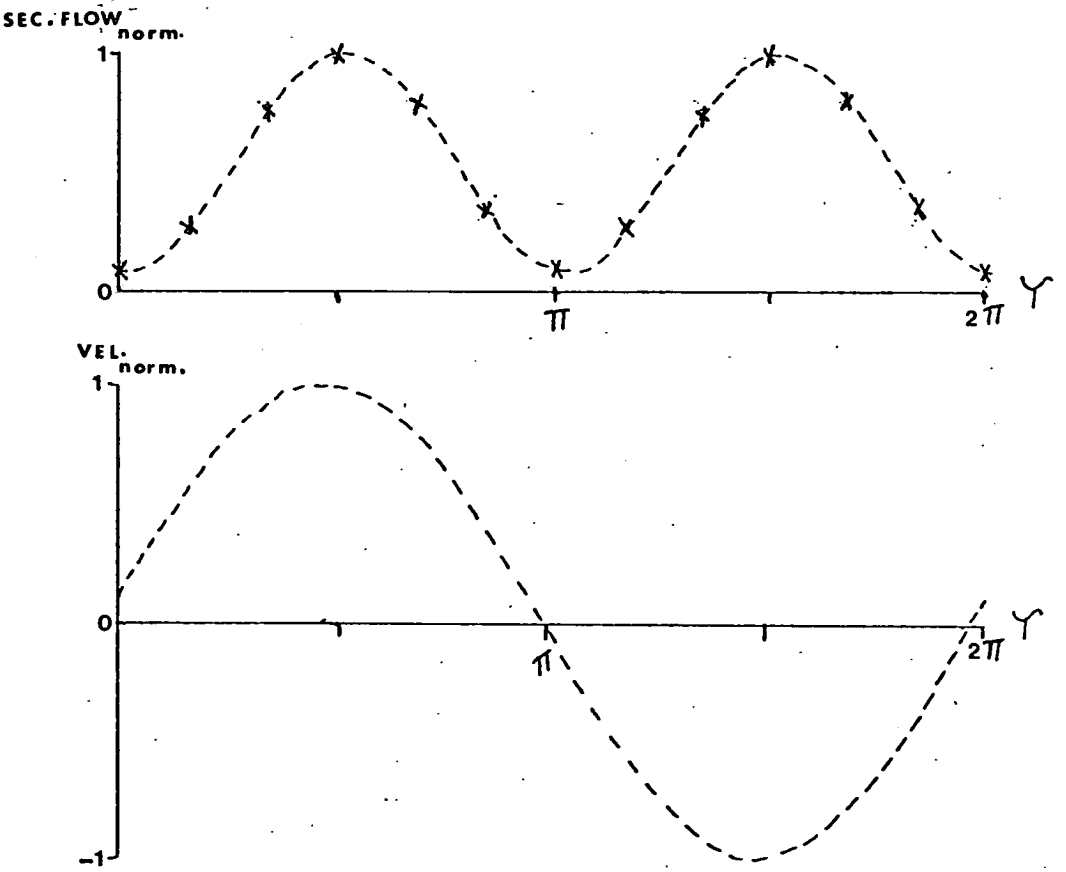

Figure (4.2.7) Secondary flow streamline patterns obtained when $\alpha = 10$ and $G = 200$

(a) Phase position 120° $\psi = 0.005 - 0.021$

(b) Phase position 33° $\psi = 0.005 - 0.035, -0.0005$

(c) Phase position 80° $\psi = 0.01 - 0.04, -0.005$

(d) Phase position 0° $\psi = 0.01 - 0.08$

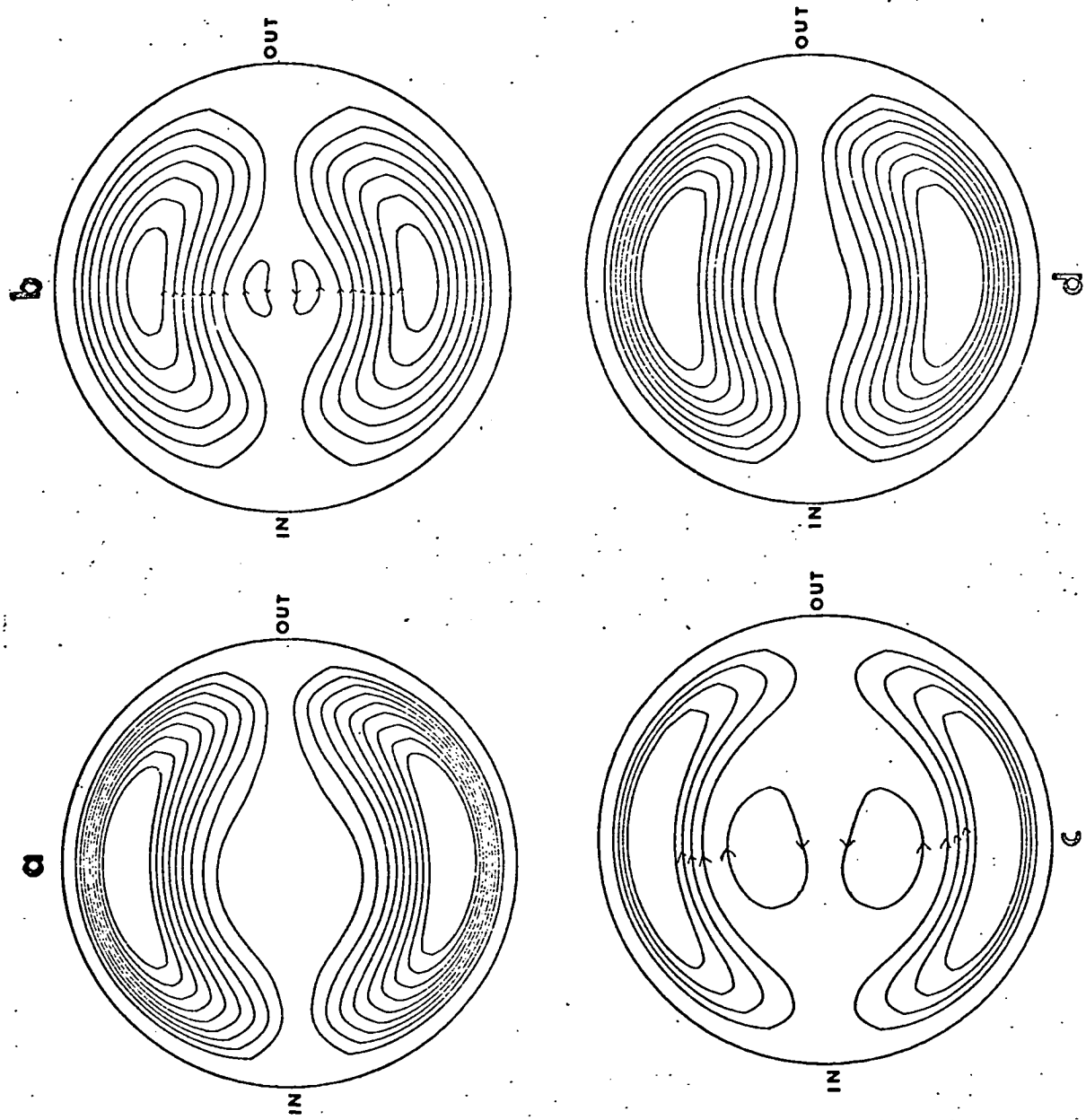

similar to the quasi-steady position and the axial flow distributions will be similar.

An investigation into the nature of the secondary flow in the central region of the tube in this α range was attempted with the experimental system. The results are shown in Fig. (4.2.6) where it can be seen that the secondary flow appears to remain in phase with the central axial velocity.

If now the α value is increased to 10, the patterns shown in Fig. (4.2.7) are obtained. The stronger main vortices are slightly thicker towards the inside of the curve at all phase positions. The stagnation zone in the centre of the tube is prominent and at a phase position of 33°, twin vortices rotating in the opposite direction to the main vortices appear. Even at phase position 80° where the largest inner vortices appear, it is clear that they only occupy a small area at the centre of the tube. Thus the situation portrayed by the boundary layer work of Lyne (1970) is only reached very gradually as α increases.

From this theoretical study it may therefore be concluded that the secondary flow is of similar form over most of the alpha range, until the boundary layer-type region is reached. There is a very gradual development of a reverse secondary flow which originates from the centre of the tube at $\alpha \geq 10$. The effect of the secondary flow on the axial velocity distribution will depend on

the phase relationship between the two, and this gives rise to a displacement of the vortices towards the inside of the curve for longer periods of the cycle as alpha increases.

While the interpretation of the appearance of secondary flow in terms of centrifugal instability is attractive from some points of view, as described above, it also has certain limitations which need to be recognized. Firstly, if the Rayleigh criterion is pushed to its logical conclusion, the secondary flow should be concentrated in the region of the cross-section where the circulation associated with the basic axial flow decreases outwards, i.e. in the half of the cross-section towards the outside of the bend; in fact, the secondary flow is distributed fairly evenly over the whole cross-section. Secondly, in the prototype Taylor instability problem (flow between rotating cylinders), the flow is unstable only when the circulation decreases outwards and the Taylor number exceeds a critical number T_c of order 1700. In the flows considered in this thesis, the Taylor number is invariably less than this critical value; and the secondary flow may then be better regarded as a flow driven by Reynolds stresses associated with the fluctuating axial velocity, rather than as a manifestation of instability as normally understood.

4.3 EXPERIMENTAL INVESTIGATION OF DEVELOPING OSCILLATORY FLOW IN A CURVED PIPE

The series of measurements presented here are of velocity profiles measured in the plane of the bend of the U-tube of curvature $^1/_7$th, described in the experimental section. Profiles were measured at various angular distances around the curve to determine when fully-developed conditions had been reached. Velocity profiles measured in the straight sections of the U-tube indicated that fully-developed conditions applied there and some of these results are shown in section (4.1).

The fully-developed state will be defined here as the case when two successive profiles are of similar shape and the areas under the profiles are within $\sim 3\%$ of one another i.e. within the experimental error. Also, where possible, comparison will be given between the theoretically predicted fully-developed state and the one measured in the experiment.

The first set of profiles, Fig. (4.3.1) show the case when $\alpha = 1$, phase position 0^o corresponding to a Dean number = 14.63 where $D_{No} \equiv Re\sqrt{\frac{a}{R}}$, Re is the Reynolds number defined as $\frac{\bar{w}d}{\nu}$, where $\bar{w}$ is the mean velocity along the centre line of the pipe, d = 2a is the diameter of the tube, ν is the kinematic viscosity and R is the radius of curvature of the bend. The dashed curve is a cubic spline drawn through the experi-

Figure (4.3.1) Velocity profiles showing flow development in the quasi-steady region. Peak D_{No} = 14.63, α = 1.0, a/R = 1/7. x - - - - -x profiles measured at stations 30°-180° ——— fully-developed profiles predicted using the result of section (2.8).

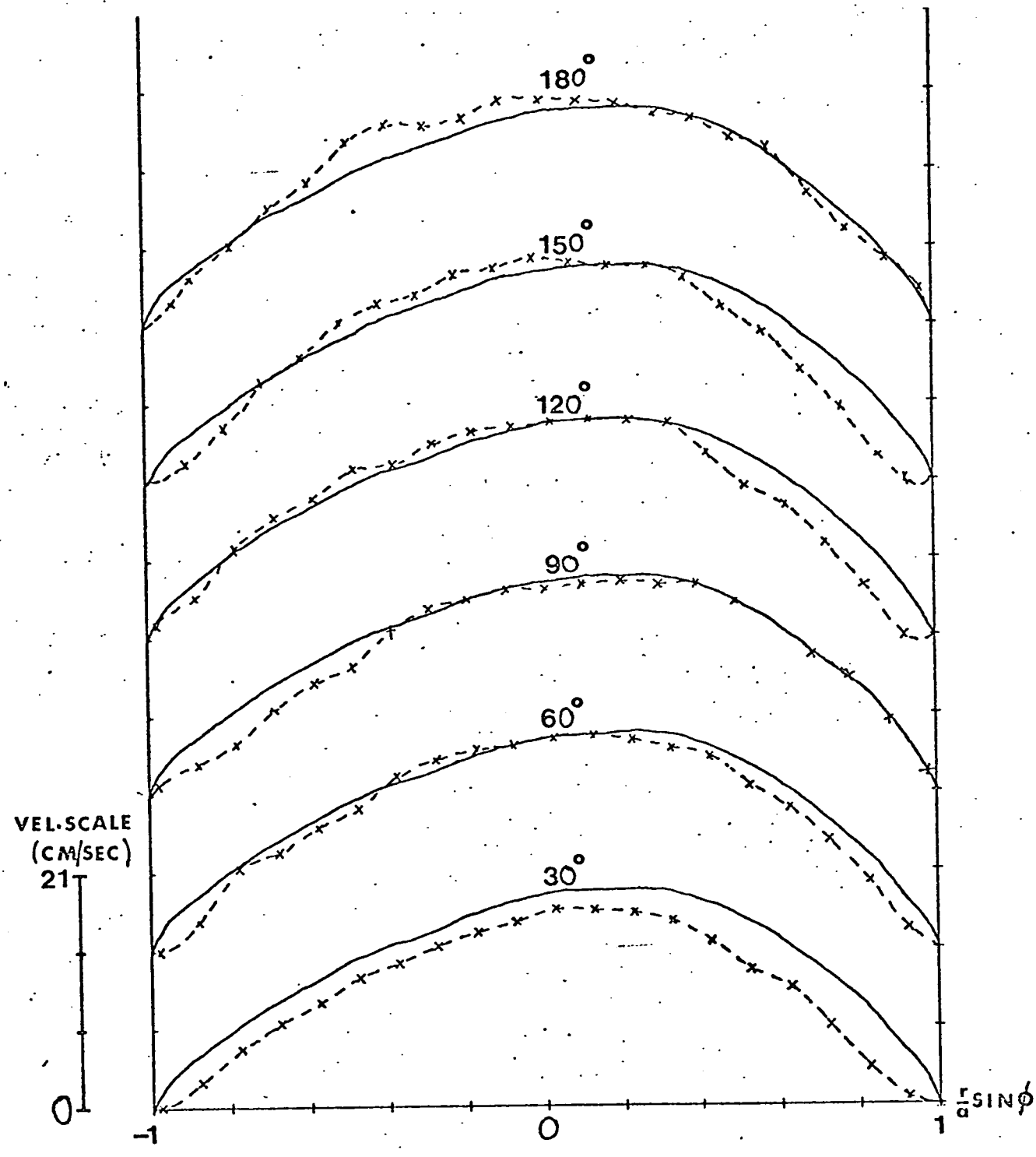

Figure (4.3.2) Series of velocity profiles measured at the 0^{o} phase position with $\alpha = 0.99$. Profiles measured at 0^{o} - 90^{o} station show flow development with $D_{No} = 23.79$.

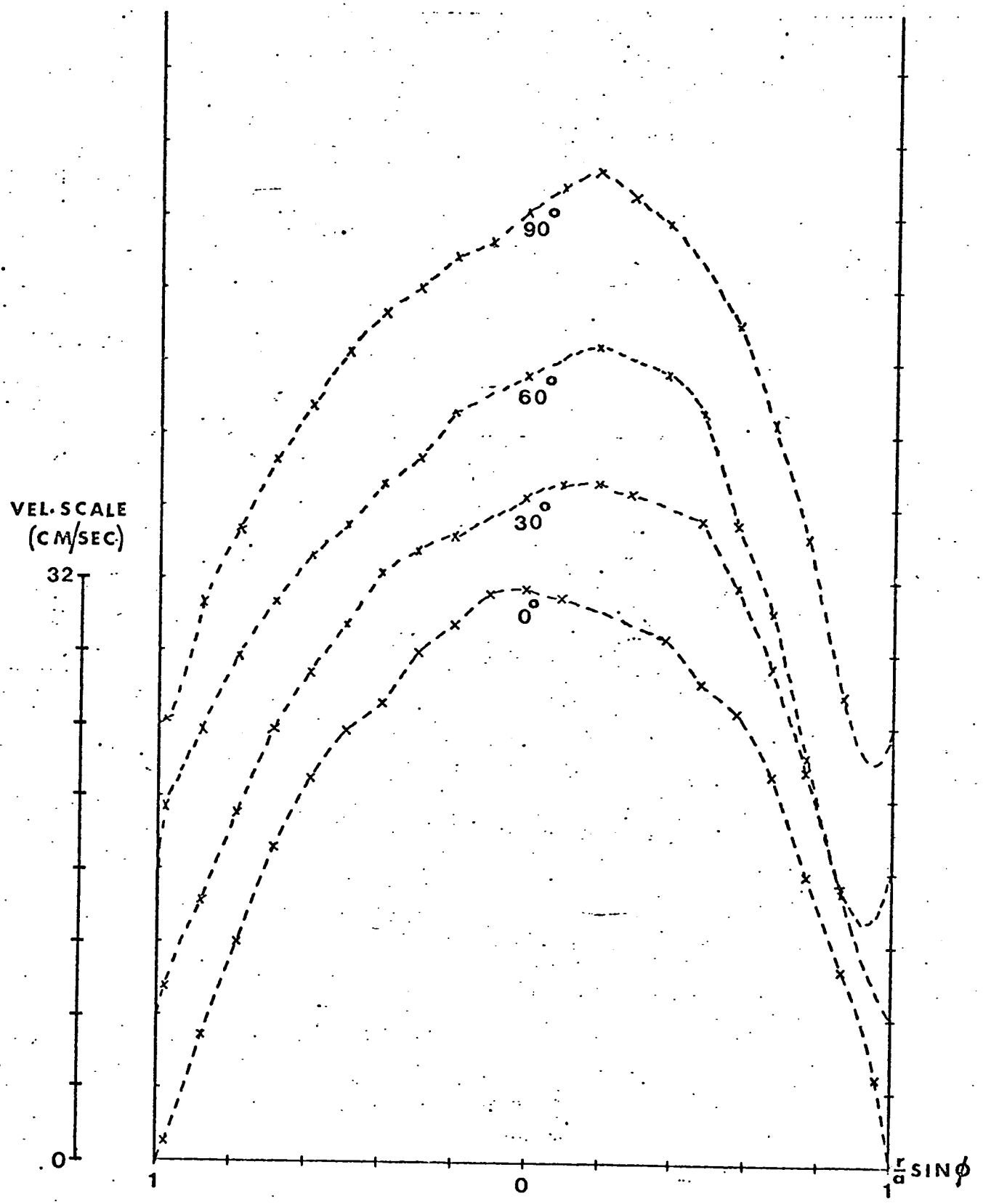

Figure (4.3.3) Series of velocity profiles measured at the 0° phase position with $\alpha = 0.99$. Profiles measured at 0° - 90° station show flow development, and comparison with 120° profile shows fully-developed state reached at 90° with $D_{No} = 64.2$.

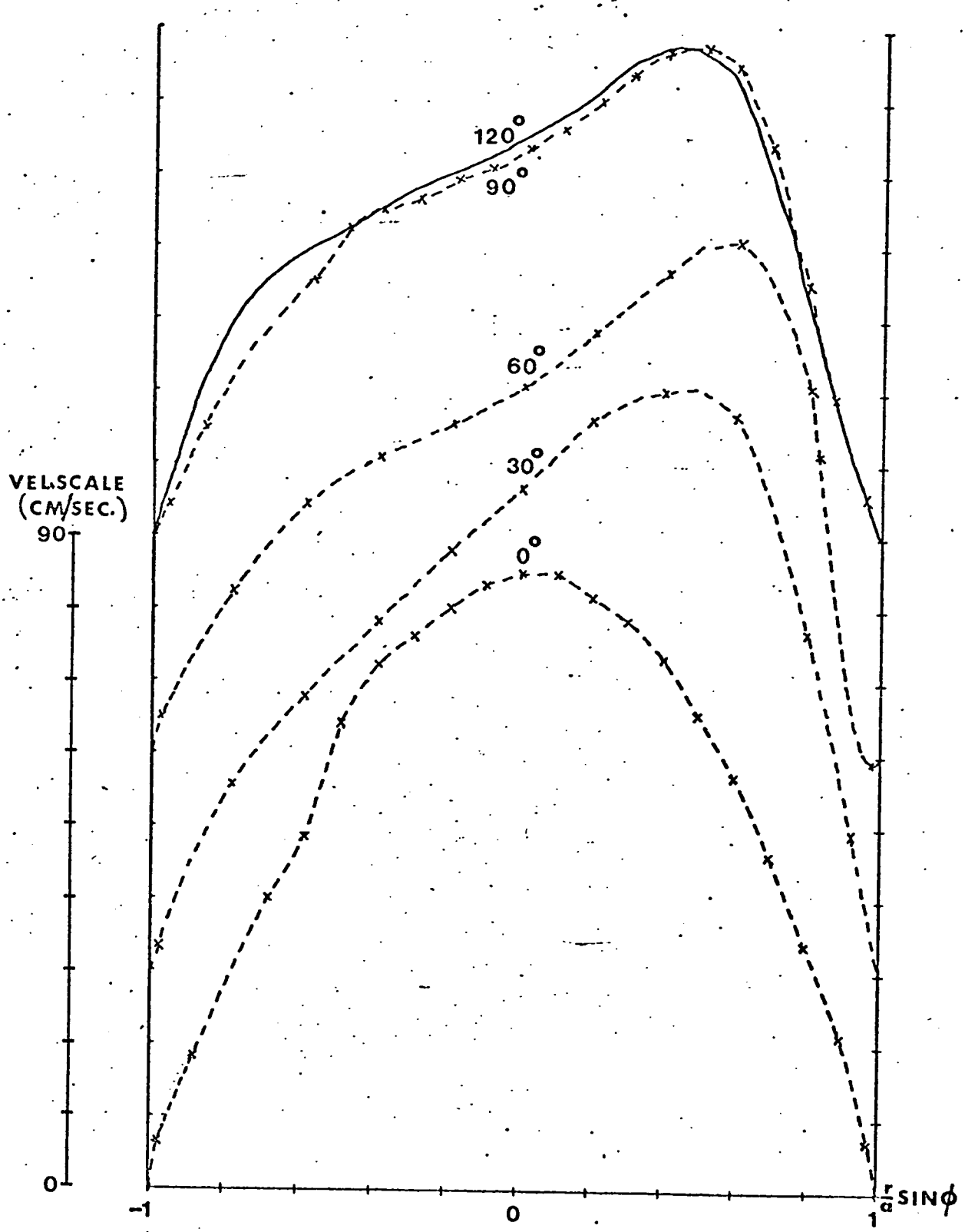

mental crosses and the solid line is the theoretical curve obtained, using the steady flow equations of Dean. Comparison between theory and experiment is seen to be good at 60° and 90° round the curve.

Other important features of the flow are that at 120° and 150° there is apparently the development of a flow reversal at the outer wall. This is probably because of the very tightly curved tube used. Lastly the profile measured at 180° indicates that the flow is more symmetric, indicating upstream influence. This is difficult to explain since the entrance profile does not exhibit any upstream influence of the curvature.

The next set of profiles shown in Fig. (4.3.2) were again measured in the quasi-steady regime, in this case with a higher $D_{No} = 23.79$. Now there is little change between the profile measured at 60° and 90° and the development of a flow reversal at the wall is clearly observable. The effect of further increasing D_{No} to 64.2 is shown in the series of profiles displayed in Fig. (4.3.3). These exhibit the main features previously found with a flow reversal indicated at 60° round the curve. No measurement was possible at the outer wall at 90° position due to the very high velocity gradient, and thus it is not known if a flow reversal occurs here. Comparison is drawn in the last result between the profile measured at 90° and one measured further round the tube. Agreement is seen to be good and thus fully-developed

conditions have been achieved at $\curvearrowright 90^{\circ}$.

It is interesting to compare the above measurements with the results of Olsen (1971). The developing flow for his steady flow experiment with a parabolic input profile and $D_{No} = 75$ is very similar to that found here for $D_{No} = 64.2$. The peak in the axial velocity profile moves immediately to the outside of the bend after the start of the curve, and fully-developed conditions are reached $\curvearrowright 135^{\circ}$. Also a more pronounced peak is found at 60° which may be due to the maximum of the secondary flow occurring here, as explained by Olsen.

The lower D_{No} results of Olsen appear to have suffered from some practical experimental problems since the profiles exhibit some odd characteristics. It is in this very low flow rate region that probe interference may become important and thus non-intrusive laser anemometry will give more reliable results and better spatial resolution than the hot-wires used by Olsen.

The main features of the flow development for a parabolic input profile are that the higher axial velocity components are directed immediately towards the outside of the curve, for low D_{No} flows fully-developed conditions are reached by $\curvearrowright 90^{\circ}$ round the curve, and flow reversals develop at the outside of the curve when the velocity gradient there becomes large.

The next set of measurements presented are those measured at 0°, 10°, 20°, 30°, 60° and 90° angular

Figure (4.3.4) Velocity profiles measured at the 0° phase position and at radial positions 0°-90° round the curve, to show flow development when $\alpha = 4.36$.

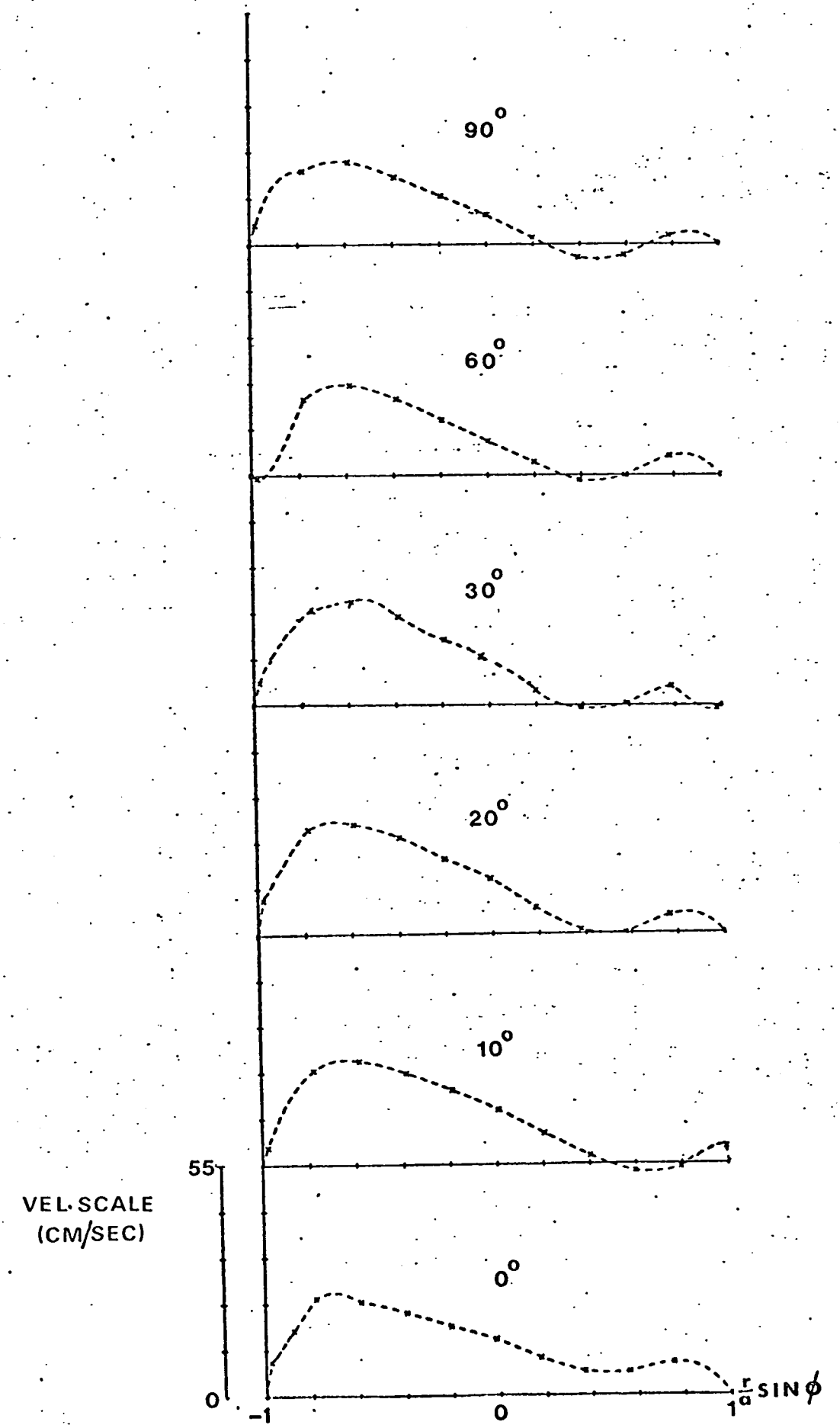

Figure (4.3.5) Velocity profiles measured at the 30° phase position and at radial positions 0°-90° round the curve, to show flow development when $\alpha = 4.36$.

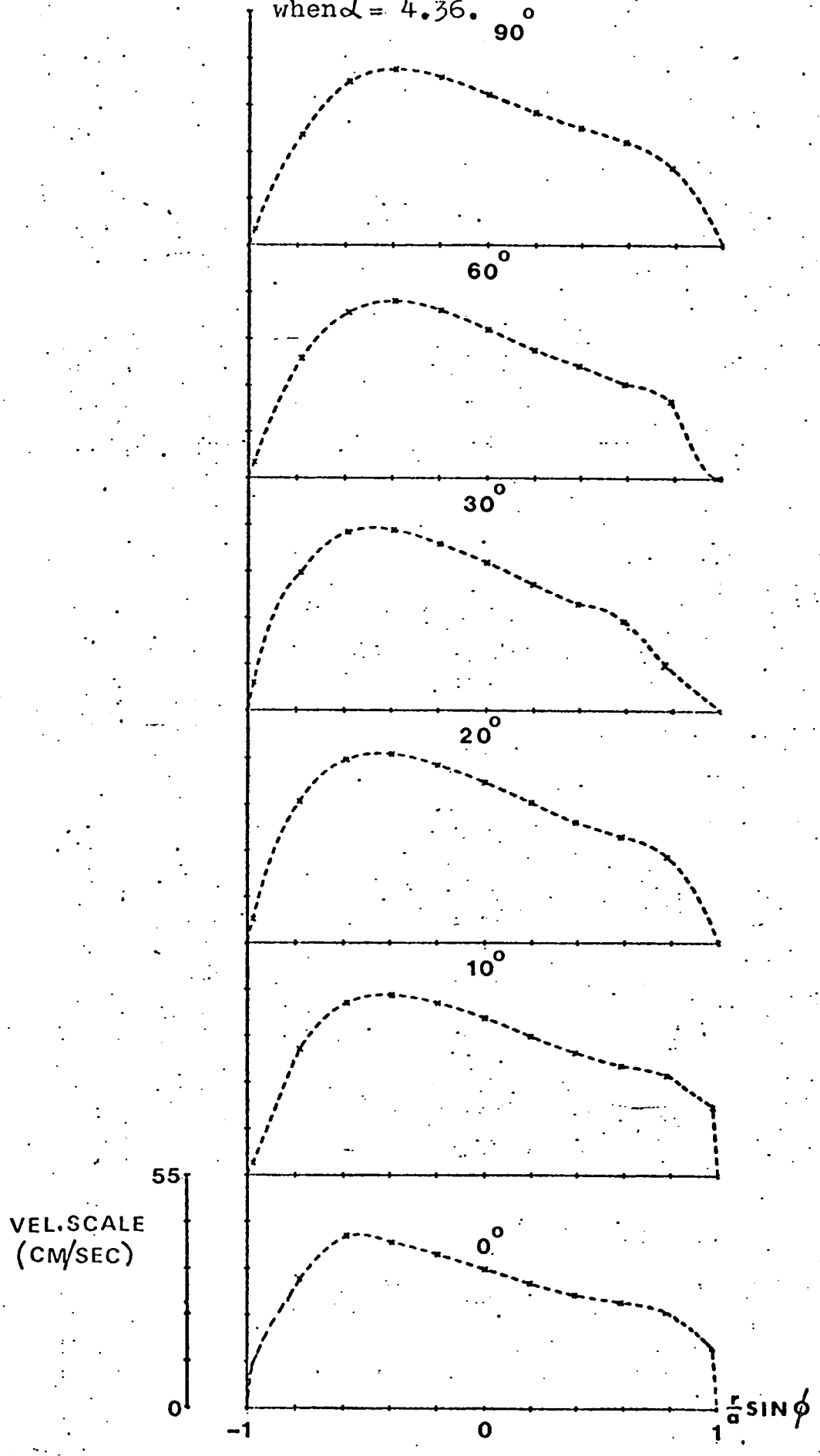

Figure (4.3.6) Velocity profiles measured at the 60° phase position and at radial positions 0°-90° round the curve, to show flow development when $\alpha = 4.36$.

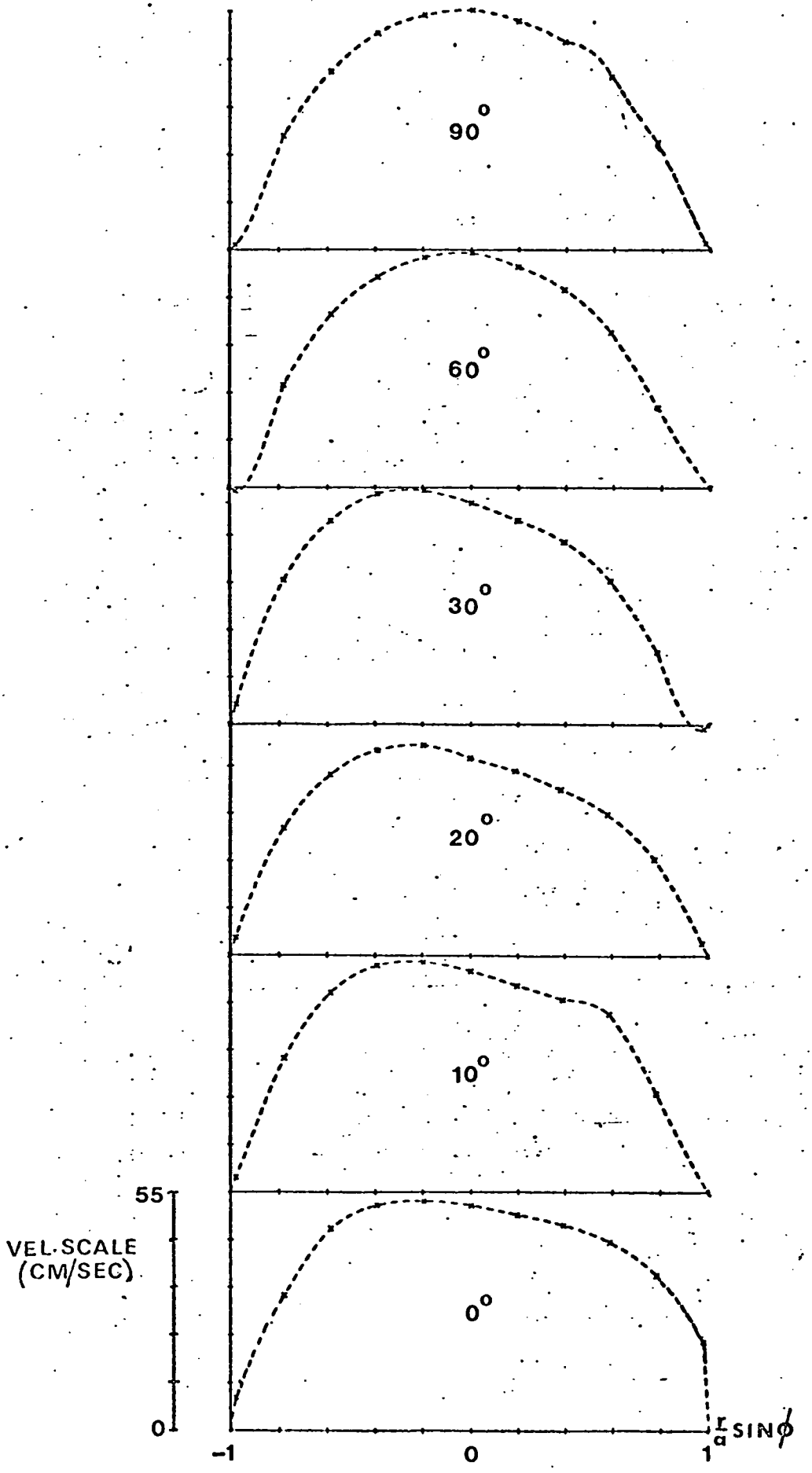

Figure (4.3.7) Velocity profiles measured at the 90° phase position and at radial positions 0°-90° round the curve, to show flow development when $\alpha = 4.36$.

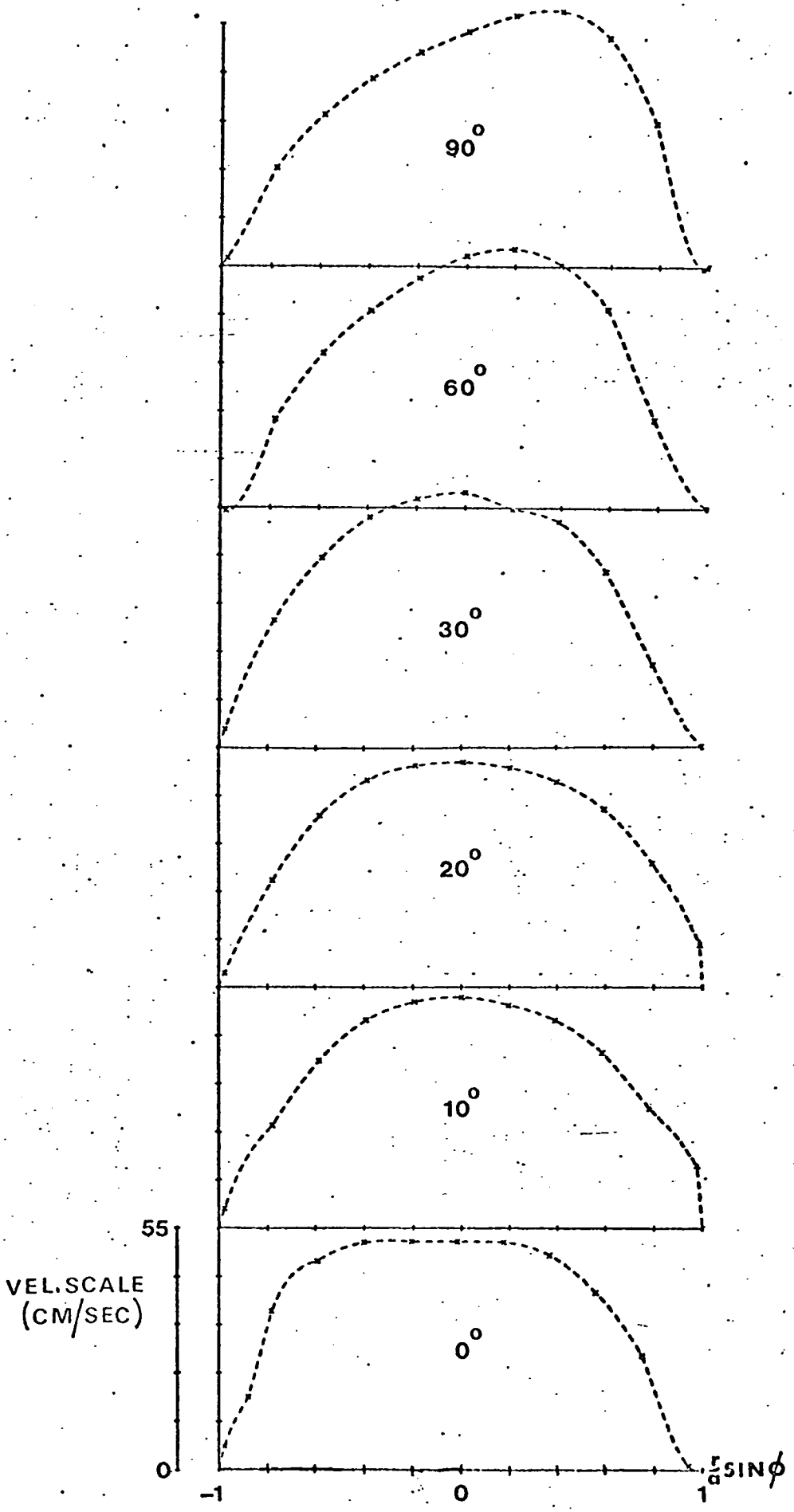

Figure (4.3.8) Velocity profiles measured at the 120° phase position and at radial positions 0°-90° round the curve, to show flow development when $\alpha = 4.36$.

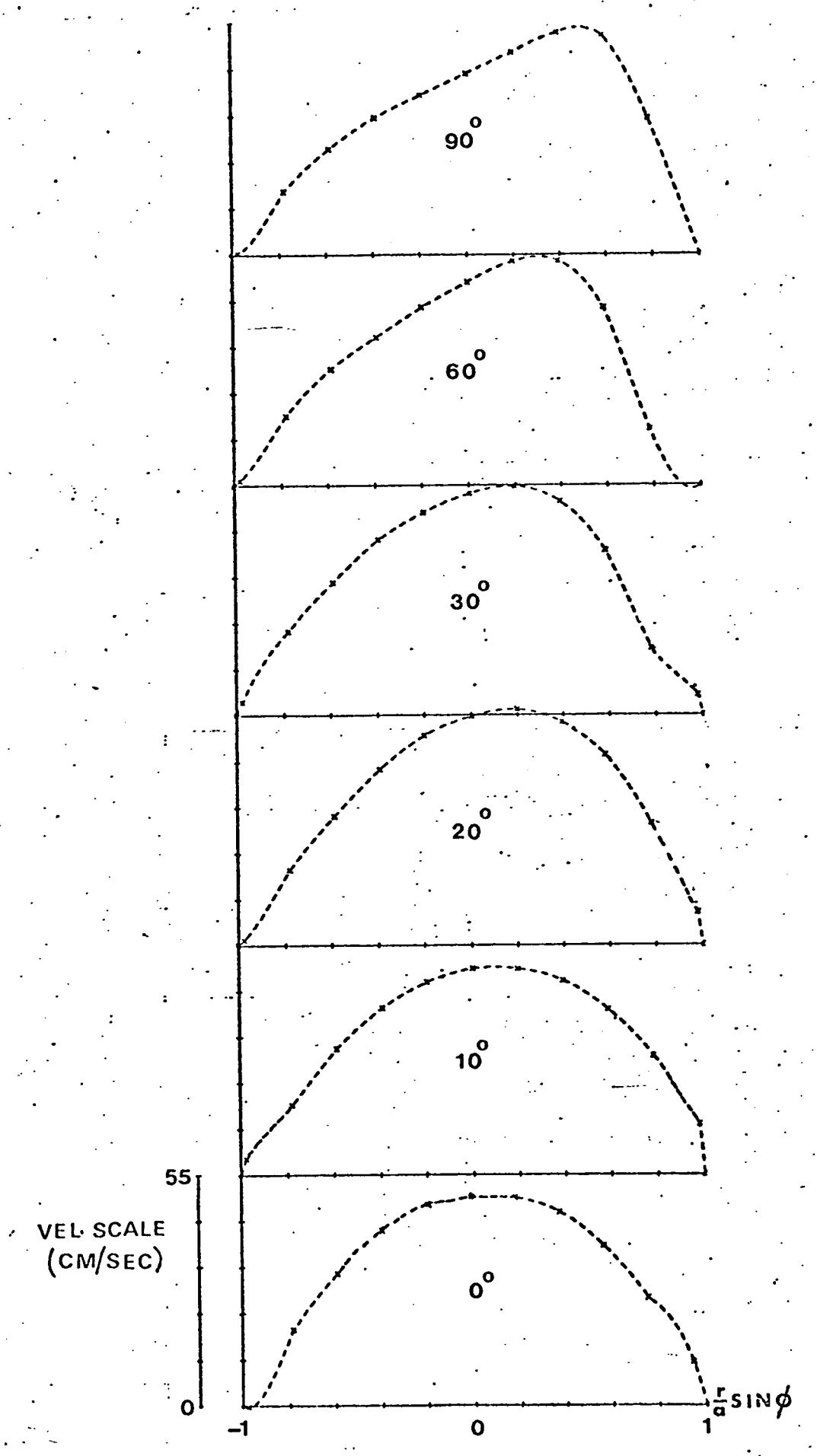

Figure (4.3.9) Velocity profiles measured at the 150° phase position and at radial positions 0°-90° round the curve, to show flow development when $\alpha = 4.36$.

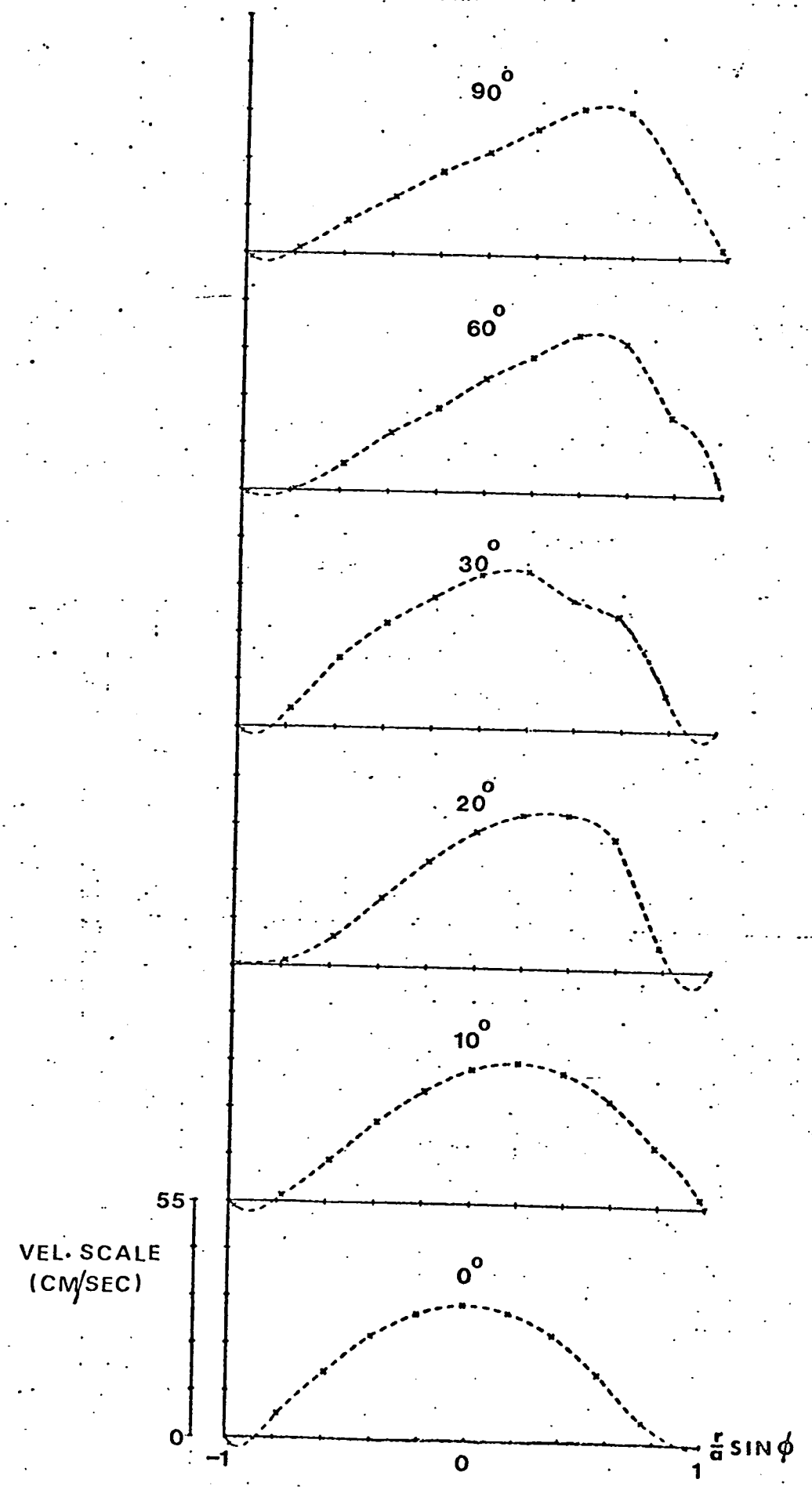

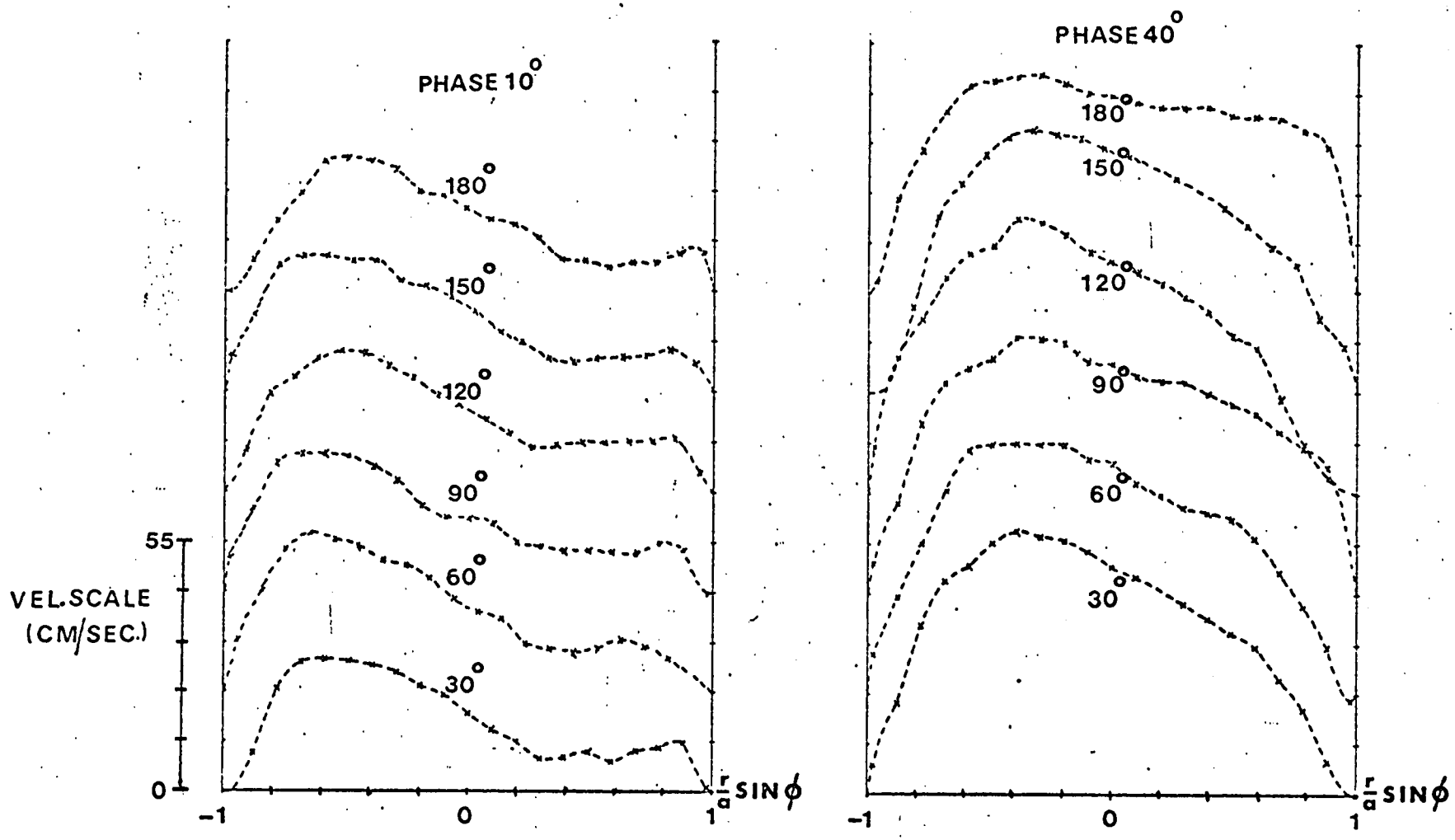

Figure (4.3.10) Series of velocity profiles measured at the 10° and 40° phase positions showing the flow development between the 30° and 180° measuring stations with $\alpha = 4.36$.

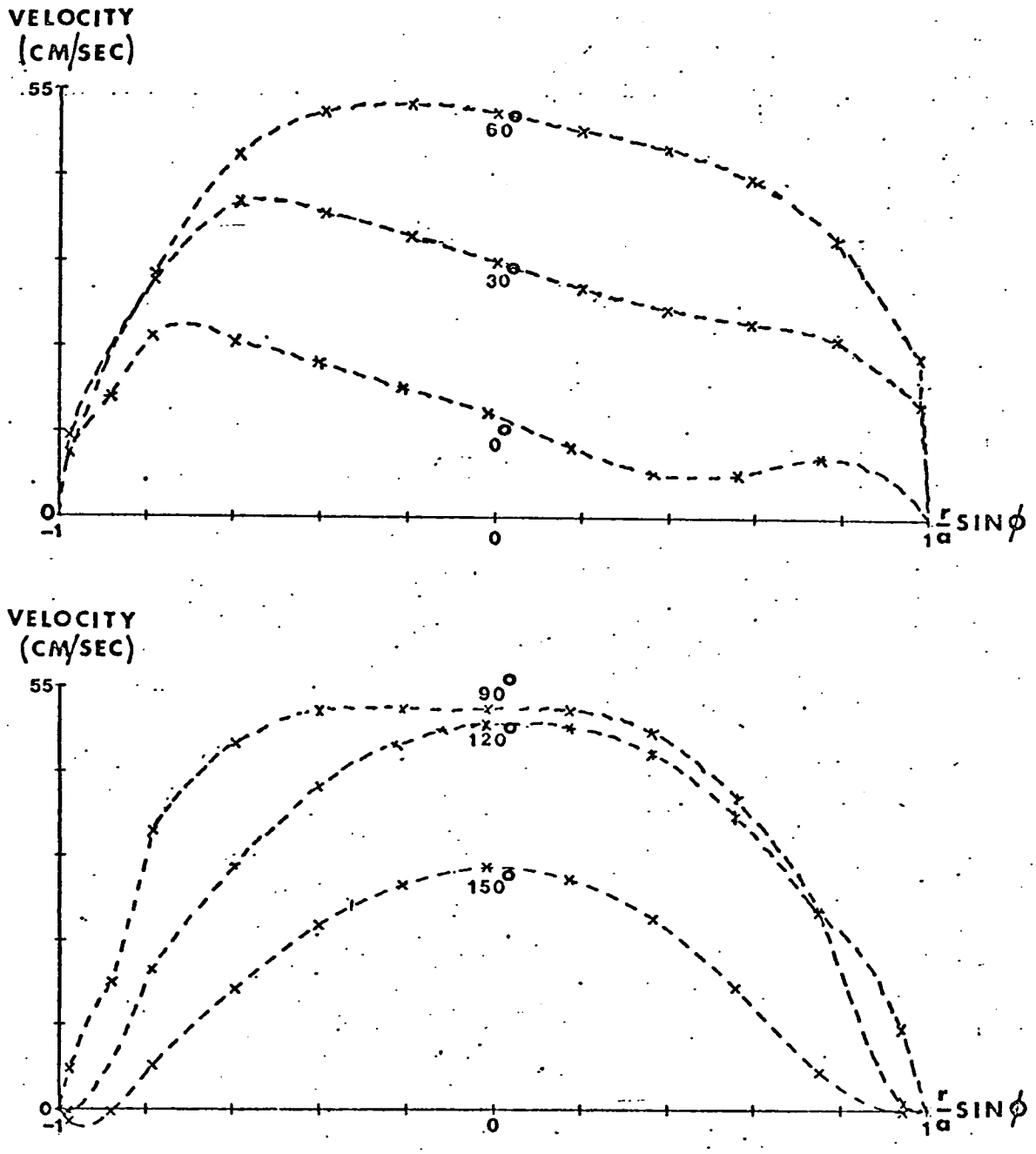

Figure (4.3.11) Velocity profiles measured at the 0° measuring station at phase positions 0° - 150° with $\alpha = 4.36$.

position round the curve at phase positions 0^{o}, 30^{o}, 60^{o}, 90^{o}, 120^{o} and 150^{o} in the pressure cycle when $\alpha = 4.36$. These are shown in Figs (4.3.4 - 4.3.9). Also shown in Fig. (4.3.10) is a series of profiles measured at 10^{o} and 40^{o} phase positions and up to 180^{o} around the curve. The profiles measured at the 0^{o} angular position for various phase positions have been used to construct Fig. (4.3.11).

Starting with the series of results shown in Fig. (4.3.11) it is seen that as the amount of vorticity in the central area of the pipe diminishes so the upstream effect of curvature at the first measuring station increases. This is in agreement with the steady flow measurements of Olsen, and Agrawal, Talbot and Gong (1978) where a vorticity free flat entrance profile produced the same effect.

The development of this type of profile for steady flow appears to proceed as follows. Initially the core of the flow goes towards the inviscid limit of higher axial velocity towards the inside of the curve. The flow is later modified by the secondary flow generated in the wall regions until a fully-developed profile as in the quasi-steady flow is reached. Although many workers have commented on the upstream influence effect there does not seem to be a simple explanation for it.

If now the development of the flow round the curve at the 90^{o} phase position is considered, then effects similar to those described for steady flow are observed.

The axial velocity distribution is initially distorted towards the inside of the curve and the effects of secondary flow are not seen until $\curvearrowright 60^{\circ}$ around the bend. At the 90° measuring station the flow profile has a similar shape to that found for steady flow with the same D_{No}. It is possible that this is not exactly fully-developed flow but as the D_{No} is only $\curvearrowright 39$ it is not expected to be very different from the fully-developed state.

The development at the 0° and 10° phase positions is now considered. It is clear that there is very little change in the profile shape around the curve except for the development of reverse flow towards the outside of the curve at the 0° phase position. Thus secondary flow effects are not appreciable and the higher velocity components remain at the inside of the curve. The 30° and 40° phase positions indicate the same development series as the previous two, although a very high velocity gradient is now found at the outside of the curve at the first two measuring stations of the 30° position.

The first effects of secondary flow are observable at the 60° phase position, where the peak in the profile is initially displaced towards the inside of the curve and is moved to a central position at 60° round the curve. As in the earlier phase position in the cycle, a higher velocity gradient is found towards the outside of the curve at the first flow measuring stations.

At 120° and 150° phase positions, the inlet flow is almost symmetric and viscosity acts over the full width of the tube. The flow development is very similar to that in the quasi-steady regime, the secondary flow taking effect at $\backsim 20^{\circ}$ round the curve in the case of the 120° profile, and $\backsim 10^{\circ}$ for the 150° one. The required length for these profiles to reach their final state is greater than that for the 0° - 40° phase position profiles and thus the conclusion may be drawn that the entrance length is not a function of D_{No} only but also of the amount of vorticity in the flow.

Another interesting feature of the 150° profile is the development of a flow reversal at the inner wall of the curve. This appears to be in anticipation of the change in sign of the pressure gradient at 180°. Thus a cycle starting from this phase position may be thought of as the slower moving fluid at the inside of the curve reacting first to the changing pressure gradient. The secondary flow, which gains in strength as the central flow develops, modifies the axial velocity distribution such that the peak is displaced towards the outside of the curve and so the cycle repeats.

The main conclusions which may be drawn from the results obtained, are that the general agreement between these sets of results and previous steady flow measurements is good. For a profile where the vorticity is confined to regions near the wall, the secondary flow

has little effect up until 30^{o} - 60^{o} round the curve and has no effect when the central axial flow is small.

The development process takes longer for flows where viscosity acts over the full width of the tube at the inlet region. This is in agreement with the steady flow results of Olsen. Gerrard and Hughes (1971) came to the same conclusion for the inlet length of oscillatory flow in a straight pipe. They explained their findings by saying that since viscosity acted over a smaller portion of the tube as α increased, therefore the time for it to act would diminish. The effect here will be complicated by the secondary flow which carries vorticity over the tube.

Comparison with the existing theories can only be made in general terms since there have only been a few steady flow studies of very limited form. Some comparison has been tried by Agrawal, Talbot and Gong (1978) with the theoretical work of Yao and Berger (1975), and is found to be reasonable for large D_{No}. For a flat entrance profile the peak in the axial velocity is found initially towards the inside of the curve and has the normal velocity distribution in the fully-developed state. This is in general agreement with what is found at the 90^{o} phase position in this study.

From the theoretical work of Smith (1976), one would expect the shear maximum to occur initially at the inside of the curve, regardless of the shape of the profile.

This general conclusion of the somewhat limited theory is not borne out by the experimental results, and in fact it can be seen that the shear maximum appears to occur at the outside of the curve almost immediately at many of the phase positions.

Finally, it is clear that essentially fully-developed conditions are reached by 90^{o} round the curve with the possible exception of the peak flow in the cycle. However, the D_{No} is ~ 39 and comparison with the results of Olsen for a similar input profile and $D_{No} = 45$, indicates that fully-developed conditions are not very different from those found here. Thus although exact fully-developed conditions may take a very long time to prevail, the main features of this state will be present at 90^{o} round the curve, which is the main measuring station for the remainder of the work presented in this thesis.

4.4 FULLY-DEVELOPED OSCILLATORY FLOW IN A CURVED PIPE

Theoretical and experimental results for fully-developed oscillatory flow in a curved pipe are presented in this section. The theoretical results were found using the results of Chapter 2 and the experimental results presented for both $^1/_{50}$th and $^1/_7$th curvature pipes. The profiles were mainly measured in the plane of the bend at 90° round the $^1/_7$th curve and 180° round the $^1/_{50}$th curve, where it was assumed that essentially fully-developed conditions occurred.

The first set of results shown in Fig. (4.4.1) are four velocity contour maps, each constructed from 6 velocity profiles measured at 30° intervals circumferentially round the tube at the fully-developed stations. The first two maps were constructed from measurements taken at the same peak D_{No} (6.57) but at phase positions 0° and 60° in the cycle at an alpha value of 0.54 in the tube of curvature $^1/_{50}$th.

At this small alpha value, the flow may be considered quasi-steady and as can be seen from the contour map, at 60° the flow is disturbed minimally by the curvature and is Poiseuille in form. At the maximum of the cycle, the effect of curvature is noticable, in that the peak of the profile is displaced towards the outside of the curve and a flattening occurs at the inner side of the 0.9 and 0.8 contour lines.

Figure (4.4.1) Velocity contour maps measured in the quasi-steady region. Contours are drawn in each map showing, $(0.1-0.9)\frac{W}{W_{max}}$ with $\alpha = 0.54$ and $a/R = 1/50$.

(a) Phase position 60^{o} peak $D_{No} = 6.57$.

(b) Phase position 0^{o} peak $D_{No} = 6.57$.

(c) Phase position 180^{o} peak $D_{No} = 6.57$

(d) Phase position 0^{o} peak $D_{No} = 7.66$.

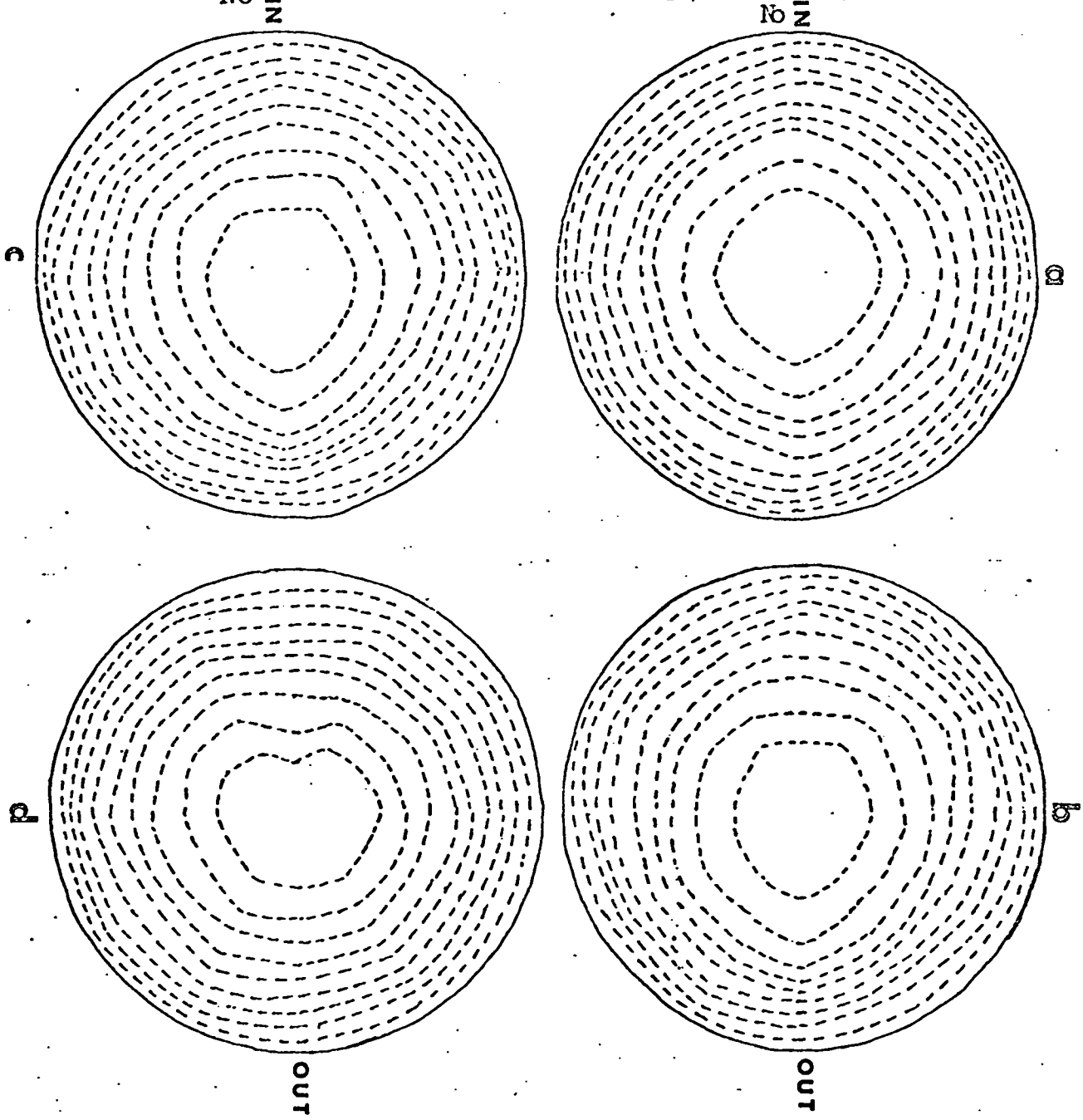

Figure (4.4.2) Fully-developed velocity profiles measured in 1/7th curved tube at phase positions 12° - 162° and $\alpha = 0.99$.

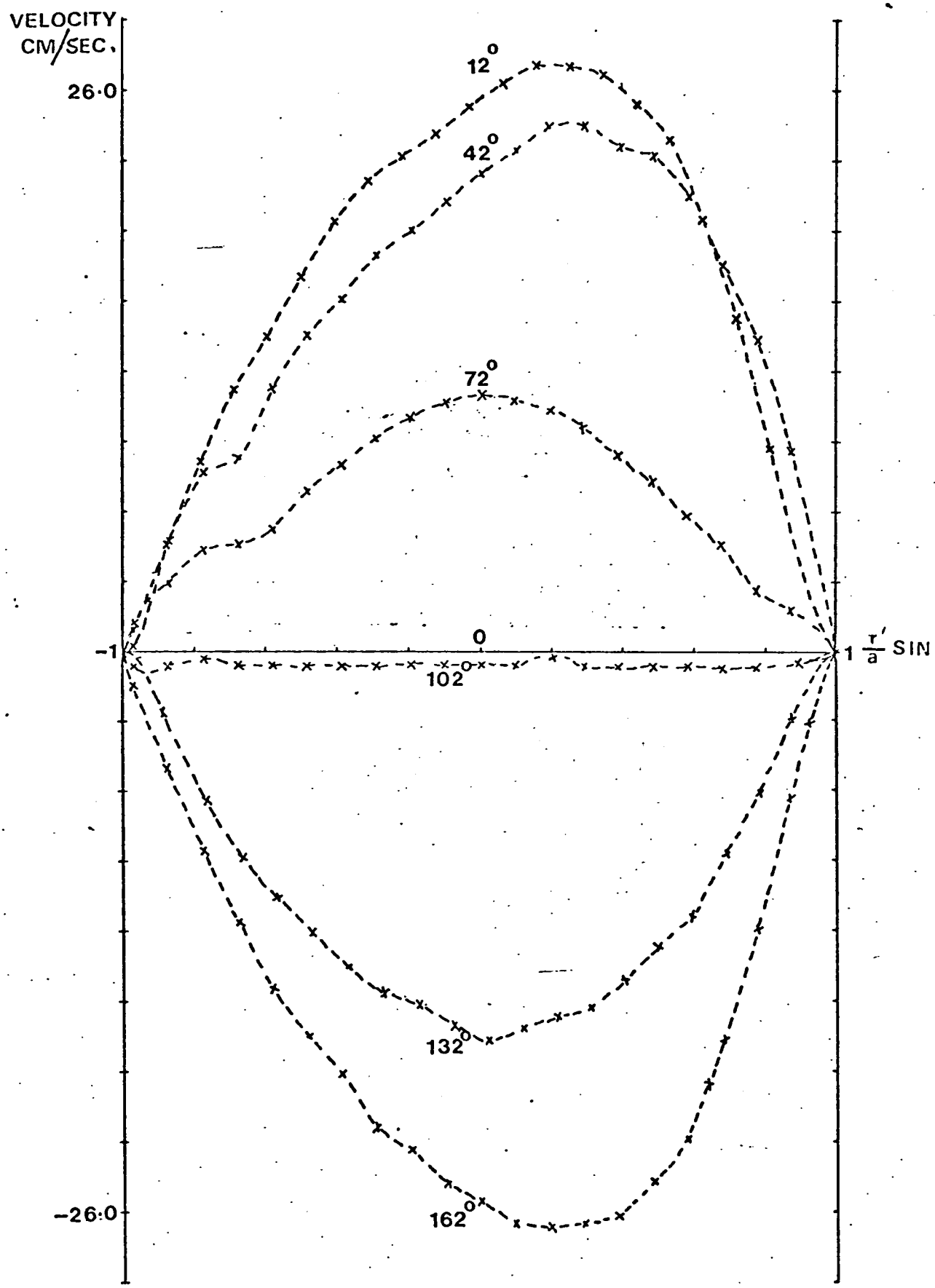

The quasi-steady analysis described in section (2.6) should be valid in this region, and thus the perturbation will be of the form $\cos^3\theta$. Thus the very noticable difference between the two phase positions illustrated, may be attributable to this time dependency of the perturbation. The measurements for the third contour map were made at the phase position 180° in the cycle. The map is found to be very similar in form to that measured at the 0° position, indicating that the flow pattern is repeatable.

The effect of an increase in the peak D_{No} to 7.66 is seen in the last contour map where now the 0.9 and 0.8 contour lines have become more concave at the inner wall and flattened towards the outer wall. The work of Dean and McConalogue and Srivastava ought to give very good agreement at these low D_{Nos}. However, although the general agreement is good, in that the peak displacement agrees, the detail of contour flattening does not appear in McConalogue's results until $D_{No} = 190$, an order of magnitude greater than the results presented here.

Another example of the flow structure in the quasi-steady region is shown in Fig. (4.4.2) where a series of profiles is presented for $\alpha = 0.99$ at phase positions 12° to 162° measured at 30° intervals. It is seen that the axial velocity peak is directed outwards at most phase positions, but at 72° to 132° the profile is almost symmetric, indicating small effects of curvature. These effects can be explained by examining the straight pipe

Figure (4.4.3) Normalised velocity time diagrams for straight pipe flow ———— and first order perturbation due to curvature - - - - - for radial positions 0.1r and 0.9r with $\alpha = 0.99$.

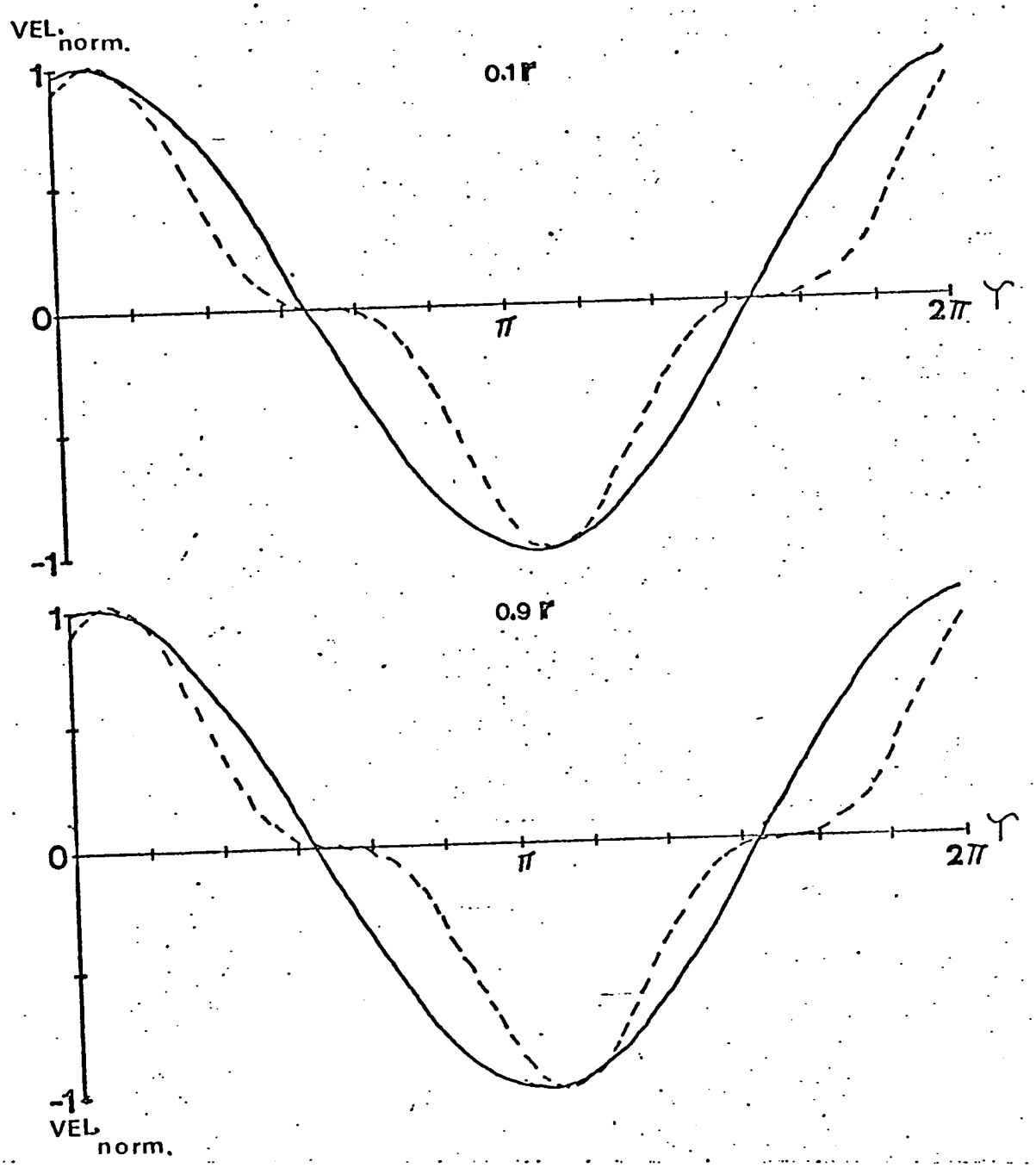

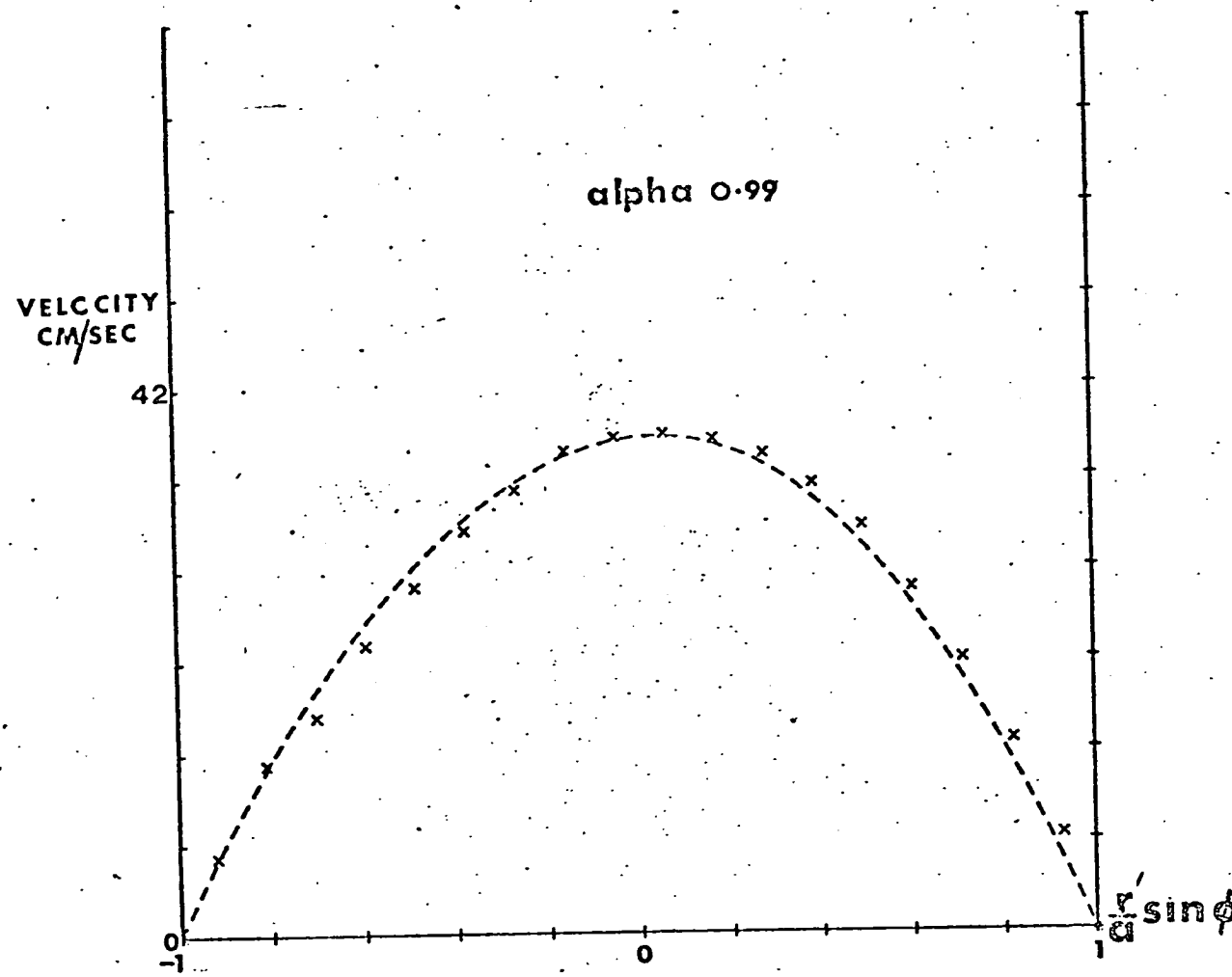

Figure (4.4.4) Comparison between experiment and theory in the quasi-steady flow region with $D_{No} = 12$, $a/R = 1/50$ phase position 0°. Crosses give experimental points and the theoretical profile was obtained using the results of section (2.8).

Figure (4.4.5) Fully-developed velocity profiles measured in 1/7th curved tube at phase positions 30° and 330° with $\alpha = 2$ and $D_{No} = 24$.

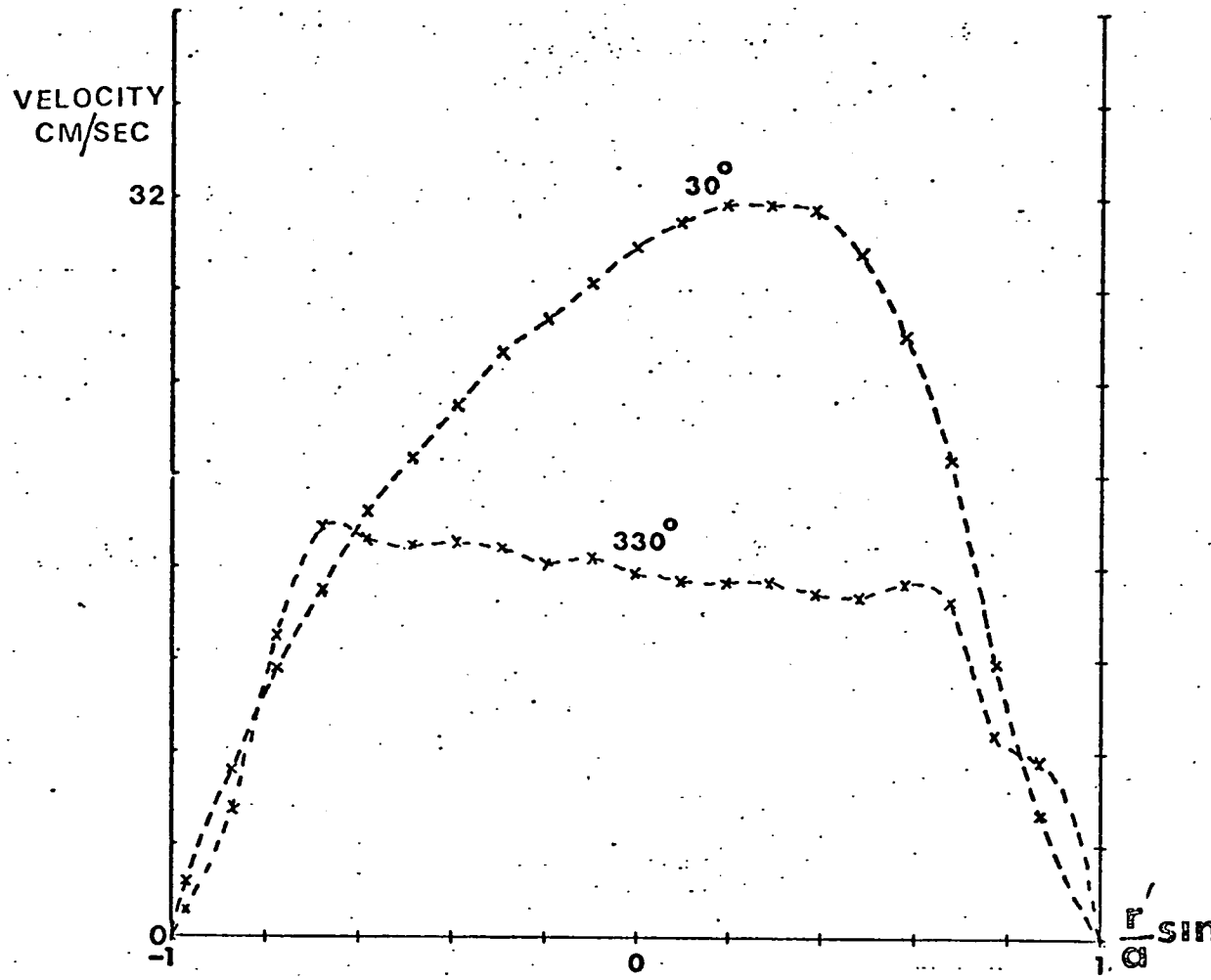

Figure (4.4.6) Normalised velocity time diagrams for straight pipe flow ——— and first order perturbation due to curvature - - - - - for radial position 0.1r and 0.9r with $\alpha = 2$.

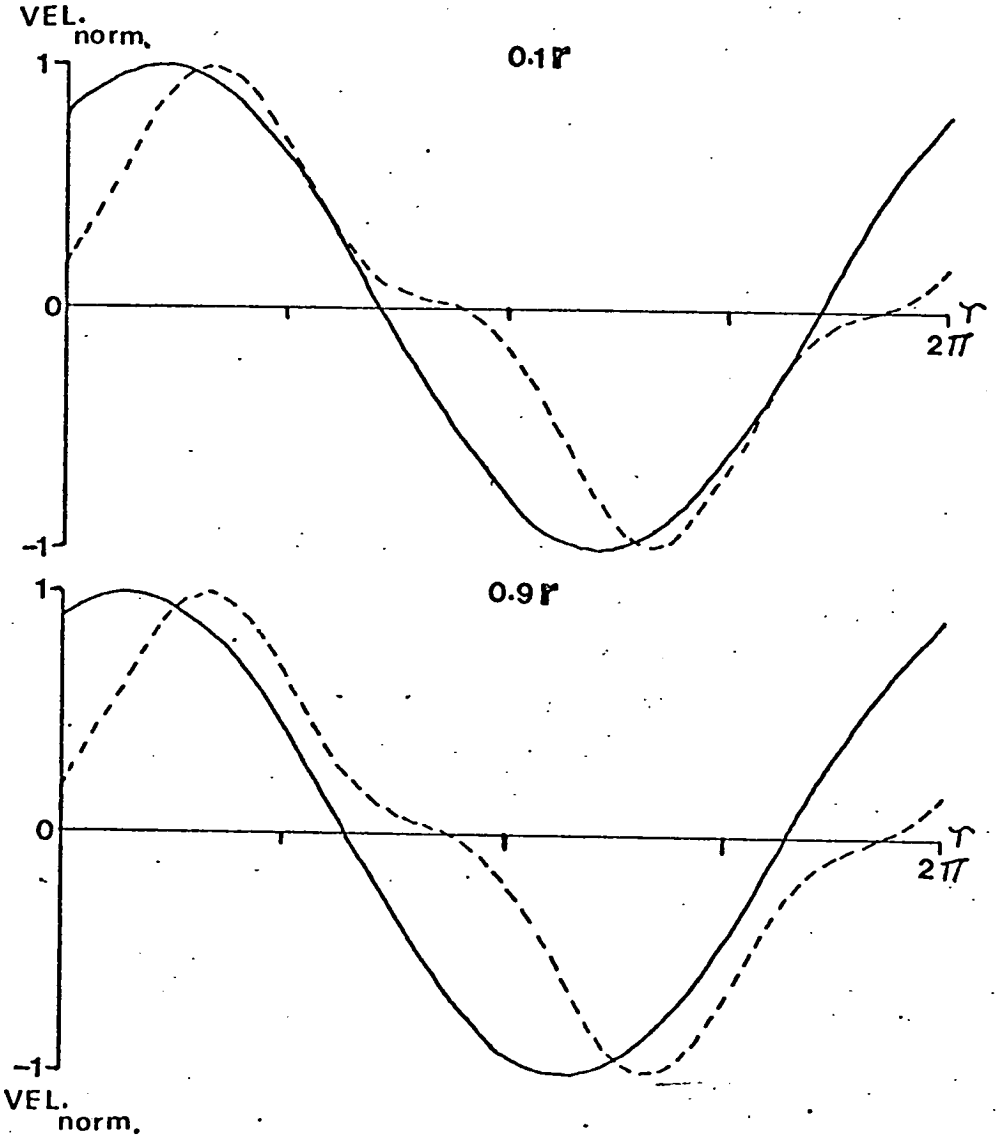

axial velocities and perturbations for the two radial positions 0.1 r and 0.9 r, plotted as functions of time. These are shown in Fig. (4.4.3).

The influence of the $\cos^3 \Psi$ term is still strong at $\alpha = 0.99$ and thus the perturbation has only a small effect between 70° and 140° and 250° and 320° in the pressure cycle. The perturbation at both radial positions remains in phase with the applied pressure gradient and thus the peak of the velocity distribution is displaced outwards at all phase positions.

A comparison is given for the quasi-steady region between theory and experiment, and this is shown in Fig. (4.4.4). The experimental measurement was made at 0° phase position, $\alpha = 0.99$ and $D_{No} = 12$ in the $^1/_{50}$th curved tube, and the theoretical result obtained using the Hankel transform solution. Since there is only a small departure from the Poiseuille distribution, comparison is found to be good.

Now the case is considered when α is doubled to $\alpha = 2$. The profiles shown in Fig. (4.4.5) were measured in the $^1/_7$th curved tube at peak $D_{No} = 24$ at phase positions 30° and 330°. The main observable effect is that the higher velocity component is found towards the inside of the curve at phase positions 330°. The perturbations and axial velocities for the two radial positions are shown in Fig. (4.4.6).

The $\cos^3$ term is still an important term in the

Figure (4.4.7) Comparison between theory and experiment for axial velocity flow profiles measured in the plane of the bend with α = 2.56, Peak D=9.53, a/R = 1/50 and phase positions 60° - 180°. No

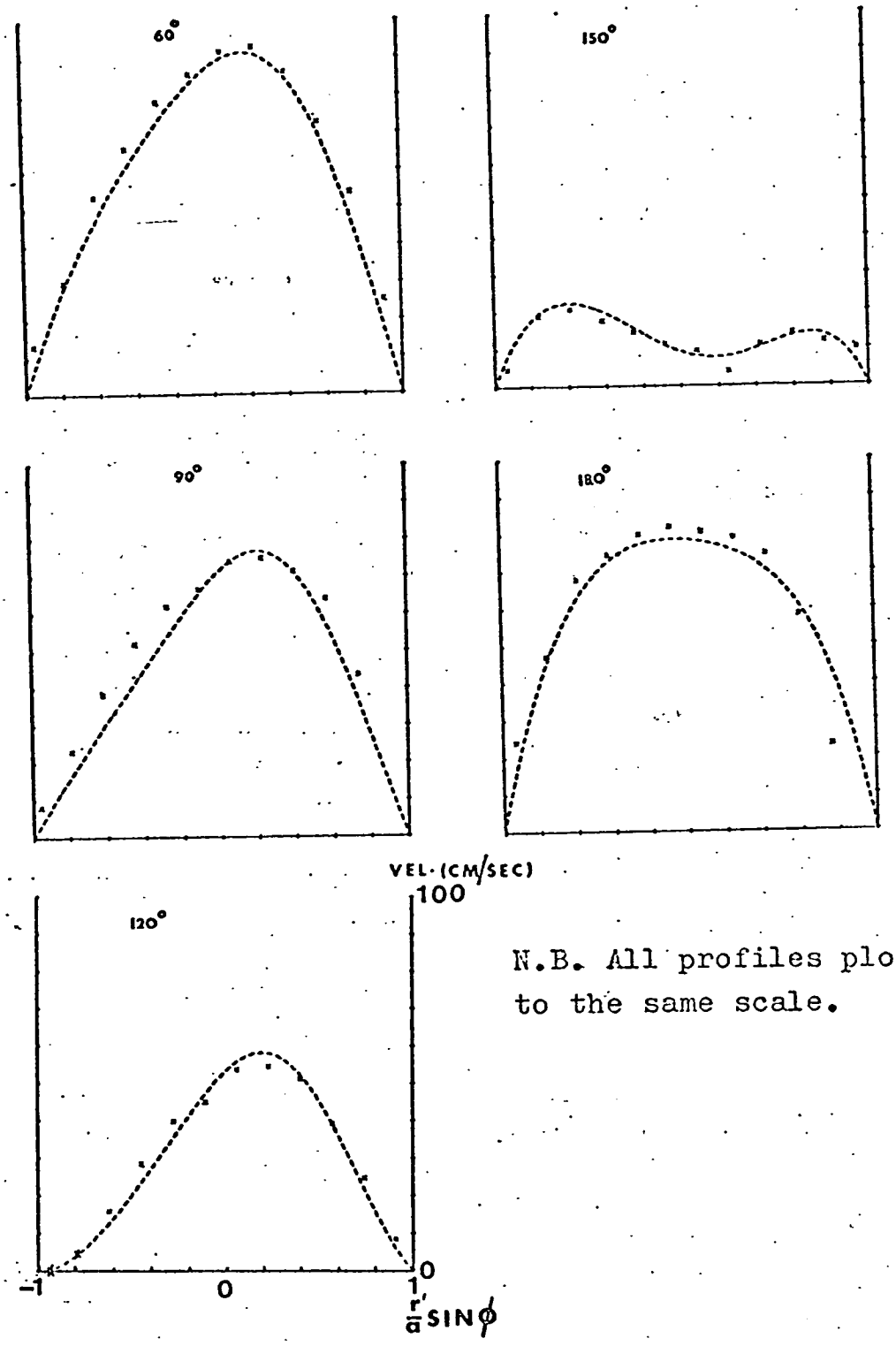

N.B. All profiles plotted to the same scale.

perturbation and between phase positions 300° - 330° it is seen to be small and acting in the opposite direction to the straight pipe flow. This small reverse effect may be accentuated by the strong curvature in the experiment, giving the large effects shown.

The perturbation at position 0.9 r is seen to have a greater phase lag between it and the straight pipe velocity component, than the corresponding quantities in the centre of the tube. The perturbations remain in phase with each other while a phase difference develops across the straight pipe flow. This would mean that as the main flow changes direction the perturbation will initially have the effect of increasing the velocity at the inside of the curve. This is because the flow near this wall is perturbed in the opposite sense to that in the central region.

The effect of a further increase in α is shown in Fig. (4.4.7) where the comparison is given between experimental measurements and theory for the case α = 2.56. The experimental measurements were made in the tube of curvature $^{1}/_{50}$ and the peak D_{No} = 9.53. Therefore the experiments are just ouside the expected limits of the theory, but as can be seen, the agreement is found to be good.

The results show that between 60° and 120°, the higher axial velocity components appear towards the outside of the curve, whereas at 150° and 180°, the opposite is

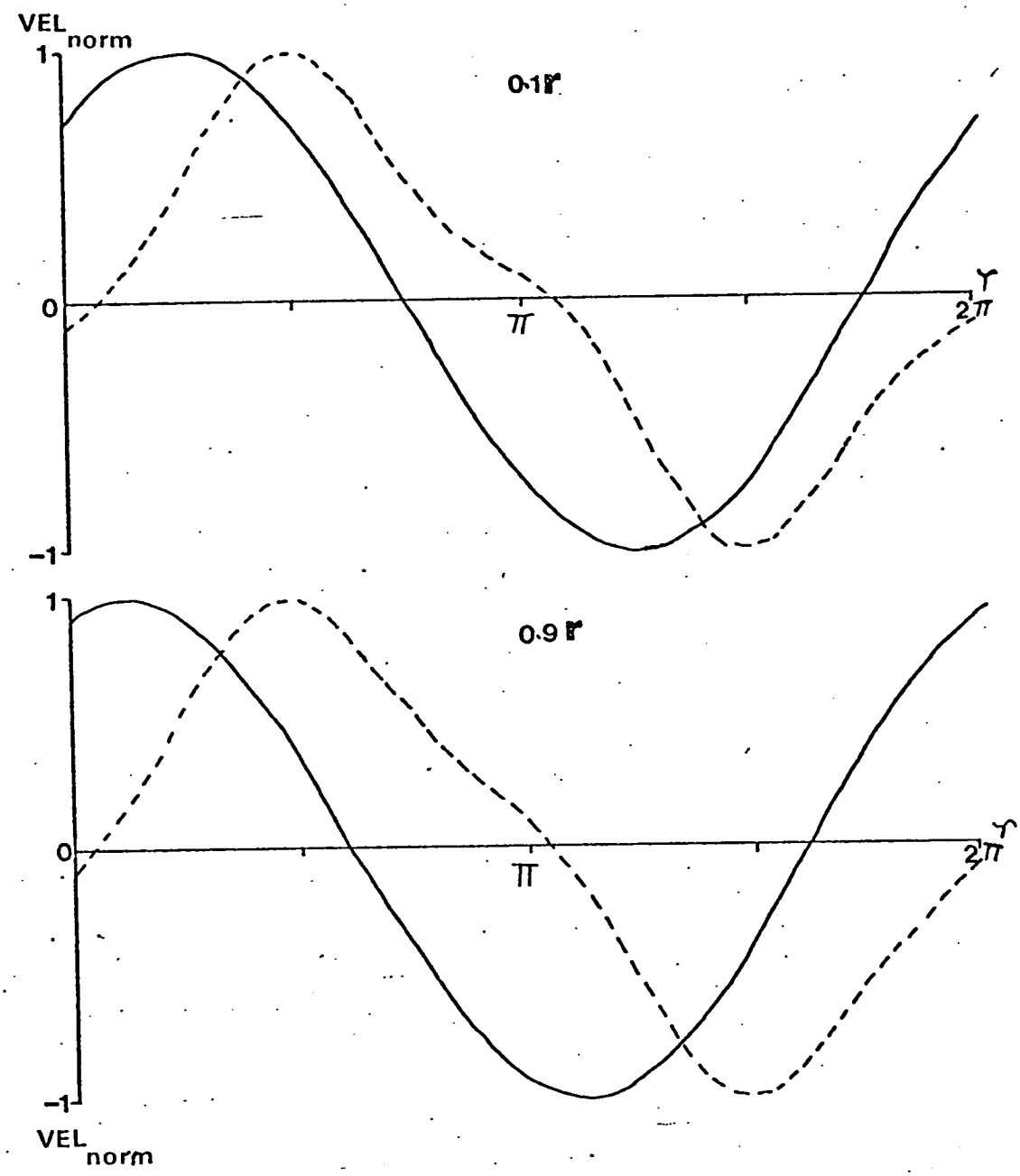

Figure (4.4.8) Normalised velocity time diagrams for straight pipe flow ———— and first order perturbation due to curvature - - - - - - for radial positions 0.1r and 0.9r with α = 2.56.

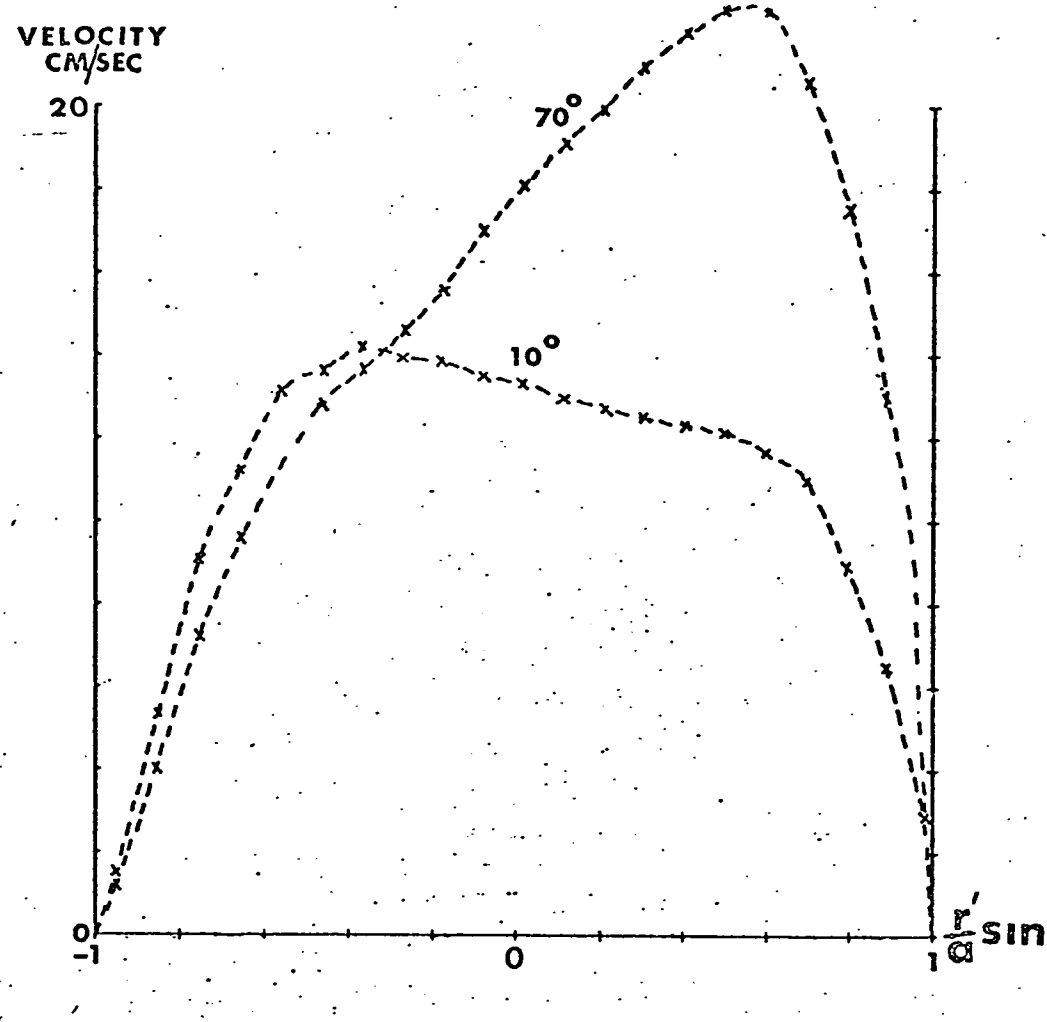

Figure (4.4.9) Fully-developed velocity profile measured in 1/7th curved tube at phase position 10° and 70° with $\alpha = 2.79$ and $D_{No} = 33.87$.

the case. Examination of the perturbations and straight pipe axial velocities given in Fig. (4.4.8) show that the perturbation acts in the opposite direction to the straight pipe flow between 130° and 200° at the edge of the tube and $\backsim$ 150° and 200° in the centre.

The effect of the increased phase lag between the perturbations and the respective straight pipe flows is noticable in the profiles measured at 120° and 150°. At the inner wall of the curve, the velocity is seen to reverse at the 120° position, and the velocity gradient is higher at the 150° position. It is also evident from the perturbation that the effect of the $\cos^3$ term is now very much smaller at the wall of the tube.

Further results measured in this α region are shown in Fig. (4.4.9) where the following parameters apply, D_{No} = 33.87, Phase positions 10° and 70°, α = 2.79 and $a/R = 1/7$. These results confirm the previous findings, but now the effects become much larger due to the increased D_{No}. Therefore, the reversal of the direction of shift of the axial velocity peak occurs in the experiments on 1/50th and 1/7th curved tubes and in the theory which is only valid for very small curvature.

A further increase in alpha would be expected to show the change in the direction of the displacement of the axial velocity peak over a greater portion of the cycle. When α is increased to 4.36 then the results of the experimental measurements made are shown in Fig.

Figure (4.4.10) Fully-developed velocity profiles measured in the 1/7th curved tube at phase positions $0^{o} - 150^{o}$. Peak D_{Nos} = 33.26 and 42.84 with α = 4.36.

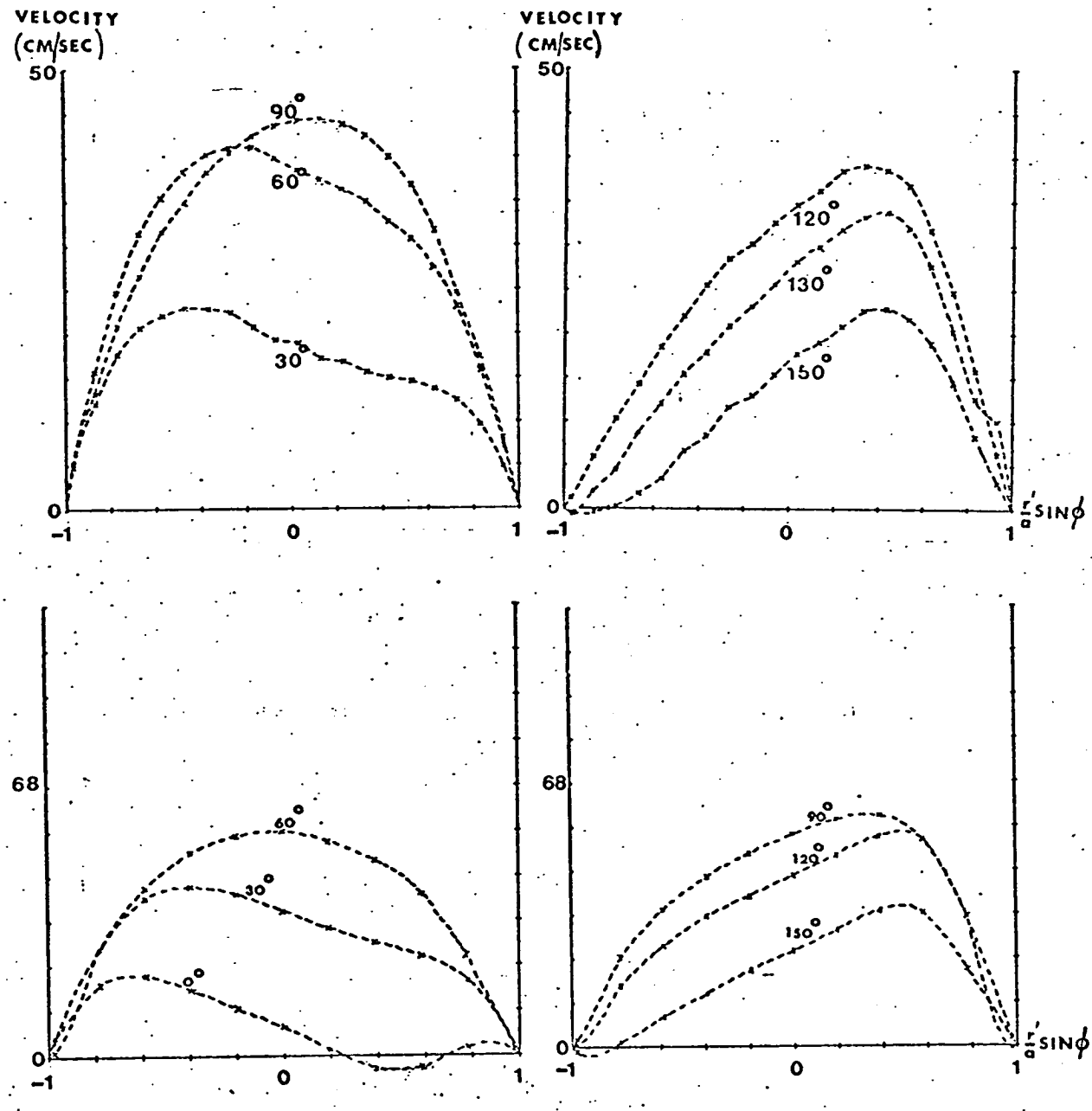

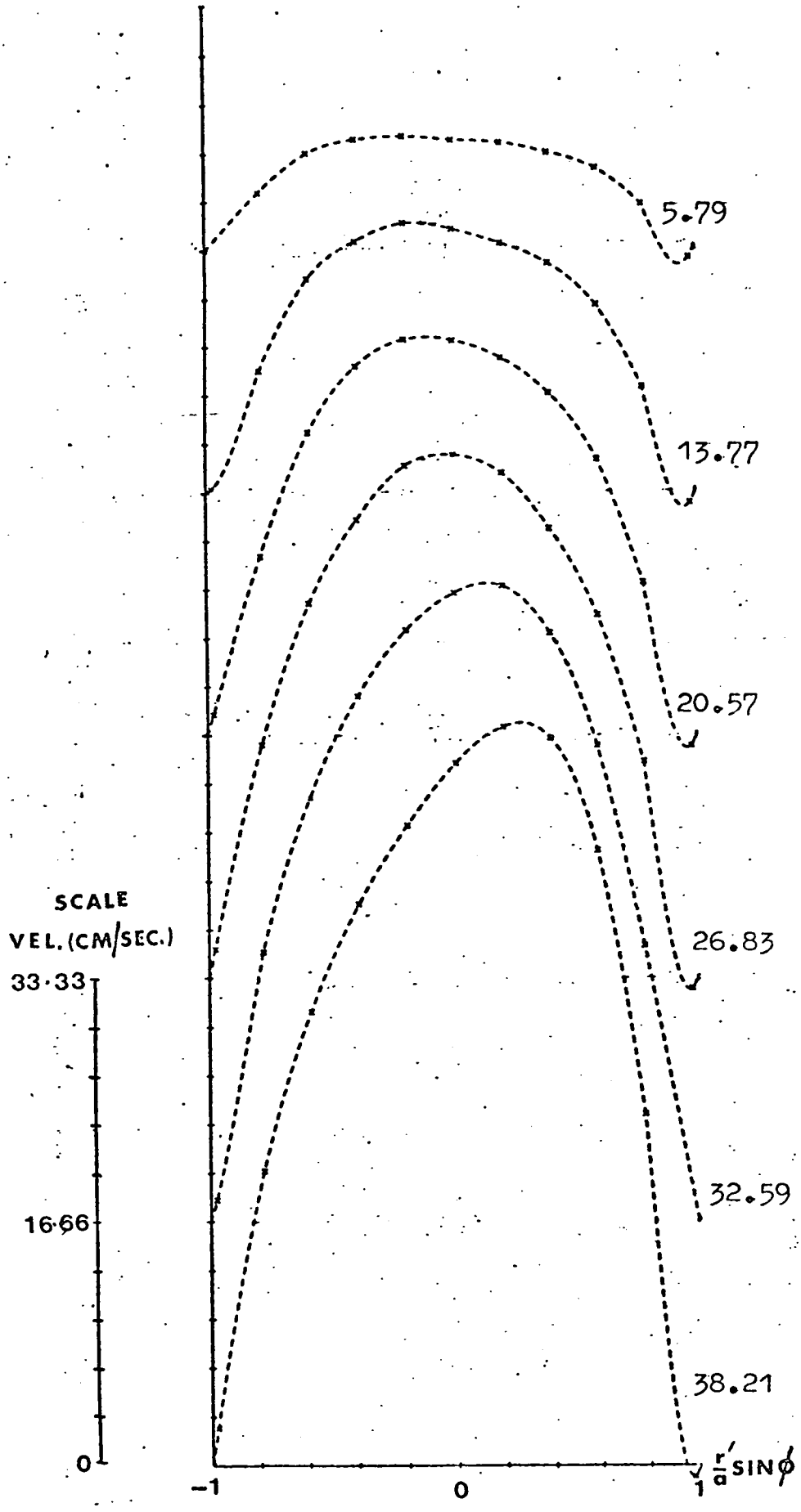

Figure (4.4.11) Series of profiles showing the effect of reducing D_{No}. Profiles measured at phase position 90° with α = 4.36 and D_{Nos} = 5.79 – 38.21.

(4.4.10) for two different peak D_{Nos}. It can be seen that the higher axial velocity components are found at the inside of the curve up to $\sim 60^{o}$ phase position, thereafter being moved to the outside of the curve by secondary flow action.

Comparison of the two sets of profiles indicate that the shapes of the profiles measured at the same phase positions for different peak D_{Nos} are similar in form. Thus the direction of the shift of the axial velocity peak would appear from these results to be independent of D_{No} and depend only on α . In order to investigate this point further, a set phase position was chosen and profiles measured for different D_{Nos}. The results are shown in Fig. (4.4.11) for the phase position 90^{o}, $\alpha = 4.36$.

The results show that as the D_{No} is decreased, the axial velocity peak moves from the outside of the curve towards the inside. Thus it can be said that the direction of shift of the axial velocity peak is not independent of D_{No}, at least for this phase position. A further interesting feature of the profiles measured, is the occurrence of a flow reversal at the outside of the curve, which appears to be independent of D_{No}.

If now profiles are measured at the same alpha value but at a very small D_{No} , then the exact nature of the decreased D_{No} effect may be found. The results are shown in Fig. (4.4.12) and show that the only apparent effect

Figure (4.4.12) Velocity profiles for phase positions 0°–150° with α = 4.36, peak D_{No} = 9.98 and a/R = 1/7. Theoretical profile derived using equation (2.4.11).

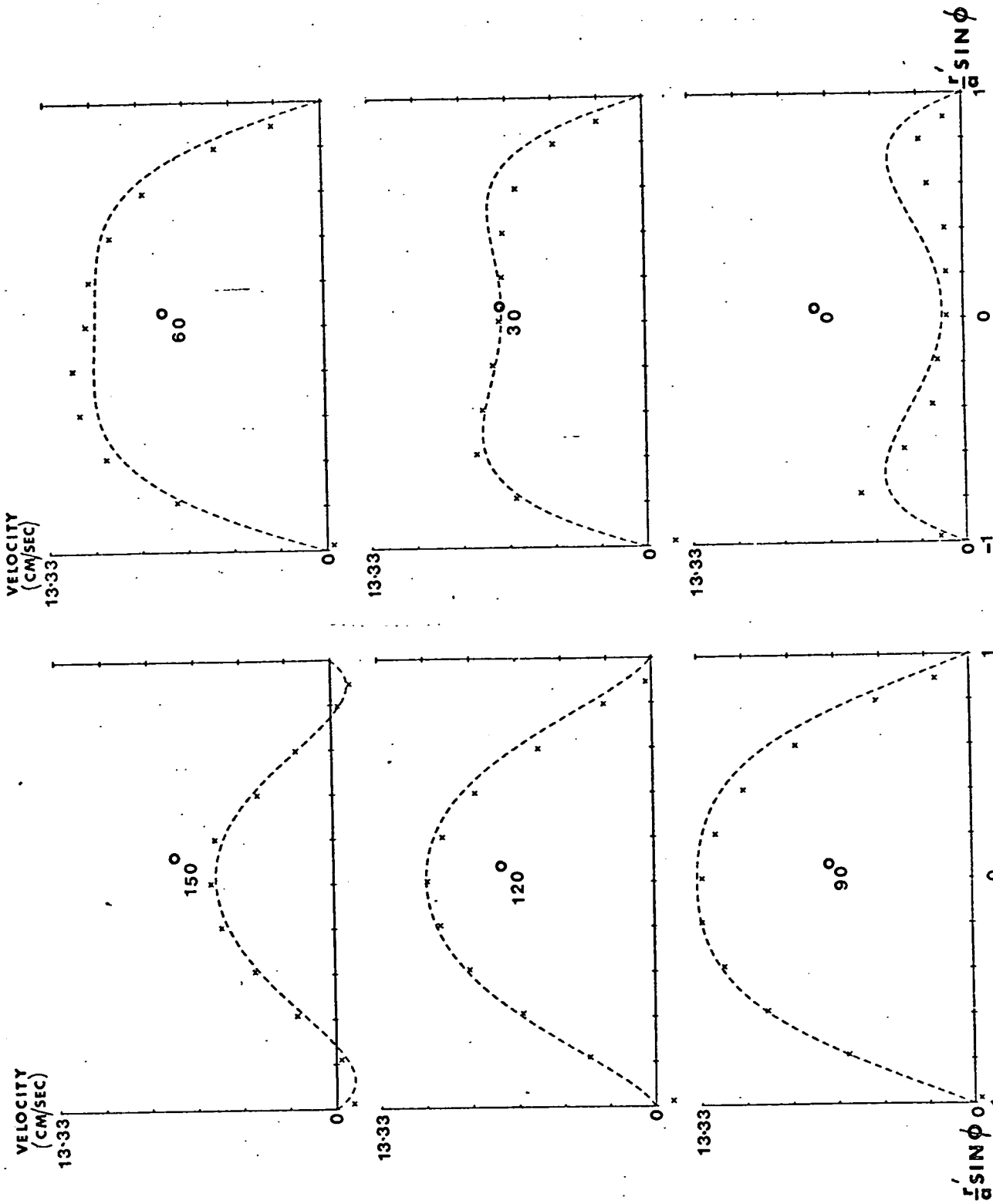

Figure (4.4.13) Normalised velocity time diagrams for straight pipe flow ———— and first order perturbation due to curvature - - - - - - for radial positions 0.1r and 0.9r with α = 4.36.

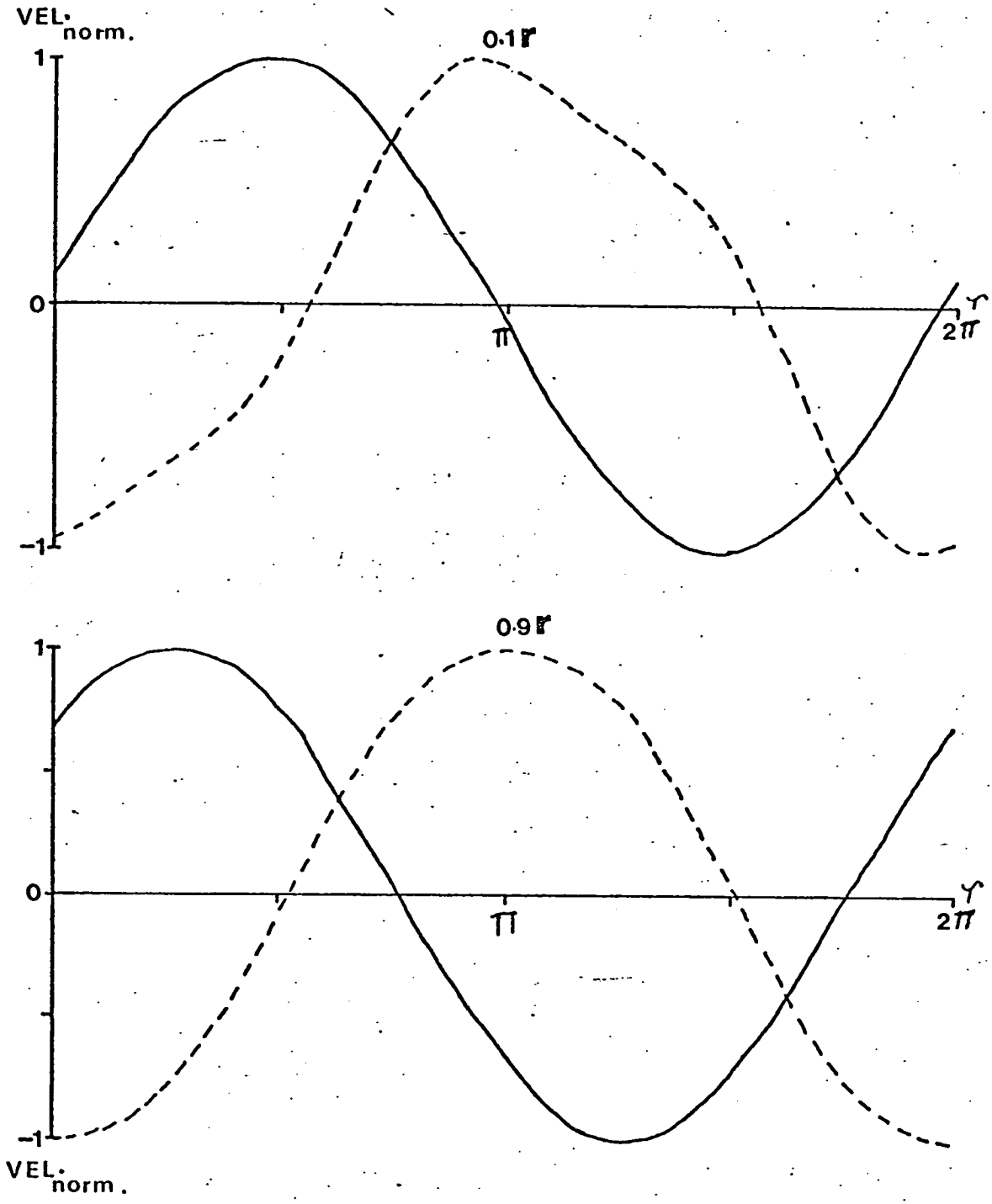

of the reduced D_{No} is to change the phase position at which the flow is unaffected by the curvature. A comparison is made in this series of results between theory and experiment and the agreement is seen to be reasonable.

The perturbation and relevant time dependent axial flow graphs are given in Fig. (4.4.13). The perturbation at the wall is now acting almost as $-\cos\Upsilon$ while that in the centre is more complicated in form, and there is now also a slight phase lag between the peaks of the perturbations. The effect at the wall would be to produce a flow reversal at the inside of the curve at 150^{o} phase position and this is what is found in the experimental results.

The perturbation in the centre of the tube acts in the opposite direction until $\backsim 120^{o}$, and thus the theory would be inadequate to explain the experimentally found D_{No} dependence. However, the main reason for the changing shift of the axial velocity peak appears to be an α dependent phase lag which develops between the perturbation and the straight pipe flow.

The next set of measurements taken were all measured at a fixed phase position on the piston, but at different frequencies. Owing to the wide range of frequencies covered, it was not possible to maintain the same peak D_{No} throughout the experiment, but by keeping the D_{No} small it is hoped the effect of varying D_{No} was negligible.

Figure (4.4.14) Series of velocity profiles measured at fixed phase position on the piston with varying alpha values. All profiles are plotted to the same scale.

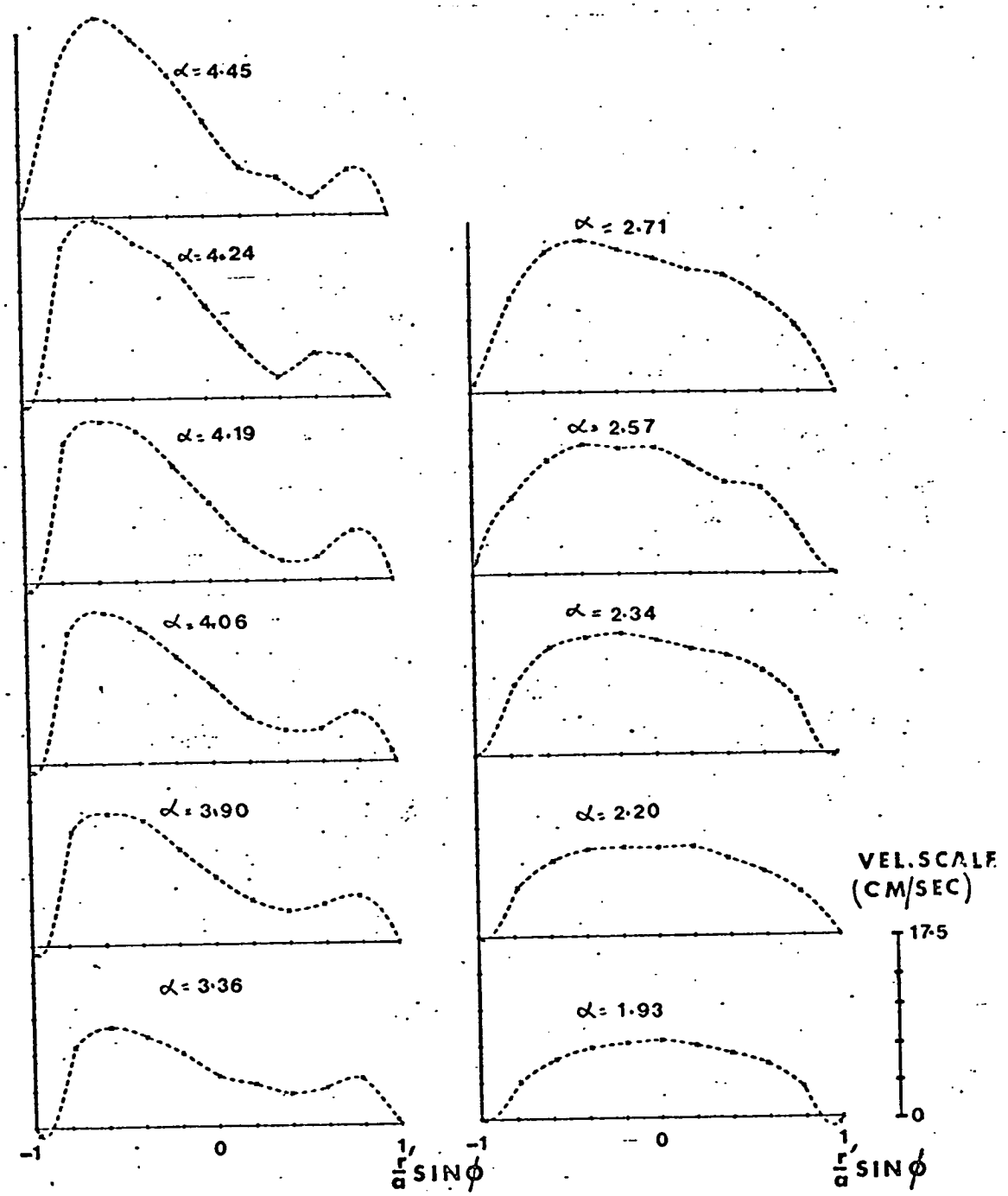

Figure (4.4.15) Velocity profiles for the case $\alpha = 3.82$, a/R = 1/50 and peak $D_{No} = 7.39$. Theoretical profile obtained using equation (2.4.11). Profile measured at phase positions $350^{\circ} \rightarrow 50^{\circ}$.

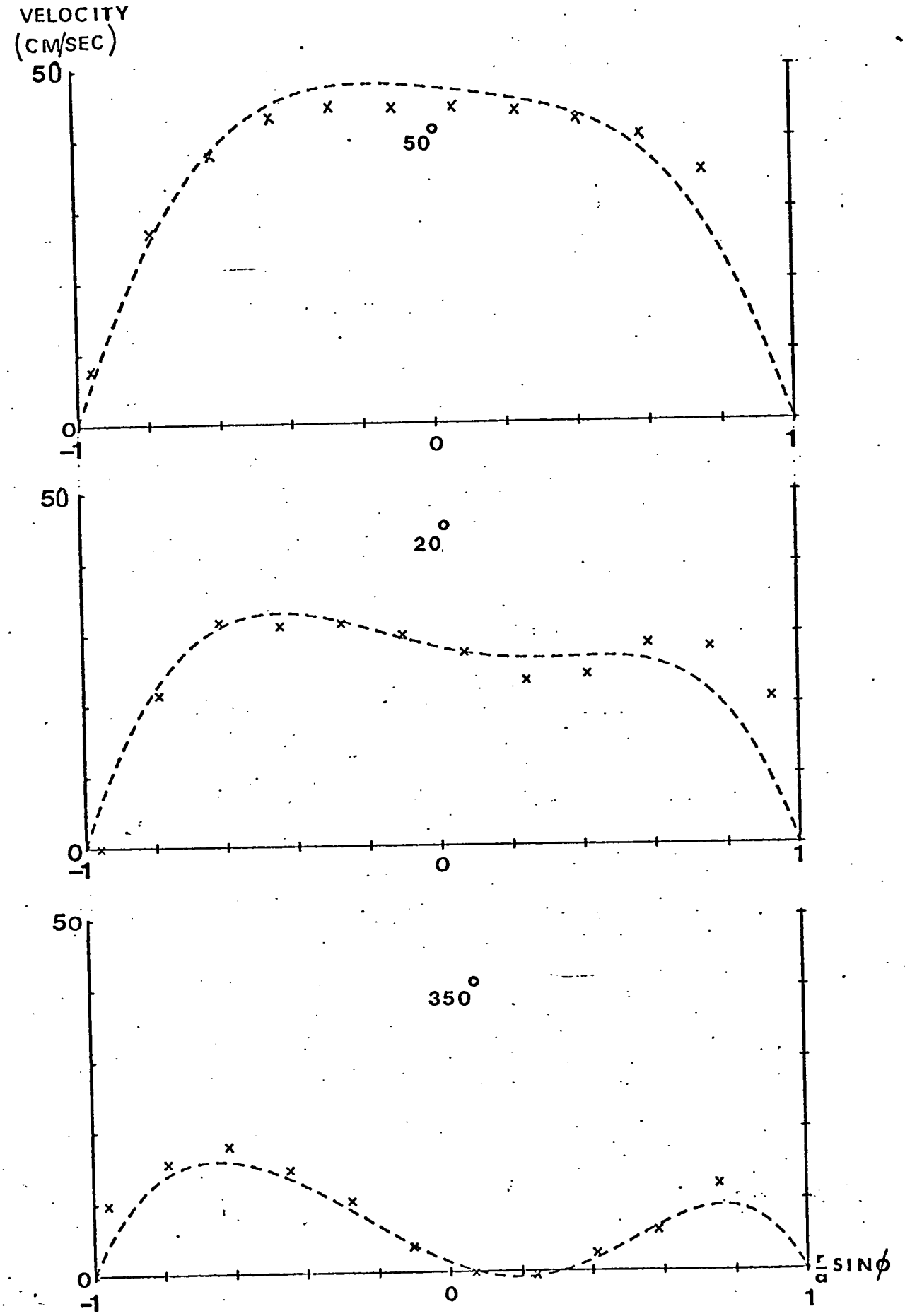

The results are shown in Fig. (4.4.14). A fixed phase position of the piston is equivalent to a fixed phase position on the mean velocity cycle, since the piston velocity is equivalent to the mean velocity. It would be a large task to examine each profile in detail, so only general observations will be made. A striking feature of the profiles is the similarity in form between $\alpha = 4.45$ and $\alpha = 3.36$. This indicates the consistency of the experiments in addition to showing some features of the flow found in other experiments. The axial velocity peak is found towards the inside of the curve down to $\alpha \sim 2$, which is in agreement with the theory for this phase position. The form of the profile changes dramatically at $\alpha \sim 2.7$, which coincides with the point where the cos term becomes important, (see Uchida (1956)), for the straight pipe flow.

The last measurement to be presented in this section was made in the $^1/_{50}$th curved tube at an α value of 3.82 at phase positions 350°-50°. These were particularly difficult profiles to measure because of the large frequency required to obtain this α value. However, the result shown in Fig. (4.4.15) indicates qualitatively the same picture that was found in the $^1/_7$th curve. Comparison is also given with theory and although the experimental measurements are outside the expected range of validity of the theory, agreement is seen to be reasonable. Thus the reversal of the shift of the axial

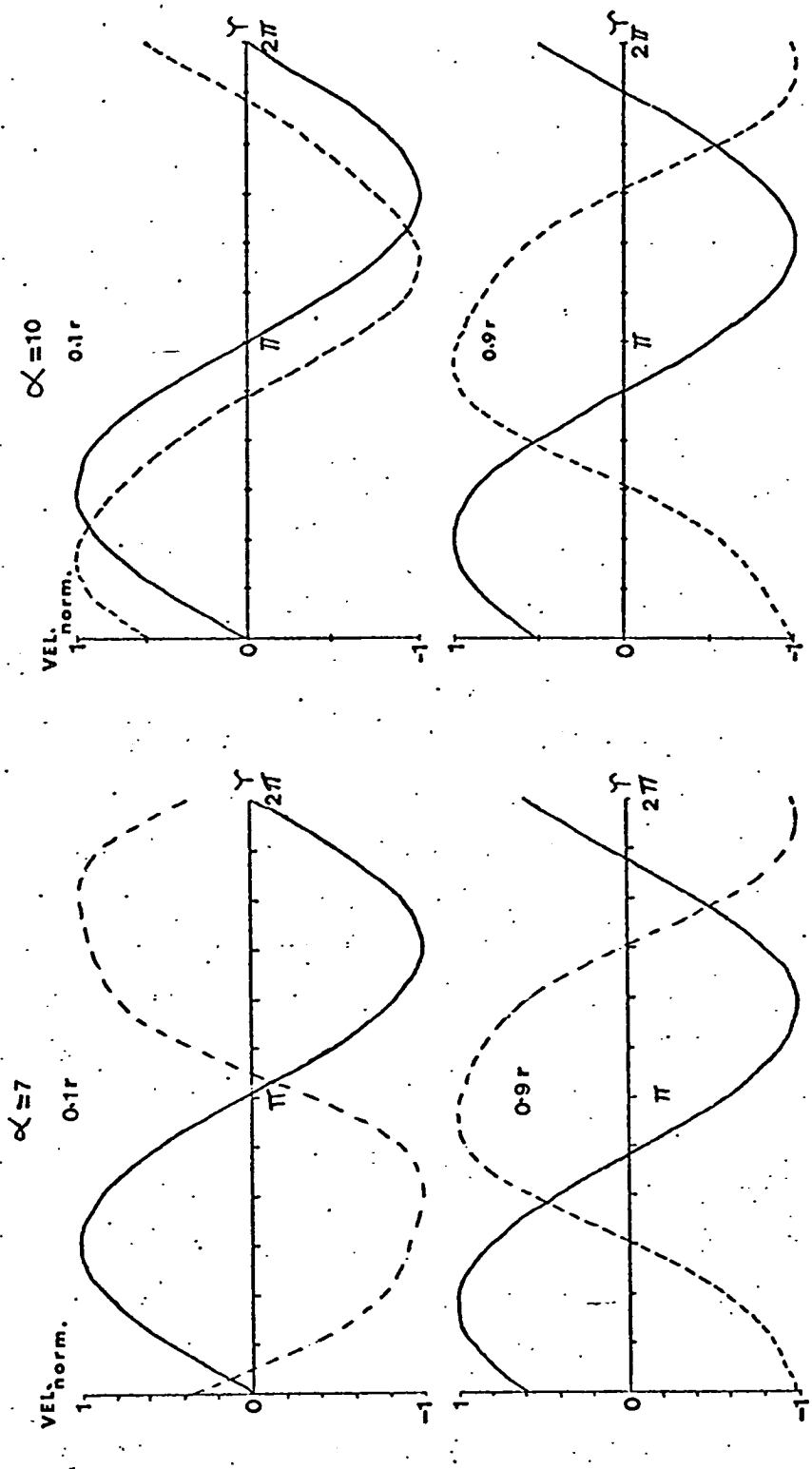

Figure (4.4.16) Normalised velocity time diagrams for straight pipe flow ———— and first order perturbation due to curvature - - - - - for radial positions 0.1 r and 0.9 r with α = 7 and 10.

velocity peak is found in the theory and in both experimental systems, and cannot be attributed to "finite curvature effect" alone, as was maintained by Bertelsen (1975).

The upper limit of the experimental system measurements was $\alpha \sim 4.5$ and now using the Hankel transform results, the axial velocity effects can be predicted up to $\alpha = 10$. The perturbations and straight pipe flow diagrams are shown for the cases $\alpha = 7$ and 10 in Fig. (4.4.16). There is very little difference between those shown for the 0.9 r position. Apart from the 90° - 150° and 270° - 330° phase positions, the action of the perturbation at the wall is to oppose the straight pipe flow.

In the centre of the tube at $\alpha = 7$, the perturbation is almost in anti-phase with the straight pipe flow and nearly returns to be in phase at $\alpha = 10$. Thus when $\alpha = 7$, apart from some flow reversals at the inside of the curve at 150° - 180° and 330° - 360°, the profile will be skewed towards the inside of the curve at all phase positions. At $\alpha = 10$ the perturbation in the central area is $\sim 40^{\circ}$ phase behind the main flow and thus there now seems to be a total change in the flow form. The velocity distribution in the central area will have its maximum value towards the outside of the curve at most phase positions. The flow along the walls will behave in a similar way to that at $\alpha = 7$, and continue to be

tilted inwards for $^{2}/_{3}$ of the cycle. Thus it would appear that as the effect of viscosity lessens over greater areas of the tube, the phase lag between the perturbation and the main flow in the central area increases from $\backsim 100^{\circ}$ at $\alpha = 5$ to 360° at $\alpha \backsim 10$. The flow in the regions around the walls of the tube is little changed over this alpha region.

The perturbation at the wall is an order of magnitude larger than that in the centre of the tube and will therefore have a greater effect. Thus it follows that the flow profile will be distorted as if the complete flow was inviscid, with the peak towards the inside of the curve at all phase positions. A completely opposite situation to that found for fully-developed steady flow will exist.

4.5 CONCLUSIONS

In this concluding section an over-all view of the flow structure of oscillatory flow in a curved tube will be presented. The theoretical and experimental results will be used to explain the events occurring in the transition stage between the quasi-steady and boundary-layer type flows of low and high α values.

The secondary flow generated by the centrifugal instability acts outwards across the central area of the tube, and returns around the walls in the quasi-steady situation exactly as in the steady flow case. As α increases so the characteristic oscillation time for the flow becomes comparable with the time for vorticity to diffuse from the wall across the tube. Thus in the central area of a straight pipe there develops a small region of essentially uniform flow which is present initially over a small portion of the cycle.

When α is ~ 5 the uniform central flow persists over $2 \times \frac{1}{4}$ parts of the cycle and a further increase in α to 10 shows that viscosity effects are now confined to the wall region and a truly boundary-layer type flow exists for a complete cycle. This uniform flow in the centre of the tube would be a stable flow situation according to the simplified analysis presented earlier. Thus the secondary motion in oscillatory flow will be controlled by the development of this region of stability within a cycle for any fixed α value.

Figure (4.5.1) Straight pipe profiles calculated using equation (2.2.4) for the case $\alpha = 3,5,10$.

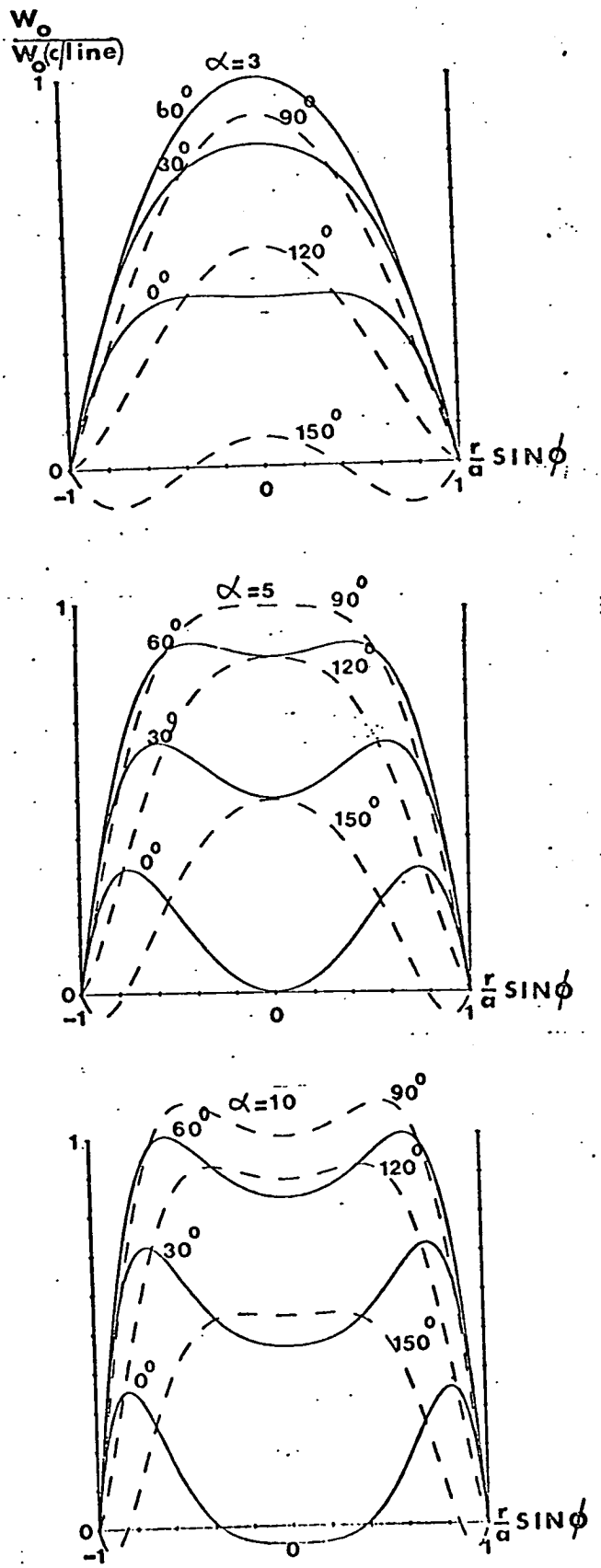

Now the cases α = 3, 5, and 10 are considered and the straight pipe profiles derived using equation (2.2.4) are shown in Fig. (4.5.1). From the relevant secondary flow plots given in section (4.3), it can be seen that the minimum in the secondary flow in the central plane of the tube corresponds to those phase positions when the uniform region is of the same order of magnitude as the flow near the wall and spread over $\gtrsim$ 0.5 of the diameter of the tube. Therefore the secondary flow is governed by the relative strength of the central stable region and the unstable region near the wall.

This simplified picture may be modified by the encroachment of the vorticity carrying secondary flow into the central region as the strength of this flow increases. Thus for a large D_{No} flow there may be some modifications to the phase positions at which secondary flow effects in the central area of the tube become important. The stable region may be swamped at these larger D_{Nos} and this could be a possible explanation for the large D_{No} effect found in the experiments.

The peak in the secondary flow in the central area does not always correspond to the maximum axial flow in the central region, but there is a phase lag between the two which increases as α increases. The centrifugal instability has first to overcome the stable situation and the time for it to do this increases as the stable region gains strength with increasing α. Thus the phase lag between peaks increases with increasing α.

When α = 10 and the boundary-layer type flow is approached, the stable area will persist throughout a cycle and the normal secondary flow effects will be confined to regions closer to the wall as the stable region grows in strength within a cycle. Once the stable region has reached a certain size it itself becomes unstable. This may be as a result of the boundary-layer generated secondary flow "dragging the core around" as postulated by Lyne (1970).

The axial velocity distribution will be radically different in fully-developed oscillatory flow from the steady flow picture except in the quasi-steady regime. If the secondary flow in the central area of the tube is small compared with the axial velocity, then the fluid will behave as if it were ideal and inviscid and adopt the "shortest path" around the curve. Thus as α increases, the time for which the secondary flow in the central area of the tube is effective decreases, and the axial velocity distribution adopts the inviscid position over more of the cycle.

The conclusion of this thesis is that oscillatory flow in a curved tube is very different in form from that of steady flow outside the quasi-steady regime. There is a complicated interplay between viscous and inertial effects which results in a total reversal of the direction of the secondary flow at large values of the frequency parameter α. The transition region

between quasi-steady and boundary-layer type flows is explained in terms of a gradual development of a stable region in the centre of the tube. This slowly becomes unstable, in the opposite sense to the region along the walls, when its area grows as α increases. The resultant modified axial velocity distribution is very different from the quasi-steady case.

Experimental measurements using a single-lens laser Doppler anemometer system, in conjunction with the sampled photon-correlation method of signal processing, have been shown to give reliable velocity information in the low to moderate α range. General agreement between theory and experiment is found to be reasonable and thus a great deal of insight into the problem has been gained.

The theoretical work given in this thesis is restricted to small values of the amplitude parameter G, which is taken as the expansion parameter. The present numerical transformation scheme used to solve the linearised Navier-Stokes equations is cumbersome, and thus a more efficient scheme may allow additional terms in the expansion, extending the upper limit on G. However, from the experimental results, it can be seen that the most influential parameter on the flow distribution is α and that the significant effects are found in the first order term. Therefore because of the complex nature of the linearised equations a numerical solution could be used to obtain more detailed information with a comparable amount of computational effort.

The experimental system developed in this study could be used in work on more complicated geometries. However many more axial velocity measurements in the high α region and secondary flow measurements over all the α range ought to be made in fully-developed flow in the curved tube. Such detailed measurements would show to what extent the limited theory presented here is correct.

APPENDIX A

CALCULATION OF SECOND ORDER EFFECTS OF CURVATURE ON SECONDARY STREAM LINE DISTRIBUTION

The R.H.S. of equation 2.20.1. is given by:-

$$\text{R.H.S.} = w_o \cos\phi \frac{\partial w_1}{\partial r} - \frac{w_o}{r} \sin\phi \frac{\partial w_1}{\partial \phi} + w_1 \cos\phi \frac{\partial w_o}{\partial r}$$

$$+ \frac{1}{r}\left(\frac{\partial \psi}{\partial \phi}\frac{\partial}{\partial r} - \frac{\partial \psi}{\partial r}\frac{\partial}{\partial \phi}\right)\nabla^2\psi_1 \quad - - - \quad (A1)$$

Each term will now be evaluated in turn from the relevant result in the main thesis.

$$w_o \frac{\partial w_1}{\partial r} \cos\phi = \frac{\sin 2\phi}{8}\left\{ B\frac{dD_{1R}}{dr} - (1-A)\frac{dD_{1I}}{dr} \right.$$

$$+ \cos 2\tau\left(B\frac{dD_{1R}}{dr} + B\frac{dD_{3R}}{dr} + (1-A)\frac{dD_{1I}}{dr} \right.$$

$$\left. - (1-A)\frac{dD_{3I}}{dr}\right) + \sin 2\tau\left((1-A)\frac{dD_{1R}}{dr} - B\frac{dD_{1I}}{dr} \right.$$

$$\left. - B\frac{dD_{3I}}{dr} - (1-A)\frac{dD_{3R}}{dr}\right) + \cos 4\tau\left(B\frac{dD_{3R}}{dr} \right.$$

$$\left. \left. + (1-A)\frac{dD_{3I}}{dr}\right) + \sin 4\tau\left((1-A)\frac{dD_{3R}}{dr} - B\frac{dD_{3I}}{dr}\right)\right\}$$

$$- - - - - - \quad (A2)$$

The functions $\frac{dD_{1R}}{dr}$ etc. can be evaluated from the relevant inversion formulae:-

$$\frac{w_o}{r}\frac{\partial w_1}{\partial \phi}\sin\phi = \frac{\sin 2\phi}{8r}\Big\{ B\,D_{1R} - (1-A)\,D_{1I}$$

$$+ \cos 2\Upsilon\,(\,B\,D_{1R} + B\,D_{3R} + (1-A)\,D_{1I} - (1-A)\,D_{3I})$$

$$+ \sin 2\Upsilon\,(\,D_{1R}\,(1-A) - B\,D_{1I} - B\,D_{3I} - (1-A)\,D_{3R})$$

$$+ \cos 4\Upsilon\,(\,B\,D_{3R} + (1-A)\,D_{3I})$$

$$+ \sin 4\Upsilon\,(\,D_{3R}\,(1-A) - B\,D_{3I})\Big\} \quad - - - \quad (A3)$$

$$w_1 \cos\phi\,\frac{\partial w_o}{\partial r} = \frac{\sin 2\phi}{8}\Big\{ D_{1R}\frac{dB}{dr} + D_{1I}\frac{dA}{dr}$$

$$+ \cos 2\Upsilon\left(D_{1R}\frac{dB}{dr} + D_{3R}\frac{dB}{dr} - D_{1I}\frac{dA}{dr} + D_{3I}\frac{dA}{dr}\right)$$

$$+ \sin 2\Upsilon\left(D_{3R}\frac{dA}{dr} - D_{1I}\frac{dB}{dr} - D_{3I}\frac{dB}{dr} - D_{1R}\frac{dA}{dr}\right)$$

$$+ \cos 4\Upsilon\left(D_{3R}\frac{dB}{dr} - D_{3I}\frac{dA}{dr}\right)$$

$$- \sin 4\Upsilon\left(D_{3I}\frac{dB}{dr} + D_{3R}\frac{dA}{dr}\right)\Big\} \quad - - - \quad (A4)$$

$$\frac{1}{r}\frac{\partial \psi_1}{\partial \phi}\frac{\partial \nabla^2 \psi_1}{\partial r} = -\frac{\sin 2\phi}{16}\Big[\,2\,C_o\frac{dM_o}{dr} + C_{2R}\frac{dM_{2R}}{dr}$$

$$+ C_{2I} \frac{dM_{2I}}{dr} + \cos 2\Upsilon \left(2 C_o \frac{dM_{2R}}{dr} + 2 C_{2R} \frac{dM_o}{dr} \right) -$$

$$- \sin 2\Upsilon \left(2 C_o \frac{dM_{2I}}{dr} + 2 C_{2I} \frac{dM_o}{dr} \right) + \cos 4\Upsilon$$

$$\left(C_{2R} \frac{dM_{2R}}{dr} - C_{2I} \frac{dM_{2I}}{dr} \right) - \sin 4\Upsilon \left(C_{2R} \frac{dM_{2I}}{dr} \right.$$

$$\left. + \frac{dM_{2R}}{dr} C_{2I} \right) \Bigg\} - - - - \quad (a5)$$

The functions M_o, M_{2R} and M_{2I} are found from the inversion formulae for C_o, C_{2R} and C_{2I} respectively in the following way:-

$$M_o = \left(\frac{d^2}{dr^2} + \frac{1}{r} \frac{d}{dr} - \frac{1}{r^2} \right) C_o = -2 \sum_{j=1}^{\infty} \frac{\bar{C}_o J_1(\xi_j r) \xi_j^2}{\left[J_o(\xi_j) \right]^2}$$

$$- - - \quad (A6)$$

Finally:-

$$\frac{1}{r} \frac{\partial \psi_1}{\partial r} \frac{\partial \nabla^2 \psi_1}{\partial \phi} = - \frac{\sin 2\phi}{16r} \Big\{ 2 M_o \frac{dC_o}{dr} + M_{2R} \frac{dC_{2R}}{dr}$$

$$+ M_{2I} \frac{dC_{2I}}{dr} + \cos 2\Upsilon \left(2 M_{2R} \frac{dC_o}{dr} + 2 M_o \frac{dC_{2R}}{dr} \right)$$

$$- \sin 2\Upsilon \left(2 M_{2I} \frac{dC_o}{dr} + 2 M_o \frac{dC_{2I}}{dr} \right)$$

$$+ \cos 4\Upsilon \left(M_{2R} \frac{dC_{2R}}{dr} - M_{2I} \frac{dC_{2I}}{dr} \right)$$

$$- \sin 4\Upsilon \left(M_{2R} \frac{dC_{2I}}{dr} + M_{2I} \frac{dC_{2I}}{dr} \right) \Bigg\} \quad - \quad - \quad - \quad (A7)$$

From the form of the terms which arise a solution is sought such that:-

$$\Psi_2 = \left\{ H_{20}(r) + H_{22} e^{i2\Upsilon} + H_{24} e^{i4\Upsilon} \right\} \sin 2\phi \quad - - - - (A8)$$

The boundary conditions relevant to these equations are:-

$$H_{2i} = \frac{dH_{2i}}{dr} = 0 \text{ at } r = 1$$

and thus the solution procedure is the same as in section (2.3.)

The following equation results for the steady component:-

$$\nabla^4 \psi_{20} = \frac{\sin 2\phi}{8} \Bigg\{ \left[(1-A) \frac{dD_{1I}}{dr} - D_{1I} \left(\frac{(1-A)}{r} + \frac{dA}{dr} \right) \right] + \left[\frac{C_{2R}}{2r} \frac{dM_{2R}}{dr} - \frac{M_{2R}}{2r} \frac{dC_{2R}}{dr} \right] + \left[\frac{C_{2I}}{2r} \frac{dM_{2I}}{dr} - \frac{M_{2I}}{2r} \frac{dC_{2I}}{dr} \right] - \left[B \frac{dD_{1R}}{dr} - D_{1R} \left(\frac{B}{r} - \frac{dB}{dr} \right) \right] - \left[\frac{M_o}{r} \frac{dC_o}{dr} - \frac{C_o}{r} \frac{dM_o}{dr} \right] \Bigg\}$$

$$- \quad - \quad - \quad - \quad (A9)$$

The transform of this equation is given by:-

$$\zeta'^{4}_{j} H_{20}(\zeta'_{j}) = I_{11} + I_{12} + I_{13} - I_{14} - I_{15} + \zeta'_{j} \frac{d^2 H_{20}}{dr^2} \Big| J'_2(\zeta'_j) \quad - - - - \quad (A10)$$

$r=1$

where in this case the second order Hankel transform is used and the relevant inversion formula is now:-

$$F(r) = 2 \sum_{j=1}^{\infty} \frac{\bar{F}(\zeta'_j) J_2(\zeta'_j r)}{[J'_2(\zeta'_j)]^2} \quad - - - \quad (A11)$$

where ζ'_j is the j_{th} eigenvalue of the equation:-

$$J_2(\zeta'_j) = 0 \quad - - - - \quad (A12)$$

The integrals are:-

$$I_{11} = \int_0^1 \left[(1-A) \frac{dD_{1I}}{dr} r - D_{1I} \left(\frac{dA}{dr} r + (1-A) \right) \right] J_2(\zeta'_j r) dr$$

$$I_{12} = \int_0^1 \left(C_{2R} \frac{dM_{2R}}{dr} - M_{2R} \frac{dC_{2R}}{dr} \right) \frac{J_2(\zeta'_j r)}{2} dr$$

$$I_{13} = \int_0^1 \left(C_{2I} \frac{dM_{2I}}{dr} - M_{2I} \frac{dC_{2I}}{dr} \right) \frac{J_2}{2}(\zeta'_j r) dr$$

$$I_{14} = \int_0^1 \left(B \frac{dD_{1R}}{dr} r - D_{1R} \left(B - \frac{dB}{dr} r \right) \right) J_2(\zeta'_j r) dr$$

$$I_{15} = \int_0^1 \left(M_o \frac{dC_o}{dr} - C_o \frac{dM_o}{dr} \right) J_2(\zeta'_j r) dr$$

As in other cases the second derivative in (A10) must be calculated before the inversion formula can be used. This is done in the same manner as in section (2.3). This results in:-

$$\left.\frac{d^2 H_{20}}{dr^2}\right|_{r=1} = - \frac{\sum_{j=1}^{\infty} \left\{ I_{11} + I_{12} + I_{13} - I_{14} - I_{15} \right\}}{\left\{ \left\{'^3_j J_1 \left(\left\{'_j \right) \right\} \right.} \qquad - - \quad (A13)$$

$$\sum_{j=1}^{\infty} \frac{1}{(\{'_j{}^2)}$$

The equation for the second harmonic is given by:-

$$\alpha^2 \frac{\partial}{\partial \tau} (\nabla^2 \psi_{22}) - \nabla^4 \psi_{22} = \frac{\sin 2\phi}{8} \Big\{ \cos 2\tau \Big[\Big(B \frac{dD_{1R}}{dr} - D_{1R} \Big(\frac{B}{r} - \frac{dB}{dr} \Big) \Big) + \Big(B \frac{dD_{3R}}{dr} - D_{3R} \Big(\frac{B}{r} - \frac{dB}{dr} \Big) \Big) + \Big(\Big[1-A\Big] \frac{dD_{1I}}{dr} - D_{1I} \Big(\Big[1-A\Big] - \frac{dA}{dr} \Big) \Big) - \Big(\Big[1-A\Big] \frac{dD_{3I}}{dr} - D_{3I} \Big(\Big[\frac{1-A}{r}\Big] + \frac{dA}{dr} \Big) \Big) - \Big(\frac{C_o}{r} \frac{dM_{2R}}{dr} + \frac{C_{2R}}{r} \frac{dM_o}{dr} - \frac{M_{2R}}{r} \frac{dC_o}{dr} - \frac{M_o}{r} \frac{dC_{2R}}{dr} \Big) \Big] + \sin 2\tau \Big[\Big(D_{3I} \Big(\frac{B}{r} - \frac{dB}{dr} \Big) - B \frac{dD_{3I}}{dr} \Big) - \Big(\Big[1-A\Big] \frac{dD_{3R}}{dr} - D_{3R} \Big(\Big[\frac{1-A}{r}\Big] + \frac{dA}{dr} \Big) \Big) - \Big(\Big[1-A\Big] \frac{dD_{1R}}{dr} - B \frac{dD_{1I}}{dr} - \frac{D_{1R}}{r} \Big[1-A\Big] + \frac{B}{r} D_{1I} - D_{1I} \frac{dB}{dr} - D_{1R} \frac{dA}{dr} \Big)$$

$$+ \frac{C_o}{r}\frac{dM_{2I}}{dr} + \frac{C_{2I}}{r}\frac{dM_o}{dr} - \frac{M_{2I}}{r}\frac{dC_o}{dr} - \frac{M_o}{r}\frac{dC_{2I}}{dr}\Big)\Big]\Big\} \quad ---(A14)$$

Using a similar technique as in section (2.3) the R.H.S. may be divided into real and imaginary parts and the resulting transformed equations arise:-

$$\bar{H}_{22R} = \Big[\Big(I_{14} + I_{16} + I_{11} + I_{17} - I_{18}\Big)\zeta_j'^2 + 2\alpha^2 \Big(I_{20} - I_{19} - I_{21}\Big) - \zeta_j'^3 \frac{d^2H_{22R}}{dr^2}\Big|_{r=1} J_1(\zeta_j') - \zeta_j' 2\alpha^2 \frac{d^2H_{22I}}{dr^2}\Big|_{r=1} J_1(\zeta_j')\Big]$$

$$\overline{\qquad\qquad\qquad\qquad\qquad\qquad\qquad\qquad\qquad\qquad\qquad\qquad\qquad\qquad\qquad\qquad}$$

$$- \zeta_j'^2 \Big(4\alpha^4 + \zeta_j'^4\Big) \quad ------(A15)$$

$$\bar{H}_{22I} = \Big[\zeta_j'^2 \Big(I_{20} - I_{19} - I_{21}\Big) - 2\alpha^2 (I_{14} + I_{16} + I_{11} - I_{17} - I_{18}) + 2\alpha^2 \zeta_j' \frac{d^2H_{22R}}{dr^2}\Big|_{r=1} J_1(\zeta_j') - \zeta_j'^3 \frac{d^2H_{22I}}{dr^2}\Big|_{r=1} J_1(\zeta_j')\Big]$$

$$\overline{\qquad\qquad\qquad\qquad\qquad\qquad\qquad\qquad\qquad\qquad\qquad\qquad\qquad\qquad\qquad\qquad}$$

$$- \zeta_j'^2 \Big(4\alpha^4 + \zeta_j'^4\Big) \quad ------(A16)$$

where:-

$$I_{16} = \int_0^1 \left(B \frac{dD_{3R}}{dr} r - D_{3R}\left(B - r \frac{dB}{dr} \right) \right) J_2 (\xi'_j r)\, dr$$

$$I_{17} = \int_0^1 \left([1-A] \frac{dD_{3I}}{dr} r - D_{3I}\left([1-A] + r \frac{dA}{dr} \right) \right) J_2(\xi'_j r)\, dr$$

$$I_{18} = \int_0^1 \left(C_o \frac{dM_{2R}}{dr} + C_{2R} \frac{dM_o}{dr} - M_{2R} \frac{dC_o}{dr} - M_o \frac{dC_{2R}}{dr} \right) J_2 (\xi'_j r)\, dr$$

$$I_{19} = \int_0^1 \left(D_{3R}\left(B - \frac{dB}{dr} r \right) - B \frac{dD_{3I}}{dr} r \right) J_2(\xi'_j r)\, dr$$

$$I_{20} = \int_0^1 \left([1-A] \frac{dD_{3R}}{dr} r - D_{3R}\left([1-A] + \frac{dA}{dr} r \right) \right) J_2(\xi'_j r)\, dr$$

$$I_{21} = \int_0^1 \left\{ (1-A) \frac{dD_{1R}}{dr} r - B \frac{dD_{1I}}{dr} r - D_{1R}\left([1-A] + \frac{dA}{dr} r \right) + D_{1I}\left(B - \frac{dB}{dr} r \right) + C_o \frac{dM_{2I}}{dr} + C_{2I} \frac{dM_o}{dr} - M_{2I} \frac{dC_o}{dr} - M_o \frac{dC_{2I}}{dr} \right\} J_2 (\xi'_j r)\, dr$$

The second derivatives are calculated using the formulae:-

$$\frac{d^2 H_{22R}}{dr^2} = \frac{2\alpha^2 S_7 S_8 - S_5 S_6}{S_6^2 + 4\alpha^4 S_7^2}$$

$$\frac{d^2 H_{22I}}{dr^2} = \frac{\left[2\alpha^2 S_7 \frac{d^2 H_{22R}}{dr^2} - S_8 \right]}{S_6}$$

where:-

$$S_5 = \sum_{j=1}^{\infty} \frac{(I_{14} + I_{16} + I_{11} - I_{18}) \zeta'^2_j + 2\alpha^2 (I_{20} - I_{19} - I_{21})}{-\zeta'_j (4\alpha^4 + \zeta'^4_j) J_1(\zeta'_j)}$$

$$S_6 = \sum_{j=1}^{\infty} \frac{\zeta'^2_j}{4\alpha^4 + \zeta'^4_j}$$

$$S_7 = \sum_{j=1}^{\infty} \frac{1}{4\alpha^4 + \zeta'^4_j}$$

$$S_8 = \sum_{j=1}^{\infty} \frac{\zeta'^2_j (I_{20} - I_{19} - I_{21}) - 2\alpha^2 (I_{14} + I_{16} + I_{11} - I_{17} - I_{18})}{-\zeta'_j (4\alpha^4 + \zeta'^4_j) J_1(\zeta'_j)}$$

A similar procedure is followed for the fourth harmonic starting from the full equation:-

$$\alpha^2 \frac{\partial(\nabla^2\psi_{24})}{\partial\tau} - \nabla^4\psi_{24} = \frac{\sin 2\phi}{8}\left\{\cos 4\tau\left[B\frac{dD_{3R}}{dr} - \frac{B}{r}D_{3R} + D_{3R}\frac{dB}{dr}\right) + \left(\left[1-A\right]\frac{dD_{3I}}{dr} - \frac{\left[1-A\right]}{r}D_{3I} - D_{3I}\frac{dA}{dr}\right)\right.$$

$$\left. - \left(\frac{C_{2R}}{2r}\frac{dM_{2R}}{dr} - \frac{M_{2R}}{2r}\frac{dC_{2R}}{dr}\right) + \left(\frac{C_{2I}}{2r}\frac{dM_{2I}}{dr} - \frac{M_{2I}}{2r}\frac{dC_{2I}}{dr}\right)\right]$$

$$+ \sin 4\tau\left[\left(\left[1-A\right]\frac{dD_{3R}}{dr} - \frac{D_{3R}}{r}\left[1-A\right] - D_{3R}\frac{dA}{dr}\right)\right.$$

$$+ \left(\frac{B}{r}D_{3I} - D_{3I}\frac{dB}{dr} - B\frac{dD_{3I}}{dr}\right) + \left(\frac{C_{2R}}{2r}\frac{dM_{2I}}{dr} + \frac{C_{2I}}{2r}\frac{dM_{2R}}{dr}\right.$$

$$\left.\left. - \frac{M_{2R}}{2r}\frac{dC_{2I}}{dr} - \frac{M_{2I}}{2r}\frac{dC_{2R}}{dr}\right)\right]\Bigg\} \text{ - - - - - - - (A17)}$$

The following formulae result for the transformation functions:-

$$\bar{H}_{24R}(\zeta'_j) = \Big[(I_{16}+I_{17}-I_{12}+I_{13})\zeta'^2_j + 4\alpha^2(-I_{22}-I_{20}-I_{19}) - \zeta'^3_j \frac{d^2H_{24R}}{dr^2}\Big|_{r=1} J_1(\zeta'_j) - \zeta'_j 4\alpha^2 \frac{d^2H_{24I}}{dr^2}\Big|_{r=1} J_1(\zeta'_j)\Big]$$

$$\frac{}{-\zeta'^2_j(16\alpha^4 + \zeta'^4_j)}$$

$$\bar{H}_{24I}(\zeta'_j) = \Big[(-I_{22}-I_{20}-I_{19})\zeta'^{2}_j - 4\alpha^2(I_{16}+I_{17}-I_{12}+I_{13}) + 4\alpha^2\zeta'_j \frac{d^2H_{24R}}{dr^2} J_1(\zeta'_j) - \zeta'^{2}_j \frac{d^2H_{24I}}{dr^2}\Big|_{r=1} J_1(\zeta'_j)$$

$$\Big] \Big/ \Big[-\zeta'^{2}_j (16\alpha^4 + \zeta'^{4}_j) \Big]$$

and the second derivatives are calculated from:-

$$\frac{d^2H_{24R}}{dr^2} = \frac{4\alpha^2 S_{11} S_{12} - S_9 S_{10}}{S_{10}^2 + 16\alpha^4 S_{11}^2}$$

$$\frac{d^2H_{24I}}{dr^2} = \frac{\Big[4\alpha^2 S_{11} \frac{d^2H_{24R}}{dr^2} - S_{12} \Big]}{S_{10}}$$

where:-

$$S_9 = \sum_{j=1}^{\infty} \frac{(I_{16}+I_{17}-I_{12}+I_{13})\zeta'^{2}_j + 4\alpha^2(-I_{22}-I_{20}-I_{19})}{-\zeta'_j (16\alpha^4 + \zeta'^{4}_j) J_1(\zeta'_j)}$$

$$S_{10} = \sum_{j=1}^{\infty} \frac{\zeta'^{2}_j}{16\alpha^4 + \zeta'^{4}_j}$$

$$S_{11} = \sum_{j=1}^{\infty} \frac{1}{16\alpha^4 + \varsigma_j'^4}$$

$$S_{12} = \sum_{j=1}^{\infty} \frac{\varsigma_j'^2 (-I_{22}-I_{20}-I_{19}) - 4\alpha^2(I_{16}+I_{17}-I_{12}-I_{13})}{-\varsigma_j' (16\alpha^4 + \varsigma_j'^4) J_1(\varsigma_j')}$$

and:-

$$I_{22} = \int_0^1 \left(C_{2R} \frac{dM_{2R}}{dr} + C_{2I} \frac{dM_{2R}}{dr} - M_{2R} \frac{dC_{2R}}{dr} - M_{2I} \frac{dC_{2R}}{dr} \right) \frac{J_2(\varsigma_j' r)}{2} dr$$

All the summations were taken over twenty terms to try to ensure convergence of the integrals. A discussion of this point will be given in Appendix B.

APPENDIX B

CONVERGENCE of INTEGRALS USED in HANKEL TRANSFORMS

All the integrals in this study were evaluated using the Gaussian quadrature scheme of Stroud (1966). The integrals are evaluated using five and six point approximations and the difference between these approximations compared with a pre-set accuracy requirement. If the required accuracy is not found then the interval is halved and the five and six point formulae applied to each sub-interval. The accuracy test is then applied to the sum of the contributions. The process continues until the required accuracy is reached, this sometimes requiring 2^7 sub-divisions when $\alpha \sim 10$ for some of the integrals.

Therefore each integral could be evaluated to a pre-determined accuracy for a fixed number of terms in a summation involved in that integral. The effect of the inclusion of more terms in the summation is shown in Fig. (B1) for the integral I_{15}. This integral was chosen as it had the greatest influence on the secondary flow, particularly for the larger alpha values, and was the one which caused the most convergence problems.

It can be seen from Fig. (B1) that as α increases then more and more terms must be included in the summation, which meant that computation times increased by a factor of 4 between the case $\alpha = 1$ and $\alpha = 10$.

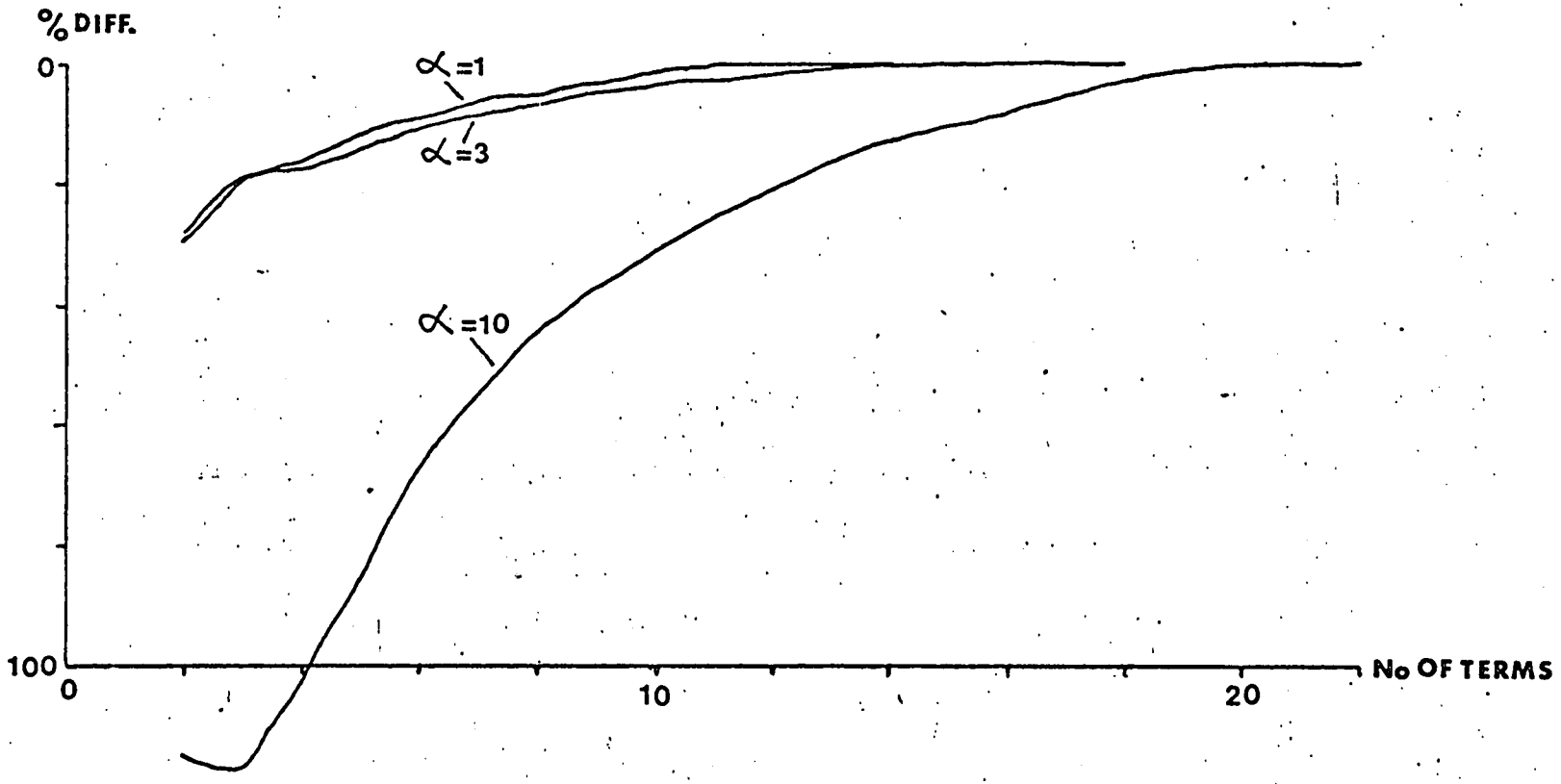

Figure (B1) Graph illustrating the convergence of the integral I_{15} for various α values. The plot shows the % difference between the final value and the actual value of the number of terms used in the summation series.

The computational time involved in obtaining a solution to the secondary flow equations for $\alpha = 10$, was $\sim$ 2 hours on an IBM 360 machine. Thus for α values greater than this, approximate methods of solution are more appropriate.

Finally, an improved method of transforming the equations may be possible, using the "Quasi fast Hankel Transform" suggested by Siegman (1977). He has used an approach very similar to the F.F.T. technique and considerably shortened computer times for some applications of the finite Hankel transform.

APPENDIX C

CALCULATION of OPTICAL PARAMETERS

Kogelnik (1966) has shown that the beam waist radius of a laser beam passing through a thin lens is modified by the lens, as shown schematically in Fig. C1.

The beam radius $\bar{w}_o$ at distance Z_o from lens of focal length f_o is transformed by the lens to a beam of waist radius $\bar{w}_1$ at distance Z_1 from the lens. The relationships between radii and distances are given by:-

$$Z_1 = f_o + (Z_o - f_o)\, f_o^2 / \left\{ (Z_o - f_o)^2 + (\pi \bar{w}_o / \lambda)^2 \right\} \quad -(C1)$$

$$\frac{1}{\bar{w}_1^2} = (1 - Z_o/f_o)^2 / \bar{w}_o^2 + (\pi \bar{w}_o / \lambda)^2 / f_o^2 \quad -(C2)$$

The laser used was operating in the TEM_{oo} mode and was of He-Ne type having a wavelength λ of 632.8 x 10^{-9} m.

The beam diameter at the front of the laser defined at the $1/e^2$ points of the intensity distribution is 1.1 m.m (Spectra Physics Handbook).

Gaussian waist diameter after L_1 (25 cm f.l.)

$= 1.81812 \times 10^{-4}$ m

Position of Gaussian waist = 25.49 cm after lens.

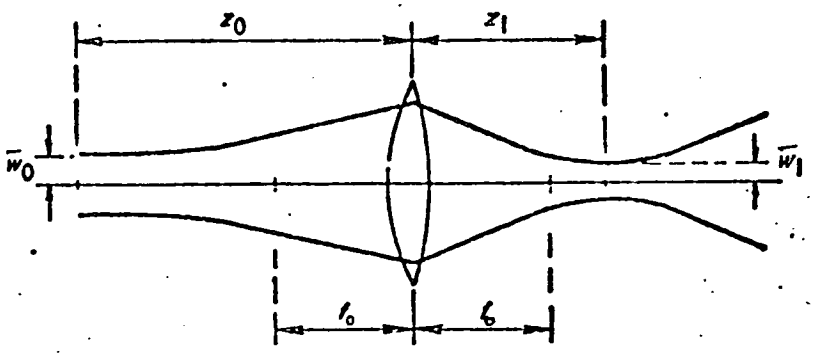

Figure C1 Transformation of a gaussian beam of light by a thin lens.

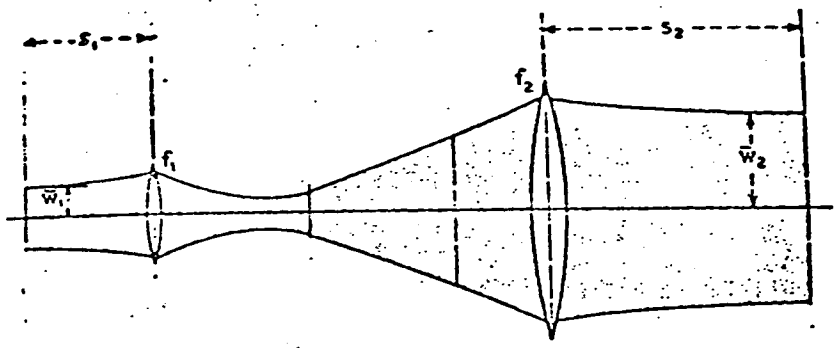

Figure C2 Gaussian beam passing through a telescope.

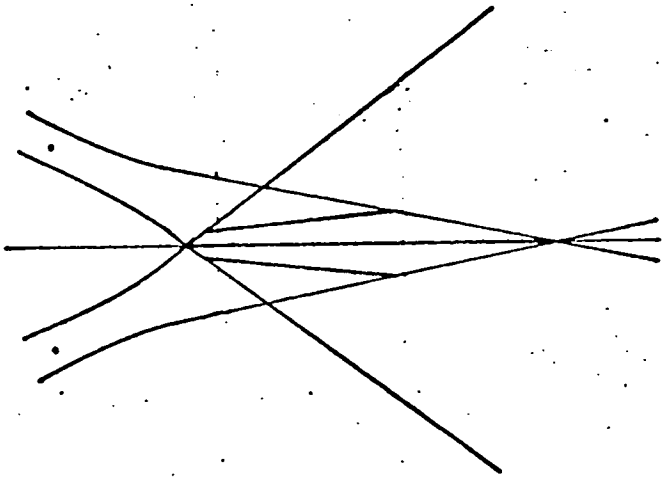

Figure C3 Interference pattern for two intersecting gaussian beams.

Lenses L_2 and L_3 form a telescope arrangement and using the work of Kogelnik, the beam transformation is shown in Fig. C2.

The telescope in this case was formed using a 13cm lens followed by a 30 cms lens. For a perfectly aligned telescope, the relationship between the input and output beam waists is given by:-

$$\bar{w}_2 = \bar{w}_1 \frac{f_2}{f_1} \quad - - - - \quad (C3)$$

The spacing between the lenses was checked by direct measurement and also by checking that the two laser beams transmitted were parallel over a length of approximately 30 metres. Since the spacing of the input beams is known, the expected output spacing is given by the ratio of the focal lengths of the two lenses and this can be used as a further check on the accuracy of the telescope. Therefore:-

Gaussian beam waist diameter after telescope

$$= 4.1956615 \times 10^{-4} \text{ m}$$

The position of the beam waist can be calculated using Kogelnik's formula:-

$$s_2 = f_2 - f_2^2 \frac{(s_1 - f_1)}{f_1^2} \quad - - - - \quad (C4)$$

where s_1 and s_2 are the distances indicated in Fig.C2.

Thus $s_2 = 32.609$ cms after L_3.

Finally, the beam parameters after the aspheric lens may be calculated using formulae (C1) and (C2) to give:-

Final beam radius = 3.5570190×10^{-5} m

Positioned at 3.7641 cm behind the lens.

This result shows that the point of intersection of the two beams does not coincide with their Gaussian waists. Since the wavefronts are planar at the Gaussian waists then, as has been shown by Hanson (1973), some distortion of the fringes will occur as illustrated in Fig.C3. This will give undesirable broadening effects on the Doppler signal.

The radius of curvature of the wavefront of the beam can be calculated using the Kogelnik formula:-

$$R(Z) = Z \left\{ 1 + (\pi \bar{w}_o^{\,2} / \lambda Z)^2 \right\} \quad - - - (C5)$$

where Z is now the distance between the Gaussian waist and the point of intersection of the beams. Thus as $Z \rightarrow 0$ (i.e. perfect alignment) then $R(Z) \rightarrow \infty$ and a truly planar wavefront exists.

Hanson has shown that the resultant broadening is given by:-

$$\frac{df}{fdZ} = -\cos\theta \,/_{R(Z_o)} \quad - - - - \quad (C6)$$

where f is the Doppler frequency and 2 θ is the angle between the beams, which are propagating in the Z direction.

The percentage broadening over the fringe volume length is given by:-

$$\% \text{ Broadening} = (-\cos\theta/R\,(Z_o)\,)\;\bar{d} \times 100\% \; - \; -(\,C7)$$

where $\bar{d}$, the fringe volume length, can be calculated using the formula given by Durrani and Greated (1977) of:-

$$\bar{d} = \frac{2r_s}{\cos\theta} \quad - - - - - - - - \quad (C8)$$

where r_s is the final beam radius defined at the $1/e^2$ points of the intensity distribution.

This gives $\bar{d}$ = 142.3 μ m
and the resultant broadening $\backsim$ 0.32% which may be considered negligible.

APPENDIX D

CORRELATION FUNCTION in a VELOCITY GRADIENT

For a Gaussian beam system the fringe volume is an ellipsoid. The case is considered where the optical axis is perpendicular to the tube wall and the fringes are aligned in the plane perpendicular to the tube axis. The distances across the fringe volume, between the e^{-2} points on the intensity distribution are 2r and 2 σ in the direction of the tube axis and the optical axis respectively. These dimensions are related to the radii r_s of the beams at the intersection point by the expressions, $r = r_s/\cos\theta$ and $\sigma = r_s/\sin\theta$ where 2θ is the angle between the beams. In order to evaluate the shape of the count correlation function, it is first noted that, apart from the origin value, it has the same shape as the auto-correlation ($R_I(\tau)$) of the scattered light intensity (Durrani and Greated (1977)). For a Gaussian beam system the intensity variation produced by a single particle moving through the fringe pattern at constant velocity U is:-

$$I(t) = I_o \exp\left[\frac{-2(t-t_o)^2 U^2}{r^2}\right] \cos^2 \frac{\pi U t}{s} \quad - - \quad (D1)$$

Here I_o is the peak scattered intensity, t_o is the time of arrival of the particle at the centre of the

measuring volume and s is the fringe spacing. The resulting intensity auto-correlation function is Daudpota (1976) :-

$$R_I(\tau) = \frac{\nu'}{4} E\left[I_{oi}^2\right] \frac{r\sqrt{\pi}}{2U} \exp\left[-\frac{U^2\tau^2}{r^2}\right] \left[1 + \tfrac{1}{2} m^2 \cos\left(\frac{2\pi U\tau}{s}\right)\right] + \frac{\nu'^2}{4} E\left[I_{oi}\right] \frac{\pi r^2}{2U^2} \quad - - - - \quad (D2)$$

Here I_{oi} is the peak intensity for the i^{th} particle, $\nu' = E\left[n/T\right]$ and $\nu'^2 = E\left[n\,(n-1)/T\right]$, where n particles have passed the centre of the measuring region in a total time T, m is the fringe visibility and E the expectation operator. The measuring volume is assumed so small that the velocity gradient perpendicular to the wall can be regarded as linear i.e. :-

$$U = U_o + C\,y \quad - - - - \quad (D3)$$

where U_o is the velocity at the centre of the volume and C is the velocity gradient. There are assumed to be no appreciable velocity gradients in the axial and tangential directions.

For this experimental arrangement $\exp\left[-U^2\tau^2/r^2\right]$ $\backsim 1$ in equation D2 since there are a large number of

fringes within the measuring volume (147 between the e^{-2} intensity points). Also v' and v'^2 are proportional to U and U^2 respectively, for a continuous stream of particles. The probability distribution of I_{oi} is Gaussian with standard deviation $\sigma/\sqrt{2}$, hence the probability distribution of I_{oi}^2 is Gaussian with standard deviation $\sigma/2$. Thus disregarding the pedestal value the observed auto-correlation function is:-

$$E\left[R(\tau)\right] = \text{const} \times \int_{-\infty}^{\infty} e^{\frac{-4y^2}{2}} \cos(U_o + Cy)D\tau dy \qquad \text{- - - - (D4)}$$

where $D = 2\pi/s$

Infinite limits are justified by the fact that the Gaussian function dies rapidly to zero and therefore the contribution to the integral from regions outside of the flow boundaries are negligible, provided that the e^{-2} points on the intensity distribution do not extend beyond the wall.

Carrying out the integration using standard integrals (Grobner W. and Hofreiter N.1949):-

$$E\left[R(\tau)\right] = \text{const} \times \exp(-\sigma^2 C^2 D^2 \tau^2/16) \cos UD\tau \qquad \text{- - - - - (D5)}$$

and Fourier transforming equation (D5) gives the

power spectrum for the intensity as:-

$$\phi(w) = \text{const} \times \exp\left[\frac{-4(DU_o - w)^2}{C^2 D^2 \sigma^2}\right] - - - \text{(D6)}$$

i.e. the spectrum is a Gaussian with standard deviation $CD\sigma/2$.

It is seen from equations (D5) and (D6) that increasing the velocity gradient has the effect of damping the correlation function more rapidly or alternatively broadening the width of the spectrum, although the position of the peak of the spectrum is unaltered. Since D and σ are known constants for a particular optical configuration, measurement of the spectrum width gives a direct measure of the velocity gradient.

APPENDIX E

RANGE OF VALIDITY OF THE PERTURBATION SCHEME

The theory presented in this thesis ought to be valid for all values of the frequency parameter α but in practice begins to break down for $\alpha \geq 11$ due to convergence difficulties in the integrals involved in the transformation procedure. The limits of the range of validity of the amplitude parameter G are more difficult to quantify and the following guidelines were used in the analysis.

In the low frequency limit, the flow can be considered as quasi-steady and the first order equations in the small alpha expansions become equivalent to those of Dean (1928) together with appropriate time dependency. Dean investigated the stability of his scheme by considering terms up to $O\{K^3\}$, where $K \equiv \frac{G}{16}$ was his expansion parameter, in the axial velocity series, which affected the volume flow rate. By doing this he found that for $K \leq 576$, the flow rate was reduced by the curvature and an upper limit on K was established.

The scheme used in this thesis only considers the $O\{K\}$ term and in fact Dean showed that the effect of curvature on flow rate was independent of this term. Further terms would therefore have to be taken to reach the limit of Dean's expansion but due to the complexity

Figure (E1) Variation of limiting value of G with α.

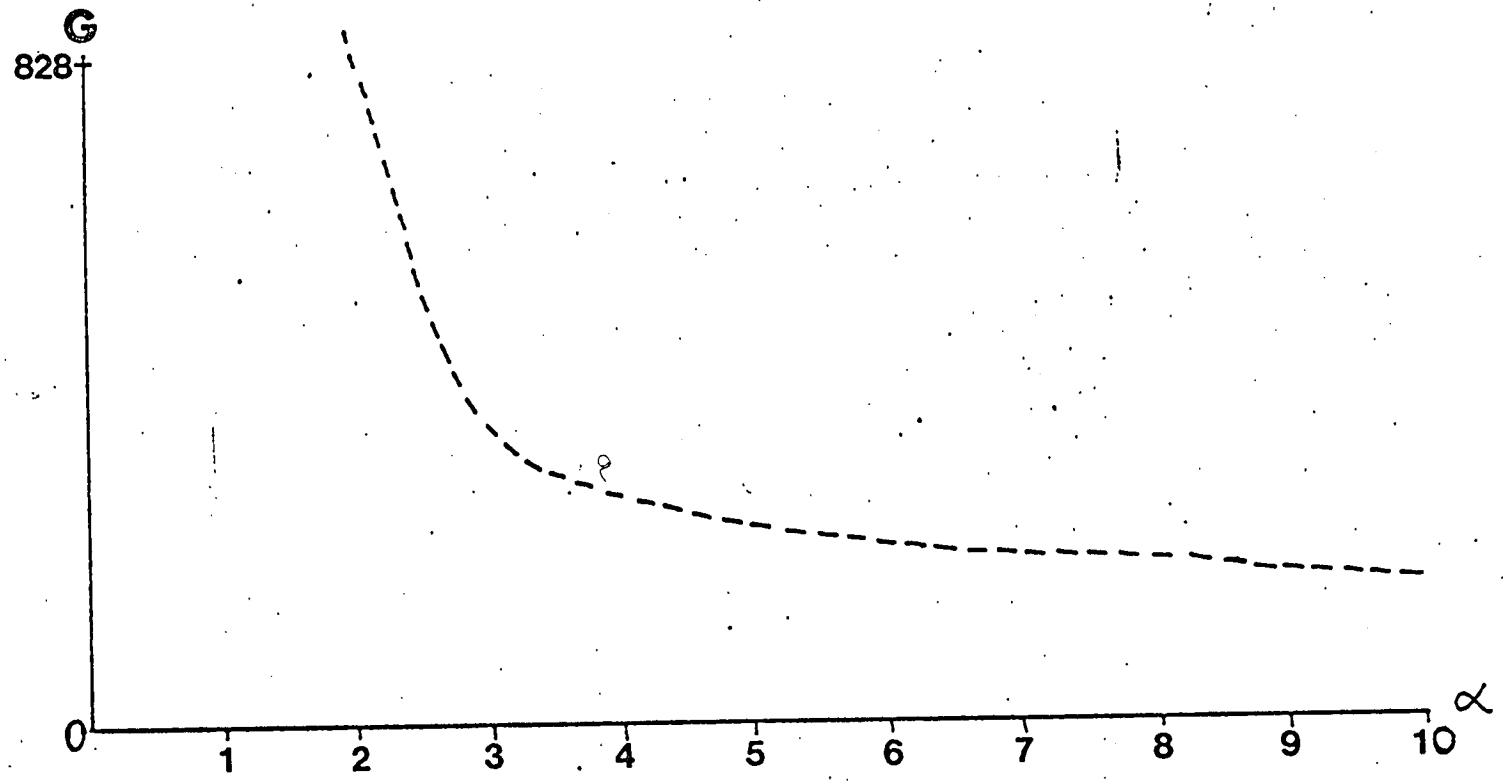

of the equations this was considered too great a task using the present transformation technique. However, as can be seen from the results presented in Chapter 4, despite this severe limitation, a reasonable agreement is found between the general flow features of the theory and experiment.

The expansion scheme used in this study of the vorticity equation goes further than the work of Dean and considers the effect of the redistribution of velocity on the secondary flow pattern. It is interesting to compare the value of ψ_{max}, the maximum value of the secondary flow stream function, with that obtained in the steady flow analysis of McConalogue and Srivastava (1968) and also the numerical work of Collins and Dennis (1976). The results taken here are from the Hankel transform solution at $\alpha = 1$ phase 0°.

	G	ψmax	G	Ψmax
McConalogue & Srivastava	9216	0.95	14607.14	1.36
Collins & Dennis	9216	0.99	——	
Present	9216	0.968	14607.14	1.21

The results indicate that in the quasi-steady limit, this expansion is probably valid up to the Dean limit.

As the curvature is considered small the flow will not be expected to differ very much from straight pipe flow and thus the relationship between $\overline{W}$, the instant-

aneous mean velocity, and the pressure gradient amplitude can be derived from the results of Uchida (1956).

$$\overline{W} = \frac{1}{\pi}\int_0^1 2\pi W' r\, dr$$

$$= \frac{K}{\omega}\left[\frac{2D}{\alpha}\cos\tau + \left(1-\frac{2C}{\alpha}\right)\sin\tau\right] - - - \quad (E1)$$

where $C = \dfrac{\text{ber}\,\alpha\ \text{bei}'\alpha - \text{bei}\,\alpha\ \text{ber}'\alpha}{\text{ber}^2\alpha + \text{bei}^2\alpha}$

$$D = \frac{\text{ber}\,\alpha\ \text{ber}'\alpha + \text{bei}\,\alpha\ \text{bei}'\alpha}{\text{ber}^2\alpha + \text{bei}^2\alpha}$$

and $\text{ber}'\alpha = \dfrac{d(\text{ber}\,\alpha)}{d\alpha}$ $\qquad$ $\text{bei}'\alpha = \dfrac{d(\text{bei}\,\alpha)}{d\alpha}$

Thus a relationship may be established for the limiting value of G over the α range of interest, using the quasi-steady limit as the starting point. This relationship is displayed graphically in Fig. (E1) and shows that as α increases so G decreases, becoming almost constant for large α values.

From the graph the expected limiting value of G when $\alpha = 10$ is 176. Putting G in the form $2\alpha^2 R_s$, this gives a value for $R_s = 0.88$, which is well within the limits imposed in the boundary layer theory of Lyne.

APPENDIX F

J. Phys. E: Sci. Instrum., Vol. 11, 1978. Printed in Great Britain

Measurement of pulsating flows by photon correlation

T Mullin and C A Greated
Fluid Dynamics Unit, Physics Department, University of Edinburgh, James Clerk Maxwell Building, The King's Buildings, Mayfield Road, Edinburgh EH9 3JZ, UK

Received 29 September 1977, in final form 2 February 1978

Abstract A photon correlation system is described which has successfully been employed to measure pulsating air flows in glass tubes down to 5 mm in diameter. A sampled version of the signal from a laser Doppler optical arrangement has been used to construct velocity profiles at different phase positions in fully reversing flows, and these agree well with theoretical predictions. Peak Reynolds numbers were of the order of 100 and the frequency range was 0·25–4·88 Hz, corresponding to flow parameters in the physiological range.

1 Introduction

The purpose of this paper is to describe a system which has been developed to generate and measure air flow velocities in very small tubes where the mean flow rate is pulsating positive and negative in a sinusoidal fashion. The system has been constructed to enable the authors to make detailed studies of air flow in models of the human bronchial system. The flow generator is in the form of two pistons which pump the air back and forth through a completely enclosed series of tubes. Velocities are measured with a laser Doppler anemometer employing a gated detector output and a photon correlation signal analyser. Laser anemometers employing photon correlation signal analysis are widely used for air flow measurement (Durrani and Greated 1977) but most applications have so far been to steady flow situations, since the correlation function gives time-averaged flow statistics. However, by gating the photodetected output so that the signal is only analysed at some predetermined phase position in each cycle, it is possible to measure time-dependent mean velocities and also the magnitudes of any velocity variations.

The flow velocities are measured by recording the frequency of the count correlation function generated by the photon correlator. Accurate estimates of this frequency are obtained by Fourier-transforming the correlation function and then noting the frequency of the spectrum peak.

In this application we are primarily concerned with measuring axial velocities in small tubes under laminar flow conditions. Thus the laser anemometer is aligned so that the optical axis is perpendicular to the wall of the tube. At right angles to the wall there are high velocity gradients and so the scattering particle velocities are a function of the distance from the wall. Velocity gradients along the axis of the tube and in the tangential direction are negligible. To assess the effectiveness of the system in measuring the correct velocities at the centre of the fringe volume under these conditions, we have evaluated an expression for the shape of the count correlation as a function of the velocity gradient perpendicular to the wall. The system has then been used to measure pulsating velocities profiles in straight tubes. From the shape of the correlations it has been possible to estimate the velocity gradients and check them against the slopes of the measured velocity profiles at the points in question. A double check is also possible for flow in a straight tube since theoretical expressions are available for evaluating the velocity profiles at different values of the parameter $\alpha = a(\omega/\nu)^{1/2}$ where a is the radius of the tube, ω the radial frequency and ν the kinematic viscosity of the fluid.

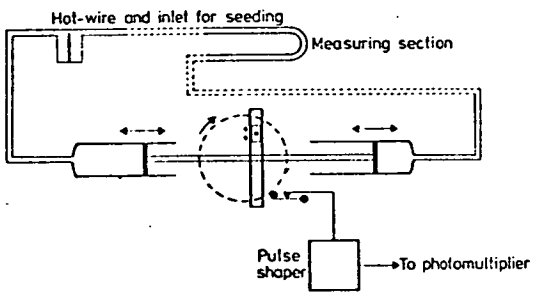

Figure 1 Layout of flow apparatus.

2 Flow inducer and sampling mechanism

The overall layout of the flow rig is indicated in figure 1. A Scotch yoke reciprocating mechanism is linked to two pistons which pump air back and forth through the model. The airways form a completely enclosed system, except that there is a facility for introducing seeding. The reciprocating mechanism itself is essentially the same as the one described by Reynolds and Hyett (1974). The frequency and amplitude of the oscillation may be readily altered by changing the speed of the driving motor and the stroke of the pistons, respectively. Since the photon correlation signal analysing system does not give a direct display of the instantaneous velocity it was found useful to have a hot-wire anemometer in the circuit to monitor instantaneous velocity. Although the hot-wire was not directionally sensitive, its output proved useful in determining the frequency of oscillation of the flow.

A major problem in measuring air velocities in glass tubes using laser anemometry is that the scattering from dust particles naturally present in air is extremely small. Although the small signals produced by the particles can easily be handled by the photon detector, they tend to be swamped by the noisy signal produced by the flare from the glass walls of the tube. This was simply overcome by introducing seeding in the form of small quantities of tobacco smoke. Since the circuit was completely enclosed, a single seeding lasted many hours. In this respect totally enclosed systems appear to offer a great advantage over open-circuit arrangements.

The optical system itself, to be described in §3, was fixed on a vibration-insulated optical table and the model was scanned across the laser beam intersection using a calibrated optical traverse. Light scattered by the seeding particles

0022-3735/78/0007-0643 $01.00

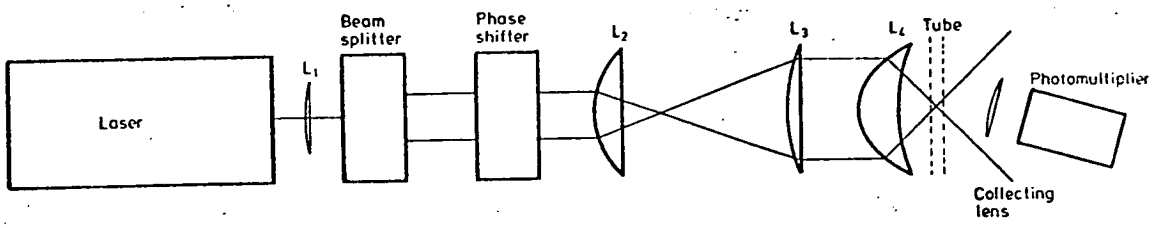

Figure 2 Laser Doppler optical system.

was collected in the forward direction using a photomultiplier fitted with a discriminator unit in order to produce a sequence of individual photon pulses. A gate circuit incorporated in the discriminator was operated by trigger pulses from switches attached to the reciprocating mechanism, so that photon pulses were only output at predetermined phase positions in the cycle. Hall effect microswitches were used for this purpose, since these produced bounce-free switching.

3 Optical system

The laser Doppler optical system used for the experiments is shown in figure 2. Its main feature is that it uses a single lens to focus the beams to the measuring point but allows a beam intersection angle in excess of 60°. A large intersection angle was important in the physiological studies in question since the measuring volume had to be kept to a minimum. Single-lens focusing is advantageous in that it greatly simplifies alignment. A Malvern Instruments beam splitter and phase shifter are employed to produce a moving fringe pattern within the measuring region, which superimposes a predetermined frequency shift on to the Doppler signal; the manner in which this frequency shift is produced is described by Foord *et al* (1974). The arrangement allows both positive and negative flow velocities to be measured.

If the Gaussian beam waists do not coincide with the intersection of the two beams, then an additional Doppler broadening arises which artificially increases the rate of damping of the count correlation function. This effect was minimised by introducing lens L_1 in front of the beam splitter. Since the phase shifter could only be used at a fixed beam separation (2 cm) and the focusing lens L_4 had a diameter of 6 cm, lenses L_2 and L_3 were used to increase the beam separation to 4·6 cm so that the maximum intersection angle could be obtained. With this arrangement we were able to obtain an intersection angle of 60° 24′ and still obtain high-quality Doppler signals. The focusing lens L_4 is an aspheric lens of focal length 3·8 cm, corrected for minimum spherical aberration (Oriel Corp., USA).

A 15 mW He–Ne laser was used for the experiments, the beam radius at the e^{-2} points on the intensity distribution being 0·55 mm. Applying the analysis of Kogelnik and Li (1966) we calculated the corresponding beam radii at the intersection point to be 0·036 mm. For an intersection angle of 60° 24′ the corresponding fringe volume length along the optical axis (Durrani and Greated 1977) was $2\sigma = 0{\cdot}144$ mm.

Using the results of Hanson (1973), we calculated the magnitude of the Doppler broadening (i.e. the standard deviation of the power spectrum/mean Doppler frequency) as 0·32%. In order to have a direct check on the extent of changes in the fringe spacing within the measuring volume the system was first used to measure the speed of a rotating Perspex disc. This was moved through the measuring volume

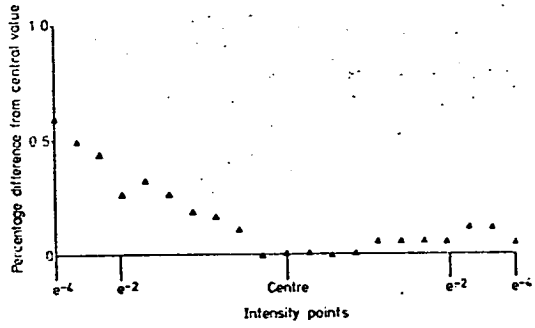

Figure 3 Variation of Doppler frequency across fringe volume.

with a precision optical traverse and measurements of the Doppler frequency were recorded at different spatial positions. Figure 3 shows the variation of Doppler frequency across the measuring volume. These results are qualitatively consistent with the predictions of Hanson (1973), since the magnitude of the Doppler signal falls rapidly towards the edge of the volume and effectively disappears beyond the e^{-4} points on the intensity distribution. However, it appears from figure 3 that the fringe volume is slightly distorted on the side closest to the lens.

4 Correlation function in a velocity gradient

For a Gaussian beam system the fringe volume is an ellipsoid. We consider the case where the optical axis is perpendicular to the tube wall and the fringes are aligned in the plane perpendicular to the tube axis. The distances across the fringe volume, between e^{-2} points on the intensity distribution, are $2r$ and 2σ in the directions of the tube axis and the optical axis, respectively. These dimensions are related to the radii r_s of the beams at the intersection point by the expressions $r = r_s/\cos\theta$ and $\sigma = r_s/\sin\theta$ where θ is the half-angle between the beams. To evaluate the shape of the count correlation function we first note that, apart from the origin value, it has the same shape as the autocorrelation function $R_I(\tau)$ of the scattered light intensity (Durrani and Greated 1977). For a Gaussian beam system the intensity variation produced by a particle moving through the fringe pattern at constant velocity u is

$$I(t) = I_0 \exp\left(\frac{-2(t-t_0)^2u^2}{r^2}\right)\cos^2\frac{\pi u t}{s}.$$

Here I_0 is the peak scattered intensity, t_0 is the time of arrival of the particle at the centre of the scattering volume and

s is the fringe spacing. The resulting intensity autocorrelation function is (Daudpota 1976)

$$R_I(\tau)=\frac{\nu}{4}E(I_{0i}^2)\frac{r\sqrt{\pi}}{2u}\exp\left(\frac{-u^2\tau^2}{r^2}\right)\left(1+\tfrac{1}{2}m^2\cos\frac{2\pi u\tau}{s}\right)+\frac{\nu^2}{4}E(I_{0i})\frac{\pi r^2}{2u^2}. \quad (1)$$

Here I_{0i} is the peak intensity for the ith particle, $\nu=E(n/T)$ and $\nu^2=E[n(n-1)/T]$, where n particles have passed the centre of the measuring region in a total time T, m is the fringe visibility and E the expectation operator. The measuring volume is assumed to be so small that the velocity gradient perpendicular to the wall can be regarded as linear, i.e.

$$u=u_0+Cy$$

where u_0 is the velocity at the centre of the measuring volume and C is the velocity gradient. There are no velocity gradients in the axial and tangential directions.

For our experimental arrangement $\exp(-u^2\tau^2/r^2)\approx 1$ in equation (1) since there are a large number of fringes within the measuring volume (147 between the e^{-2} intensity points). We also note that ν and ν^2 are proportional to u and u^2, respectively, for a continuous stream of particles. The probability distribution of I_{0i} is Gaussian with standard deviation $\sigma/\sqrt{2}$; hence the probability distribution of I_{0i}^2 is Gaussian with standard deviation $\sigma/2$. Thus, disregarding the pedestal value, the observed autocorrelation function is

$$E(R(\tau))=\text{constant}\times\int_{-\infty}^{\infty}\exp(-4y^2/\sigma^2)\cos[(u_0+Cy)D\tau]\,dy$$

where $D=2\pi/s$. Infinite limits are justified by the fact that the Gaussian function dies rapidly to zero and therefore the contribution to the integral from regions outside the flow boundaries is negligible, provided that the e^{-2} point on the intensity distribution does not extend beyond the wall.

Carrying out the integration we find (Grobner and Hofreiter 1949)

$$E(R(\tau))=\text{constant}\times\exp(-\sigma^2C^2D^2\tau^2/16)\cos uD\tau, \quad (2)$$

and Fourier-transforming equation (2) gives the power spectrum for the intensity as

$$\phi(\omega)=\text{constant}\times\exp\left(\frac{-4(Du_0-\omega)^2}{C^2D^2\sigma^2}\right), \quad (3)$$

i.e. the spectrum is Gaussian with standard deviation $CD\sigma/2$.

It is seen from equations (2) and (3) that increasing the velocity gradient has the effect of damping the correlation function more rapidly or alternatively broadening the width of the spectrum, although the position of the spectrum peak is not altered. Since D and σ are known constants for a particular optical configuration, measurement of the spectrum width gives a direct measure of the velocity gradient.

5 Analysis of correlograms

The correlograms obtained in the experiments were analysed by direct cosine Fourier transformation, i.e. the power spectra were computed from the relationship

$$\phi(f)=R(0)T+2T\sum_{s=1}^{m}R(sT)\cos 2\pi fsT \qquad f\leq\tfrac{1}{2}T$$

where sT is the time lag for channel number s and m is the total number of correlation lags.

This method is particularly simple to apply and it has been found that it leads to accurate determinations of both the peak frequency and the variance (Daudpota 1976), provided that the correlogram has decayed to effectively a constant level within the range of the channels available (in our case 48). A suitable decay rate can easily be achieved by choosing an appropriate optical phase shift. If a fast Fourier transform had been employed it would have necessitated extending the correlation function to 64 channels, which would have yielded 32 Fourier coefficients. The cosine transformation, on the other hand, yields 48 coefficients directly. Since the zero value of the count correlation function is not proportional to the mean square intensity, this value is disregarded in the transformation. Instead, the value of $R(0)$ is set to be just greater than max $|R(sT)|$. The precise value chosen is unimportant since it only introduces a constant pedestal level into the spectrum.

If the transformation technique just described is used together with a peak detection routine, computer-constructed mean velocity plots may readily be obtained. A typical computation time on the IBM 370 computer for a mean velocity profile was 45 s.

6 Experimental results

Although the system was intended for the study of flow in bends and bifurcations, preliminary experiments were carried out for pulsating flow in straight tubes, since there are proven theoretical results for the velocity profiles in this case. The axial velocity profile at any given phase position is a function of the parameter α^2 which may be interpreted either as an oscillating Reynolds number or as the ratio of a characteristic diffusion time $a^2\nu^{-1}$ to a characteristic oscillation time ω^{-1}. For small α, the flow is quasi-steady and for large values the flow is frequency-dominated. Two sets of measurements are presented here for different glass tubes and different values of α.

The first set of measurements was made in a tube of internal diameter 5 mm at a frequency parameter of $\alpha=0{\cdot}83$ and a peak Reynolds number of 96. At this low frequency the velocity profile can be considered quasi-steady and should therefore be parabolic in form. Figure 4 shows the experimental profiles at three phase positions in the cycle, 0, 30 and 180°, the 0 and 180° profiles representing the maximum velocity in the two directions. The parabolic form is easily seen. As a double check on the validity of the results, particularly in regions of high velocity gradient, the widths of the transformed spectra were measured and the velocity gradients calculated by applying the theoretical predictions detailed in section 4. In regions close to the wall the predicted and measured gradients agreed to as close as 1 %.

The second set of measurements was made in a tube of internal diameter 6·2 mm at a frequency parameter of $\alpha=4{\cdot}36$ and a peak Reynolds number of approximately 100. At this higher frequency the profiles are expected to deviate considerably from the quasi-steady parabolic form. An analytical solution of the Navier–Stokes equation has been given by Uchida (1956) which covers this case. He shows that the axial velocity $u(r, t)$ at time t and radial distance r from the centre of the tube for a pressure gradient $K\cos\omega t$ is

$$u(r,t)=(Ka/\omega\nu)[B\cos\omega t+(1-A)\sin\omega t], \quad (4)$$

where

$$B=\frac{\text{bei}\,\alpha\,\text{ber}\,\alpha r-\text{ber}\,\alpha\,\text{bei}\,\alpha r}{\text{bei}^2\,\alpha+\text{ber}^2\,\alpha}$$

and

$$A=\frac{\text{ber}\,\alpha\,\text{ber}\,\alpha r+\text{bei}\,\alpha\,\text{bei}\,\alpha r}{\text{bei}^2\,\alpha+\text{ber}^2\,\alpha}$$

where a is the tube radius, K the maximum pressure gradient

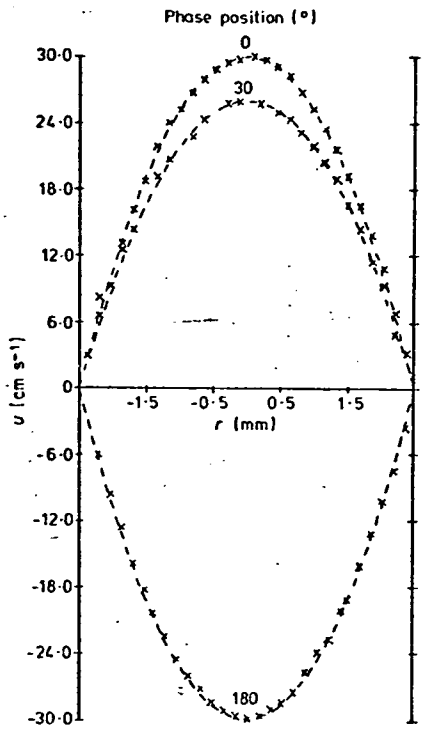

Figure 4 Velocity (u) profiles measured in 5 mm diameter tube, where r is the distance from the centre line.

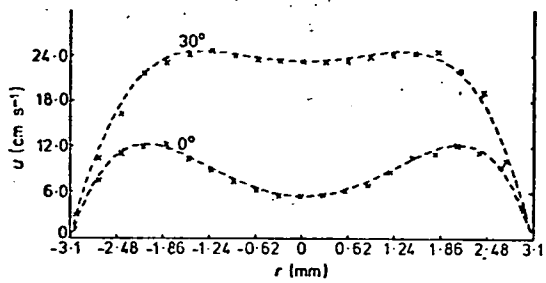

Figure 5 Velocity (u) profiles in 6·2 mm tube. × Measured points; broken curve as predicted by equation (4). r is the distance from the centre line.

and ber and bei are Kelvin functions. Figure 5 shows measured velocity profiles across the tube at phase positions of 0 and 30°, and also the profiles predicted by equation (4) for comparison. It is seen that the agreement is good.

7 Conclusions

The single-lens laser Doppler system, in conjunction with the sampled photon correlation method of signal analysis, is seen to give very reliable velocity profile measurements for pulsating air flows in glass tubes down to 5 mm in diameter. The arrangement is being used by the authors to study pulsating flow patterns in bends and bifurcations and other geometries of physiological significance. Theoretical predictions of flow patterns are less well established in these cases. Measurements have also been made by the authors in a tube of 3·5 mm diameter and the system appears to work well. It is possible that, with care, velocity profiles in tubes down to 2 mm diameter could be obtained.

Acknowledgments

The authors wish to acknowledge the assistance of Mr D Molyneux, who constructed most of the flow apparatus. Mr T Mullin is financially supported by the Science Research Council.

References

Daudpota Q I 1976 Estimation of flow parameters using laser anemometry
PhD Thesis Edinburgh University

Durrani T S and Greated C A 1977 *Laser Systems in Flow Measurement* (New York: Plenum)

Foord R, Harvey A F, Jones R, Pike E R and Vaughan J M 1974 A solid-state electro-optic phase modulator for laser doppler anemometry
J. Phys. D: Appl. Phys. 7 L36–9

Grobner W and Hofreiter N 1949 *Integraltafel* vols I, II (Wien: Springer)

Hanson S 1973 Broadening of the measured frequency spectrum in a differential laser anemometer due to interference plane gradients
J. Phys. D: Appl. Phys. 6 164–71

Kogelnik H and Li T 1966 Laser beams and resonators
Appl. Opt. 5 1550–67

Reynolds J A and Hyett A W 1974 A simple sine wave pressure generator
J. Phys. E: Sci. Instrum. 7 166–7

Uchida S 1956 The pulsating viscous flow superposed on the steady laminar motion of incompressible fluid in a circular pipe
Z. Angew. Math. Phys. 2 403–22

APPENDIX G

Measurement of Oscillatory Flow in Small Tubes using the Photon Correlation Technique

by

T. Mullin and C.A. Greated

Department of Physics, University of Edinburgh, U.K.

ABSTRACT

The application of photon-correlation methods to the measurement of oscillatory air flows in small diameter tubes is described. It is shown that with a laser Doppler optical arrangement in the forward scatter mode, a sampled version of the signal may be used to obtain instantaneous velocity measurements in fully reversing flows.

With a single aspheric converging lens sufficient spatial resolution is obtained to enable velocity profiles to be measured in tubes ranging in diameter from 3.5 mm to 6.0 mm. Peak Reynold's numbers ~ 100 at a frequency of 0.25 Hz which correspond to parameters associated with the middle airways of the lung, are thus easily obtained.

Experimental results are shown for both straight and curved tubes of varying radii of curvature and a description will also be given of ongoing experimental work.

PROC. OF "PHOTON CORRELATION TECHNIQUES IN FLUID MECHANICS", CAMBRIDGE 1977.

1. INTRODUCTION

Air flow, in model bronchial bifurcations has been studied by Olsen (1971) using large models and hot-wire instrumentation. However, the large models used presented great practical difficulties when measurements at realistic Reynolds numbers were attempted. Also the measurements were all made in steady flow conditions.

A technique has now been developed, using photon-correlation anemometry, which enables studies of pure oscillatory air motion in small diameter tubes to be made. Using a gated version of the signal from the output of the photomultiplier, "instantaneous" velocity profiles may be obtained at predetermined points in a cycle.

Reynolds numbers in the range 0 - 200 are readily obtained in the frequency range 0.25 - 5 Hz and thus bronchial parameters are satisfactorily simulated.

2. PUMPING ARRANGEMENT

As shown in diagram (1) the basis of the pumping system is a scotch yoke which provides a sinusoidal flow. The frequency of oscillation may be readily altered by changing the speed of the motor driving the system. Also the amplitude of oscillation, and thus the peak Reynolds number, may be changed by adjusting the stroke of the piston.

An advantage of using this system is that it is totally enclosed and thus any seeding which may be required is directly controlled and also remains in the system for a considerable amount of time. This second point is important here since each correlation function takes 2 - 3 minutes to build up.

The function of the hot-wire in the system is to indicate the peaks of the flow cycle and thus give a check on the sample point position.

Using a simple rotary switch with all contacts removed except one,

a pulse is derived as shown schematically in diagram (1). This pulse is used to switch the output of the photomultiplier on for a pre-determined part of a cycle such that "instantaneous" velocity measurements are made.

3. OPTICAL MEASURING SYSTEM

The optical system consisted of a 15 mW He-Ne laser with a Malvern Instruments beam splitter. The two beams through a Malvern type K9023 phase modulator which has a fixed separation of 2 cm. The beam spacing was expanded to 4.6 cm using a telescope-type arrangement consisting of a 13 cm focal length lens followed by a 30 cm focal length lens. Compensation for the expansion of each individual beam was obtained by use of a 25 cm focal length lens placed in front of the beam splitter.

The beams were made to intersect by use of a 3.8 cm focal length aspheric lens (F/No. 0.55) corrected for minimum spherical aberration. This gave a beam intersection angle of 60^{o}. Using the laser beam propagation theory of Kogenlik (1966) the measuring volume was calculated to be 145 μm at the $1/e^{2}$ intensity points with 147 "fringes" contained in the measuring volume.

Scattered light was collected in the forward scattering direction using a collecting lens which focussed the measuring volume region on to the front of a photomultiplier tube. A 200 μm pinhole was placed in front of the P.M.T. in order to reduce flare which occurred especially near side walls of the measuring tube.

The optical system was kept stationary throughout each experiment and the tube was moved relative to this on a precision optical table graduated in 0.01 mm steps. In this way velocity profiles could be obtained.

Optical alignment problems were minimised using the above single lens system but several checks had to be made on the system before its reliability was accepted.

According to Hanson (1973) if the intersecting beams do not cross at their Gaussian waists then the "fringes" formed will be unequally spaced across the fringe volume. Using the formula he derived, the value for the broadening in this case came out to be ~ 0.4%.

In order to verify this a simple experiment was carried out which involved moving a rotating perspex disc through the "fringe" volume and noting any change in velocity measured. The result was that the volume appeared to be distorted towards one edge giving an error of ~ 0.5% but that was outside the 1/e limits where the signal strength is low.

4. DATA COLLECTION AND ANALYSIS

The correlograms obtained on the Malvern correlator are automatically stored on a PDP 8 computer. At the end of each experimental session the data is transferred to a IBM 370 computer where each correlogram is transferred using a direct cosine Fourier transform and an interpolation procedure is used to obtain the mean velocity. The computation time involved to obtain a mean velocity profile plot of 20 points is of the order 45 seconds.

As mentioned previously the effect of the velocity gradient is to broaden the spectrum obtained. Thus velocity gradient information may be obtained from the width of the spectrum of those correlograms which have decayed within the 48 channels of the correlation. The velocity gradients measured in this way were within the calculated value to better than 1%, a further indication of the quality of the "fringes" produced in the measuring volume.

5. RESULTS

A few results are now presented which give an indication of the type of information which may be obtained using the above system.

The first profiles, Diagram 2, were taken in a straight tube of

inside diameter 5 mm, at Re. No. 96 (peak) at a frequency of 0.25 Hz. The two profiles are taken at the 60° and 90° phase positions in a cycle and as predicted by Uchida (1956) the flow is quasi-steady. The dashed line indicates true Poiseulle flow and the crosses experimental points.

The velocity contour plot,Diagram 3, is constructed from 6 profiles taken at 30° intervals around the tube. A 3.5 mm curved tube was used here with radius of curvature 1/50, Re. No. 110, frequency 0.25 Hz and taken at phase position 30°, 90° around the bend. The nett effect is that the contours are distorted slightly towards the outside of the bend as is expected. The odd shape in the centre of the plot is repeatable and appears to rotate with changing phase position.

The final sequence of profiles, Diagrams 4-6, were taken in at 6 mm diameter curved tube with radius of curvature 1/7. The frequency of oscillation was 5 Hz with Re. No. = 186 (peak). The peak of the profile at 30° phase is at the inside of the curve working its way towards the middle at 90° phase and finally towards the outside later on in the cycle. Inward centrifuging effects have been predicted theoretically by Lynne (1970) but the frequency parameters quoted in his theory are just outside the range of this experiment. Further work is being carried out in this field.

6. CONCLUSIONS

It has been shown that, using a relatively simple single lens optical system, high quality results may be obtained from the measurement of air velocities in small diameter tubes using photon-correlation anemometry.

ACKNOWLEDGEMENTS

We would like to thank Mr. A.D. Molyneux for his work and inventiveness in constructing the apparatus described above.

Mr. T. Mullin is financially supported by the Science Research Council.

REFERENCES

1. Olsen, D.E. (1971) Ph. D. Thesis, University of London.

2. Kogenlik, H. Li, T., Applied Optics, 5, 10, 1550-1567 (1966).

3. Hanson, S. (1973) J. Phys. D.: Appl. Phys., 6, 164-171, 2.13.

4. Uchida, S. (1956) Z. Agnew. Math. Mech. 7, 403.

5. Lynne, W.H., (1970) J. Fluid Mech. 45, 1, 13-31.

PUMPING ARRANGEMENT

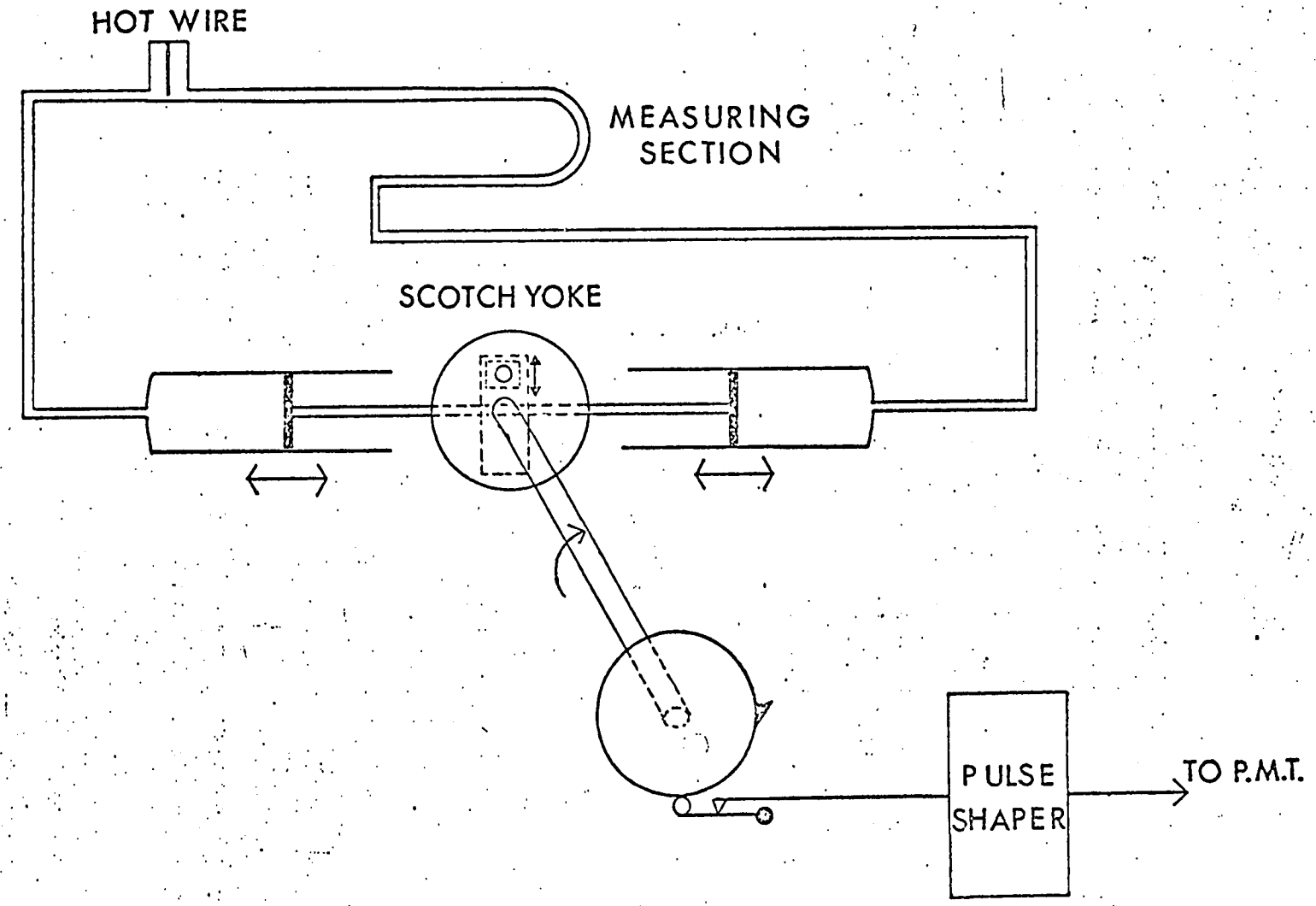

DIAGRAM 2

Velocity Profiles for 5 mm tube

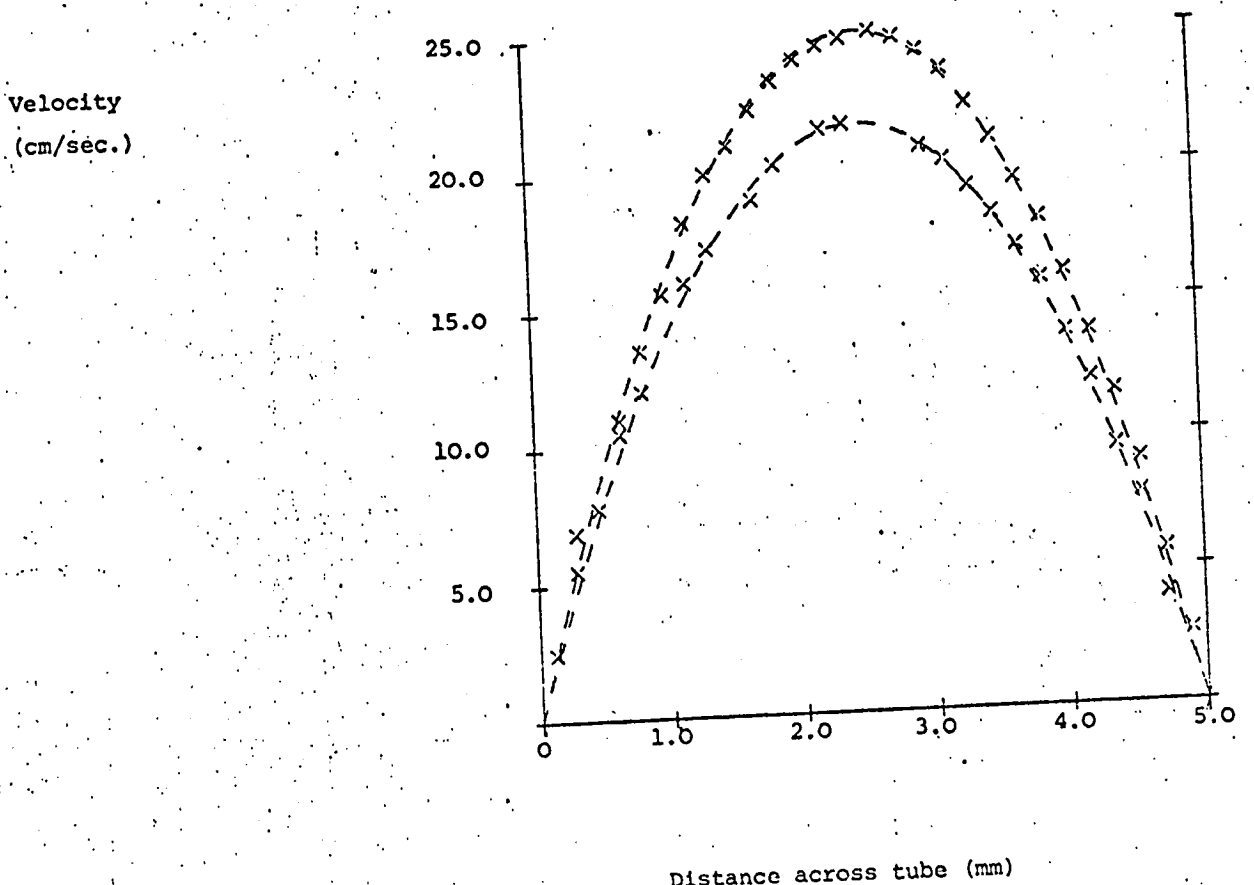

VELOCITY CONTOUR PLOT

R_c=1/50

Re=110

β =2·6

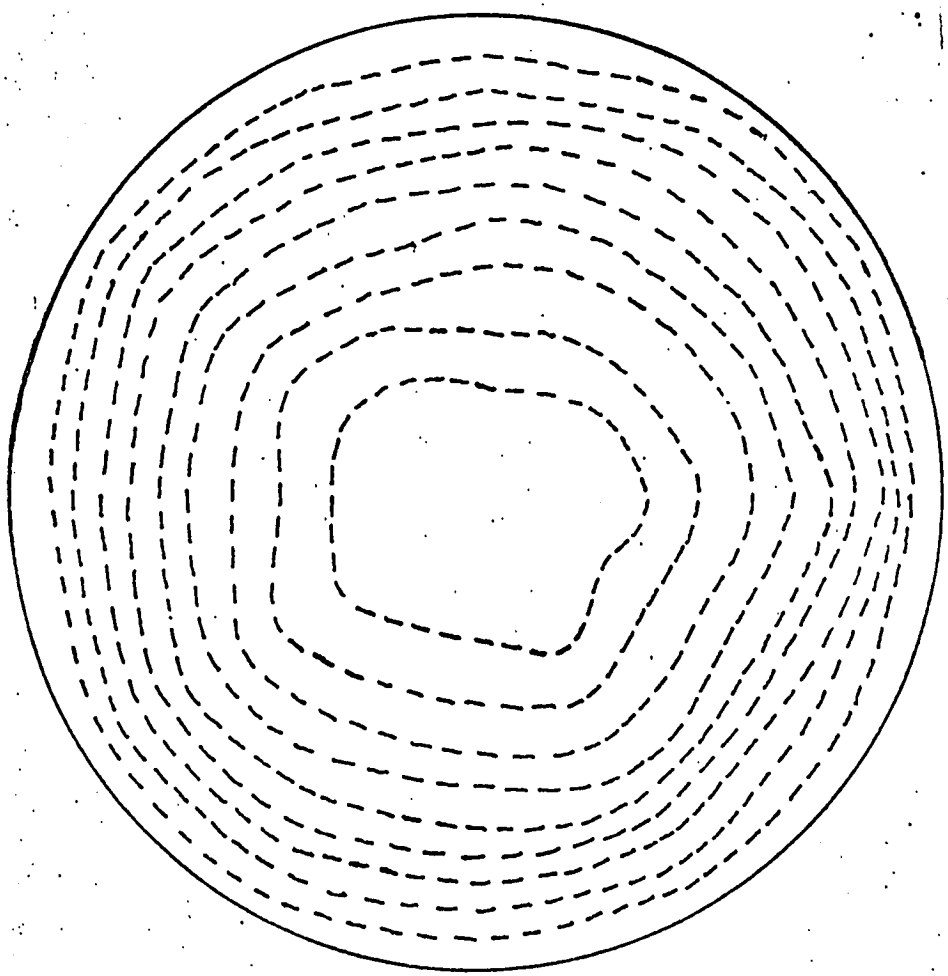

OUTSIDE

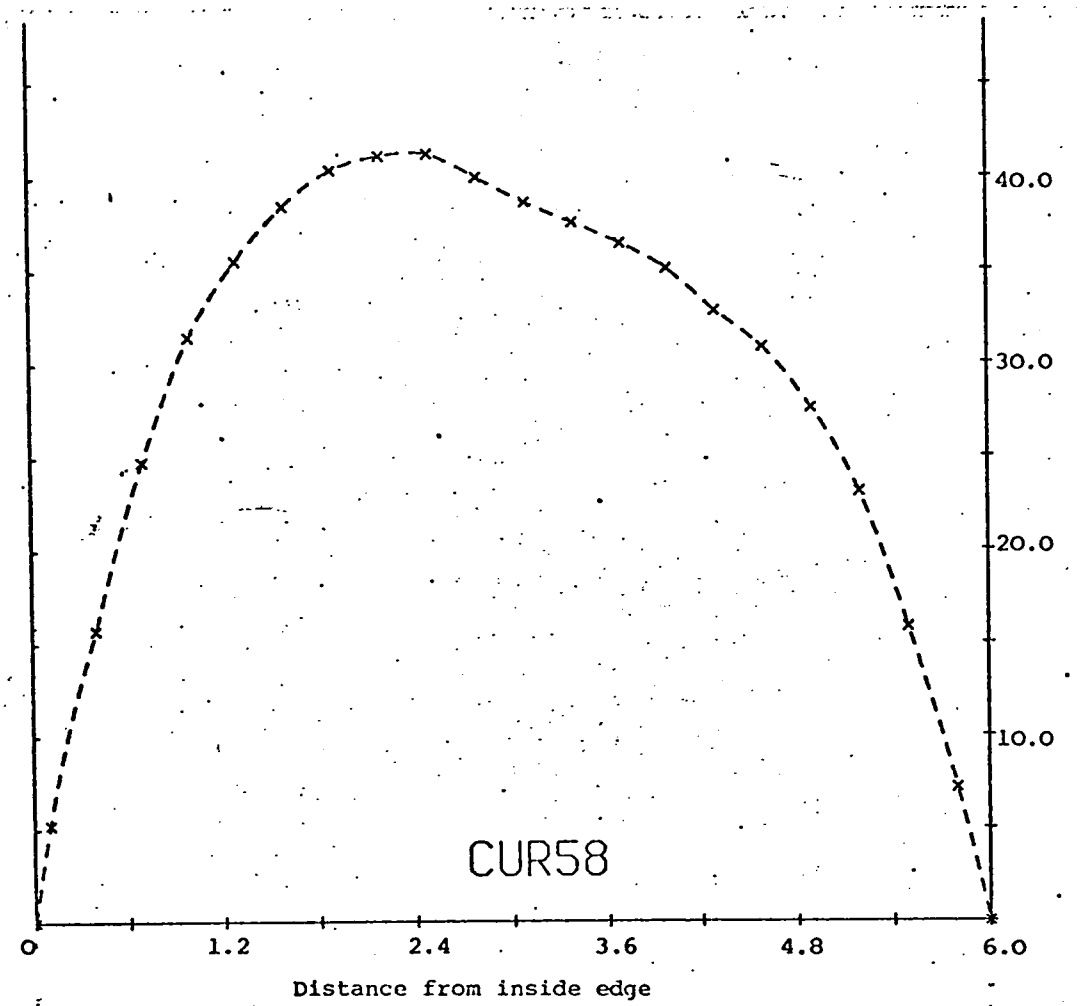
40.0
30.0
20.0
10.0
Velocity
(ms/sec.)
CUR58
0
1.2
2.4
3.6
4.8
6.0
Distance from inside edge

DIAGRAM 4

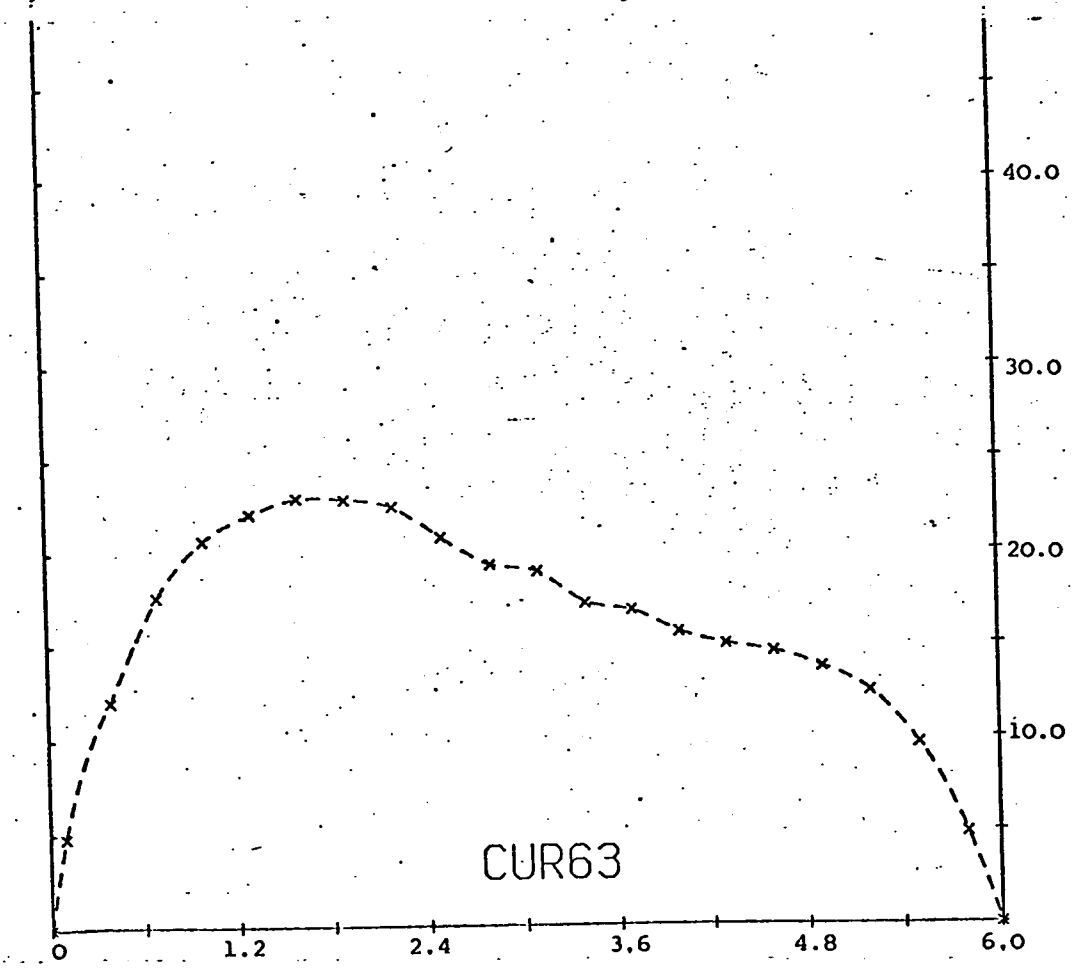
40.0
30.0
20.0
10.0
Velocity
(ms/sec.)
CUR63
0
1.2
2.4
3.6
4.8
6.0

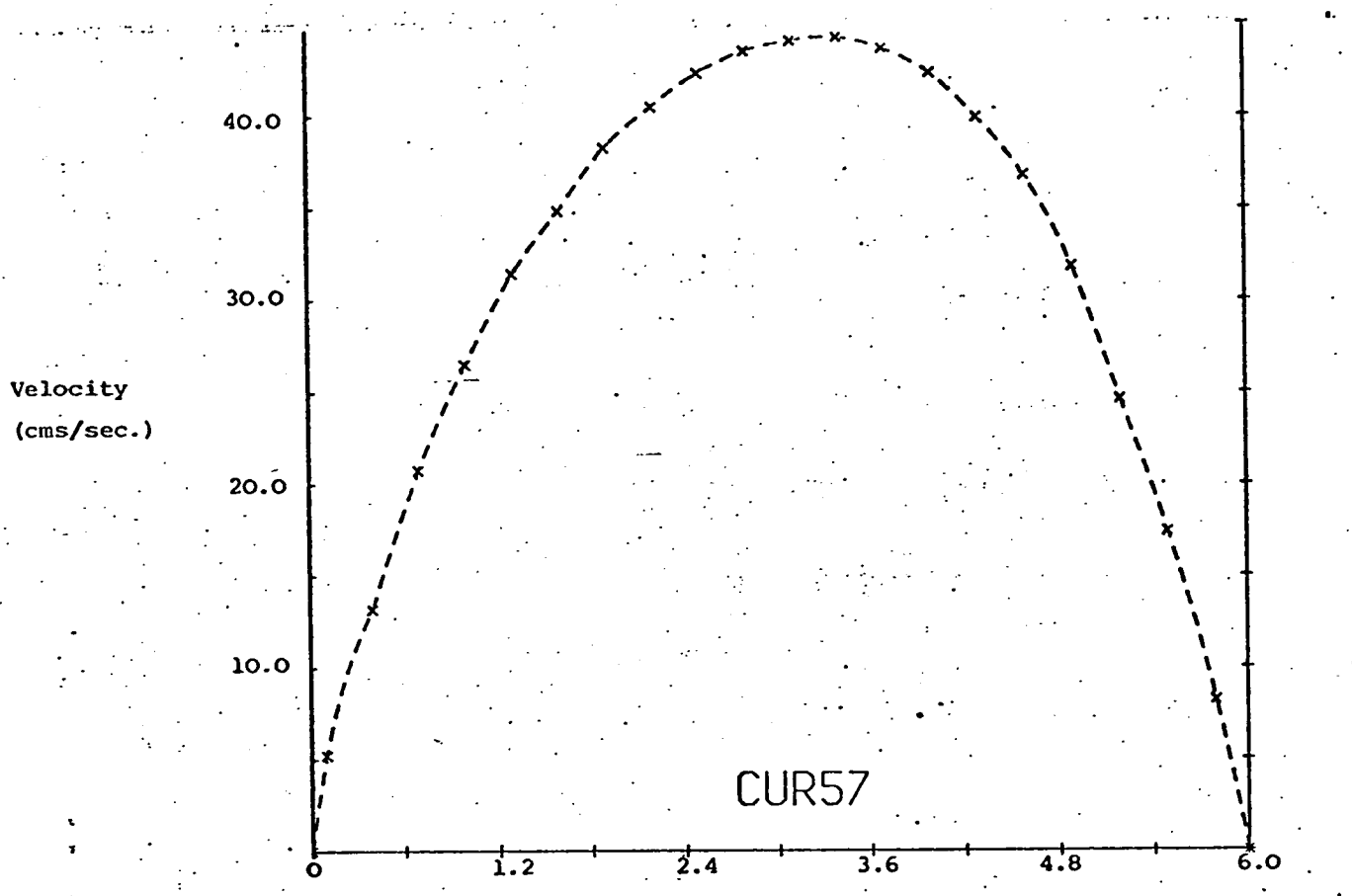
Velocity
(cms/sec.)
40.0
30.0
20.0
10.0
CUR57
0
1.2
2.4
3.6
4.8
6.0
Distance from inside edge

DIAGRAM 5

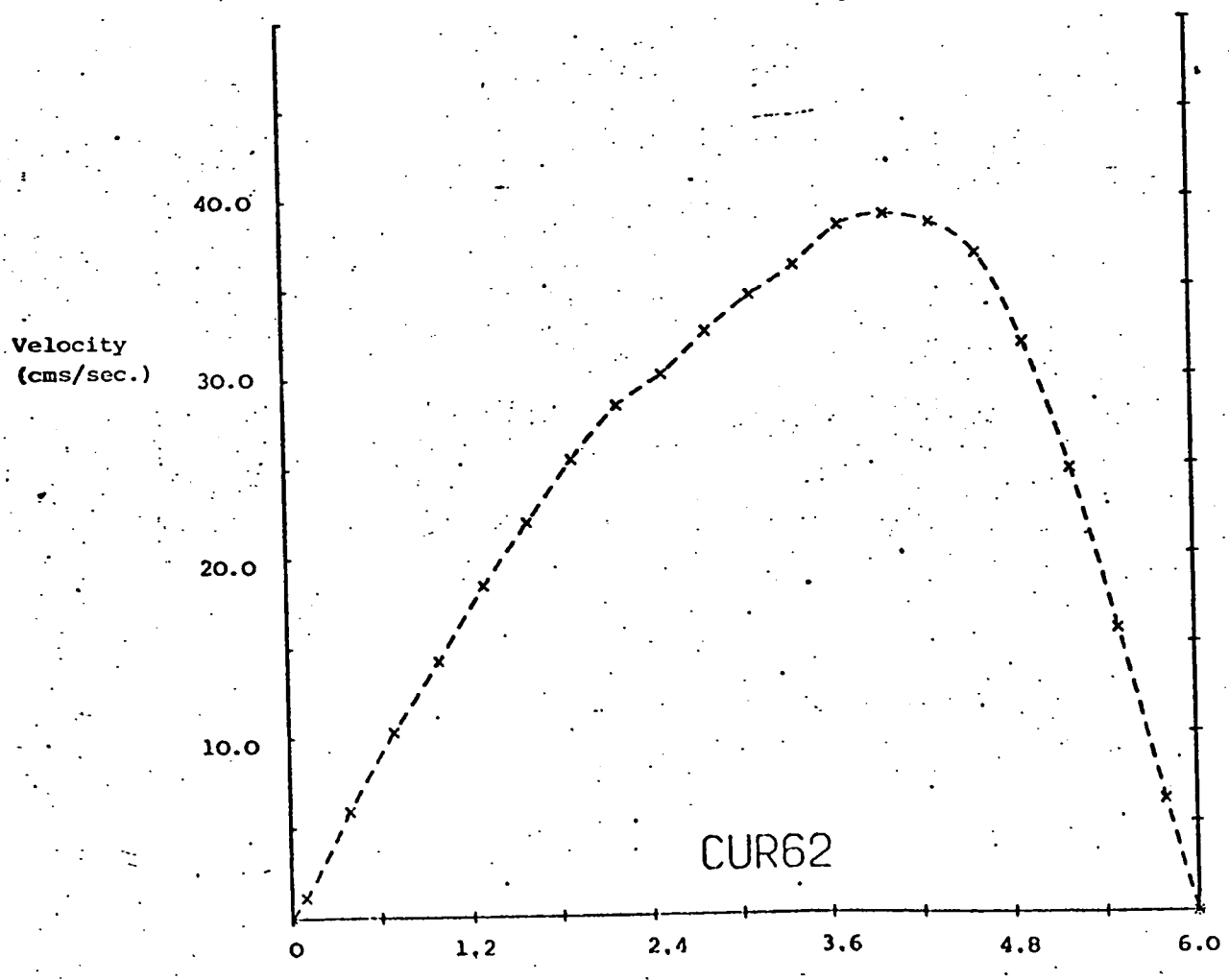
Velocity
(cms/sec.)
40.0
30.0
20.0
10.0
CUR62
0
1.2
2.4
3.6
4.8
6.0

DIAGRAM 6

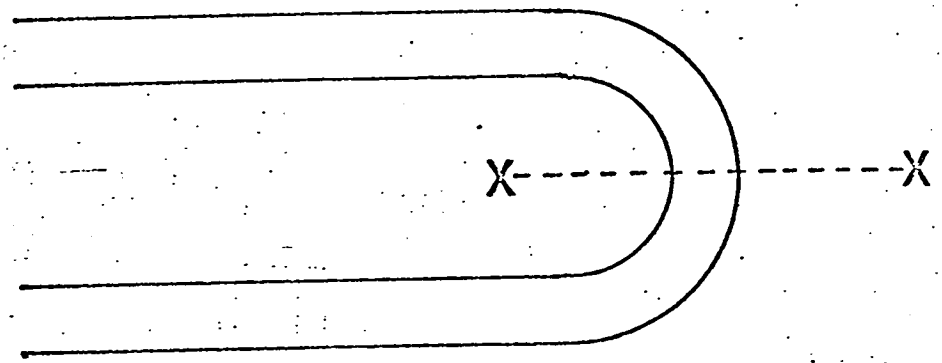

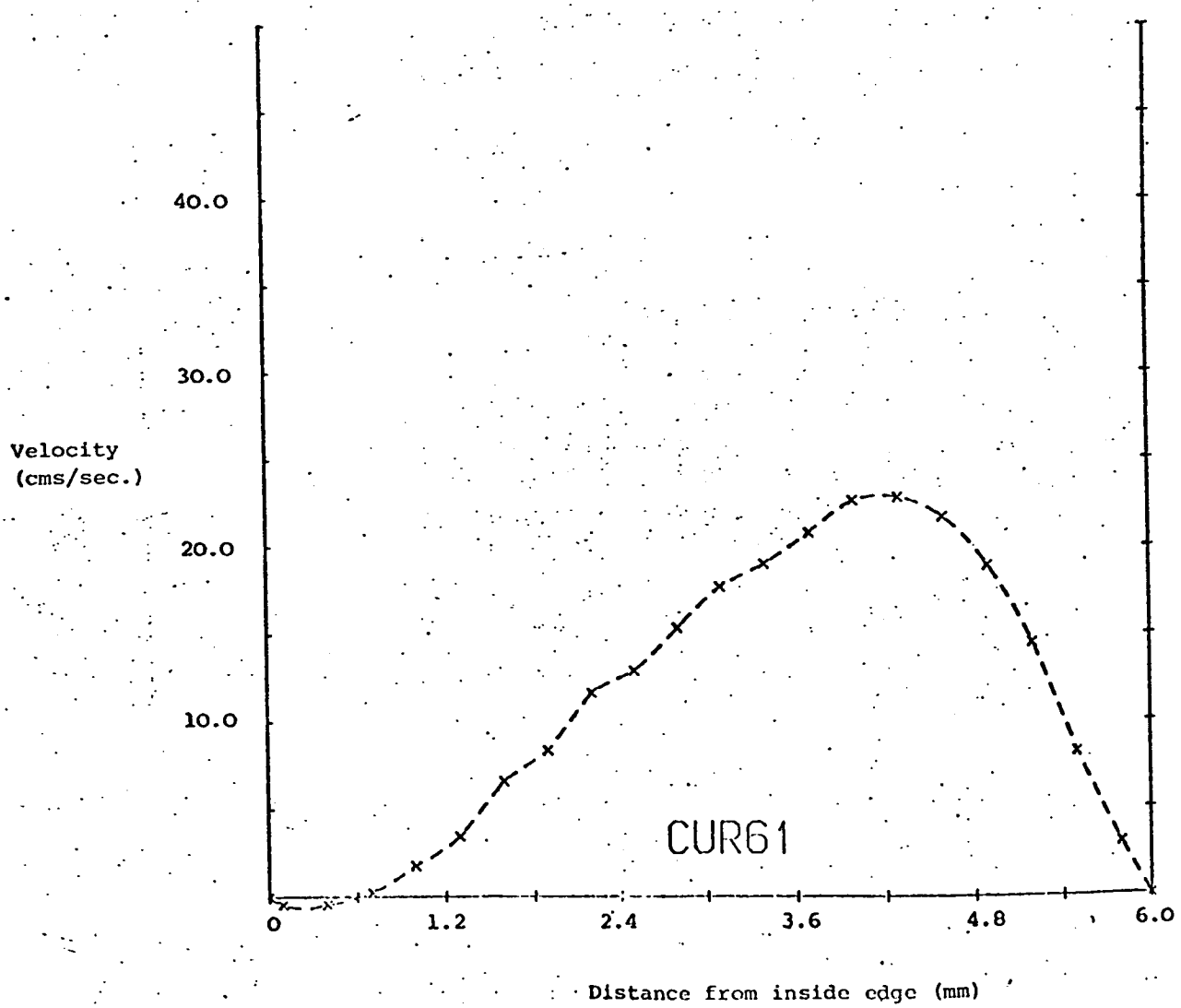
40.0
30.0
Velocity
(cms/sec.)
20.0
10.0
CUR61
0
1.2
2.4
3.6
4.8
6.0
Distance from inside edge (mm)

NOTATION

This section contains a list of notation used throughout the thesis. The appendices contain some additional symbols and these are defined as they are used within each appendix.

A	$\dfrac{\text{bei}_2\alpha\ \text{bei}_2'\alpha\ r + \text{ber}_2\alpha\ \text{ber}_2'\alpha\ r}{\text{bei}_2'\alpha + \text{ber}_2'\alpha}$
B	$\dfrac{\text{bei}_2\alpha\ \text{ber}_2'\alpha\ r - \text{ber}_2\alpha\ \text{bei}_2'\alpha\ r}{\text{bei}_2'\alpha + \text{ber}_2'\alpha}$
C_o, C_{2R}, C_{2I}	radial functions associated with the Hankel transform solution of the first order secondary flow equation
D	amplitude parameter used by McConalogue and Srivastava (1968) $D = 4\sqrt{K}$
$D_{1R}, D_{1I}, D_{3R}, D_{3I}$	radial functions associated with the Hankel transform solution of the first order axial velocity perturbation equation
D_{No}	Dean number of flow $= Re\sqrt{\frac{a}{R}}$, when quoted as peak D_{No} this means that it is based on the maximum value of the instantaneous mean velocity
$\bar{F}(\xi_j)$	finite Hankel transform of the function F(r)
F_n	radial function number n associated with the small α approximation of equations

G	Amplitude Parameter = $\frac{2 K' a^3}{R \nu^2 \omega^2}$
$H_{20I}, H_{22R}, H_{22I}$ H_{24R}, H_{24I}	radial functions associated with the Hankel transform solution of second order secondary flow equations
I_n	definite integral number n, each one is defined in the text.
$J_\mu(x)$	Bessel function of order μ
$J'_\mu(x)$	$\frac{d J_\mu(x)}{dx}$
K	Dean expansion parameter
K'	Amplitude of applied pressure gradient
P	Pressure
R	radius of curvature of curved tube
R_s	Reynolds number of the steady component of the secondary flow
Re.	Reynolds number of flow = $\frac{\bar{w} d}{\nu}$
Re [ ]	real part of function enclosed in brackets
R (sT)	correlation lag value
R (Z)	radius of curvature of wavefront of laser beam at distance Z from the beam waist
S_n	summation number n, each one is defined in the text
T	time
U'	r component of secondary flow

V'	ϕ component of secondary flow
W'	axial velocity
W_o	maximum value of the amplitude of instantaneous mean velocity

- - - - -

a	radius of the tube
ber (x), bei(x)	real and imaginary Kelvin's functions
ber′ (x), bei′(x)	$\frac{d(\text{ber}(x))}{dx}$, $\frac{d(\text{bei}(x))}{dx}$
d	pipe diameter
$\bar{d}$	fringe volume length
e	Napierian logarithm base
f	stream function
f_o	Doppler difference frequency
f_n	focal length of lens n
g(r)	radial function of straight pipe equation
r	non-dimensional radial co-ordinate = $\frac{r'}{a}$
r'	radial co-ordinate
r_s	beam radius defined at the $\frac{1}{e^2}$ points of the intensity distribution
t	time
w	non-dimensional axial velocity = $\frac{W'\omega}{K'}$
w_o, w_1	straight pipe and first order axial velocity component

$\bar{w}$ mean velocity

- - - -

α frequency parameter of flow = $a\sqrt{\frac{\omega}{\nu}}$

β frequency parameter of Lyne (1970) = $\frac{\sqrt{2}}{\alpha}$

θ half angle between intersecting laser beams

θ' angular distance around curved tube

λ wavelength

ν kinematic viscosity

ρ density

τ non-dimensional time = ωt

ϕ angular co-ordinate within pipe

ψ non-dimensional stream function = $\frac{f}{\nu}$

ψ_1, ψ_2 first and second order secondary flow stream functions

$\Phi(f_o)$ power spectral function

ω angular frequency of flow

ω_o angular Doppler difference frequency

χ scaled variable associated with Stokes layer in boundary layer approximation = $\frac{\alpha}{\sqrt{2}}(1-r)$

ξ_j jth eigen value of the equation $J_1(\xi_j) = 0$

ξ'_j jth eigen value of the equation $J_2(\xi'_j) = 0$

REFERENCES

ADLER,M.1934,"Stromungin Gekrummten Rohren",Z.Ang.Math. Mech.,PP 257-275.

AGRAWAL,Y.,TALBOT,L. and GONG,K.,1978,"Laser anemometer study of flow development in curved circular pipes", J.Fluid Mech.,Vol.85,PT.3,PP 497-518.

BARUA,S.N.,1963,"On secondary flow in stationary curved pipes",J.Mech.Appl.Math.,16,61-77.

BATCHELOR,G.K.,1967,"An introduction to Fluid Dynamics", Cambridge University Press.

BERTELSEN,A.F.,1975,"An experimental investigation of low Reynolds number secondary streaming effects associated with an oscillating viscous flow",J.Fluid Mech.,Vol.70, PT.3,PP 519-527.

COLLINS,W.M. and DENNIS,S.C.R.,1975,"The Steady Motion of a Viscous Fluid in a Curved Tube",Q.Jnl.Mech.Appl.Math. Vol.28,PT.2,PP 133-156.

DAUDPOTA,Q.I.,1976,"Estimation of flow parameters using laser anemometry",PH.D.Thesis,Edinburgh University.

DEAN,W.R.,1927,"Note on the motion of a fluid in a curved pipe",Phil.Mag.(7)4,PP 208-223.

DEAN,W.R.,"The Stream-line Motion of Fluid in a Curved Pipe (Second Paper),Phil.Mag.(7),5,PP 673-695,1928.

DEAN,W.R. and HURST,J.M.,1959,"Note on the Motion of Fluid in a Curved Pipe",Mathematika(6),PP 77-85.

DENISON,E.R. and STEVENSON,W.H.,1970,"Oscillatory flow measurements with a directionally sensitive laser velocimeter",Rev. of Sci.Inst.,Vol. 41,10,PP 1475-1478.

DURRANI,T.S. and GREATED,C.A.,1977,"Laser Systems in Flow Measurement",(New York:Plenum).

FOORD,R.,HARVEY,A.F.,JONES,R.,PIKE,E.R. and VAUGHAN,J.M., 1974,"A solid-state electro-optic phase modulator for laser Doppler anemometry",J.Phys.O.Appl.Phys.7,L36-39.

GANT,R.P.,1967,"Electronic Speed Control for Electric Drills and Food Mixers",Mullard Technical Communications, No. 89.

GERRARD,J.H. and HUGHES,M.D.,1971,"The Flow due to an oscillating piston in a cylindrical tube: a comparison between experiment and a simple entrance flow theory", J.Fluid Mech.,Vol. 50,PT. 1,PP 97-106.

GREENSPAN,D.,1973,"Secondary Flow in a Curved Tube", J.Fluid Mech.,Vol. 57,PT. 1,PP 167-176.

GROBNER,W. and HOFREITER,N.,1949,Integraltafel Vols. I,II, (Wien:Springer).

HANSON,S.,1973,"Broadening of the measured frequency spectrum in a differential laser anemometer due to interference plane gradients",J,Phys.D:Appl.Phys.Vol. 6,PP 164-171.

KARMAN,Th.V.,1934,"Some aspects of the turbulence problem", Proc.4th Int.Congr.Appl.Mech.Cambridge,PP 54-59.

KOGELNIK,H.,1965,"Imaging of Optical Modes-Resonators with Internal Lenses",The Bell System Tech.Journal, PP 455-494.

KOGELNIK,H., and LIN,T.,1966,"Laser beams and resonators", Appl.Opt. 5,PP 1550-1567.

KREID,D.K.,1974,"Error estimates for laser Doppler velocimeter in non-uniform flow",Appl.Opt.,Vol. 13, PP 1872-1881.

LARRAIN,J. and BONILLA,C.F.,1970,"Theoretical Analysis of Pressure Drop in the Laminar Flow of Fluid in a Coiled Pipe",Trans. of the Soc. of Rheol.,14:2,PP 135-147.

LYNE,W.H.,1970,Ph.D Thesis,Univ. of London.

LYNE,W.H.,1970,"Unsteady Viscous Flow in a Curved Pipe", J.Fluid Mech.,45,1,PP 13-31.

McCONALOGUE,D.J. and SRIVASTAVA,R.S.,1968,"Motion of a fluid in a Curved Tube",Proc.Roy.Soc.(A),PP 37-53.

MUNSON,B.R.,1975,"Experimental Results for Oscillating Flow in a Curved Pipe",Phys.Fluids 18:12, PP 1607-1609.

MUNSON,B.R.,1976,"Secondary Flows in a slowly oscillating torus",Phys.Fluids,19:11, PP 1823-1825.

OLSEN,D.G.,1971,"Fluid Mechanics Relevant to Respiration-Flow Within Curved or Elliptical Tubes and Bifurcating Systems",Ph.D Thesis,Imperial College,London.

PIKE,E.R. and CUMMINS,H.Z.,1977,"Photon-correlation Spectroscopy and Velocimetry",(New:Plenum).

RAYLEIGH,LORD,1916,"On the dynamics of revolving fluids", Scientific Papers,Vol. 6,PP 447-453.

REYNOLDS,J.A., and HYETT,A.W.,1974,"A simple sine wave pressure generator",J.Phys.E.Sci.Instrum.,7,PP 166-167.

RICHARDSON,E.G. and TYLER,E.,1929,"The transverse velocity gradient near the mouths of pipes in which an alternating or continuous flow of air is established", Proc.Roy.Soc.A., Vol. 42,PT. 1,PP 1-15.

SCHLICTING,H.,1932,"Berechnung Ebener Periodischer Grenzschichtstro Mungen",Phys.Z., 33,PP 327-335.

SCHLICHTING,H.,1955,"Boundary Layer Theory",Permagon.

SEXL,T.,1930,"Uber der von E.G.Richardson entdeckten 'Annulareffekt' ".Zeitschrift fur Physik,PP 349-362.

SIEGMAN,A.E.,1977,"Quasi-fast Hankel Transform",Optics Letters,Vol. 1,No. 1,PP 13-15.

SINGH,M.P.,1974,"Entry flow in a curved pipe", J.Fluid Mech.,65,PP 517.

SMITH,F.T.,1975,"Pulsatile flow in curved pipes",J.Fluid Mech.,Vol. 71,PP 15-42.

SMITH,F.T.,1976,"Fluid Flow into a Curved Pipe",Proc.R.Soc. London,A,Vol. 351,PP 71-87.

SNEDDON,I.N.,1946,"Finite Hankel transforms",Phil.Mag., 37,PP 17-25.

STROUD,A.H.,1966,"Gaussian Quadrature Formulae",(Prentice Hall).

STUART,J.T.,1963,"'Unsteady Boundary Layers' in Laminar Boundary Layers",ed.L.Rosenhead,Oxford.

TAYLOR,G.I.,1923,"Stability of a viscous liquid contained between two rotating cylinders",Phil.Trans.A.,Vol.223, PP 289-343.

TAYLOR,G.I.,1929,"The Criterion for Turbulence in Curved Pipes",Proc.Roy.Soc.(London),A.Vol. 124,PP 243-249.

TRANTER,C.J.,1951,"Integral Transforms in Mathematical Physics",Methuen.

UCHIDA,S.1956,"The Pulsating Visccus Flow Superposed on the Steady Laminar Motion of Incompressible Fluid in a Circular Pipe",Z.A.M.P. Vol.7,PP 403-421.

VLACHOS,N.S. and WHITELAW,J.H.,1974,"The Measurement of Blood Velocity with Laser Anemometry",Proc.Second Int. Workshop on Laser Velocimetry,Purdue University,PP521-540.

WHITE,C.M.,1929,"Streamline Flow Through Curved Pipes", Proc.Roy.Soc.(London),A.Vol.123,PP 645-663.

WOMERSLEY,J.R.,1955,"Method for the Calculation of velocity, rate of flow and viscous drag in arteries when the pressure gradient is known",J.Physiol.,PP 127,553.

WOMERSLEY,J.R.,1957,"An elastic tube theory of pulse transmission and oscillatory flow in mammalian arteries",W.A.D.C. Technical Report,TR 56-614,Wright Air Development Center.

YAO,L.S. and BERGER,S.A.,1975,"Entry flow in a Curved Pipe", J.Fluid Mech.,Vol. 67,PT. 1,PP177-196.

ZALOSH,R.G.,1970,"Pulsating Flow in a Curved Tube",PH.D Thesis, Northeastern University, Boston.

ZALOSH,R.G.,1973,"Pulsating Flow in a Curved Tube",J.F.M. Vol. 59,PT. 4,PP 693-705.